ORNL/TM-9994

ornl

OAK RIDGE NATIONAL LABORATORY

MARTIN MARIETTA

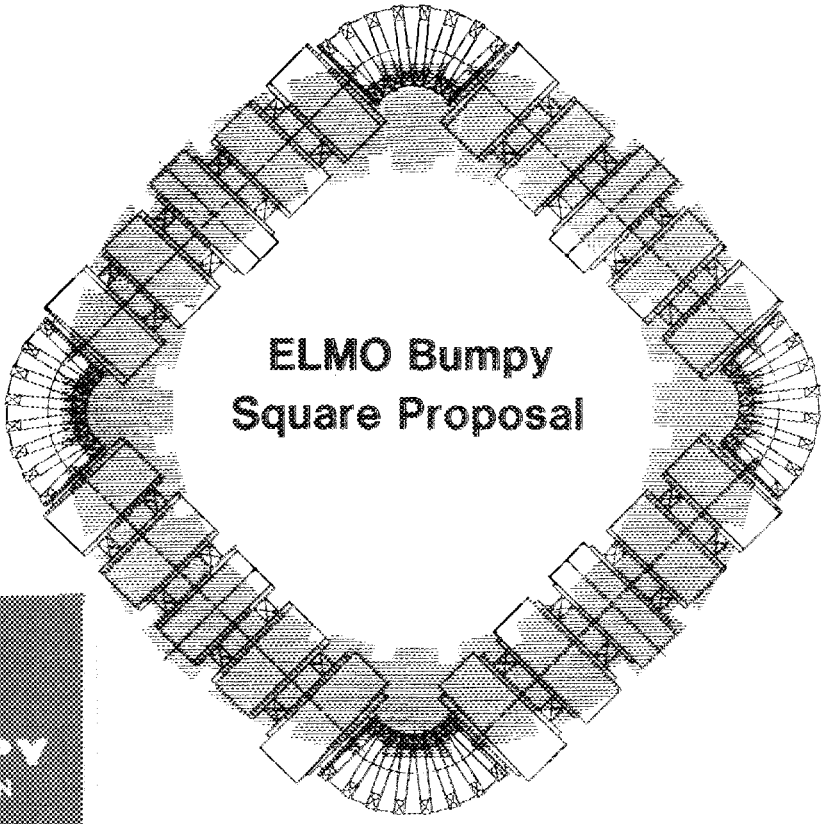

ELMO Bumpy Square Proposal

R. A. Dory
N. A. Uckan

W. B. Ard
D. B. Batchelor
L. A. Berry
W. E. Bryan
R. A. Dandl
G. E. Guest
G. R. Haste
D. E. Hastings
C. L. Hedrick
D. K. Lee
T. J. McManamy
R. L. Miller
L. W. Owen
J. F. Pipkins
R. J. Schmidt
J. Sheffield
D. A. Spong
P. B. Thompson
J. S. Tolliver
T. Uckan
W. L. Wright

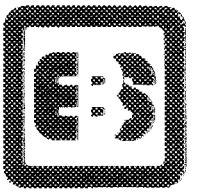

Elmo Bumpy Square

OPERATED BY
MARTIN MARIETTA ENERGY SYSTEMS, INC.
FOR THE UNITED STATES
DEPARTMENT OF ENERGY

Printed in the United States of America. Available from
National Technical Information Service
U.S. Department of Commerce
5285 Port Royal Road, Springfield, Virginia 22161
NTIS price codes--Printed Copy: A18 Microfiche A01

ORNL/TM-9994
Dist. Category UC-20 f,g

Fusion Energy Division

ELMO BUMPY SQUARE PROPOSAL

R. A. Dory N. A. Uckan

W. B. Ard*
D. B. Batchelor
L. A. Berry
W. E. Bryan†
R. A. Dandl‡
G. E. Guest**
G. R. Haste
D. E. Hastings††
C. L. Hedrick
D. K. Lee‡‡
T. J. McManamy†
R. L. Miller‡
L. W. Owen‡‡
J. F. Pipkins*
R. J. Schmidt*
J. Sheffield
D. A. Spong
P. B. Thompson†
J. S. Tolliver‡‡
T. Uckan
W. L. Wright†

*McDonnell Douglas Astronautics Company, St. Louis.
†Engineering Division, Martin Marietta Energy Systems, Inc.
‡Applied Microwave Plasma Concepts, Inc., Encinitas, Calif.
**GA Technologies, Inc., San Diego.
††Now at Massachusetts Institute of Technology, Cambridge.
‡‡Computing and Telecommunications Division, Martin Marietta Energy Systems, Inc.

Date Published: October 1986

Prepared by the
OAK RIDGE NATIONAL LABORATORY
Oak Ridge, Tennessee 37831
operated by
MARTIN MARIETTA ENERGY SYSTEMS, INC.
for the
U. S. DEPARTMENT OF ENERGY
under Contract No. DE-AC05-84OR21400

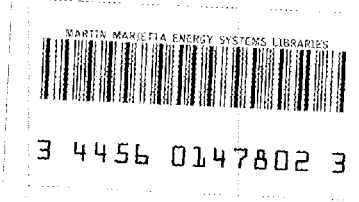

PREFACE

The proposal documented in this report was submitted to the U.S. Department of Energy (DOE) in September 1985. It was reviewed by a panel of fusion experts who were generally favorably disposed toward the proposal. The panel observed that the arguments in the proposal did not prove that the device would operate as suggested; it was, of course, the object of the experimental program to address that issue.

Although DOE was apparently also favorably disposed toward the proposed experiment, a limited fusion budget precluded the possibility of proceeding in the near term. For this reason, the proposal is issued here as a technical memorandum, so that the information collected will be available should a later, more favorable funding climate allow reopening of the issues raised in the EBS program plan. Some of this material was published in the *ELMO Bumpy Square Status Report* (ORNL/TM-9110) in October 1984 and is included here only for purposes of completeness. Other sections provide an abundance of new material not available elsewhere.

R. A. Dory

February 1986

CONTENTS

ACKNOWLEDGMENTS

We appreciate strong support and contributions from the staff at Oak Ridge National Laboratory and from the members of the EBT community. Special acknowledgments are owed to N. A. Krall for dedicated efforts and advice. The continued interest of H. L. Berk, H. Grad, H. Ikegami, N. H. Lazar, J. B. McBride, K. Moses, M. N. Rosenbluth, J. W. Van Dam, and H. Weitzner is gratefully acknowledged.

ABSTRACT

The ELMO Bumpy Square (EBS) concept consists of four straight magnetic mirror arrays linked by four high-field corner coils. Extensive calculations show that this configuration offers major improvements over the ELMO Bumpy Torus (EBT) in particle confinement, heating, transport, ring production, and stability. The components of the EBT device at Oak Ridge National Laboratory can be reconfigured into a square arrangement having straight sides composed of EBT coils, with new microwave cavities and high-field corners designed and built for this application. The elimination of neoclassical convection, identified as the dominant mechanism for the limited confinement in EBT, will give the EBS device substantially improved confinement and the flexibility to explore the concepts that produce this improvement.

The primary goals of the EBS program are twofold: first, to improve the physics of confinement in toroidal systems by developing the concepts of plasma stabilization using the effects of energetic electrons and confinement optimization using magnetic field shaping and electrostatic potential control to limit particle drift, and second, to develop bumpy toroid devices as attractive candidates for fusion reactors.

This report presents a brief review of the physics analyses that support the EBS concept, discussions of the design and expected performance of the EBS device, a description of the EBS experimental program, and a review of the reactor potential of bumpy toroid configurations. Detailed information is presented in the appendices.

1. INTRODUCTION

1.1 BACKGROUND

The ELMO Bumpy Torus (EBT) concept was developed in the 1970s to test the idea of stabilizing a multiple-mirror plasma through the use of electron rings, while eliminating end losses by closing the device into a toroid. It was expected to overcome both the end losses of a simple mirror system and the instability inherent in a simple bumpy torus.

The EBT device at Oak Ridge National Laboratory (ORNL) demonstrated the existence of a quiescent mode of operation in which the plasma was stabilized by hot electron rings and the confinement was better than that in single mirrors of comparable size. Although these design goals were successfully achieved, the confinement properties of the EBT device remained limited by major radial losses of particles and energy.

During the last few years, improved diagnostics permitted better measurements of plasma parameters on EBT, and detailed theoretical calculations helped to identify and quantify the important heating and transport mechanisms. The underlying physics that limited the performance characteristics was attributed to poor particle confinement, caused by toroidal effects inherent in the circular torus. These effects caused substantial direct particle losses, convective losses (because of asymmetric equipotential surfaces), an inefficient geometry for electron cyclotron heating (ECH), and less than optimal ring formation.

The ELMO Bumpy Square (EBS) configuration, developed at ORNL by L. W. Owen in 1982, is one of several concepts (including the Andreoletti torus, the twisted racetrack, and the snakey torus) proposed to solve the problems of the EBT. As discussed at the U.S.-Japan Workshop on Advanced Bumpy Torus Concepts in July 1983,[1] common features of these devices include improved particle confinement or improved centering of drift orbits, reduced neoclassical step size, reduced loss cone or direct particle loss, and increased confinement efficiency. Detailed studies of these concepts show that the reconfiguration of the EBT device from a torus into a square, with stronger magnetic fields at the corners, is feasible and is the logical direction for further investigation. This judgment was confirmed in the report of the Magnetic Fusion Advisory Committee Subpanel IX, which stated:

> Among the configurations which offer the improvements described above, the EBS has emerged as the one that can be developed most rapidly and with the smallest budget.... Based on contributions of the EBT program to

> fusion development as a whole, as well as the reactor development potential, the Panel recommends that the program be carried out even in constrained budget case....

The selection of the EBS concept for experimental testing was based on three factors:

- its ability to address and resolve critical issues in a cost-effective manner,
- its potential contributions to the physics and technology of fusion as a whole, and
- its intrinsic desirability as a reactor configuration.

The plan presented in this report was developed by ORNL staff members in collaboration with scientists and engineers from the universities, industrial groups, and laboratories listed in Table 1.

Table 1. Organizations collaborating on EBS proposal

Oak Ridge National Laboratory	Rensselaer Polytechnic University
Auburn University	Science Applications International Corp.
Applied Microwave Plasma Concepts, Inc.	TRW, Inc.
JAYCOR Corp.	University of Texas
McDonnell Douglas Astronautics Co.	University of Wisconsin
New York University	

The reconfiguration of the EBT device into an EBS is summarized in Sect. 1.2. The physics advantages of the EBS configuration are briefly discussed in Sect. 1.3, and Sect. 1.4 describes the projected performance. The reactor aspects of bumpy toroids are addressed in Sect. 1.5, and the contributions of the EBT program to the development of fusion are summarized in Sect. 1.6. Section 1.7 describes the organization of the remainder of the report.

1.2 CONFIGURATION

A conceptual design has been completed for EBS, involving removal of the EBT device and reconfiguration of its components. Plan views of the existing EBT device and of the EBS experiment are shown in Fig. 1.

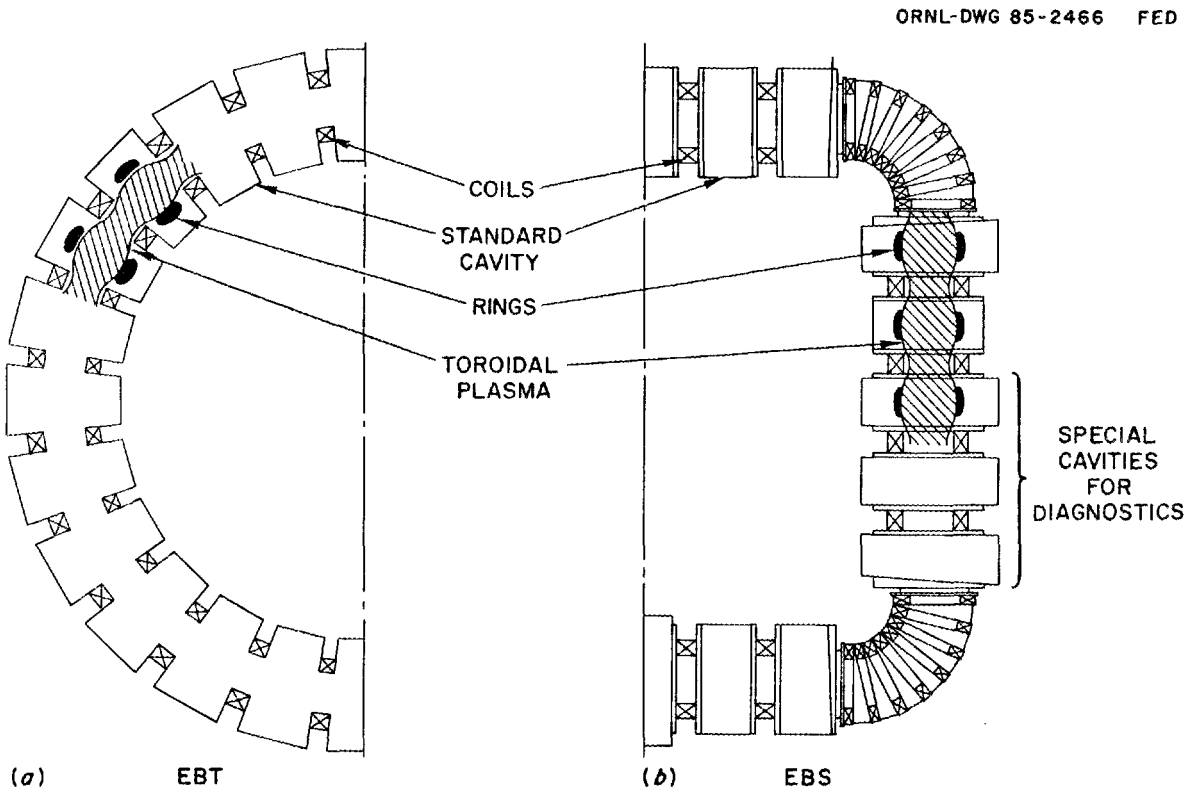

Fig. 1. Top view of the EBT configuration (left) and the EBS reference configuration (right). The diagram shows how the existing EBT mirror coils will be used in the sides of EBS, which will require new corner coils and microwave cavities. There will be 14 standard cavities and 6 instrumented cavities for diagnostics.

The straight sides of EBS are composed of EBT coils, four on each side, installed between new microwave cavities. The straight sections are connected by high-field corners, which will be designed and built for EBS.

The engineering analysis presented in this report is based on corners consisting of half-width EBT coils, constructed using the design and engineering drawings developed for the original EBT coils to generate a field with negligible field ripple. This approach minimizes engineering cost and construction time, but it entails substantial operating costs for electricity. As described in the appendices, two alternatives that would reduce operating costs have been studied. The first calls for more copper in the corner coils, and the second calls for superconducting wire (already on hand) and requires dewar fabrication and refrigeration. A final decision will be made following more detailed analysis.

The EBS device has been planned to make maximum use of the facilities developed to support the EBT experiment. As shown in Fig. 2, EBS will be placed in the lead-walled enclosure formerly occupied by EBT. A new substructure will

be installed following removal of the EBT device, and a new microwave duct and vacuum manifold will be provided. Because each set of eight corner coils will be powered by a 3-MW generator, an additional 12 MW of power will be required. The power distribution and cooling water systems will be modified to meet this requirement.

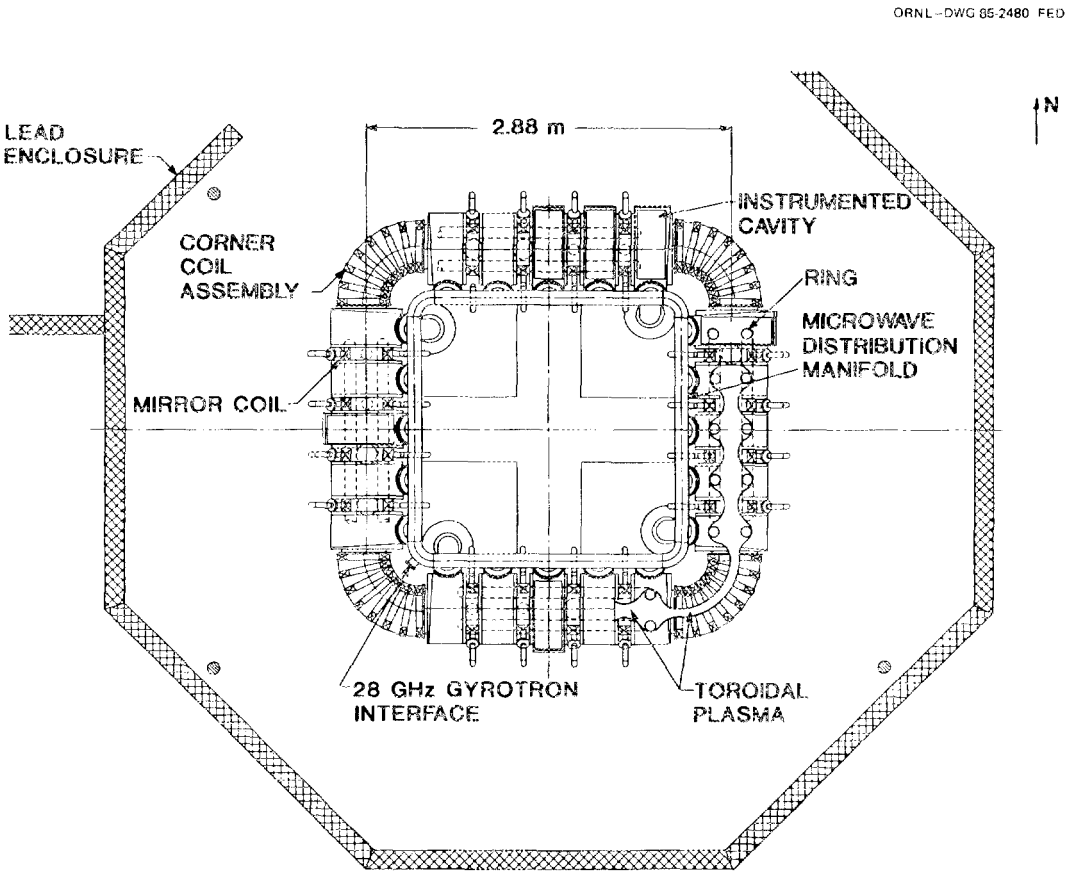

Fig. 2. Plan view of an EBS device within the lead-walled biological shield enclosure originally used for EBT.

Instrumentation and control (I&C) systems and the microwave network used for EBT can be adapted to EBS with minimal changes. Diagnostics, data acquisition systems, and computer systems will also be removed from EBT and reinstalled on EBS.

The capital investment involved in the reconfiguration of EBT into EBS is minimal. The estimated construction cost is $4 million (as of September 1985).

No critical elements, in terms of new or ongoing component research and development, are required for the EBS device. Design, fabrication, and assembly can be carried out using available technology.

1.3 PHYSICS CONSIDERATIONS

The results presented in this report show that the EBS configuration offers distinct advantages over EBT in particle confinement, heating, transport, ring production, and stability. These results may be summarized as follows.

1. The drift orbits for all classes of particles (trapped, passing, and transitional) are better centered in EBS than in EBT, as shown in Fig. 3.

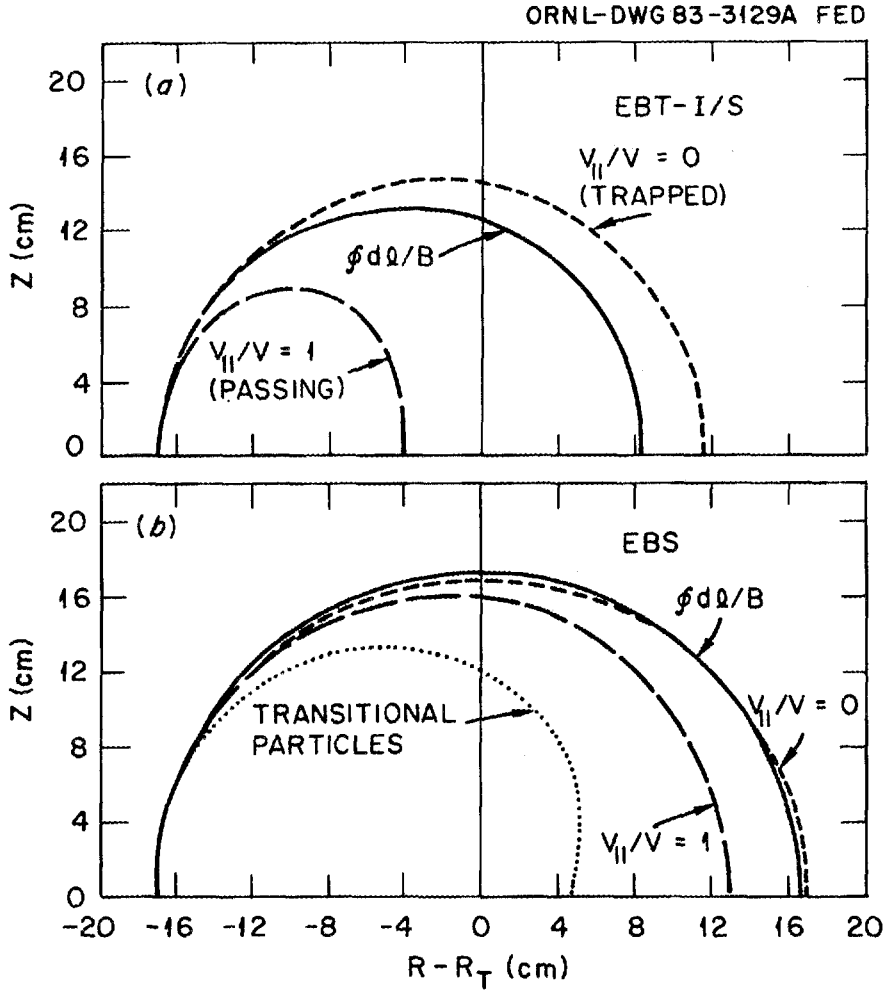

Fig. 3. Drift orbits (dashed lines) and $\oint dl/B$ contours (solid lines) in the reference midplane of EBT (top) and EBS (bottom). Deeply trapped ($v_{||}/v = 0$), extreme passing ($v_{||}/v = 1$), and transitional particles near the boundary between the trapped and passing zones (most poorly confined drift orbit) are shown. Transitional particle orbits were absent from EBT (i.e., the worst orbit did not close within the volume) but are reasonably well contained in EBS.

2. The orbits of deeply trapped particles ($v_\parallel/v \approx 0$) and the core pressure surfaces ($\int dl/B$ contours) almost coincide in EBS and are centered on the minor axis (see Fig. 3). Because there is little radial shift in major radius, the hot electron rings will be well centered (i.e., they will form in nearly axisymmetric fields) and will experience less of the radial broadening that occurred in EBT. This should make it easier to form an average magnetic well and thus to provide strong MHD stabilization at higher pressures and pressure gradients.

3. The velocity-space loss region for transitional particles (those near the boundary between the trapped and passing zones) at high energy is greatly reduced, which produces improved volume utilization, as shown in Fig. 4. This also provides an increased radius of confined plasma, a significant reduction in direct particle losses, more nearly symmetric potential surfaces, and increased microwave heating efficiency. For an isotropic distribution, more than 95% of the particles are confined (vs ~50% in EBT).

4. The combination of nearly concentric particle orbits and small radial displacements in the high-field corners reduces the neoclassical *diffusive* losses by an order of magnitude, as shown in Fig. 5. Monte Carlo calculations show that symmetric potential surfaces decrease *convective* losses to an order of magnitude below those obtained with the asymmetric potential surfaces of EBT, as shown in Fig. 6. The theory supporting these conclusions is presented in Appendix 10, which provides a kinetic theory of the formation of the potential by the action of the warm electron tail population. This theory predicts both the 30% asymmetry of the equipotentials in EBT and a reduction by a factor of 100 in the asymmetry for EBS.

5. The neoclassical confinement time τ improves with the global mirror ratio M_G, which is the ratio between the field in the corners B_{corner} and the field in the straight sides or midplane B_{mid}, as $\tau \sim M_G^2$. This relationship is shown in Fig. 7. The ability to change B_{corner} and B_{mid} provides a valuable means of testing neoclassical confinement over a wide range of conditions in a single device.

6. Because of the high B_{corner} and the relatively weak curvature there (about half of the curvature in the straight sides), the core beta limit is largely determined by the ring-core interaction [i.e., the Lee–Van Dam–Nelson (LVDN) limit] in the straight sections, not by ballooning modes in the corners (provided $M_G \gtrsim 4$), as shown in Fig. 8. The narrower ring (resulting from the reduced broadening) will lower the beta for LVDN modes, putting the threshold (100-keV rings) at $\beta_{warm} \sim$ 1–2%, which is energetically possible in EBS. In future devices, rings at about 400 keV would be required to raise β_{warm} to the ~10% range, or, alternatively,

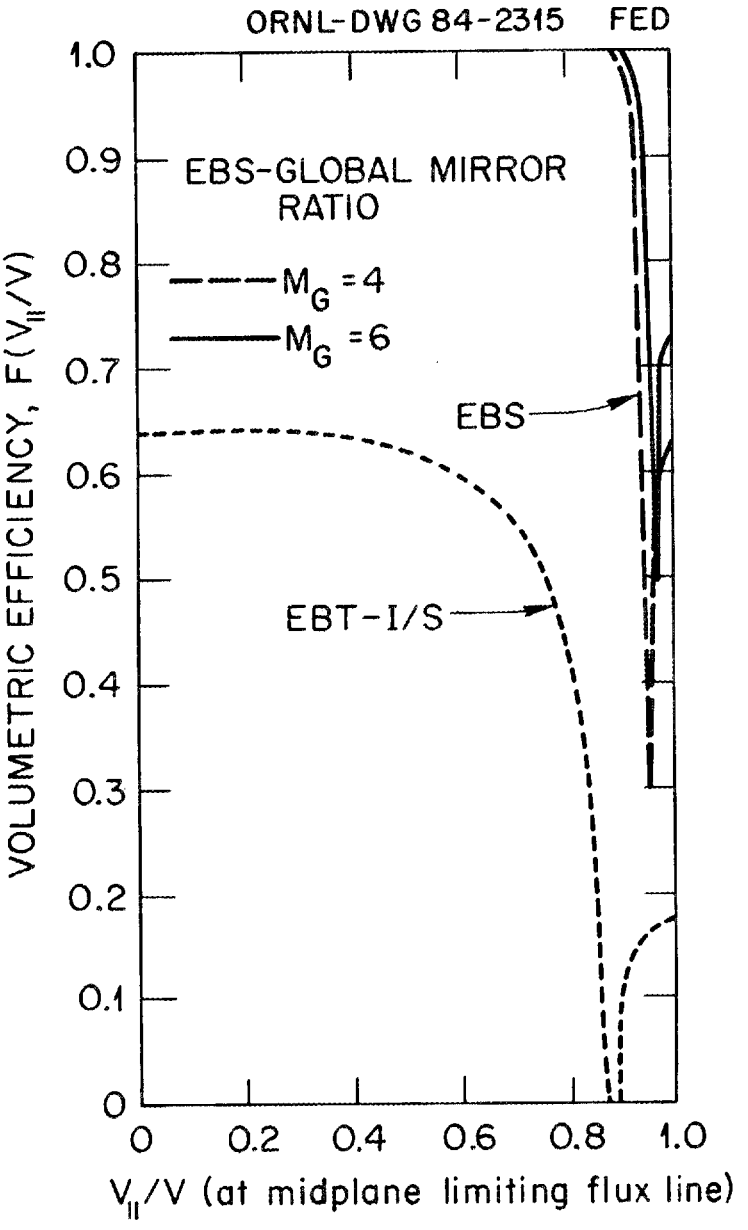

Fig. 4. Volumetric efficiency curves for EBT and EBS as a function of pitch angle at the limiting flux line in the midplane. These show containment of more than 95% of the particle in EBS, compared with ~50% in EBT. (That is, the direct loss fraction is less than 5% in EBS and ~50% in EBT for vacuum fields.)

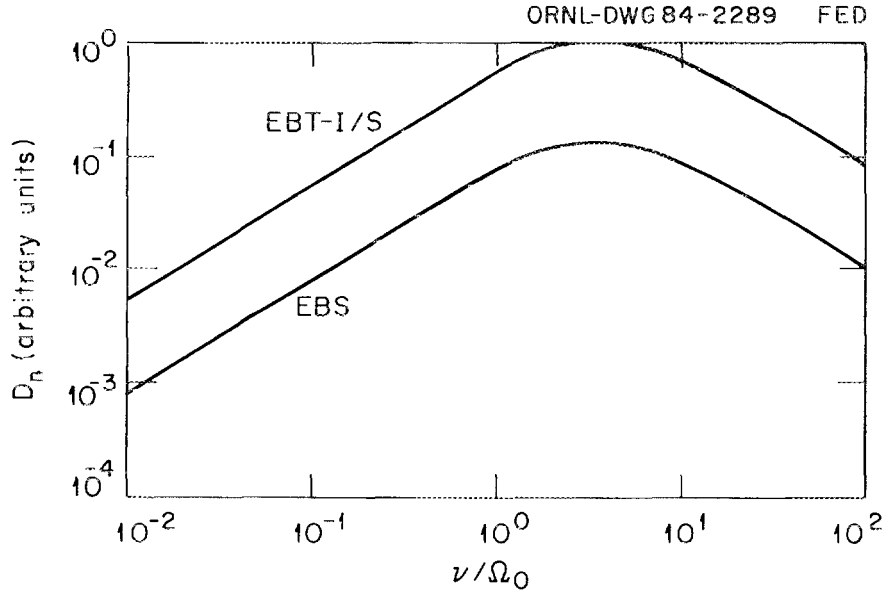

Fig. 5. Particle transport coefficient D_n as a function of collisionality ν/Ω_0 for EBT and EBS. Similar curves are obtained for D_T, K_n, and K_T with the same ratio of improvement in EBS over that in EBT. [Note that $\tau(\text{EBS})/\tau(\text{EBT}) \sim D(\text{EBT})/D(\text{EBS}) \sim 5$–15.]

multiple-frequency heating could be applied to raise the ring width and the LVDN beta value.

7. Heating efficiency is much improved in EBS because the heating zone is well separated from the transitional particle zone. Losses of ECH power are a factor of 5 to 10 lower than in EBT, in which the heating effect was mainly concentrated near the transition boundary between trapped and passing particles, where drifts were most severe. The difference is shown in Fig. 9.

8. The EBS concept is a step toward a reactor design in the regime leading to *attractive* fusion reactors, as described in a recent study (ORNL/TM-9311).[2] The improvement in transport resulting from orbit control leads to an overall size that is a factor of 2 to 3 smaller than that of earlier EBT designs, as shown in Fig. 10. Moreover, a recent assessment[3] of all the candidates for fusion reactors has shown that the EBS shares with tokamaks, stellarators, tandem mirrors, reversed-field pinches, etc., the property of adequate confinement to produce energy at a cost comparable to that of fission energy.

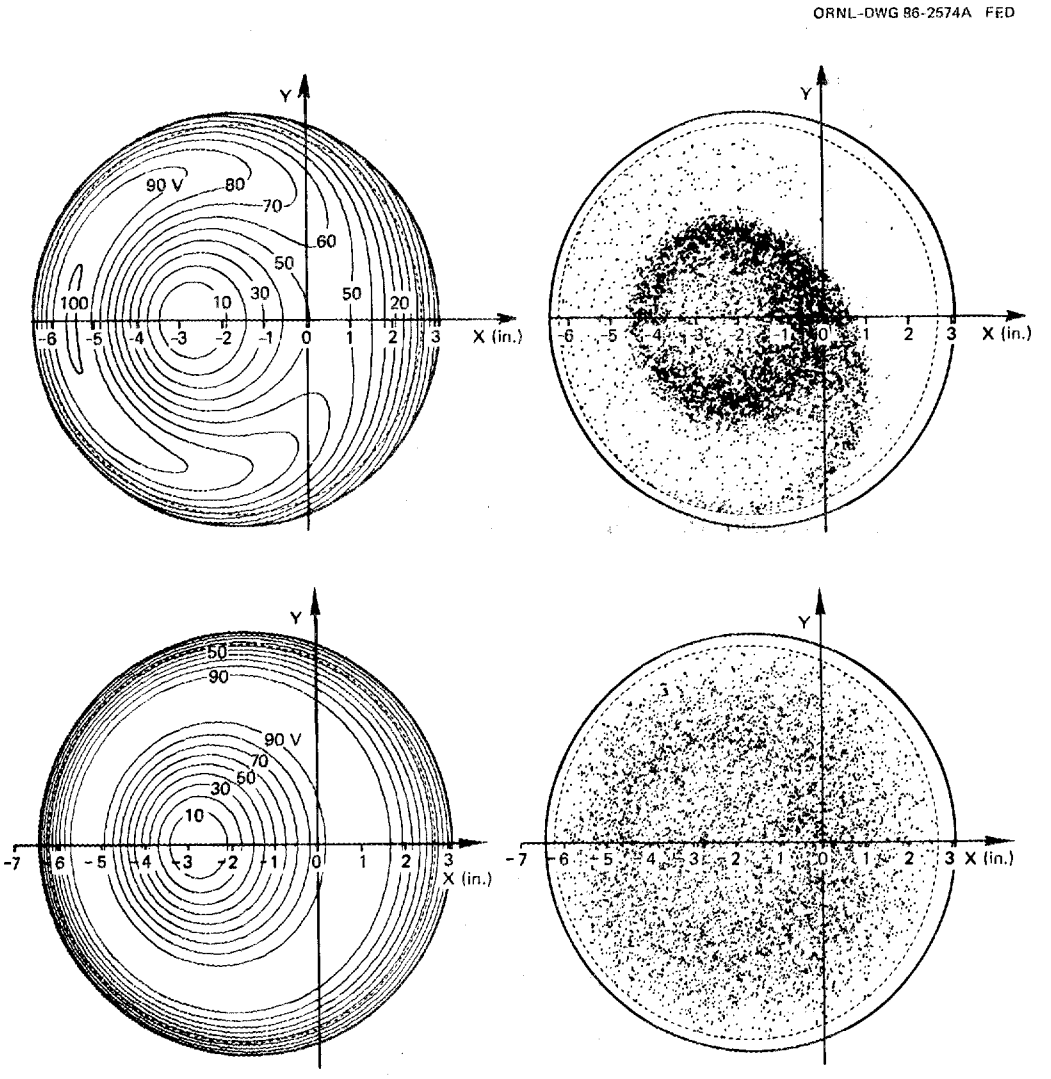

Fig. 6. Potential surfaces (left) and Monte Carlo results (right) for (top) symmetric potentials and (bottom) asymmetric potentials. For symmetric potentials, only diffusive processes are present; for asymmetric potentials, strong $\mathbf{E} \times \mathbf{B}$ drift (convection) is evident. For similar plasma parameters, diffusion lifetimes improve by an order of magnitude.

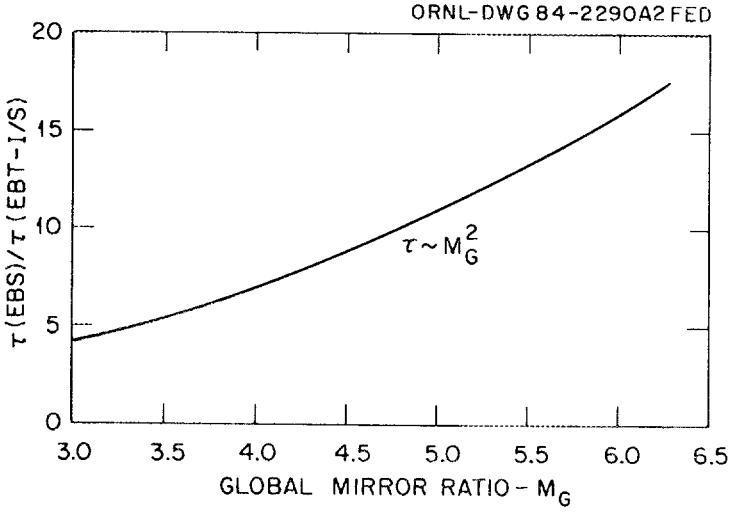

Fig. 7. Variation of confinement time τ with global mirror ratio $M_G = B_{corner}/B_{mid}$.

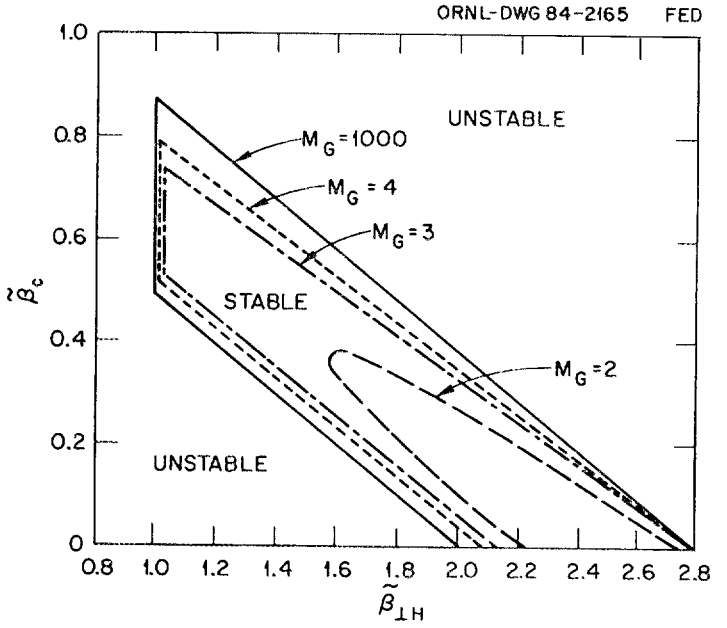

Fig. 8. Stability boundaries in EBS for several values of M_G. Beta values here are scaled to the Lee–Van Dam threshold $\beta_0 = 2\Delta r/R_c$, where Δr is the ring radial width and R_c is the field line radius of curvature in the ring region. Here, $\tilde{\beta}_c = \beta_c/\beta_0$ and $\tilde{\beta}_{\perp H} = \beta_{\perp H}/\beta_0$.

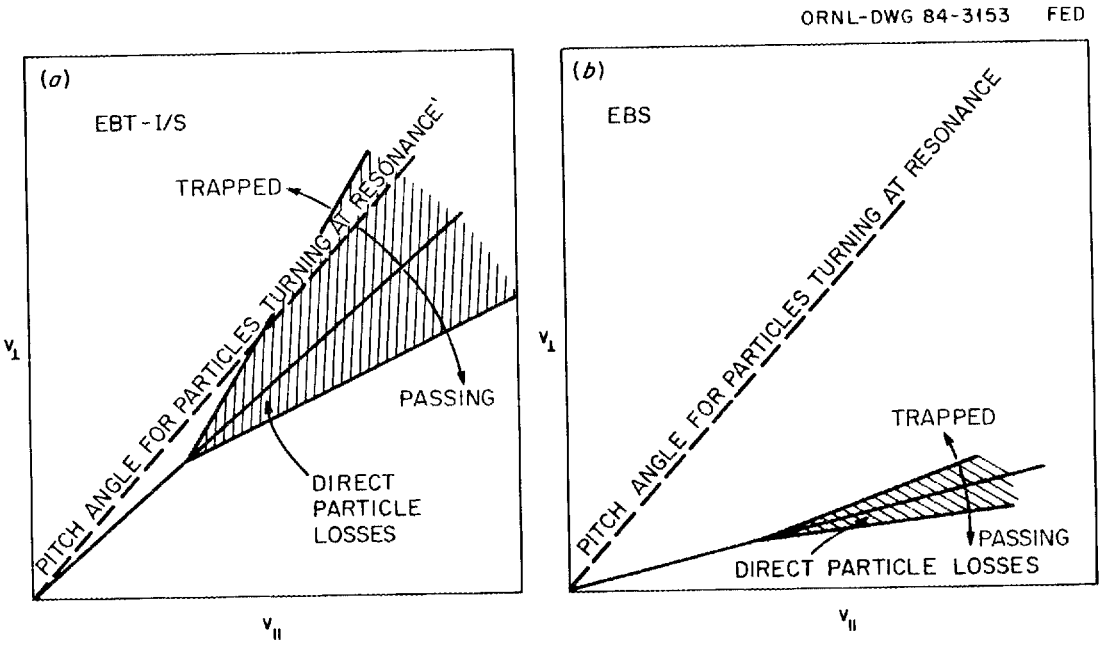

Fig. 9. Heating zone (pitch angle for particles turning at resonance) for (a) EBT and (b) EBS.

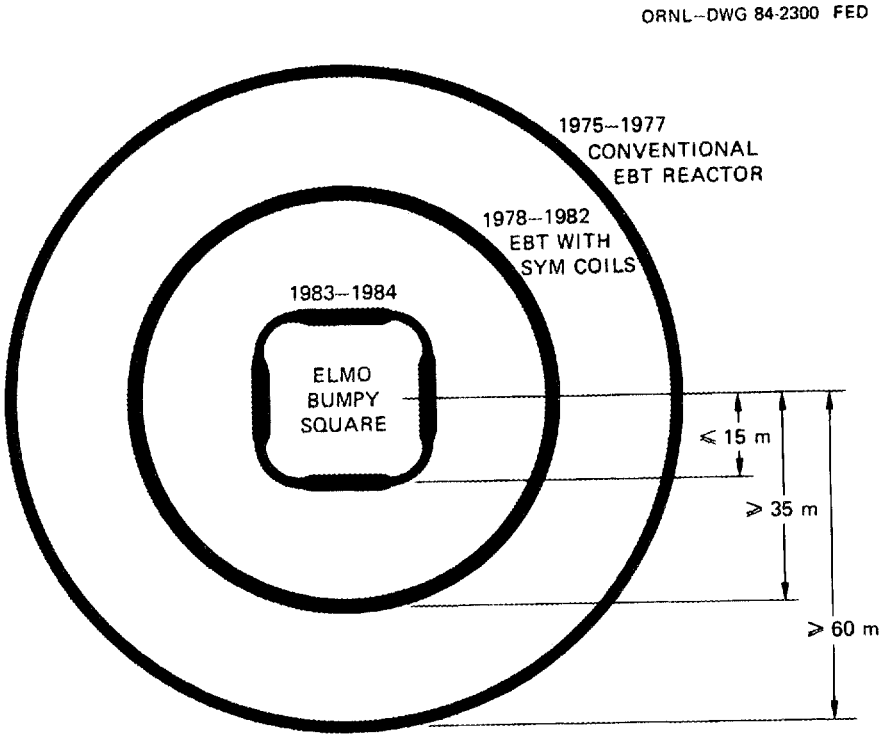

Fig. 10. Trend to smaller EBT reactor systems, which is exploited by EBS. Relative dimensions of EBT reactor configurations are shown, with corresponding years of development.

1.4 PERFORMANCE PROJECTIONS

The performance of the EBS configuration is predicted to be a substantial improvement over that of the EBT device, as shown by the comparison of performance parameters in Table 2.

Table 2. EBT and projected EBS performance data

Parameter	EBT	EBS
Density, cm^{-3}	10^{12}	10^{13}
Power to thermal plasma, %	20	55
Electron temperature, eV	80 in bulk population, 400 in warm population	1000
Ion temperature, eV	50	500
τ_E(gross), ms	$\leq$0.25	5–30
$\beta_{ring}/\beta_{well}$	<1	>2
β_{plasma}, %	0.1	1–2, phase 1 4–8, phase 2

The amount of power delivered to the confined plasma in EBS should be three to five times higher than that in EBT, using the same sources; additional ECH sources are available at ORNL. The EBS plasma density should not be limited by power availability and may therefore approach the microwave cutoff density. The plasma electrons should reach a temperature near 1 keV, with the plasma ions at about half that (allowing for charge-exchange losses) until additional ion heating is applied. Energy confinement times will be in the tens of milliseconds, and beta values will be about 1–2%.

In a second experimental phase, EBS would be operated with the field in the cavities (B_{ring}) reduced to about half the nominal 7 kG in order to achieve higher beta values for testing stability. The field in the corners (B_{corner}) would be held at full value, 22–25 kG, so that the 28-GHz microwaves would continue to heat the bulk plasma, while 18-GHz power would be used to form the rings using second harmonic heating. In this phase, beta values are predicted to be about 4–8%.

Much of the improvement in performance results from the substantial reduction in EBS of parasitic losses of energy, as shown by the power flow diagram in Fig. 11. The reduced losses arise from several factors, which are discussed in detail in Chap. 2. A brief summary of these factors follows.

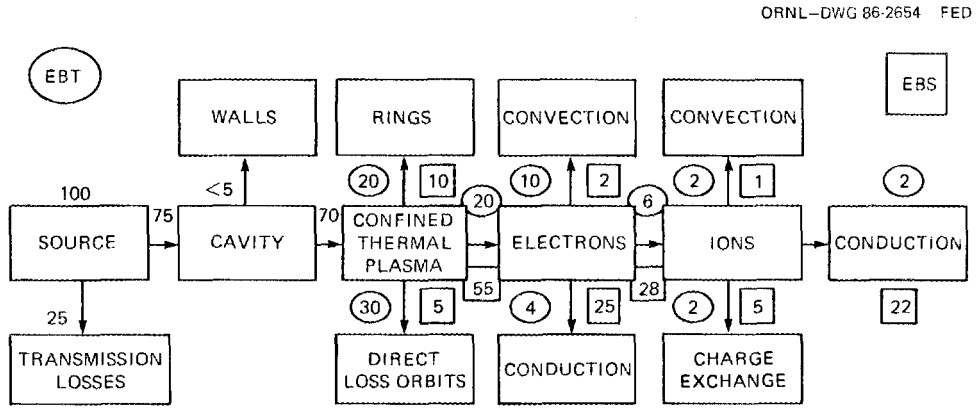

Fig. 11. Schematic power flow diagram for EBS and EBT. Parasitic side losses are substantially reduced in EBS. The numbers are percentages of the microwave source output power; EBT data are enclosed in circles and EBS data in squares.

- Improved heating efficiency leads to a strong reduction in direct losses.
- A reduction in orbit shifts leads to reduced asymmetry in the ambipolar potential, which in turn leads to a large reduction in convection losses.
- Improved orbit centering reduces the heat conduction coefficients for ions and electrons.
- Operation at higher density reduces the proportion of losses from charge exchange.

These factors have been considered self-consistently using the WHIST toroidal transport code with benchmark tests using EBT data. The WHIST runs incorporate radially resolved analysis of ion and electron thermal and particle transport from neoclassical processes, including self-consistently calculated ambipolar potential, and analysis of neutral particle gas feeds, ionization rates, and charge-exchange losses.

The resulting performance curves are shown in Figs. 12 and 13. Figure 12 shows contours in the plane of average density vs average temperature for the regions accessible with varied amounts of microwave power absorbed in the plasma (P_{abs}). Figure 13 shows the resulting beta values obtained with full-field operation.

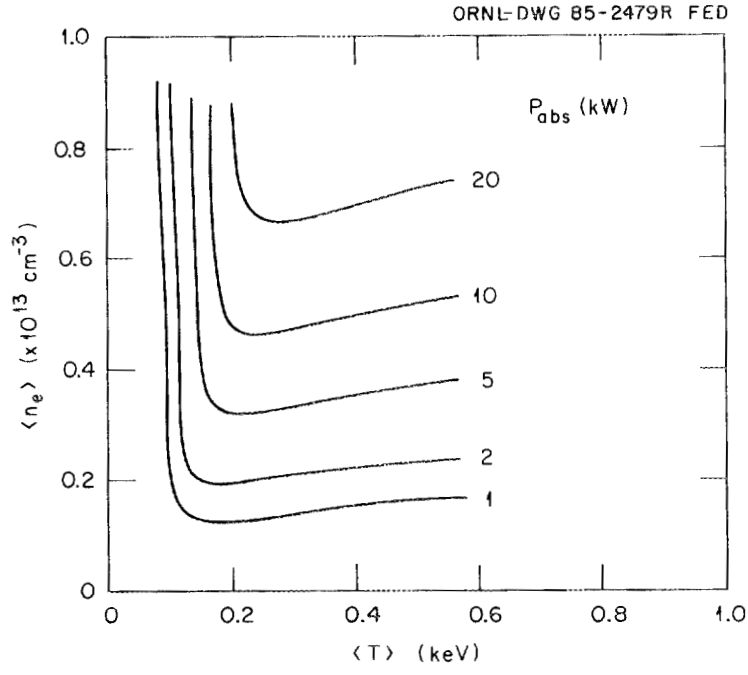

Fig. 12. WHIST code plasma operation contours. The contours show the amount of power that must be delivered to a confined plasma in order to achieve operation at any point in the plane of average density vs temperature. The entire area is predicted to be accessible with the available power, subject to limitation by cutoff at a density of 10^{13} cm^{-3}.

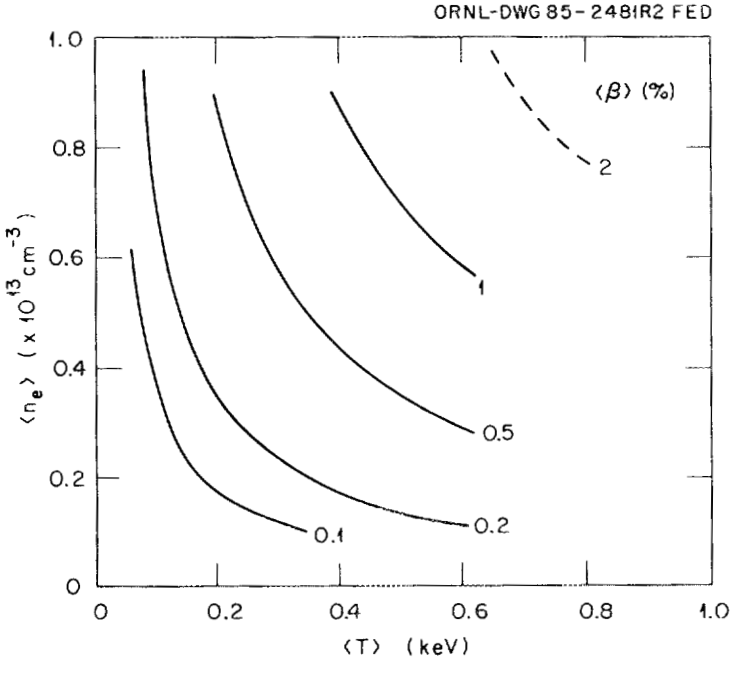

Fig. 13. WHIST code plasma operation contours, showing the beta values achieved during operation at full field.

1.5 REACTOR ASPECTS OF BUMPY TOROIDS

A recent study by Sheffield et al.[2] has determined the general properties of fusion reactors that could be economically competitive with fission reactors under circumstances conjectured for the next century. This study shows that superconducting systems with an aspect ratio less than 15 and with a ratio of magnetic field in the plasma to maximum field in the coils of about 0.5 must have the following characteristics to represent attractive reactor candidates:

- beta values of about 10%,
- thermal transport less than 0.3 $m^2 \cdot s^{-1}$, and
- recirculating power less than 15%.

Two additional characteristics greatly ease the design, operation, and maintenance of a practical fusion plant:

- simple coil and blanket geometry and
- steady-state operation.

The bumpy toroid concept, as represented by the bumpy square and several variants, has the potential to fulfill all of these criteria, and it has the simplest geometry of any steady-state confinement system.

At present, the most critical issues to be addressed in reactor studies are optimization of ring heating, to reduce the sustaining power needed in the new improved confinement geometries, and further reduction of the (effective) toroidal aspect ratio of the device. In the last three years, improvements in field design have led to reduction of this parameter from 60 to 30 to <15, which is at the edge of the attractive reactor regime for this configuration.

The generic reactor studies at ORNL[3] have identified the scale of reactors with superconducting coils that should be competitive with alternative power sources in the future. A simple model can be used to obtain scaling formulae for the key engineering and technology parameters (R/a, b/a, a_w/a, p_{wn}, P_F) of these attractive devices. A rearrangement of the criteria for a self-sustaining D-T plasma then permits us to relate the required $\langle\beta\rangle$ and χ_E to these engineering and technology parameters and obtain

$$\langle\beta\rangle \gtrsim \frac{380(R/a)^{1/4}(a_w/a)^{3/4}(p_{wn})^{3/4}}{(b/a)^{1/8}B_p^2 P_F^{1/4}} \quad (\%), \tag{1}$$

$$\chi_E \lesssim \frac{9.3 \times 10^{-3}(b/a)^{3/8} P_F^{3/4} f_\alpha}{(R/a)^{3/4}(a_w/a)^{1/4}(p_{wn})^{1/4}} \quad m^2 \cdot s^{-1} , \tag{2}$$

where R/a is the aspect ratio, b/a is the ellipticity, a_w is the wall radius ($= a + 0.2$ m), p_{wn} is the neutron flux to the first wall (in megawatts per square meter), P_F is the fusion power (in megawatts), and f_α is the fraction of alpha power lost by thermal diffusion.

In the simple model, which approximates well the more detailed calculation of the generic reactor model, we consider a reactor with electric power output $P_e = 1200$ MW(e), a gross thermal power $P_t = 3750$ MW(t), and $P_F = 3378$ MW(t). The reactor is a simple torus with an average radial build from the plasma to the outside of the coils of $t = 2$ m. The average mass density is $\rho \simeq 5600$ kg $\cdot$ m^{-3}. The reactor material volume is given by

$$M_c \simeq 2\pi^2 R[(a + b)t + t^2]\rho \text{ (kg)} . \tag{3}$$

The unit cost is taken to be 100 \$/kg (direct and indirect), and the fusion island cost for an attractive reactor is \$1000 million (in 1984 dollars). With these assumptions, we use Eq. (3) to find the minor radius,

$$a = \left[\frac{90}{R/a(1 + b/a)t} + \frac{t^2}{4(1 + b/a)^2}\right]^{1/2} - \frac{t}{2(1 + b/a)} \text{ (m)} . \tag{4}$$

Thus, we may calculate a, R, a_w, and p_{wn} as functions of R/a and b/a. For the bumpy torus,

$$\chi_E \simeq \frac{(3.3 \times 10^4)\bar{a}^2(b/a)\langle\beta\rangle B_p^2}{M(R/a)^2(\phi/T_e)^2(T_{ek})^{5/2}} \text{ (m}^2 \cdot \text{s}^{-1}) , \tag{5}$$

where $\bar{a}$ is the average plasma minor radius, allowing for the bumpiness, and M is a factor defined as $M = 1$ for a simple bumpy torus such as EBT and as $M = M_G^2$ for a bumpy square, where M_G is the global mirror ratio. The better confinement of the square configuration is obtained at a smaller aspect ratio (R/a) than that of the torus ($\simeq$15 for EBS vs $\simeq$30 for EBT). As an example, we take $R/a = 15$, $b/a = 1.5$, $B_p = 6$ T, $R = 11.5$ m, $\bar{a} = 0.78$ m, $a_w/a = 1.26$, and $p_{wn} = 5$ MW $\cdot$ m^{-2}. For these values, with $T_{ek} = 20$ keV and $(\phi/T_e) = 3$ (as typically observed in bumpy tori), we find from Eqs. (1) and (2) that we need $\langle\beta\rangle \geq 10\%$ and $\chi_E \lesssim 0.3$ m$^2 \cdot$s^{-1}, where the volume-average beta $\langle\beta\rangle$ is the plasma pressure normalized to the average magnetic field B_p and χ_E is the average radial thermal diffusivity in the mirror cell.

Theoretically, an EBS should attain this beta level. From Eq. (5), the expected thermal diffusivity for this case is $\chi_E = 0.1\ m^2 \cdot s^{-1}$, which leaves a margin on confinement of a factor of 3.

The results of these calculations for a range of effective aspect ratio values are plotted in Fig. 14, along with corresponding curves for other fusion confinement schemes. It can be seen that the physics capability of EBS devices to be attractive reactors is on the same order as that of other devices.

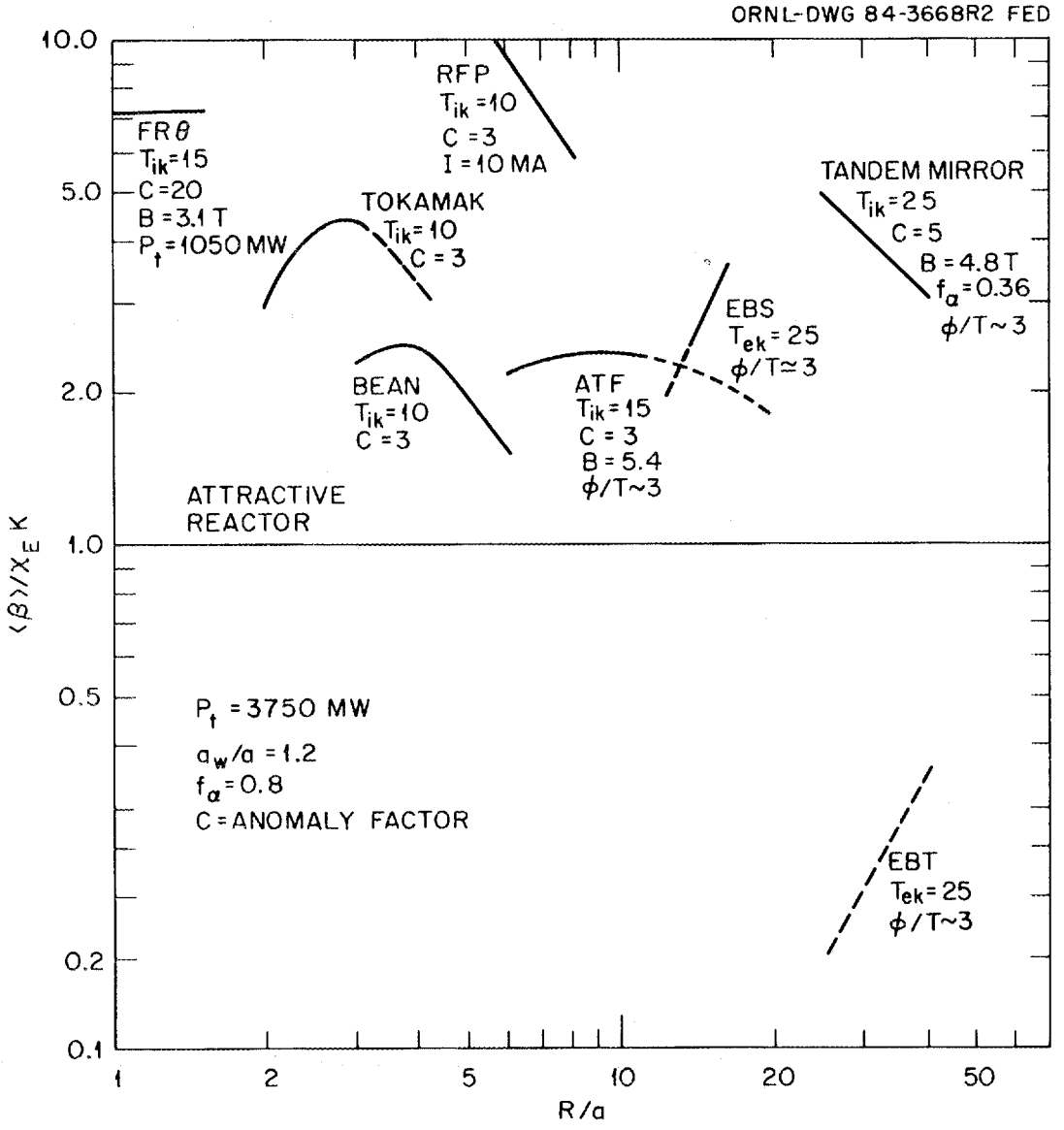

Fig. 14. Neoclassical predictions for attractive reactors. The EBS margin of safety for achieving attractive reactor performance is of the same order as that of other fusion reactor candidates.

The issues to be resolved experimentally are, therefore, the following:

- To what extent does χ_E match classical predictions?
- What is the level of ϕ/T_e and can it be varied profitably?
- What $\langle\beta\rangle$ level can be sustained with good confinement?
- Can rings be produced efficiently at an average field of 6 T?

1.6 CONTRIBUTIONS OF BUMPY TOROIDS TO THE FUSION REACTOR PROGRAM

The contributions of the EBT program to the development of fusion cover a broad range, including

- ECH physics and technology,
- nonaxisymmetric transport (ambipolar potential),
- heavy-ion beam diagnostics,
- steady-state plasma-wall interaction,
- stabilization of plasmas by hot electrons and physics of very high temperature plasmas, and
- steady-state, modular reactor concepts.

The EBS program will allow continued contributions in these areas and will also advance research in the following areas:

- kinetic stabilization of plasmas by hot electrons in systems with higher pressures and pressure gradients,
- control of the ambipolar potential,
- effect of high fields on confinement,
- rf-driven transport,
- advanced configuration design, and
- improved coupling of ECH to plasma.

The EBT program has been a major driver for the development of a number of physics areas, including:

- stabilization by energetic particles,
- three-dimensional equilibrium, stability, and transport (including ambipolar electric fields), and
- ECH.

For example, in the area of stability theory, EBT provided the major impetus for extensive studies of the spatial stability properties of energetic-particle plasmas. These studies have been fruitful in extending the fundamental theory of stability and in obtaining fusion-relevant stability criteria for EBT devices, mirrors, and tokamaks. Also inspired by EBT was the development of a new variational principle and of detailed eigenmode analyses valid in the previously unexplored regime of modes that grow on the hot electron curvature drift time scale. The EBT device served as the motivation for generalization of the gyrokinetic equation to arbitrary frequencies and relativistic energies. These theories were applied to EBT and have productive applications to both mirrors and tokamaks.

1.7 ORGANIZATION OF THE REPORT

Chapter 2 of this report presents a description of the experimental program proposed for the EBS device, and Chap. 3 is an overview of the existing and required facilities. Resources, cost, and schedule are briefly addressed in Chap. 4. The opportunities for collaboration with the fusion community are addressed in Chap. 5.

The appendices present a great deal of information gained during studies of EBS. Detailed discussions of magnetics, single-particle drift orbits, numerical calculations of neoclassical transport coefficients, field ripple effects in the corners, and field error calculations are presented in Appendices 1–3. Appendix 4 includes discussions of the MHD equilibrium properties and single-particle orbit characteristics of EBS, extensions of closed-line magnetic equilibrium theories, vacuum field approximations, a qualitative discussion of the modifications produced by high-beta rings, estimates of the parallel electric fields from parallel currents, and the connection of single-particle drift orbits to equilibrium via the drift kinetic equations.

Discussions of the characteristic instability modes associated with the square configuration, and their parallels in other confinement devices, are given in Appendices 5–7. In particular, the limitations in core plasma beta that result from ballooning modes (in corners) are analyzed using an MHD formalism in Appendix 6 and a generalized kinetic energy principle in Appendix 7.

The conceptual design of the EBS device is summarized in Appendix 8. The results of the reactor assessments for advanced bumpy torus configurations, which include the favorable prospects for EBS, are discussed in Appendix 9. Appendices 10–12 present some new results on symmetrization of the potential and the resulting improvements to the transport. Finally, Appendix 13 is an analysis of alternative corner coils for EBS.

2. RESEARCH PROGRAM

The principal objectives of the research program, summarized below, are discussed further in Sect. 2.1. The research program is described in detail in Sects. 2.2 - 2.5.

Stabilization of toroidal plasmas by energetic electron rings. It is known both theoretically and experimentally that plasma stability is enhanced by "magnetic wells" or "reversed grad-B." Energetic electron rings provide magnetic wells when the ring energy, or beta, is sufficiently high. In EBT, stabilization from ring effects occurred even before the beta value for average well formation was reached. The EBS experiment should have substantially higher beta than EBT because of improved heating efficiency and particle confinement; it should therefore provide both a clearer test of the principles of stabilization and the capability to explore the severity of possible limitations, such as unstable coupling between the ring and toroidal plasmas.

Reduction of thermal losses by drift optimization. In toroidal confinement devices, the particle and energy losses can be controlled by shaping of the magnetic field geometry and by radial electric fields. The EBS is the first fusion device in which detailed optimization of drift orbits has been incorporated *ab initio* to control transport. A key factor in assessing and understanding the effectiveness of orbit improvement is the ability to vary the degree of optimization in EBS by changing the relative magnetic fields of the corners and sides and by changing the electric potential through selective heating of particle subpopulations.

Evaluation of reactor prospects for bumpy systems. The bumpy torus has long presented the prospect of an attractive fusion reactor because of its simple field structure and inherently steady-state nature. Its drawbacks have been twofold. The first is that, in the circular toroidal form, any reduction of the effects of toroidal curvature required a large major radius and system output. This problem is substantially reduced in the EBS concept and is subject to further improvement. The second drawback has been the need for a continuous feeding of power to the rings, which is also reduced by better particle confinement in EBS. Both of these improvements are brought about by the isolation of the toroidal curvature in the corners, which leaves the system sides at an effectively infinite aspect ratio.

2.1 PRINCIPAL OBJECTIVES

2.1.1 Stabilization of Toroidal Plasmas by Energetic Electrons

The beneficial effect on stability of rings generated by ECH has been observed in EBT, in the Nagoya Bumpy Torus (NBT) in Japan, and in a variety of mirror devices. This observation has led to interest in using energetic electron rings as a means to stabilize toroidal devices (such as tokamaks, stellarators, and heliacs) and open-ended devices. Although simple MHD theory predicts instability in mirror geometry, the experiments and more sophisticated theory that incorporates kinetic effects have encouraged pursuit of the ring stabilization idea.

The EBS device provides a simple geometry for testing this concept, and generation of rings with sufficiently high beta seems assured. Data from the early Canted Mirror Facility (CMF) showed that rings in symmetrized geometry could have values of beta twice those achieved in EBT, with its curved mirror sectors and lack of symmetry. Moreover, the SM-1 device showed that multiple-frequency heating could further enhance the ring beta, and theory suggests that symmetrization will reduce the ring thickness in EBS, which also supports the expectation of higher beta values.

An important question about stability persists: Are the rings adequately decoupled from the toroidal plasma at higher frequencies in the range of the hot electron precessional drift frequency? The negative-energy drift wave is expected to couple to background plasma waves or dissipation mechanisms when the diamagnetic well is deep enough to reverse the hot electron drift velocity. A key task for the EBS experiment would be to determine the extent to which this coupling affects ring stabilization of the toroidal plasma. The issue is complicated; if the ring beta is too high, then an instability could occur, with consequences that are not predictable with the linear theory now available, and at lower beta values, windows of instability are predicted. However, with control of profiles it appears possible to avoid these windows and achieve average well formation or to provoke them in order to assess their importance.

In summary, EBS offers the opportunity to test the physics of ring stabilization in a device in which the rings can be produced and controlled in the presence of a well-confined toroidal plasma.

2.1.2 Reduction of Plasma Thermal Losses by Orbit Optimization

The principle of orbit optimization has been adopted into the open-ended confinement systems program; in the toroidal systems program, it represents an avenue for improving the conventional tokamak concept.

The EBS device is a striking example of the benefits to be gained by optimizing particle drift orbits, and it provides a very simple geometry in which to calculate and test the principle. Theoretical calculations have been made of the reduced dispersion in magnetic drift orbits for transitional and passing particles and of the near-perfect symmetrization of trapped-particle orbits. In EBS, the separation between the electron cyclotron fundamental resonance zone and the trapped-passing transitional region would reduce the direct losses of cyclotron heating power by about an order of magnitude below those in EBT.

Symmetrization of the ring electron orbits in EBS would produce a more symmetric ambipolar potential. This would lead to still further centering of all the particle orbits and to reduction of convective losses. Experiments in EBT demonstrated that the structure of the potential contours is strongly affected by the details of ring formation, such as the geometry of the cyclotron resonance surfaces. In toroidal systems, as well as open-ended devices, the exploitation and control of the potential are now recognized as critical factors in the development of adequate confinement. Thus, EBS can supply important information on these factors to the rest of the fusion program.

In addition to the reductions in direct and convective losses, there is a tenfold reduction in residual diffusive losses in EBS as a result of the improved orbits.

Another key feature of the proposed experiments in EBS is the strong dependence of the loss processes on the ratio of the magnetic fields in the corners to those in the centers of the mirror sections. The ability to change this ratio provides both experimental flexibility to select the desired amount of orbit optimization and the opportunity to verify the importance of improved orbits.

2.1.3 Evaluation of the Reactor Prospects of Bumpy Toroidal Systems

A sequence of experiments on improved bumpy toroids is described in Sect. 2.5. The philosophy behind this sequence is to move in small but significant steps toward a system with improved confinement and higher beta at a smaller overall effective toroidal aspect ratio. Other possible lines of development, summarized in Appendix 9, show that there are many approaches to the challenge of improving confinement and performance. Most of the collateral approaches depend on the same

principles of improvement and optimization, and the course of future development can best be determined after experimental results have validated the concepts.

Earlier physics and engineering analyses and cost sensitivity studies show that bumpy torus reactors with β_{core} of 6–10%, output power of 1200–1700 MW(e), wall loadings of 1–2.5 MW/m^2, and a recirculating power fraction (including ring-sustaining power and all other reactor auxiliaries) of 10–15% are possible. The advantages identified in earlier EBT reactor studies as important properties of bumpy toroids have been recognized and adopted by proponents of other confinement schemes. Among these are the steady-state nature of EBT devices, which strongly reduces the requirements on materials and structures, and the simple modular nature of the coil systems, which provides ease of accessibility and maintenance.

Recent reports[4,5] have collated the relevant ingredients for an assessment of bumpy toroid reactors. However, the orbit improvement properties of the bumpy square are not fully integrated into these reports. The first of these reports[4] includes some analysis of the generic effects of confinement improvement, presented as "aspect ratio enhancement." These led to a credible reactor concept with an aspect ratio of about 25. This is higher than the desirable values calculated in recent generic assessments of attractive fusion reactor systems, but it does not include the optimization offered by the bumpy square concept and related ideas. The more recent estimates presented in the second report[5] bring the effective aspect ratio of bumpy square reactors down to less than 15 and the wall loading up to the range from 2 to 4 MW/m^2, values that are competitive with the optimistic possibilities for other confinement schemes and with the requirements for attractive fusion reactors.

2.2 STABILITY AND FLUCTUATION MEASUREMENTS

The goal of the EBS experimental program is to make the measurements that are essential to validate the EBS premises. The first of these premises is that the energy density of the rings will be higher in the nearly linear geometry and that the stronger rings will result in greater stability for the core plasma. The second is that the orbit optimization in EBS will result in reduced transport, which will be manifest in enhanced parameters for the core plasma.

The initial experiments will use a few relatively simple diagnostic devices. Later in the program, advanced measurements will use more sophisticated devices that can answer more detailed questions about the plasma.

The first question to be addressed is that of ring formation. Ring diamagnetism can be used to infer the stored energy; it will be measured with multiple-turn loops wound directly on the device cavities. Well-known techniques for integrating the loop signals and compensating for the effects of nearby rings will be used in determining the stored energy in the rings. The current observed in simple ionization chambers will serve to demonstrate the formation of energetic electrons, via the X rays produced by the hot electrons.

Correlation of the ring measurements with density measurements, which can be made with a single-channel interferometer, can be used to investigate the connection between the presence of rings and the enhanced confinement. Variation of the field strength will change the location of the resonant surface and, therefore, the location and stored energy of the ring. This technique for varying the ring parameters can be used to investigate the interplay between ring and core parameters. Conversely, the core parameters can be changed by varying the mirror ratio, that is, the ratio between the field in the corners to that in the center of a cavity. Both techniques can be used to investigate the ring-core interaction.

The presence of fluctuations can be determined with magnetic or electrostatic probes, by observation of the phase shift of a microwave interferometer, or with Langmuir probes. All of these techniques are sensitive to fluctuations in the outer portion of the plasma and give only limited data. However, these data can be used with more advanced measurements to investigate the premise that the rings stabilize the plasma that lies within them.

The next level of diagnostics will use devices that can determine the energy and/or spatial distribution of the ring electrons. An array of hard X-ray detectors would be ideal for this purpose. A single detector, optimized for the intermediate-energy (5- to 50-keV) rings, would be used to investigate the "feed population" from which the high-energy electrons are formed. Germanium detectors are well suited to this task. Time-resolved measurements of the synchrotron emission will show the fluctuations in ring temperature or density.

The spatial distribution of the hot electrons in the midplane can be measured with three types of beam probes. A heavy-ion beam probe, used primarily for determining potential distributions, will give both direct and indirect measurements of the hot electron spatial location. Direct measurements employ multiple ionization of the primary ions, which requires high-energy electrons. Indirect measurements use the connection between the hot electron population and the peaks in the potential profiles.

A second beam probe system uses heavy atoms as internal targets for producing characteristic X rays. A detector that scans the source region of the X rays delineates the region populated by energetic electrons.

A third beam probe, using Zeeman spectroscopy, will be used to determine the magnetic field in the vicinity of the hot electron distribution, thereby giving a direct measurement of the field modification. The ability to modify the vacuum field is of central importance to the bumpy torus concept.

Skimmer probes can be used to provide additional information on the location of the hot electrons. As a material object enters the hot electron distribution, it removes a portion of that distribution. Thus, a correlation of the stored energy as a function of skimmer position gives a measurement of the spatial distribution of the hot electrons.

2.3 PLASMA CONFINEMENT MEASUREMENTS

For budgetary reasons, EBS experiments will begin with the essential minimum of diagnostics needed to establish that the hot electron rings are stronger than in EBT, that a quiescent regime of operation exists, and that confinement is substantially better than in EBT. When these points have been established, additional diagnostics will be attached and activated so that more detailed measurements and correlations can be made. Figure 15 is a diagram of the available diagnostics as they were installed on EBT. Table 3 lists the planned diagnostics for EBS.

2.3.1 Initial Measurements

The premise that orbit optimization will result in enhanced confinement can be validated by measuring the core plasma parameters. Initial measurements made with simple diagnostics can provide crucial information.

A single-channel interferometer, which measures the line integral of the plasma density, will quickly determine whether the density in EBS is higher, producing improved orbit characteristics, than in EBT. It will also tell whether the range of neutral density for the T-mode is extended in EBS.

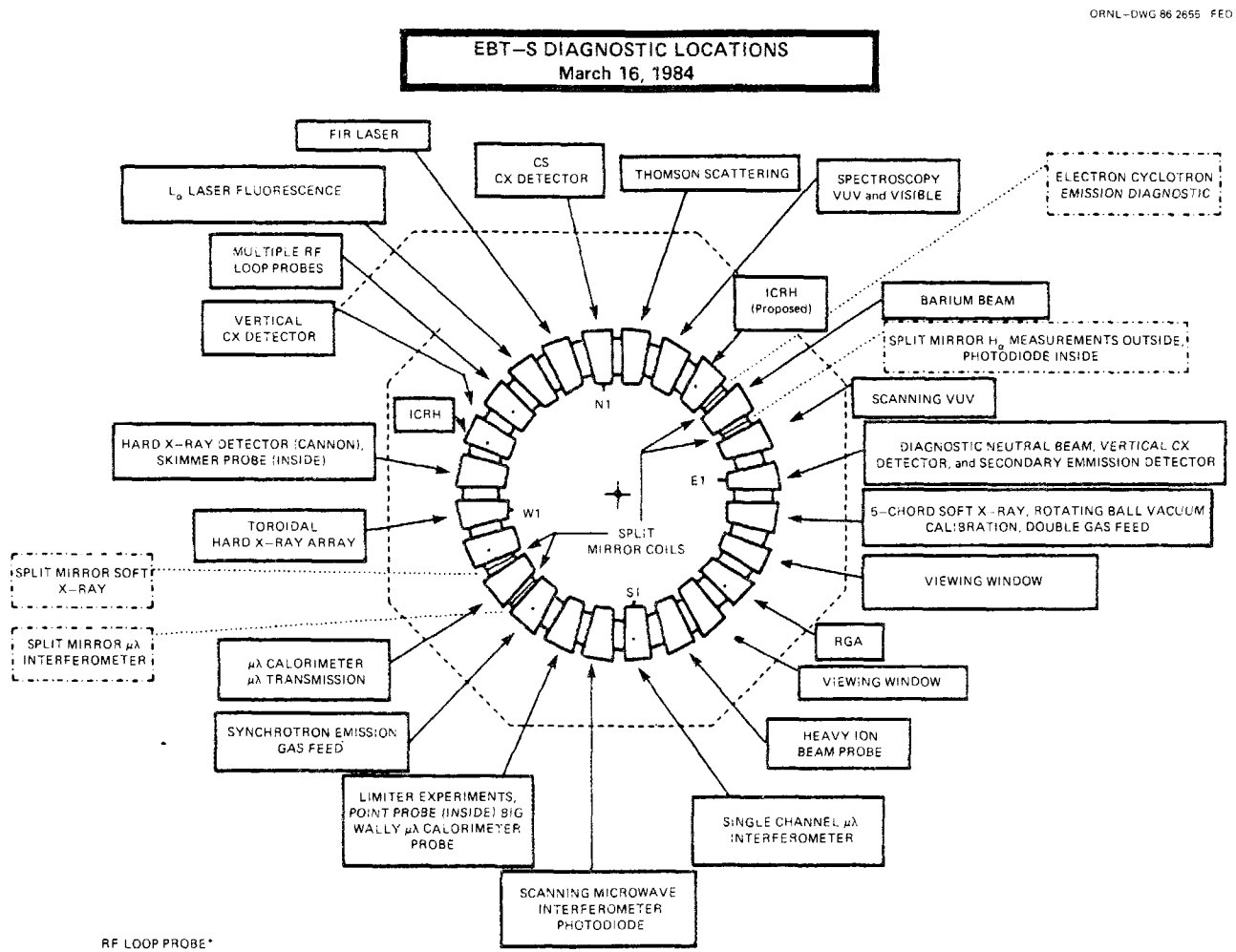

Fig. 15. Schematic diagram of diagnostic devices installed on EBT. A similar array is eventually planned for EBS, although operation will begin with the minimum diagnostic set needed to demonstrate ring stabilization and improved confinement.

Table 3. Diagnostic facilities for EBS

Rings	Warm plasma
Initial operation	
Diamagnetic loops	Thermocouple arrays in mirror throats
Ionization chamber	Toroidal pickup coils
	Single-channel interferometer
	Langmuir probes
	RF probes
	Residual gas analyzer
After 1 year	
Single-channel bremsstrahlung	Visible and ultraviolet spectrometers
Single-channel synchrotron emission system	Single-channel soft X-ray detectors (cavity and coil midplanes)
	Heavy-ion beam probe
	Magnetic loop probes (in one corner section)
After 2 years	
Bremsstrahlung array	Multichannel interferometer
Zeeman splitting probe	Thomson scattering system
Intermediate-energy bremsstrahlung detector	
Internal target X-ray source probe	

A second benefit of increased density would be enhanced attenuation of neutral atoms and molecules. Spectroscopic measurements can provide evidence for the depletion of neutrals, particularly if the plasma can be scanned radially to permit the use of Abel inversion techniques.

The best, and most direct, measurement of the symmetry of the electrostatic potential requires a heavy-ion beam probe; however, plans are to defer the expense of installing this diagnostic until later in the program. In the earlier stages, some indication of the potential symmetry will be given by Langmuir probes, which can be used on the midplane of a cavity and in the coil plane of the existing split mirror

coils. With probes in both locations, it will be possible to measure the potential distribution in the outer portions of the plasma and to obtain evidence of axial variation as well.

Plasma losses are expected to be asymmetric in the corner regions, where the plasma will scrape off on the inside. In the straight sections, losses should be symmetric. Several of the existing EBT coils have provisions for thermocouples to measure temperature in the coil throats. The symmetry of that temperature distribution will serve as a measure of the symmetry of the plasma losses.

The sensitivity of EBS to field errors will be checked with an electron beam probe. During plasma operation, a monitor of toroidal current (e.g., a toroidal pickup loop) will be used. The level of toroidal current will indicate the presence and severity of global field errors, which can be compensated by using external coils to induce errors of the opposite sign.

2.3.2 Advanced Measurements

A second type of toroidal current is of particular interest in EBS. Pfirsch-Schlüter currents are expected to peak near the transitions between corners and straight sections. The spatial variation of these currents should be determined with simple forms of magnetic probes. The variations in the magnitude and distribution of these currents will furnish excellent opportunities for a collaboration between experiment and theory to elucidate the transport and stability properties of EBS.

As described in Appendix 10, the electrostatic potential in EBS is expected to be much more symmetric than that in EBT. This will be checked with a heavy-ion beam probe.

In EBS, the effects of the toroidal curvature on the potential profile can be checked in stages by using plates to isolate the plasma being measured. For example, it will be possible to change the effective configuration from a straight multiple mirror, with no toroidal effects, to a multiple mirror that has curved end sections, with some toroidal effects, to a full torus, with full toroidal effects.

2.4 HEATING MECHANISMS AND GEOMETRY

The magnetic geometry of EBS, which results in improved drift orbits, has the added benefit of improving the heating efficiency. The particles that are most efficiently heated are those that turn near the resonant field location. For large values of the global mirror ratio M_G, these particles have pitch angles much smaller

than the loss cone angle, so that heating takes place far from the loss region, in pitch angle space.

The improved heating efficiency should have a measurable effect on the electron distribution function. In EBT, the absence of warm electrons, as measured with a soft X-ray detector in the coil throat, was one of the principal clues to the confinement problem that resulted from drift orbit effects. In EBS, however, particles should be able to penetrate to the mirror throat regions, and beyond, without encountering the loss cone. Thus, a measurable population of warm electrons can be expected in the mirror throats, and the density of this population will serve as a measure of the increased heating efficiency.

Another related benefit of the EBS geometry results from the decoupling of the field strengths in the corners and the straight sections. Although the field strength in EBT could be varied, which changed the geometry of the ring and the resonant surface, this variation also changed the mirror ratio between the resonant field and the field for particles in the loss cone. Thus, it was very difficult to separate heating effects from confinement effects. In EBS, where the confinement is principally due to the field in the corners, changes in heating efficiency with local geometry (e.g., ring size, resonant field locaton) can be more easily studied.

The EBS device also offers several attractive prospects for advanced heating techniques. For example, multifrequency heating, which was shown to be effective in a linear geometry, can be used to good advantage on EBS to enhance the ring parameters. Two frequencies, 27.7 and 28.0 GHz, are already available from gyrotrons in separate tube sockets at the EBS site. A demonstration of the effectiveness of two-frequency heating could be used to make a case for increasing the number of available frequencies.

Off-resonant heating, in which the incident power does not encounter a resonant surface, is also an interesting prospect for EBS. This technique has been demonstrated in linear systems. Upper off-resonant heating results in higher energies for the ring electrons and in a greater energy spread. These changes, particularly the energy spread, are useful in alleviating ring microinstabilities, such as whistlers. Lower off-resonant heating reduces the ring stored energy by increasing the pitch angle for ring particles. This is not an appealing prospect in open-ended devices, but it may be very useful in controlling the distribution function in a torus.

The modular nature of EBS makes it easy to install multiple antennas for ion cyclotron heating (ICH). Initial experiments are likely to use slow-wave launch, with power provided by a variety of high-power transmitters, which are already in place

and operational. These experiments are attractive because they permit the use of simpler antennas without Faraday shields.

2.5 ADVANCED BUMPY TOROID EXPERIMENTS

A sequence of experiments that leads from the initial EBS experiment toward a reactor is outlined in this section, and a possible EBS reactor configuration is described.

The nearer-term configurations are designed to permit experiments with *larger global mirror ratio, larger core plasma beta,* and *larger minor radius.* The means for extending the range of these important physics parameters is a step-by-step approach that maximizes the use of existing hardware.

A wider range of global mirror ratio than that of the initial EBS configuration can be achieved in two ways. The one that requires the minimum modification uses trim coils in the mirror cells adjacent to the corners (i.e., in the transition cells). These trim coils counteract the $1/R$ fringing fields of the corner coils so that for all values of M_G the field in the transition coils is more like the field of the other mirror cells. (Without trim coils, this can be accomplished only for a limited range of M_G values.) This method of increasing M_G also involves lower magnetic field B in the straight sides. This offers the possibility of raising the core plasma beta, which will allow tests of the beta limits associated with stability.

Achieving high beta by lowering B in the sides increases M_G and hence the diffusive lifetime. Thus, if nT is limited by the diffusive lifetime, then at comparable power levels nT should be higher than in the initial EBS experiments. Lowering B by a factor of 2 to 3 (and taking no credit for the increased lifetime) should increase core beta by a factor of 5 to 10.

The heating technique for exploring high beta uses existing 28-GHz microwave sources. The fundamental resonances would be placed in the parts of the transition coils nearest the corners. This type of heating is advantageous because it minimizes microwave cutoff problems and because the entire device can be heated by illuminating only the transition cells adjacent to two diagonally opposed corners. The magnetic field can be adjusted so that the resonance is far enough from the lossy region of phase space to make the heating inefficiencies that occurred in EBT insignificant. Because the magnetic scale lengths are comparable to those of the initial EBS configuration, heating efficiency (absorbed power) should be comparable.

The high-beta experiments will also require the 18-GHz or 10.6-GHz microwave sources to heat the rings in the straight sides. Because the density at the ring position should be somewhat less than the central value, microwave cutoff should not be as much of a problem as usual for these lower frequency microwaves. Nonetheless, this problem depends to some extent on profile, and it may be necessary to start at low density and use gas puffing (and the long lifetime of the rings, $\gtrsim 0.1$ s) to avoid it.

Exploring the full range of M_G with lower B in the sides requires a comparably low frequency for the microwaves (e.g., 10.6 GHz) to produce the same local heating geometry as that in the initial EBS experiments. This is attractive because lower frequency microwave sources are more readily available and generally less expensive. There are, however, lower bounds on the frequency because of microwave cutoff.

To take full advantage of the high M_G at low B, 28-GHz microwaves will probably be needed to provide upper off-resonant heating. This technique, proven on the ELMO and CMF devices, raises the hot electron temperature (e.g., by a factor of 7 in the CMF), which makes it possible to achieve high ring beta without increasing the ring density to levels near the plasma core density. This avoids the hot electron interchange mode, which occurs (as demonstrated theoretically and experimentally) when the ring density is comparable to the core plasma density. Upper off-resonant heating might also be useful to sustain rings in high-beta experiments.

The second way of achieving higher M_G is by using elliptical coils in the corners. The long axes of these coils would be vertical. This configuration reduces the variation in field line length due to toroidal effects (important for passing particles) without requiring significantly more coil power, and it allows full magnetic field in the sides.

Larger minor radius can be obtained through another modification. With the elliptical coils providing higher M_G, fewer coils are needed for the straight sides, and a somewhat lower "local" mirror ratio can be tolerated in the individual mirror cells. (Particle orbits and the associated lifetime improve with M_G, number of mirror cells, and the "local" mirror ratio of individual cells.) For a fixed separation between corners, fewer cells per side (and perhaps a lower local mirror ratio) allow an increase in the diameter of the coils in the straight sides and hence in the plasma diameter.

3. FACILITY SYSTEMS

The detailed conceptual design report for the reconfiguration of EBT into EBS has been given elsewhere.[6] In this section, some of the engineering drawings and equipment specifications for carrying out this project are presented.

3.1 OVERVIEW

The EBS project will provide for the complete disassembly of the existing EBT device, demolition of its substructure, and assembly of new and existing components to form a square configuration. The 24 EBT mirror coils will be salvaged; 16 of them will be installed between new cavity sections, as shown in Fig. 1. The connecting corner sections forming the vacuum vessel will be toroidal sectors, each with eight new mirror coils half the size of the EBT coils.

Each set of corner coils will be powered by a 3-MW generator, so that an additional 12 MW of power will be required. The power distribution system and cooling water system will be modified to accommodate the additional needs. A new device substructure and a new microwave duct and manifold will be installed.

The instrumentation and control (I&C) systems and the microwave waveguide network from EBT will be installed on EBS without changes, except as required to adapt to the new configuration. The biological shield, which is shown in Fig. 2, will also remain unchanged. Figure 16 is an elevation view of the EBS device in the shielded enclosure, and Fig. 17 is a typical elevation cross section. The relation of the vacuum vessel to the flux surfaces is shown in Fig. 18, which also illustrates the construction of the corners.

Because EBS is chiefly a reconfiguration of the existing EBT device, the capital investment involved is minimal. No critical elements are required by EBS (i.e., no new or ongoing component research and development must be successfully completed). Design, fabrication, and assembly require only existing technology, and no particular element takes precedence over the others.

3.2 MECHANICAL SYSTEMS

3.2.1 Vacuum System

The vacuum pumping system for EBS will be essentially the same as that for EBT. A new vacuum manifold will be required to match the square configuration;

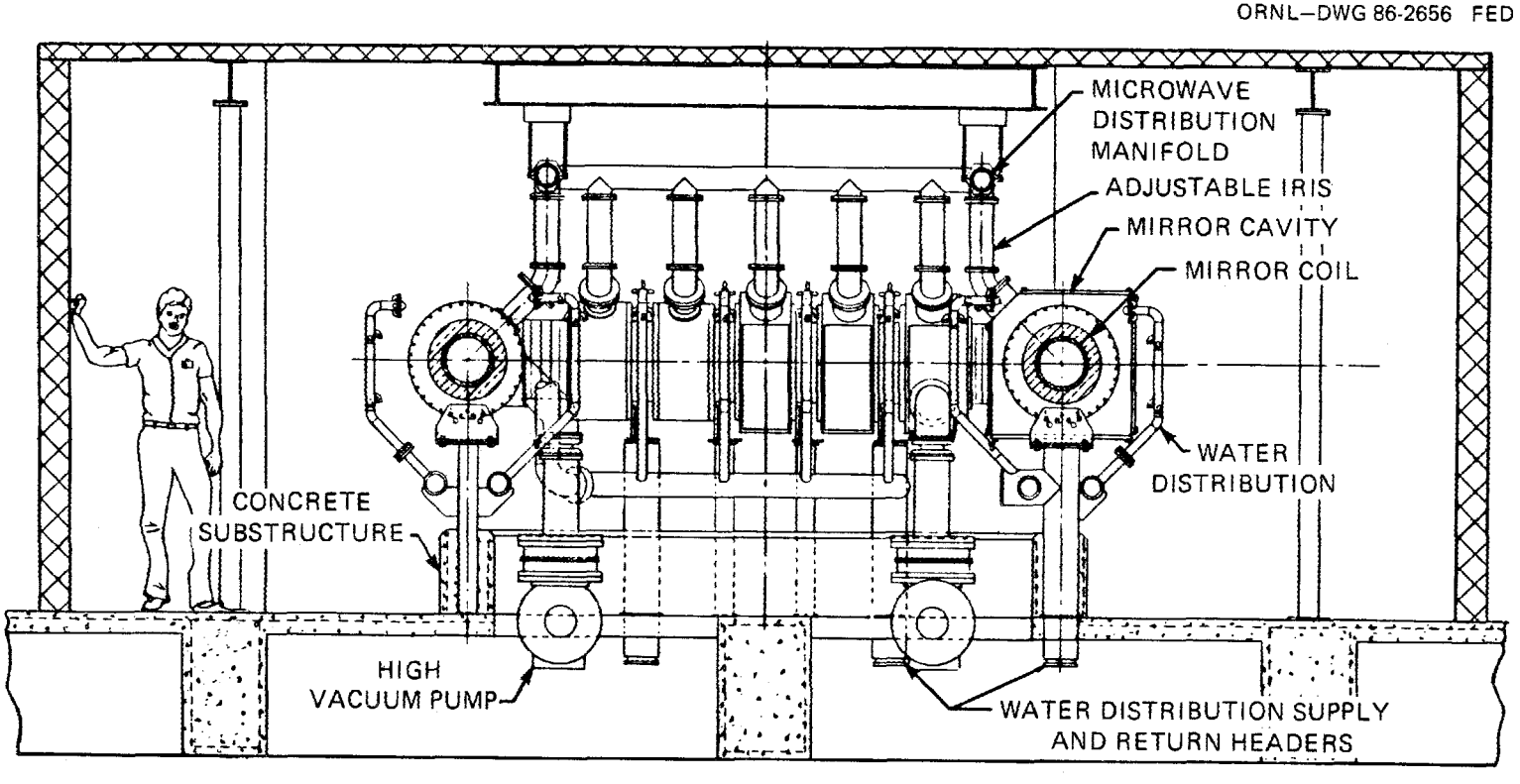

Fig. 16. Elevation view of EBS.

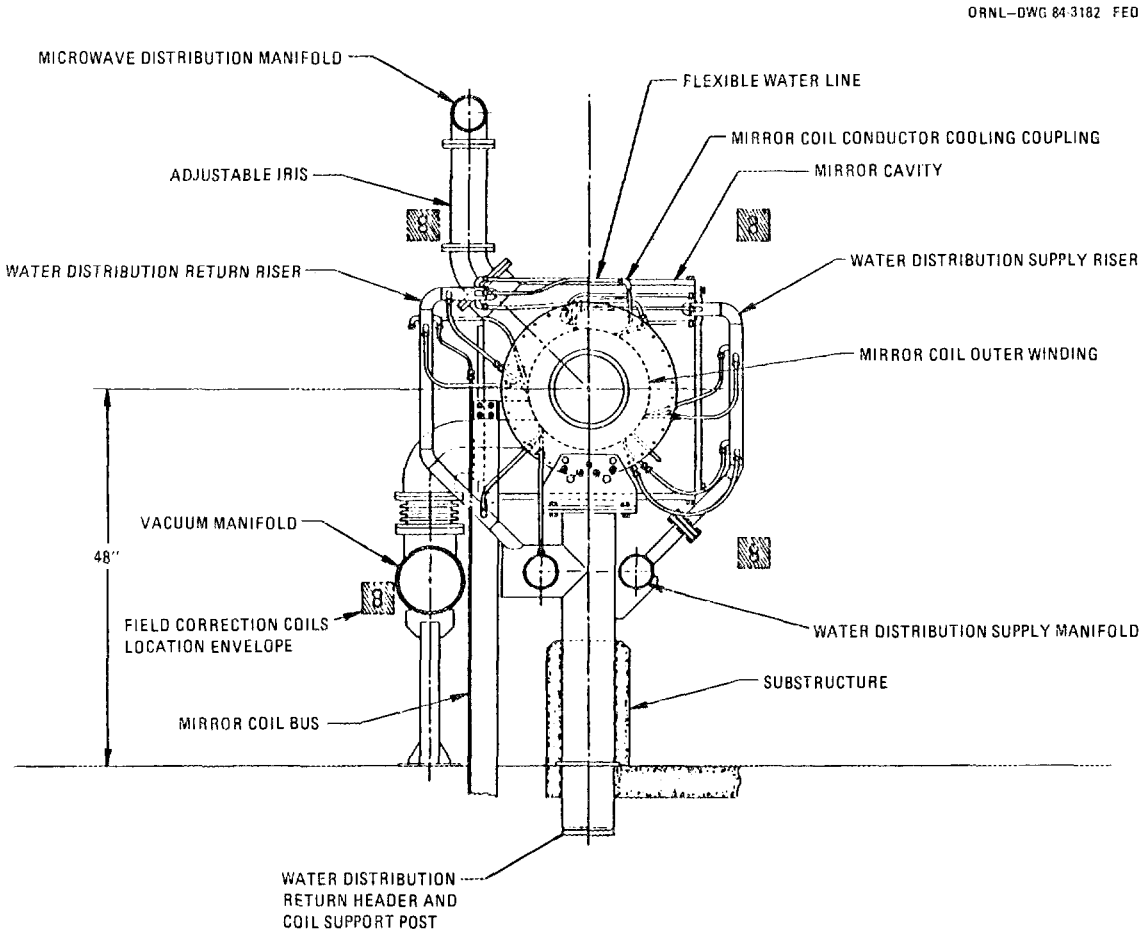

Fig. 17. Cross section of typical elevation of EBS.

flanges on the new manifold will mate to the three turbomolecular vacuum pumps and one cryogenic pumping system already installed. The I&C for the pumping system will be unchanged, as will the mechanical foreline and tank roughing pumps.

A total of 14 new cylindrical aluminum standard cavities, shown in Fig. 19, and 6 box-shaped diagnostic cavities, shown in Fig. 20, will make up the vacuum vessel in combination with the mirror coil cases. The diagnostic cavities have large cover plates on four sides to simplify the installation and removal of diagnostics.

3.2.2 Cooling System

The cooling system for the mirror coils will be modified to accommodate the heat load imposed by the new corner coils. The number of cooling water paths will increase from 288 to 532, which increases the requirements for water flow (at 4 gal/min) from about 1200 gal/min to about 2100 gal/min. The existing cooling water manifolds for the mirror coils will be modified and reinstalled. The cooling

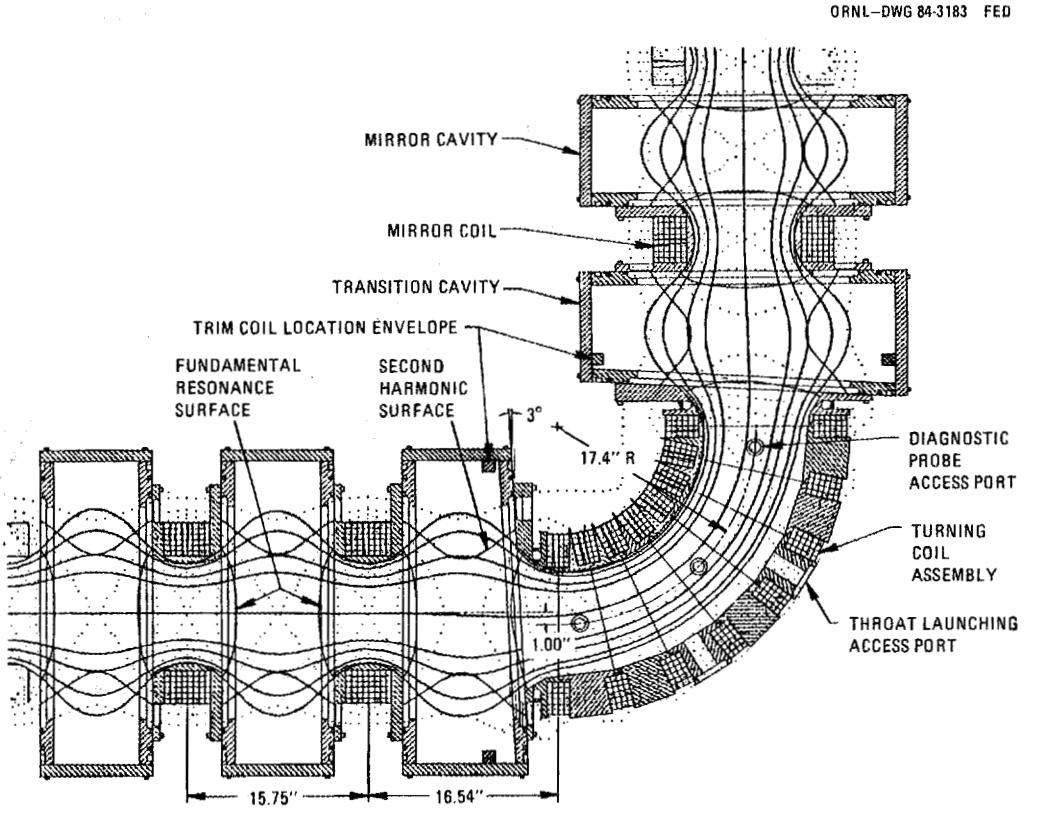

Fig. 18. Relation of microwave cavities and field coils to magnetic field lines.

system for the corner coils is shown in Fig. 21. New manifolds will be fabricated for the corners. The cooling systems for the 28-GHz, 200-kW, cw gyrotrons will not require modification.

3.2.3 Vacuum Vessel Support Structure

Figure 21 also shows the support structure for the corner coils. Each corner assembly and mirror coil case will be directly supported on a stand bolted to the floor. The individual stands will then be coupled by a concrete collar to distribute all centering and out-of-plane magnetic forces over the centerline span of the machine.

3.3 ELECTRICAL SYSTEMS

3.3.1 Magnet System

One of the four split mirror coils from EBT will be installed on each side of EBS. The coils on each side of the square are in series with one another and with

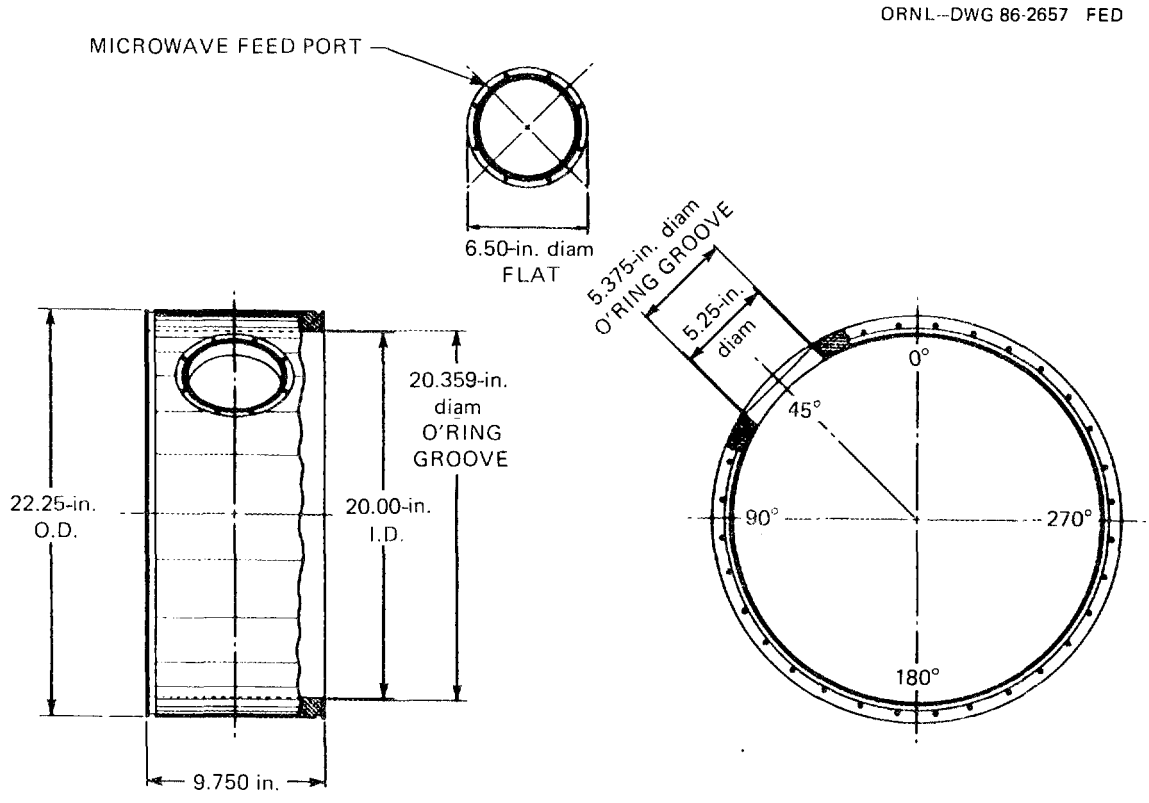

Fig. 19. Detail of standard microwave cavity.

the coils on the opposite side of the square; they are powered by two dc generators in series with a combined rating of 700 V and 7140 A.

Each corner assembly contains eight coils, each of which consists physically of half a straight-side mirror coil (two pancake coils instead of four). The eight coils are series connected and are in series with the opposite corner; they are powered by two dc generators in series with a combined rating of 700 V and 8750 A. The positive and negative copper bus around the machine is in close parallel alignment to cancel stray field effects.

Space is provided for error field correction coils. Four continuous vertical and four continuous horizontal coils will be located on 45° planes out from the machine centerline.

As shown in Fig. 18, space is provided for trim coils next to the corner coil assemblies. One circular coil, twice the diameter of a mirror coil, can be mounted inside each of the eight transition cavities to align the hot electron ring position, if needed. This location optimizes the function of the trim coils while avoiding space conflicts with other machine systems.

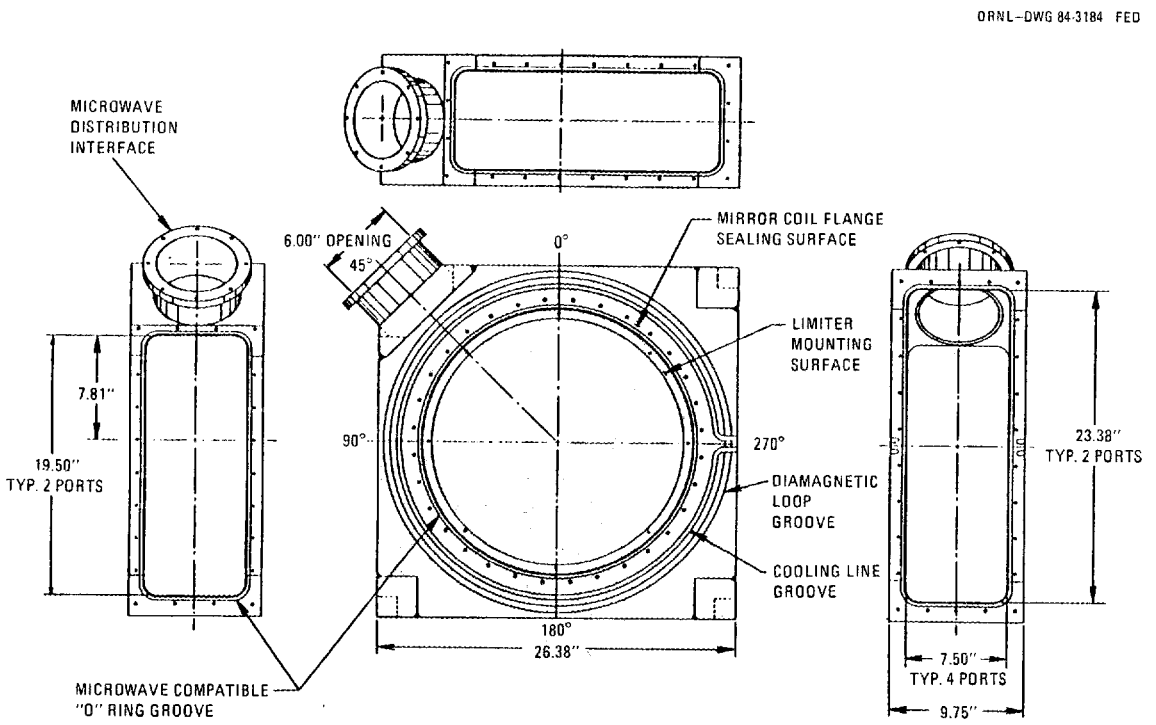

Fig. 20. Detail of instrumented diagnostic microwave cavity.

3.3.2 Microwave Systems

The microwave manifold will be a 10-cm-diam copper duct square configured to match the coil-cavity arrangement. The manifold will connect to each straight-side cavity section through a 10-cm-diam port that has an adjustable iris to control power distribution. The system is shown in Figs. 16 and 17. Input power from one or both gyrotrons will be fed into the square manifold at a single point and split for symmetric distribution at the ports.

3.3.3 RF Sources

No changes in the rf sources will be required for EBS, other than a minor rerouting of ducts to fit the square geometry. New duct flanges will be required at the cavity interfaces. The following sources of rf power are in place and operational.

- Two 28-GHz, 200-kW, cw gyrotrons. Each gyrotron is powered by a supply consisting of two stacked, variable-voltage, regulated supplies. The beam supplies have a rating of 100 kV at 1.0 A, and the gun supplies are rated at 40 kV at 1.0 A.
- Five transmitters, all capable of cw operation at the following levels:
  a. 2 to 30 MHz, 100 kW,

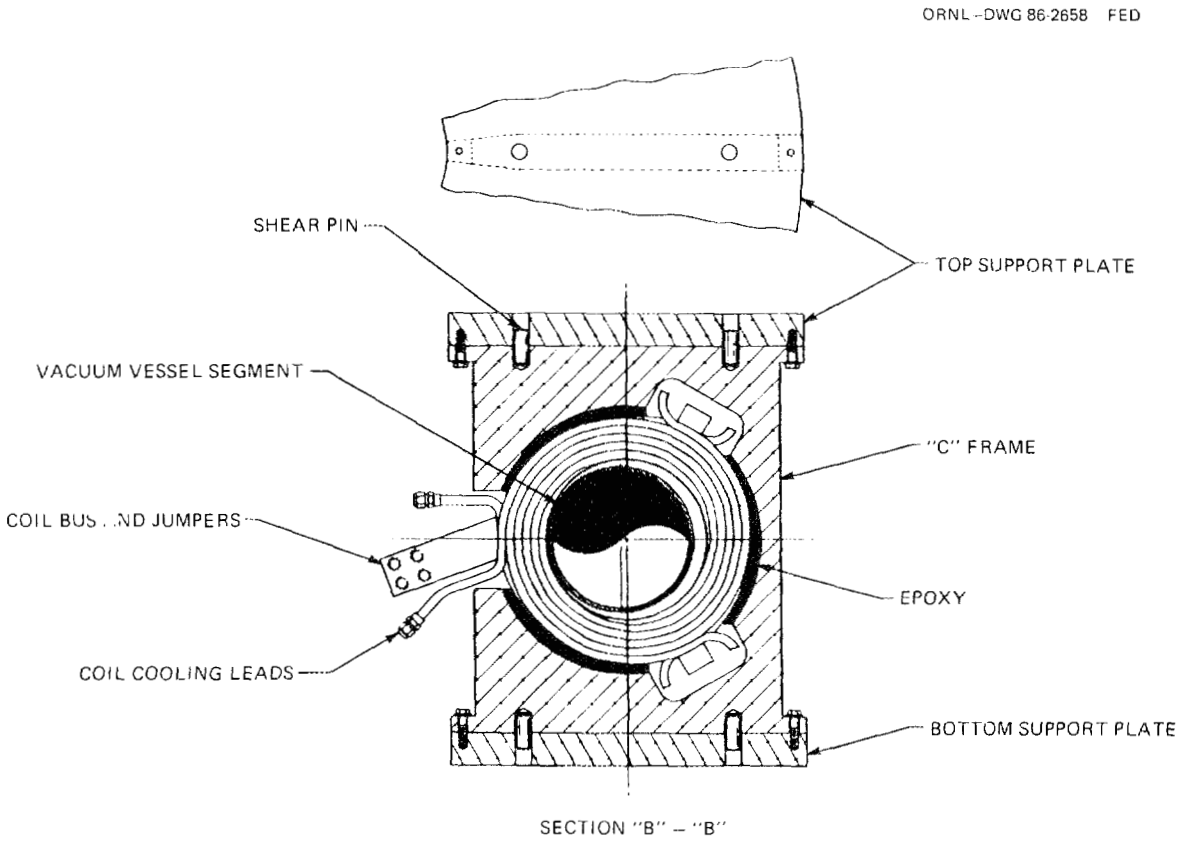

Fig. 21. Detail of support structure and cooling for standard corner coil.

b. 2 to 30 MHz, 200 kW,
c. 175 to 215 MHz, 50 kW,
d. 2 to 30 MHz, 20 kW, and
e. 30 to 60 MHz, 20 kW.

3.3.4 Instrumentation and Controls

Most of the needed I&C systems for EBS already exist. Additions will be made primarily in the cooling and generator control systems. The vacuum instrumentation systems exist and will be installed directly on EBS without change.

4. RESOURCES, COST, AND SCHEDULE

4.1 RESOURCES

Experiments on the EBT device made use of an extensive set of computer equipment, plasma diagnostics, and machine facilities. Most of these assets will be suitable for use on the EBS device. Although many of the diagnostics and other components have been lent to other experiments (which is a testament to their utility), they are, in principle, recallable and thus available for the EBS program. Brief descriptions of these assets follow.

4.1.1 Computers

Many of the EBT diagnostics used dedicated computers for data acquisition and experiment control. These "diagnostic" computers were connected to larger VAX computers used for data storage and rapid analysis. These, in turn, were linked through a DCA 355 to the Fusion Energy Division's central PDP-10 computer. Terminals and monitors were used to control machine and diagnostic operation, to provide analysis capability in staff offices, to provide word processing and graphics, and to enable after-hours computing from remote locations. These assets include the following:

2 VAX computers	50 terminals with monitors
5 PDP-11 computers	5 hard-copy units
1 DCA-355	1 Versatec printer

4.1.2 Diagnostics

A record of the diagnostic complement on EBT was maintained on one of the word processing devices. One of the latest of these is shown in Fig. 15.

4.1.3 Machine Facilities

Two motor-generator (MG) sets, comprising four generators, were used on EBT to provide up to 10 MW. Another pair of MG sets that can provide up to 12 MW was refurbished using EBT funds but has not been used. The buswork necessary to deliver power from these sets to the EBS site is in place, and the control circuitry for regulating their output has been designed and partially constructed. The available power is more than adequate for EBS.

A closed-cycle demineralized water system is in place at the EBS site. It is connected to a cooling tower with a 50-MW capacity, ensuring the removal of the heat generated by the experiment.

Available power supplies and microwave tubes can provide power at 10.6, 18, 27.7, and 28 GHz. This mix of frequencies allows a very interesting range of experiments. Although it is unlikely that all of the microwave power would be used simultaneously, it is possible to provide roughly 500 kW of heating to the plasma using the available sources (two 200-kW, 28-GHz tubes; four 15-kW, 18-GHz tubes; and three 15-kW, 10.6-GHz tubes).

About half this amount of continuous heating in the ion cyclotron range of frequencies is available (one 100-kW, 5- to 30-MHz transmitter; one 20-kW, 5- to 30-MHz transmitter; one 200-kW, 5- to 15-MHz transmitter; one 20-kW, 30- to 60-MHz transmitter; and one 1.5-kW, 1- to 200-MHz transmitter).

4.2 COST AND SCHEDULE

The cost of the EBS project is $4 million (as of September 1985). The estimated completion date is 24 months after project approval.

5. PROGRAM COLLABORATION

The program for EBS is expected to involve significant collaboration, both experimental and theoretical, with individuals and groups outside ORNL. International collaboration, especially with the Japanese, is expected, as is involvement of staff from U.S. industry, universities, and national laboratories. The effectiveness of the planned collaboration can be predicted from the collaborative program for EBT.

The EBT program involved extensive collaboration with the Japanese, primarily with the NBT group at Nagoya. There were personnel exchanges, data workshops, collaborative experiments, and many overseas telephone conversations between the EBT and NBT groups. This collaboration should continue for the new program.

Various industrial groups planned experiments, built equipment, transported it to Oak Ridge for installation on EBT, and participated in experiments. This type of involvement will be actively sought and encouraged for EBS.

Innovative theoretical work, which has had a profound effect on the course of bumpy torus research, has been done by individuals at other national laboratories and in university and industry settings. The program on EBS is expected to be interesting enough to result in continued involvement of this nature.

REFERENCES

1. N. A. Uckan, ed., *Advanced Bumpy Torus Concepts: Proceedings of the Workshop*, CONF-830758, Oak Ridge National Laboratory, 1983.

2. J. Sheffield, R. A. Dory, S. M. Cohn, J. G. Delene, L. F. Parsly, D. E. T. F. Ashby, and W. T. Reiersen, *Cost Assessment of a Generic Magnetic Fusion Reactor*, ORNL/TM-9311, Oak Ridge National Laboratory, March 1986.

3. J. Sheffield, "Physics Requirements for an Attractive Magnetic Fusion Reactor," *Nucl. Fusion* **25**, 1733 (1986).

4. N. A. Uckan, E. F. Jaeger, R. T. Santoro, D. A. Spong, T. Uckan, L. W. Owen, J. M. Barnes, and J. B. McBride, *EBT Reactor Analysis*, ORNL/TM-8712, Oak Ridge National Laboratory, August 1983.

5. N. A. Uckan, L. W. Owen, D. A. Spong, R. L. Miller, W. B. Ard, J. F. Pipkins, and R. J. Schmidt, *Reactor Assessments of Advanced Bumpy Torus Configurations*, ORNL/TM-8985, Oak Ridge National Laboratory, January 1984.

6. N. A. Uckan, C. L. Hedrick, D. A. Spong, T. Uckan, L. A. Berry, L. W. Owen, D. K. Lee, W. E. Bryan, T. J. McManamy, P. B. Thompson, and W. L. Wright, *ELMO Bumpy Square*, ORNL/TM-9110, Oak Ridge National Laboratory, October 1984.

1. MAGNETICS, SINGLE-PARTICLE DRIFT ORBITS, AND NONRESONANT ELECTRON TRANSPORT COEFFICIENTS FOR THE ELMO BUMPY SQUARE

L. W. Owen

The ELMO Bumpy Square (EBS) is formed by four linear arrays of simple magnetic mirrors linked by 90° sections of a high-field toroidal solenoid. The EBS is shown to have single-particle confinement properties that are distinctly superior to those of a standard EBT consisting of a toroidally linked array of circular mirror coils. Specifically, EBT-I/S is compared to EBS configurations having 24 mirror sectors with EBT-I/S mirror coils in the sides of the square. Each corner is formed by eight new circular or elliptical coils that generate a field with negligible edge ripple, so that trapping in local minima in the corners does not occur.

1.1 INTRODUCTION

The EBS is one member of a class of closed field line devices, called bumpy polygons, in which improved confinement results from localizing the unavoidable toroidal curvature in regions (vertices of the polygon) where the magnetic field is much stronger than the average field in the mirror sectors comprising the sides. In a bumpy polygon the number of symmetry planes is equal to the number of sides or vertices of the polygon, and the number of field periods is twice this number. In a sense, the bumpy square is a compromise between the desirability of a high degree of reflection symmetry (as in EBT) and the necessity of having the well-centered drift orbits and pressure surfaces exhibited by the bumpy racetrack, triangle, square, etc., for the best plasma performance. Since the vertices of the polygon have the 1/R field characteristic of a toroidal solenoid, the magnetic field in the two mirror sectors adjacent to each vertex (transition sectors) is not axisymmetric, unlike the nearly axisymmetric field in the other sectors comprising the sides. For this reason, among others, one would like to maximize the number of axisymmetric mirror sectors and minimize the number of transition sectors. EBS is not only a reasonable compromise between symmetry and confinement, but it also has the added practical advantage of fitting nicely (with 24 sectors) into the existing EBT-I/S enclosure. Hence, a reconfiguration of EBT-I/S into

an EBS would not necessitate a demolition and reconstruction of the enclosure, as would a 24-sector bumpy racetrack, for example.

In addition to the superior core plasma confinement properties exhibited by EBS, a number of other potentially useful and important advantages can be cited. The hot electron rings that are necessary for macrostability in EBS, just as in EBT, are exceedingly well centered, since they are formed in a near-axisymmetric field. For the same anisotropy in EBS, there should be little or none of the radial broadening of the ring that occurs in EBT-I/S because of dispersion in the magnetically confined trapped particle drift orbits. Hence, it may be easier to form an average magnetic well in EBS. The geometry of the EBS configuration suggests the possibility of using very interesting heating techniques that would not be practical in a standard EBT. Access at the corners permits a long path length for parallel neutral beam injection, and the lack of magnetic moment conservation at typical beam energies should quickly isotropize the hot ion distribution. (Simultaneous co- and counterinjection is necessary so as not to drive a parallel current in the plasma.) In an EBS that utilizes an EBT-S-like magnetic field (1 T in the mirror cavities), slow wave ion cyclotron resonance heating (ICRH) and 60-GHz electron cyclotron resonance heating (ECRH) can be launched from the high-field corners with the rings sustained by 28-GHz second harmonic heating.

1.2 MAGNETICS

In Fig. 1.1 the innermost, outermost, and central magnetic field lines in EBS configurations with circular (top) and elliptical (bottom) coils in the corners are displayed. Each of the five EBT-I/S coils in each side is approximated by two circular filaments, and each of the eight coils in each corner is approximated by a single circular or elliptical filament. (Only those filaments within a single field period are displayed.) The sector length or coil spacing in the sides is 40 cm, and the angular spacing in the corners is (90/7)°. The major radius of the corner sections is 44.2 cm, with the axis of each corner section displaced radially outward by 2.5 cm from the axis of the sides. This displacement is necessary to form the rings in the transition sectors on the same flux lines on which they are formed in the axisymmetric sectors. Depending upon the strength of the solenoidal field in the corners, the transition sector length is typically larger (by 3 to 5 cm) than the length of the other sectors.

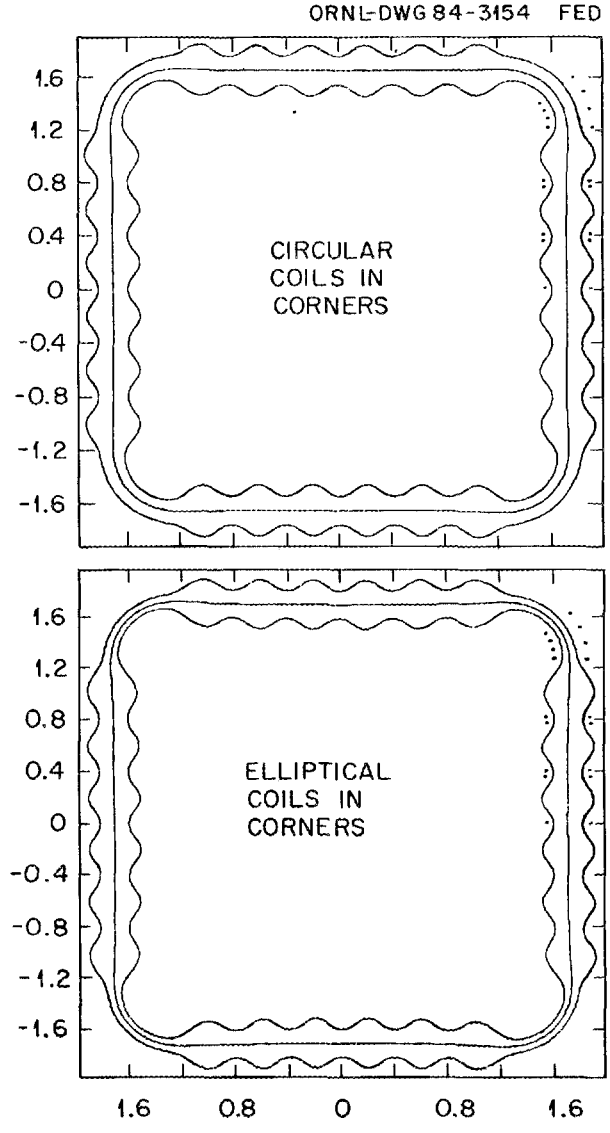

Fig. 1.1. The innermost, outermost, and central magnetic field lines in EBS configurations with circular (top) and elliptical (bottom) coils in the corners.

Alternatively, a "trim coil" in each transition sector is required to line up all of the rings if the relative fields in the corners and sides are to be varied. (It will be shown later that this is a very desirable feature of the EBS configuration that permits a rather broad variation of the confinement properties of the device.)

Magnetic field lines (dotted) are shown in more detail in Fig. 1.2, along with mod-B contours (solid) in the equatorial plane of EBS. In particular, one observes that the small outward displacement of the corners discussed above results in the symmetrization of mod-B in the midplane of the transition sector with respect to the machine axis or the magnetic field lines. It is also seen in the corner section graph that there is no significant field ripple, even on the outermost flux line that just grazes the coil cases in the equatorial plane of the mirror cavities.

In Fig. 1.3, the normalized magnetic field strength is plotted as a function of arc length along the central field line in EBS for two values of the "global" mirror ratio M_G. The cavity mirror ratio is the same as that in EBT-I/S (≈ 1.88) and is determined by the mean coil radius and spacing. The global mirror ratio is defined as the ratio of B at the corners to $B = B_{oo}$ at the center of the reference sector midplane. Presently available motor-generator sets, cooling tower capacity, and electron cyclotron heating (ECH) frequencies that could be dedicated to EBS permit a variation of $M_G \approx 3$-6 with circular coils in the corners. The upper limit corresponds to an EBT-I-like field (18 GHz) in the sides and the maximum field (≈ 3 T) in the corners. If elliptical coils were used in the corners (see Fig. 1.1, bottom), then the maximum global mirror ratio would be limited to $M_G \approx 4.7$, with an additional 8 MW of dc power required to obtain $M_G \approx 6$ (since the turn length is approximately two-thirds larger than that for the circular coils).

1.3 SINGLE-PARTICLE DRIFT ORBITS AND PLASMA PRESSURE SURFACES

We now turn from magnetics to a discussion of single-particle drift orbits and plasma pressure surfaces in EBS. For the EBS configuration with circular coils in the corners and $M_G \approx 4$, Fig. 1.4 shows core plasma pressure contours and extreme passing particle ($V_{\parallel} = V$) drift orbits in the reference sector midplane. For a small minor radius, it is seen that the pressure contours are centered at $x \approx -1.5$ cm, whereas for a large minor radius, the contours are almost

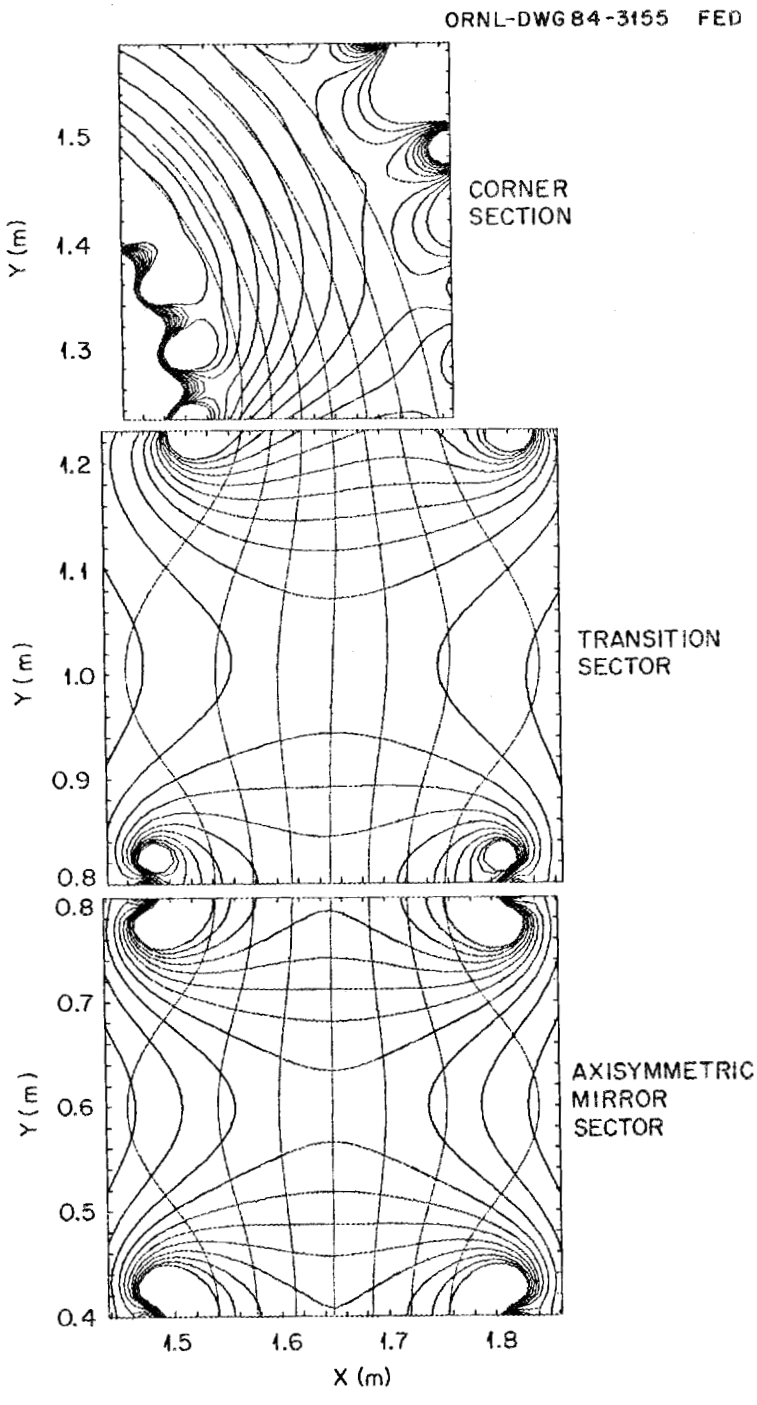

Fig. 1.2. Mod-B contours (solid) and magnetic field lines (dotted) in the equatorial plane of an EBS configuration with circular coils in the corners. Small outward displacement of the corners (top) symmetrize the mod-B in the transition sector (middle). This allows rings to form on the same flux lines on which they are formed in the axisymmetric sectors (bottom).

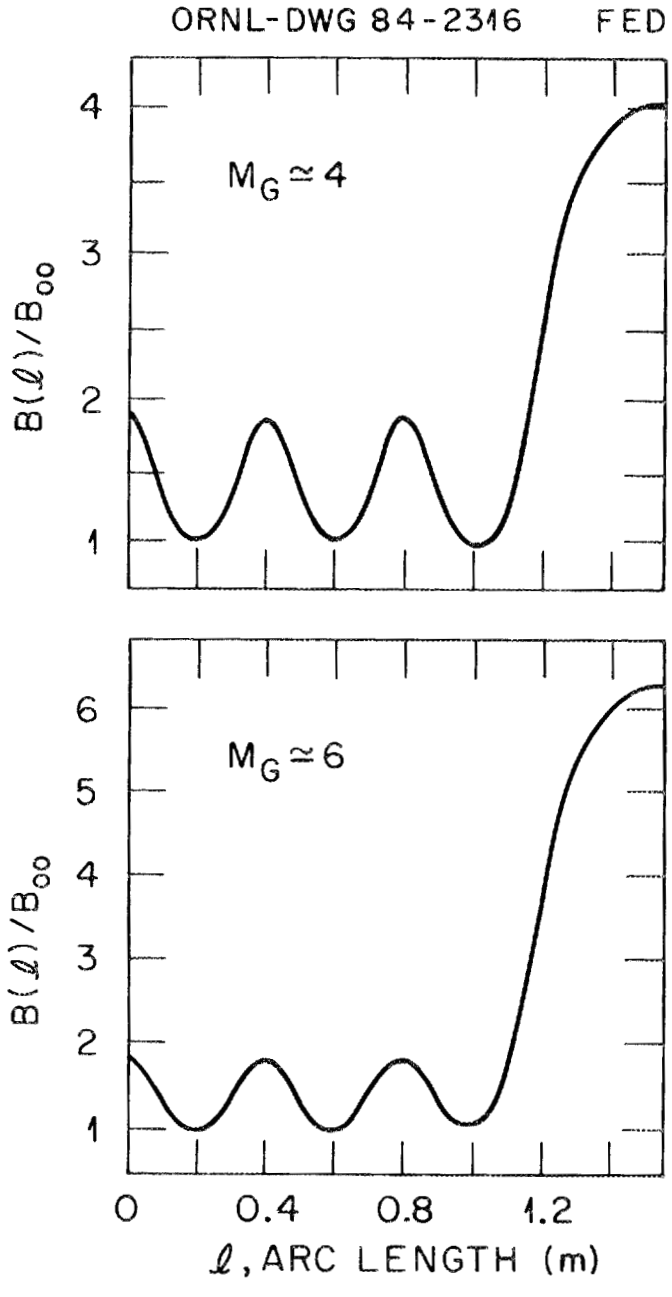

Fig. 1.3. The normalized magnetic field strength is plotted along the central field line in EBS for two values of the global mirror ratio M_G; $M_G = 4$ (top) and $M_G = 6$ (bottom).

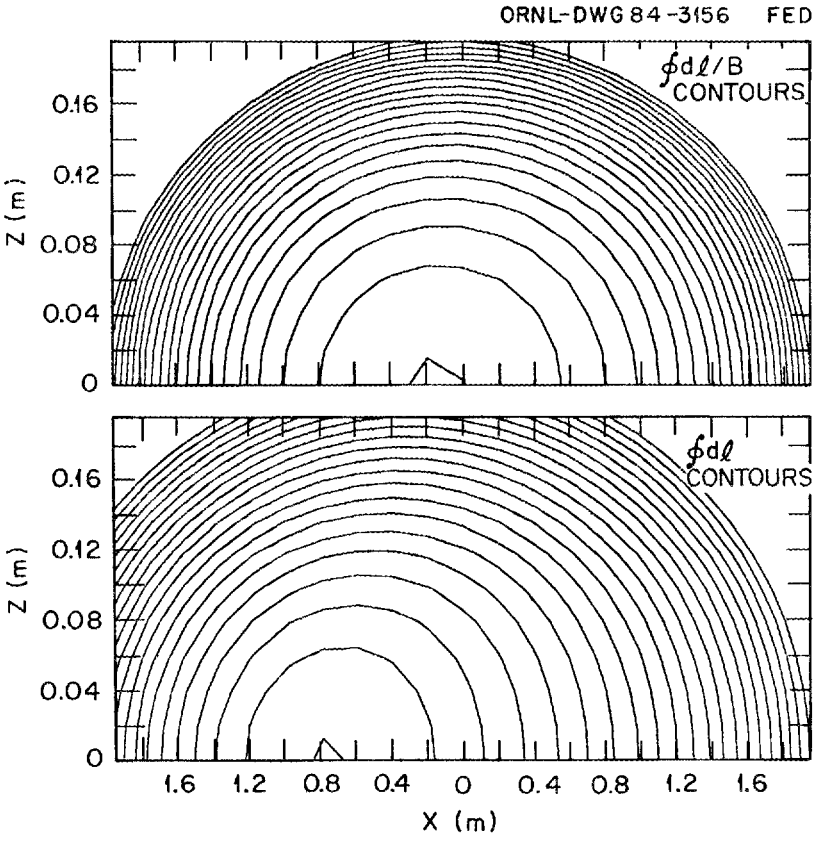

Fig. 1.4. For an EBS configuration with circular coils in the corners and a global mirror ratio $M_G \approx 4$, core plasma pressure surfaces (contours of constant $\oint d\ell/B$) are shown at the top and passing particle drift orbits (contours of constant $\oint d\ell/B$) are shown at the bottom.

exactly centered on the minor axis ($x \approx 0$). Although not shown, the drift orbits for transitional particles that turn in the corners are also approximately circular, unlike those in EBT-I/S that tend to be "fat" banana orbits shifted to the inside of the torus.

The utility of the longitudinal invariant J, plotted as a function of radius in the equatorial plane, is illustrated in Fig. 1.5. The variation with pitch angle of the radial position of the minimum of J, R_{JMIN}, is a useful measure of drift orbit centering and dispersion in the plasma interior. In addition, if it has been determined that the drift orbits are approximately circular, then level lines on J determine the center and the diameter (or approximate area) of a given drift orbit without the necessity of computing J over the entire reference plane. In Fig. 1.6 curves of R_{JMIN} $(V_{\parallel}/V)$, with $V_{\parallel}/V$ defined at the midplane center, are shown for EBS with circular or elliptical coils in the corners and compared to the curve for EBT-I/S. Also noted by an arrow is the radial position of the minimum of $\oint d\ell/B$ for each case. Several points should be noted in these graphs. For EBS, little or no dispersion is apparent until the midplane $V_{\parallel}/V$ is large enough for the particle to turn in the corners. The peak of the transitional particle R_{JMIN} is much lower and its width much smaller than for EBT-I/S. Also, because the global mirror ratio M_G is larger than the cavity mirror ratio in EBT-I/S, the peak occurs at larger $V_{\parallel}/V$, where there are fewer particles (assuming constant density along field lines). Likewise, the centering of passing particles is much better in EBS than in EBT-I/S. Perhaps most striking in EBS is the improvement in the centering of the core plasma pressure contours ($U \equiv \oint d\ell/B$ contours), denoted by U_{MIN}. The scaling of U_{MIN} with M_G is also very favorable; $U_{MIN} \propto (M_G)^{-1.25}$ with circular coils in the corners and $U_{MIN} \propto (M_G)^{-1.5}$ with elliptical coils. Extreme passing particle drift orbit centering is also seen to scale as an inverse power of M_G; R_{JMIN} $(V_{\parallel}/V = 1) \propto (M_G)^{-0.25}$ (circular) and $\propto (M_G)^{-0.5}$ (elliptical). These effects are a direct result of concentrating the toroidal curvature in the high-B corners of EBS. The reason that elliptical coils give better results than circular coils is apparent in Fig. 1.1. An important effect of the high-field corners is to minimize the difference in length between the inner and outer field lines. This is obtained most efficiently by vertical fanning in the corners, rather than by a radial compression of the flux. Hence, corner coils which are elongated vertically are expected to be superior to circular coils in centering drift orbits and pressure surfaces, as indeed they are.

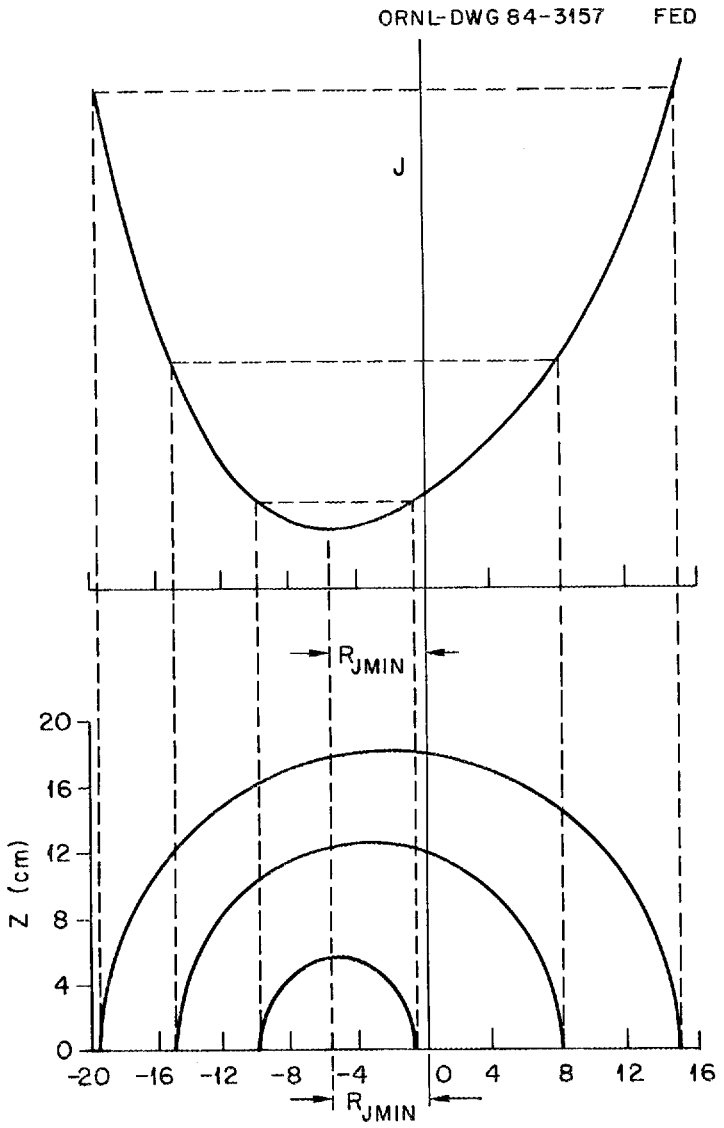

Fig. 1.5. R_{JMIN} is a useful measure of drift orbit dispersion in the plasma interior. It represents the radial distance from the minor axis of the center of that drift orbit (for a particular pitch angle) which has the largest inward shift toward the major axis of the torus.

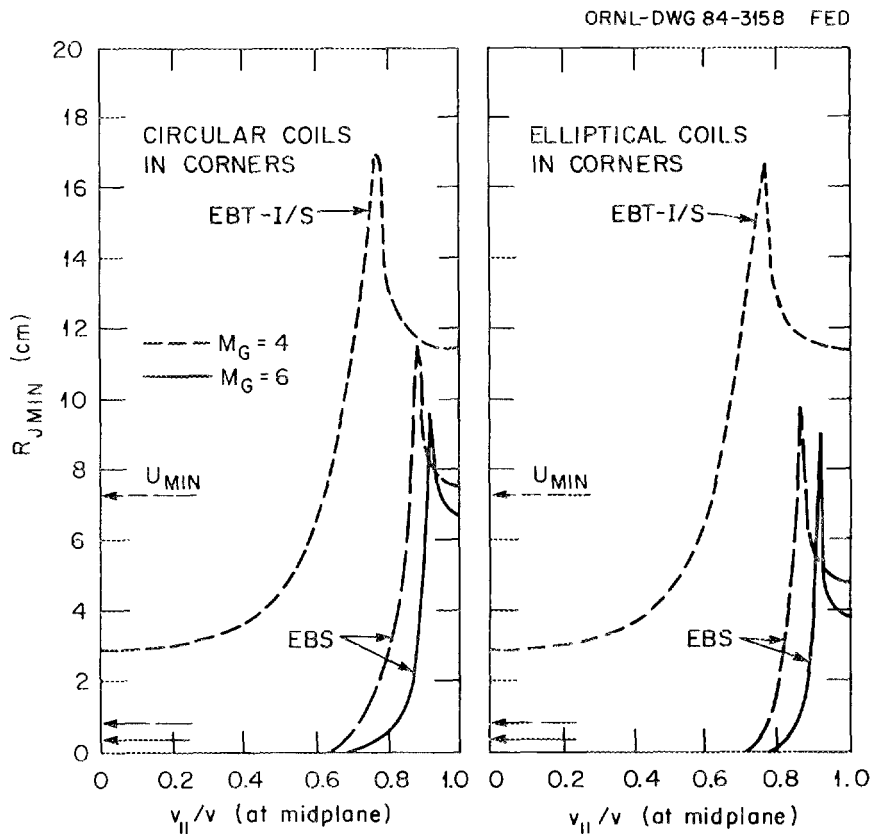

Fig. 1.6. R_{JMIN} $(V_{||}/V)$ and the radial position of the minimum of $\oint d\ell/B \equiv U_{MIN}$ for EBT-I/S and EBS with circular and elliptical coils in the corners for two values of the global mirror ratio.

However, as mentioned previously, the dc power requirements increase with elongation for copper coils. A fixed amount of dc power for the corners, therefore, sets an upper limit on the elongation for a given desired global mirror ratio. It should be stressed that elliptical coils are not necessary to test the EBS concept. If an EBS with circular coils in the corners performs as predicted, then the circular coils can be later replaced with elliptical ones in a second phase of the experiment. In fact, a staged experiment such as this is the most desirable alternative because it minimizes schedule, initial cost, and risk, as well as permitting a range of operating fields in which neoclassical transport rates can be varied by as much as a factor of 4 (discussed later).

1.4 VOLUMETRIC EFFICIENCY

For the cases considered in Fig. 1.6, the volumetric efficiency or filling factor for EBT-I/S is compared to that for EBS in Fig. 1.7. The volumetric efficiency reflects the confinement of particles at a large minor radius corresponding to the limiting flux lines which just graze the coil throat. It is particularly useful as a measure of direct particle losses caused by unconfined drift orbits which intercept the walls of the vacuum chamber. The volumetric efficiency is defined as the ratio of the area of the drift orbit that passes through the limiting flux line in the midplane for a given pitch angle to the area intercepted by the limiter. The limiter is taken to be a circle in the midplane defined by projecting the coil throat along flux lines. In Fig. 1.7 $V_{\parallel}/V$ is defined at the center of the reference sector midplane. As seen in Fig. 1.6 in the R_{JMIN} curves, the width of the transitional particle "notch" in F is much smaller and much narrower for EBS than for EBT-I/S. The passing particle volumetric efficiency is also four to five times as large for EBS. Since the particles with $V_{\parallel}/V \lesssim 0.7$ are trapped in a near-axisymmetric field in EBS, there is no dispersion in F until penetration into the 1/R field of the corners begins to occur.

Figure 1.8 shows the effect on F of defining $V_{\parallel}/V$ on the limiting flux line, rather than at the midplane center. In these curves, for example, particles with $V_{\parallel}/V = 0$ are trapped in the midplane and drift on a mod-B contour in the midplane, whereas in Fig. 1.7 such particles have appreciable $V_{\parallel}$ at the limiting flux line (since B at the midplane limiting flux line is less than B_{oo}, where $V_{\parallel}/V$ is defined).

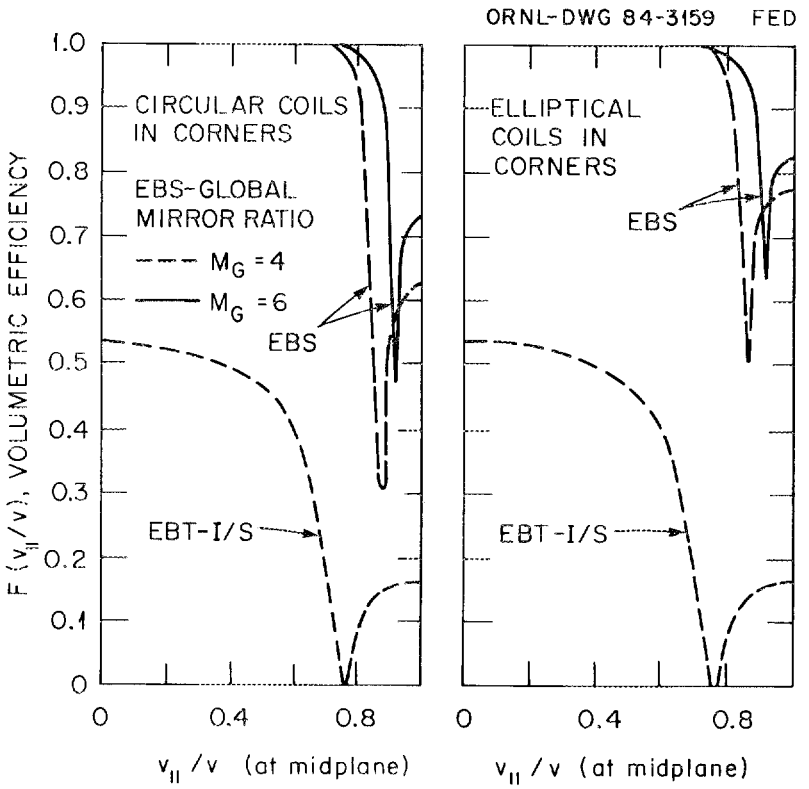

Fig. 1.7. Volumetric efficiency curves for EBT-I/S are compared to those for EBS configurations with circular and elliptical coils in the corners for two values of the global mirror ratio. The cosine of the pitch angle $(V_{||}/V)$ is defined at the center of the reference midplane.

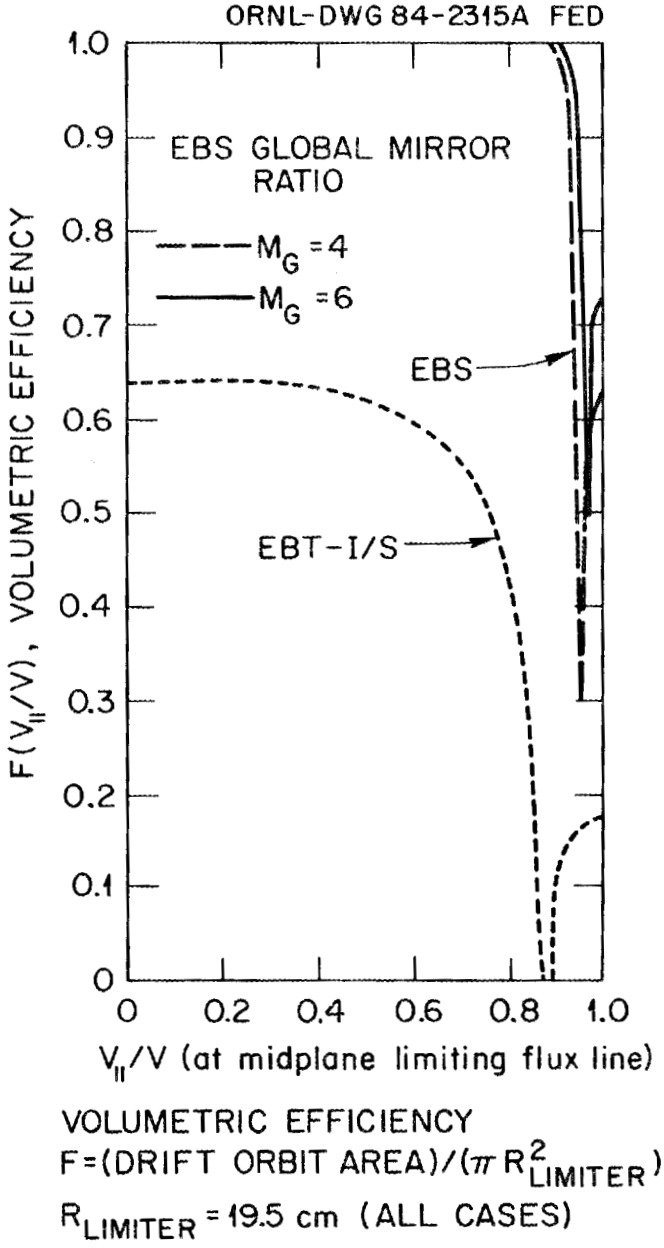

Fig. 1.8. Volumetric efficiency curves for EBT-I/S and the EBS configuration with circular coils in the corners are plotted as functions of $V_{||}/V$ defined at the limiting flux line in the midplane, rather than at the center of the midplane.

Figure 1.8 reflects the fraction of the available plasma volume (defined by the limiting flux lines) within which particles of a given pitch angle are confined. The quantity $F_{LOSS} = 1 - \int F(V_{\parallel}/V)\, d(V_{\parallel}/V)$, with $V_{\parallel}/V$ defined as in Fig. 1.8, is the direct loss fraction for an isotropic distribution in the vacuum magnetic field. The curves in Fig. 1.8 show $F_{LOSS} \approx 47\%$ for the EBT-I/S vacuum field and $F_{LOSS} < 5\%$ for EBS.

1.5 DIFFUSION STEP-SIZE AND TRANSPORT COEFFICIENTS

In this section we discuss and compare an approximate diffusion step-size and nonresonant electron transport coefficients for EBT-I/S and EBS configurations. Figure 1.9 shows isometric plots of the square of a diffusion step-size as functions of kinetic energy and midplane $V_{\parallel}/V$. The step-size is defined as

$$(\Delta X) = \frac{V_y}{\Omega_B + \Omega_E}$$

where V_y is the vertical drift velocity induced by toroidicity, Ω_B is the poloidal drift frequency due to the bumpy magnetic field, and Ω_E is the poloidal $E \times B/B^2$ drift frequency due to the ambipolar electric field. V_y and Ω_B are functions of particle kinetic energy and pitch angle, and Ω_E is characterized by the parameter

$$W_o = \frac{|e\Phi|}{kT_e}\left(\frac{R_B}{R_E}\right) \approx 3\text{-}5$$

for EBT-I/S. Here (R_B/R_E) is the ratio of the magnetic to electric field scale lengths. In Fig. 1.9, $W_o = 3$ is assumed, and V_y and Ω_B are calculated from the gradient of the longitudinal invariant J, evaluated at a radial position near the hot electron ring in the reference sector midplane. The terms $(\Delta X)^2$ in Fig. 1.9 and $(\Delta X)^2 f$ (Maxwellian) in Fig. 1.10 have been normalized to unity at their respective maxima for EBT-I/S. Hence, the results for EBS are relative to those for EBT-I/S. Note that $(\Delta X)^2$ for EBS is extremely small for $V_{\parallel}/V \lesssim 0.8$, reflecting the small dispersion of trapped particle drift orbits about the average drift surface.

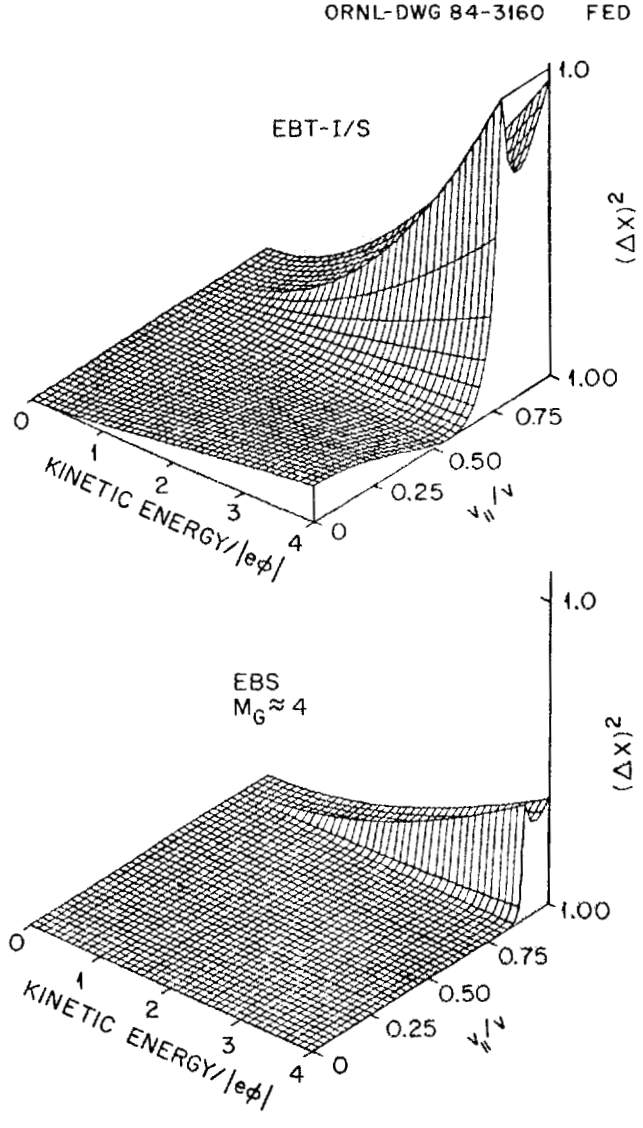

Fig. 1.9. Isometric plots of the square of the diffusion step-size for EBT-I/S and the EBS configuration with circular coils in the corners are displayed as a function of $V_{\parallel}/V$ and the ratio of particle kinetic energy to ambipolar potential well depth. $|e\Phi|/kT \approx 1$ is assumed.

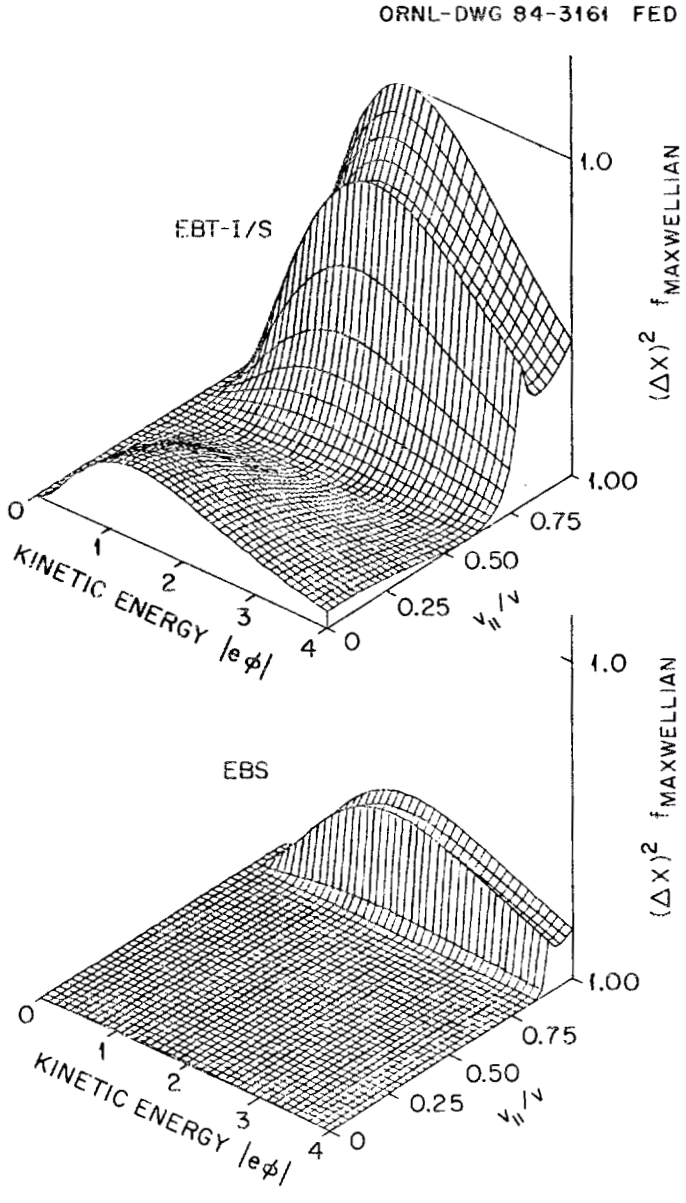

Fig. 1.10. The square of the diffusion step-size, shown in Fig. 1.9, is multiplied by a Maxwellian distribution function.

Nonresonant electron particle and energy transport coefficients for EBT-I/S and EBS have been evaluated and compared in Figs. 1.11 and 1.12. The coefficients are given in refs. 1 and 2 in terms of integrals over energy and pitch angle. A particle- and energy-conserving BGK collision operator is assumed. Rather than using approximate analytic expressions for V_y and Ω_B, we evaluate these quantities numerically, as discussed above. The longitudinal invariant J and the bounce or transit time τ are evaluated for each pitch angle by integrating along field lines in the vacuum magnetic field. The drift velocity (in terms of midplane magnetic field B_{MP})

$$x\bar{v}_D = \frac{\nabla J \times \hat{b}}{eB_{MP}\tau} , \quad \hat{b} = B/B$$

is then decomposed into vertical and poloidal components to get V_y and Ω_B as functions of $V_{\parallel}/V$. Figure 1.11 shows the particle transport coefficient D_n as a function of collisionality ν/Ω_o for EBT-I/S and EBS. Here ν is the collision frequency and Ω_o is poloidal precession frequency

$$\Omega_o = \frac{kT_e}{reB_{MP}R_B} .$$

Similar curves are obtained for D_T, K_n, and K_T, with the ratio of the transport coefficient for EBS to that for EBT-I/S approximately the same in each case. In Fig.1.12 the ratio of D_n for EBT-I/S to D_n for EBS is plotted as a function of the global mirror ratio in EBS. This curve shows the striking result that neoclassical transport in EBS should improve as the inverse square of M_G (i.e., confinement time should increase as M_G^2). For the configuration with circular coils in the corners, available dc power and ECH frequencies should permit about a factor of 4 variation in the neoclassical transport rates (since it is possible to vary M_G from about 3 to 6).

1.6 CONCLUSION

The results discussed in this report indicate that a reconfiguration of the EBT-I/S device into an EBS offers the very

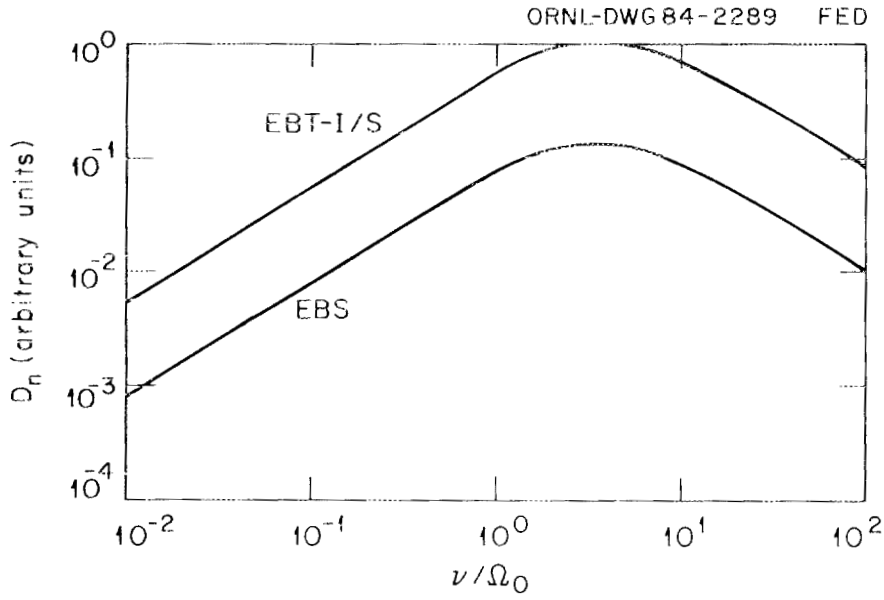

Fig. 1.11. The particle transport coefficient D_n is plotted as a function of collisionality ν/Ω_0 for EBT-I/S and for the EBS configuration with circular coils in the corners and $M_G \approx 4$. Similar curves are obtained for D_T, K_n, and K_T, with the ratio of the transport coefficient for EBS to that for EBT-I/S approximately the same in each case.

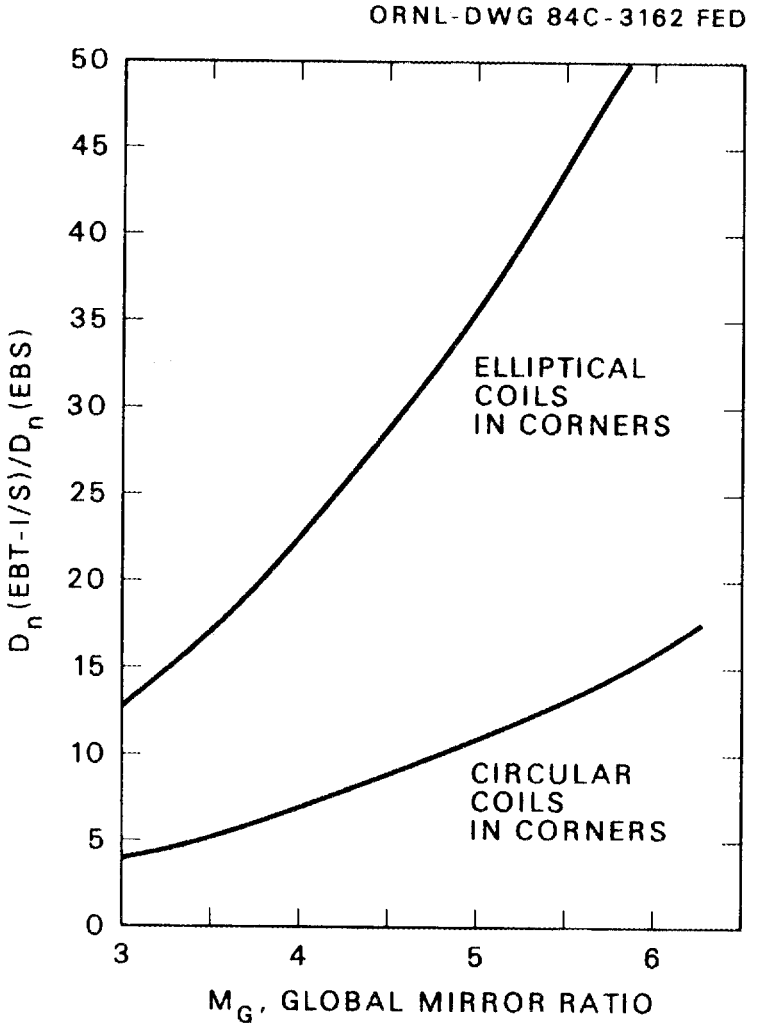

Fig. 1.12. EBS transport coefficients are seen to improve roughly as the inverse square of the global mirror ratio M_G. For the configuration with circular coils in the corners, available dc power and ECH frequencies should permit about a factor of 4 variation in the neoclassical transport rates.

exciting possibility of (1) obtaining an order of magnitude improvement in the neoclassical confinement time, (2) using interesting new heating techniques that would not be possible in a standard bumpy torus, (3) significantly improving ECH efficiency and energy confinement through better centering of drift orbits, (4) testing neoclassical scaling by varying the effective aspect ratio via the global mirror ratio, and (5) improving stability by forming the hot electron rings in a nearly axisymmetric geometry that is more favorable to obtaining an average magnetic well than in toroidal geometry. Each of these possibilities can be investigated in an EBS in which the corners are constructed with EBT-I/S half-coils (eight per corner), the sides use EBT-I/S full coils, and presently available motor-generator sets, cooling tower capacity, and ECH frequencies are utilized.

REFERENCES

1. D. A. Spong, E. G. Harris, and C. L. Hedrick, "Kinetic Transport Properties of a Bumpy Torus with Finite Radial Ambipolar Field," Nucl. Fusion 19, 665 (1979).

2. D. E. Hastings and D. A. Spong, "Nonresonant Electron Transport in the ELMO Bumpy Torus Experiment Using a BGK Operator," Phys. Fluids 26, 1551 (1983).

2. RIPPLE EFFECTS IN ELMO BUMPY SQUARE

N. A. Uckan

The allowable magnitudes of the magnetic field ripple in the high-field toroidal solenoids (corners) of the ELMO Bumpy Square (EBS) are calculated. The enhanced transport coefficients associated with the ripple-induced drifts are compared with the ELMO Bumpy Torus (EBT) neoclassical diffusion coefficients.

2.1 INTRODUCTION

The EBS geometry consists of linear segments of simple mirrors that are linked by sections of high-field toroidal solenoids (corners) as shown in Fig. 2.1. In this configuration the toroidal effects are localized in the corners. For an experimental-size device (similar in size to an EBT-S), EBS has been shown to have single-particle confinement properties and plasma volume utilization that are distinctly superior to those of a standard EBT of comparable size.[1] Numerically calculated transport coefficients (from single-particle drift orbits) indicate that the neoclassical confinement time should be a factor of 5 to 15 larger [depending on the global mirror ratio $M_G = B_{corner}/B_{side}$ (midplane)] for the EBS than for an EBT of comparable size.[1,2]

In order for neoclassical losses to be dominant, ripple-induced losses from the toroidal solenoid sections (corners) should be smaller than the neoclassical losses from the straight sections. The ripple is produced by the finiteness of the number of coils in the corners. This ripple will introduce additional particle trapping and, if large enough, may be the main factor determining the transport of particles and energy in the region of low collision frequencies.[3] In the phenomenon known as ripple trapping, the particles become trapped in the field minimum between coils (between coils that produce the toroidal solenoid field in the corners) that are localized in the toroidal direction and experience a unidirectional toroidal drift that leads to the ripple diffusion. A similar phenomenon occurs in other toroidal configurations (i.e., tokamaks). We note that the ripple trapping affects only a relatively small group of particles, namely,

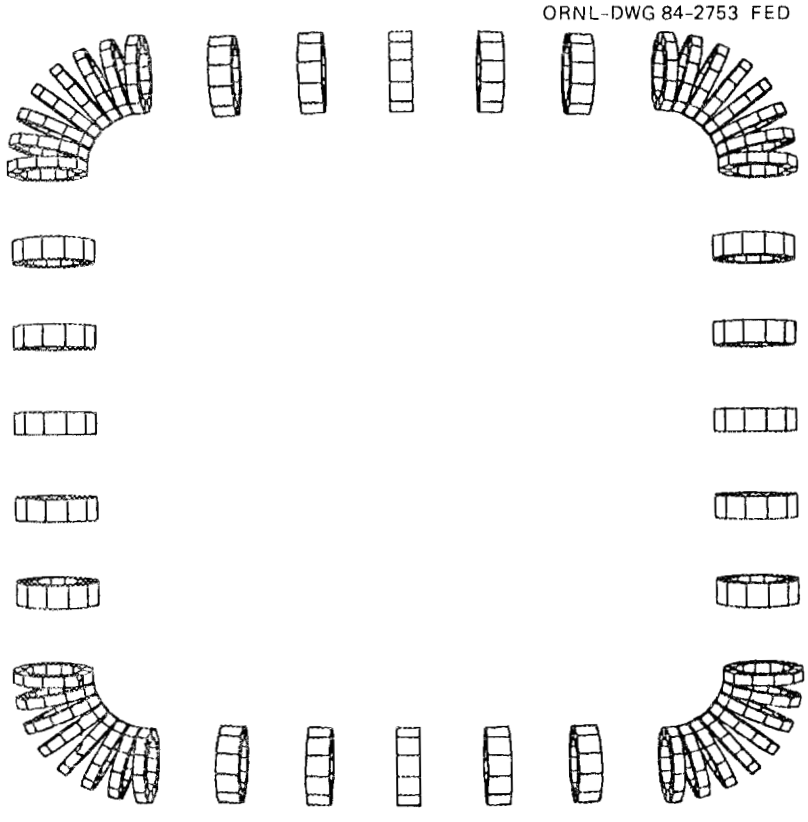

Fig. 2.1. Geometry of an EBS configuration (top view of coil arrangement).

those with $v_{\|}$ (parallel velocity) so small that they can be trapped in the ripple.

In general, the ripple modulation δ (magnitude of field ripple) varies both radially and poloidally. The poloidal variation has the effect of reducing or completely eliminating the ripple well depth on the inside of the toroidal sections, with the precise degree of reduction depending on the shape of the coils and the position of the plasma within the coils.[3,4] For simplicity, we will neglect the poloidal variations, with the result of overestimating the ripple effects.

In our examples we will consider an EBS configuration whose sides are constructed from EBT-I/S mirror coils (five mirror coils per side with a mirror ratio of ~1.9) and whose corners are 90° sections of a toroidal solenoid in which the field is produced by (1) four EBT-I/S mirror coils or (2) eight half-size EBT-I/S coils per corner. Figures 2.2 and 2.3 show the innermost, central, and outermost magnetic field lines in the equatorial plane for these two cases, respectively. The inner and outer field lines are defined by the clear bore in the throat of a mirror coil in the sides. The central field line defines a minor axis or magnetic axis of the device.

2.2 MAGNETIC FIELD MODEL

Figures 2.4 and 2.5 show the magnetic field strength as a function of arc length along the magnetic axis of a four- and eight-coil per corner EBS, respectively. The on-axis mirror ratio in the sides is seen to be 1.9, and the global mirror ratios [B_{corner}/B_{side} (midplane)] for these particular cases are 3.4 and 3.85, respectively. In both cases the corner coils have the same total number of ampere-turns. Although the field ripple is apparent for a four-coil per corner case (Figs. 2.2 and 2.4), the ripple is practically zero for most of the plasma cross section for an eight-coil per corner case (Figs. 2.3 and 2.5). A variation of field ripple as a function of normalized radius is shown in Fig. 2.6 for both cases and is summarized in Table 2.1.

For high-field toroidal corners, a simple model for the magnetic field is

$$\mathbf{B} = \frac{B_o}{1 + \epsilon \cos\theta}\left[\frac{B_r}{B_\phi}\,,\ 0\,,\ 1 - \delta(r,\theta)\cos N\phi\right], \qquad (2.1)$$

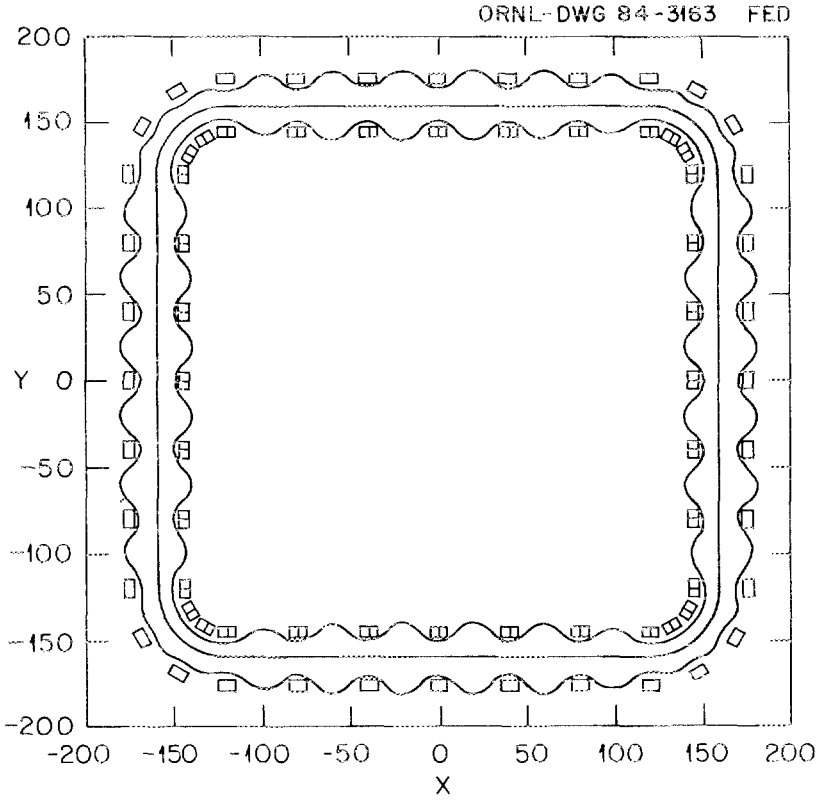

Fig. 2.2. Magnetic field lines in the equatorial plane of an EBS with a four-coil corner. Each side of the EBS configuration consists of a linear array of five EBT-I/S mirror coils, and the corners are formed by 90° sections of toroidal solenoids in which the field is produced by four EBT-I/S mirror coils. Current in straight section coils is 7.25 kA and in the corner coils 9 kA.

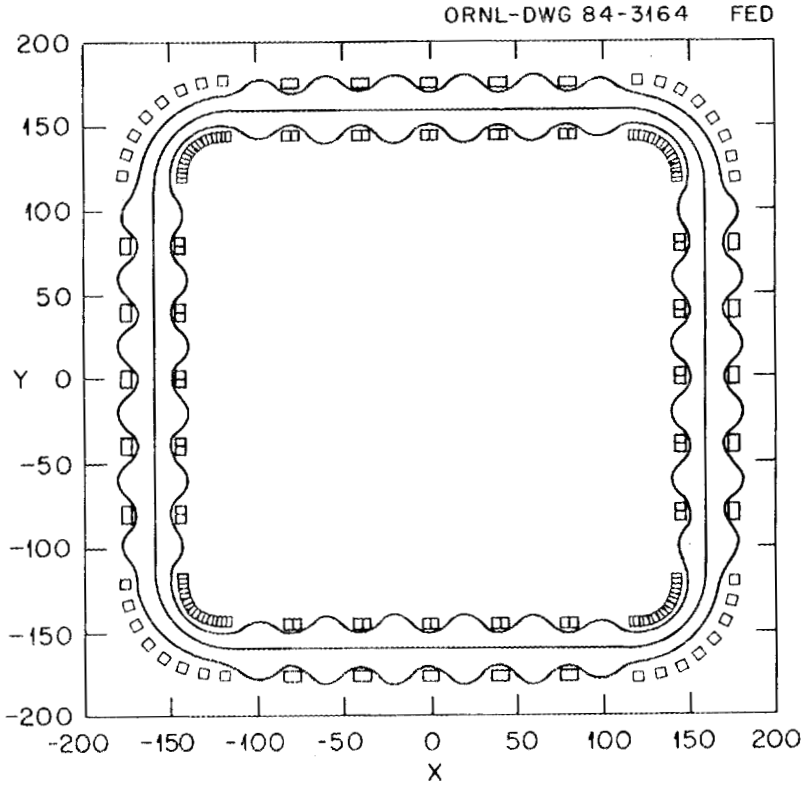

Fig. 2.3. Magnetic field lines in the equatorial plane of an EBS with eight coils per corner. The corner field is produced by eight half-size (ampere-turns) EBT-I/S coils. Total ampere-turns are the same as in Fig. 2.2.

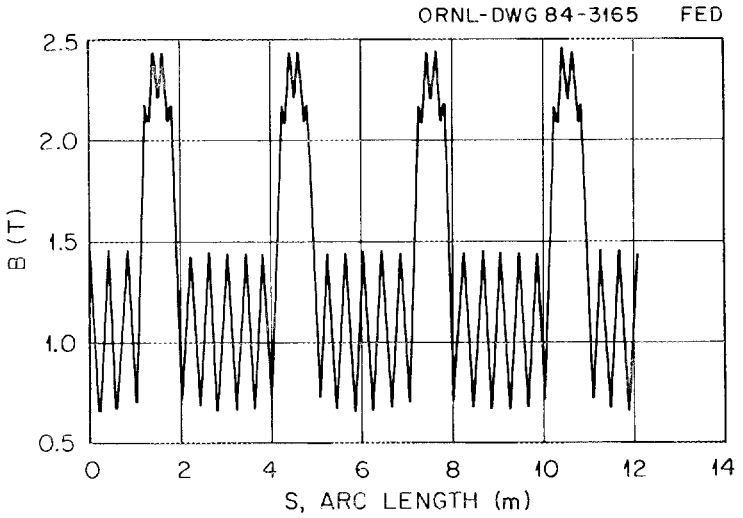

Fig. 2.4. Magnetic field strength as a function of arc length along the magnetic axis for a four-coil per corner EBS (Fig. 2.2).

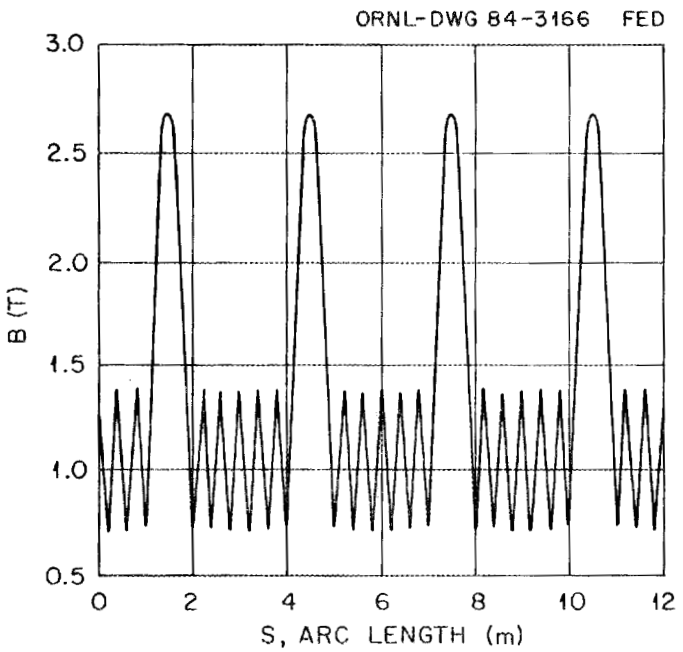

Fig. 2.5. Magnetic field strength as a function of arc length along the magnetic axis for an eight-coil per corner EBS (Fig. 2.3.).

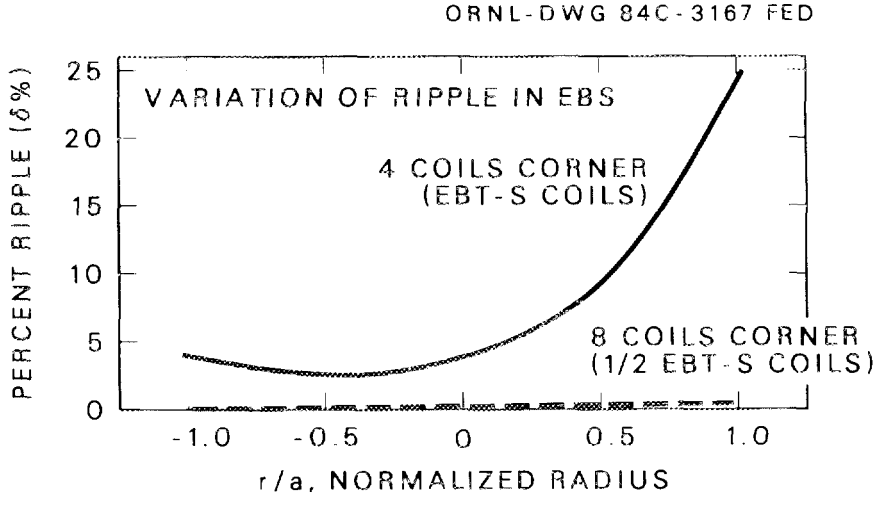

Fig. 2.6. Variation of ripple amplitude δ as a function of radius for (a) four coils per corner (solid line) and (b) eight coils per corner (dashed line).

Table 2.1. Ripple variation in the corners of EBS

Normalized radius[a] r/a	Ripple amplitudes, % Four-coil/corner	Eight-coil/corner
-1.0	3.5	0
-0.5	2.5	0
0.0	4.0	0
+0.5	8.5	~0
+1.0	~25.0	~0.5

[a]Here a is the last field line that just grazes the coil throat in the straight sections (a ≃ 11 cm).

where r and θ are polar coordinates in the minor cross section of the corners, ϕ is the angular coordinate (toroidal angle) along the magnetic axis of the corners, $\epsilon = r/R_o$ is the inverse aspect ratio of the toroidal corner (R_o is the major radius of the corner), N is the number of coils in the corners (a four-coil per corner case corresponds to an N = 12-coil torus and an eight-coil per corner case corresponds to an N = 28-coil torus), and $\delta(r,\theta)$ is the ripple well depth (modulation), defined as

$$\delta(r,\theta) = \left(\frac{B_{max} - B_{min}}{B_{max} + B_{min}}\right)_{corner} \simeq \left(\frac{\Delta B}{B_o}\right)_{corner} \tag{2.2}$$

(see Fig. 2.7 for definitions). The radial component of **B**, necessary to satisfy $\nabla \cdot B = 0$, is small (on the order of $B_r \sim \delta B_o \sin N\phi$). Thus, the field strength in the corner is approximately

$$B \simeq B_\phi \simeq B_o[1 - \epsilon \cos\theta - \delta(r,\theta)\cos N\phi] \ . \tag{2.3}$$

2.3 CRITICAL ENERGIES (ref. 3)

2.3.1 Threshold Energy

The threshold energy is defined as the energy above which particles execute more than one bounce motion in a ripple before being scattered out of the loss region ($v_\parallel < \delta^{1/2} v_\perp$) associated with ripples (Fig. 2.8). This energy can be obtained by setting

$$\tau_{eff}(\text{scattering}) = \tau(\text{bounce}) \tag{2.4a}$$

or

$$\nu_{eff}(\text{scattering}) = \nu(\text{bounce}) \ , \tag{2.4b}$$

where

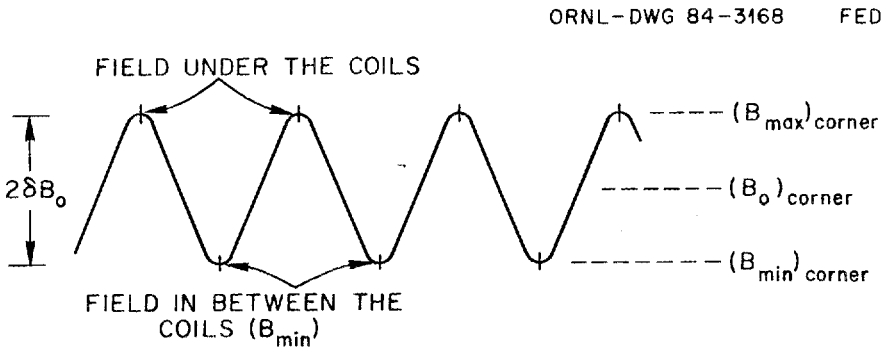

Fig. 2.7. Definitions of field maxima and minima in the corner.

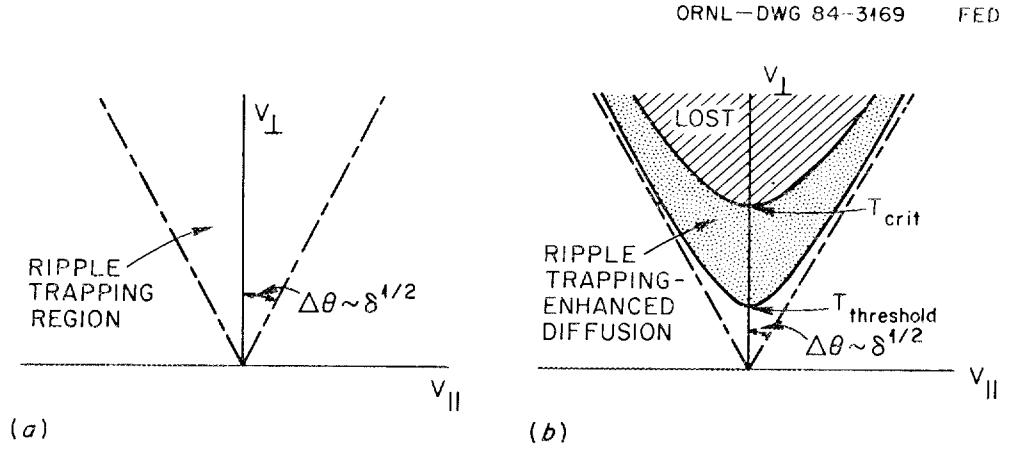

Fig. 2.8. (a) Ripple loss region and (b) critical energies.

$$\nu_{eff} = \frac{\nu_{90}}{(\Delta\theta)^2} = \frac{\nu_{90}}{\delta} , \tag{2.5a}$$

$$\nu(\text{bounce}) = \frac{v}{L} (\delta)^{1/2} = \frac{vN}{2\pi R_o} (\delta)^{1/2} . \tag{2.5b}$$

Here ν_{90} is the 90° collision frequency, v is the particle speed, L is the length of the ripple well ($L = 2\pi R_o/N$), and the fraction of particles that is ripple trapped is equal to $(\delta)^{1/2}$. Combining Eqs. (2.5a) and (2.5b) in Eq. (2.4b), we have

$$\frac{\nu_{90}}{\delta} = \delta^{1/2} \frac{vN}{2\pi R_o} , \tag{2.6}$$

which gives the threshold energy (temperature) as (in cgs units with temperature in electron-volts)

$$T_{th} = \delta^{-3/4} \left(\frac{R_o}{N}\right)^{1/2} (8 \times 10^{-13} n_e)^{1/2} \text{ (eV)} . \tag{2.7}$$

For the four-coil per corner case, considering plasmas with mid-10^{12} cm^{-3} density and $R_o \simeq 40$ cm, the threshold energy is about 30 eV (10 eV) at the plasma center (edge). For the eight-coil per corner case, $T_{th} \simeq 125$ eV at the plasma edge and is several orders of magnitude larger at the plasma center.

2.3.2 Critical Energy

The critical energy is defined as the energy above which particles will reach the wall if they are trapped in the ripple. When a particle is trapped in a ripple ($T > T_{th}$), its guiding center drifts along a contour of constant B. Because mod-B contours are not closed in a toroidal field, the particles are not confined unless they are scattered out of the ripple loss region before they can reach the wall. Thus, the critical energy can be determined by setting

$$\tau_{eff}(\text{scattering}) = \tau(\text{drift}) = a/v_{drift} , \tag{2.8}$$

where

$$v_{drift} \simeq \frac{cT}{eBR_o} = 10^8 \frac{T\ (eV)}{B\ (gauss)\ R_o\ (cm)}\ \ (cm/s)\ . \qquad (2.9)$$

For ions this gives a critical energy (in cgs units with T in electron-volts) of

$$T_{*,i} \simeq \left(10^{-14}\ \frac{BR_o a}{\delta}\ n_e\right)^{2/5}\ . \qquad (2.10)$$

The critical energy is a factor of $(m_i/m_e)^{1/5}$ ($\simeq 4.5$ for a hydrogen plasma) larger for electrons. Again, considering the four-coil per corner case, $T_{*,i}\ (r = 0) \simeq 600$ eV and $T_{*,i}\ (r = a) \simeq 250$ eV. Corresponding electron temperatures are higher (by a factor of ~4.5). For an eight-coil per corner case, $T_{*,i}\ (r = a) \simeq 1.5$ keV and $T_{*,i}\ (r = 0) >> T_{*,i}\ (r = a)$.

The critical energy defined by Eq. (2.10) is for a zero electric field. In the presence of a finite electric field, if the particles are trapped in the ripple and if their energy exceeds the energy given by Eq. (2.10) ($T > T_*$), the particle orbits are not necessarily open because of the $\mathbf{E} \times \mathbf{B}$ precessional drift, which balances the vertical (toroidal) drift.[5] The shift in particle drift orbits is

$$\Delta x = v_{drift}/\Omega\ , \qquad (2.11)$$

where

$$\Omega = \frac{cE}{rB} + \frac{cT}{eB_r R_c} \qquad (2.12)$$

with $R_c = -\ (\partial\ \ell n\ B/\partial r)^{-1}$. For particle orbits to be closed, $\Delta x \leq a/2$, or, conversely, for particles trapped in the ripple to drift to the wall,

$$\Delta x \geq a/2\ . \qquad (2.13)$$

Combining Eqs. (2.11) and (2.13) gives a critical energy in the presence of an electric field above which particles will reach the wall:

$$T_{*E} \geq \frac{a(eE/r)}{\left(\frac{1}{R_o} - \frac{a}{rR_c}\right)} . \tag{2.14}$$

For weak ripples, rR_c in the corner is very large (approaches infinity). With approximately $E \simeq \Delta\phi/\ell_E$, where ℓ_E is the electric field scale length (which is on the order of plasma radius), Eq. (2.14) reduces to

$$T_{*E} \gtrsim \left(\frac{a}{\ell_E}\right)\left(\frac{R_o}{a}\right)\Delta\phi \simeq \frac{\Delta\phi}{\epsilon} . \tag{2.15}$$

Here ϵ is the inverse aspect ratio ($\epsilon \sim 1/3$–$1/5$). Thus, only if $T_{*E} \gtrsim (3\text{–}5)\Delta\phi$ will particles be directly lost.

From Eqs. (2.10) and (2.14) we define for ions

$$T_{crit,i} = \max\left(T_{*,i} \; ; \; T_{*E}\right) \tag{2.16a}$$

and for electrons

$$T_{crit,e} = \max\left(T_{*,e} \; ; \; T_{*E}\right) . \tag{2.16b}$$

2.4 RIPPLE-ENHANCED DIFFUSION—SIMPLE ESTIMATES

From the critical energies (T_{th}, T_{crit}) defined earlier we can see that the ripple collisionality regime can be divided into three regions, as shown in Fig. 2.9. The upper collision frequency point ($\nu > \nu N\delta^{3/2}/R_o$), above which transport losses diminish to zero, is the point at which the plasma particle temperature decreases below the threshold energy ($T < T_{th}$). In the middle range of the collisionality regime ($\rho\nu\delta/Ra < \nu < \nu N\delta^{3/2}/R_o$, where ρ is the gyroradius), transport coefficients scale as ν^{-1} because the particles are scattered out of

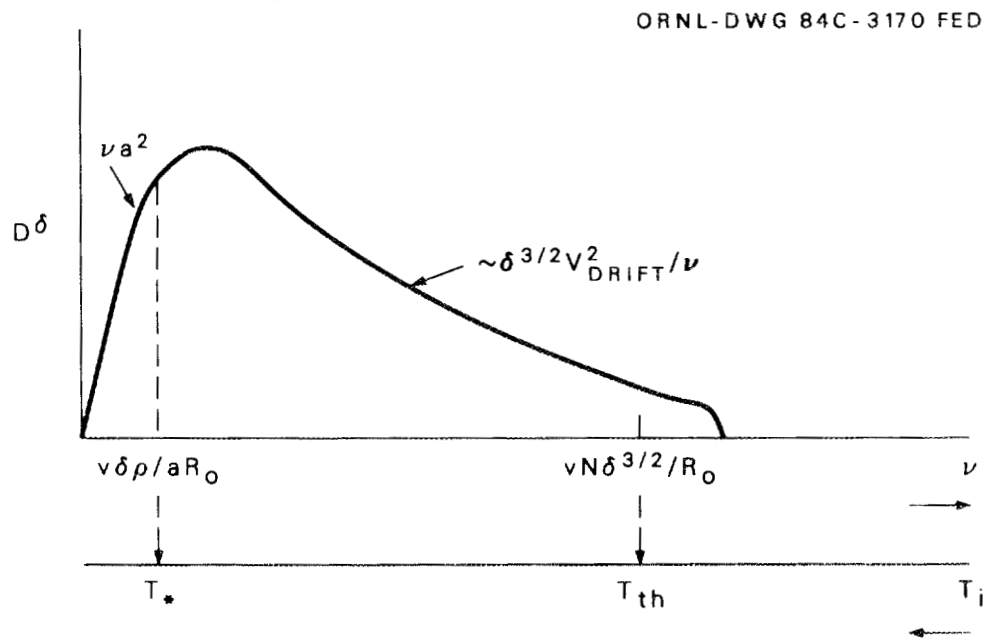

Fig. 2.9. Ripple collisionality regime.

the loss region before they can drift out of the device. To convey the spirit of simple diffusion estimates, we give a rough picture of the random walk process.

The average step-size taken by a ripple-trapped particle is

$$(\Delta x)^{\delta} \sim v_{drift} \cdot \tau_{eff}^{\delta} = v_{drift} \cdot \frac{\delta}{\nu_{90}} . \tag{2.17a}$$

The frequency with which such steps are taken is

$$\nu_{eff}^{\delta} = \nu_{90}/\delta . \tag{2.17b}$$

The fraction of particles participating in this ripple trapping is

$$f^{\delta} = \delta^{1/2} . \tag{2.17c}$$

Thus, the diffusion coefficient associated with ripple trapping is

$$D^{\delta} \sim [(\Delta x)^{\delta}]^2 \cdot \nu_{eff}^{\delta} \cdot f^{\delta}$$

$$\sim \frac{\delta^{3/2} v_{drift}^2}{\nu_{90}} . \tag{2.18}$$

Finally, in the absence of electric fields, at very low collision frequencies ($\nu < \rho v \delta / R_o a$), the particle temperature increases above the critical energy, and all particles trapped in the ripples will drift to the wall without being scattered out of the loss region. The corresponding diffusion coefficient is

$$D \sim \nu_{90} a^2 . \tag{2.19}$$

We compare these ripple-enhanced diffusion coefficients with the conventional EBT neoclassical diffusion coefficients to determine the

allowable range for the magnitude of the field modulations (ripples). The neoclassical diffusion coefficient for EBT is given by

$$D^{NC} \sim (\Delta x)^2 \frac{\nu}{1 + \nu^2/\Omega^2} , \tag{2.20}$$

where

$$\Delta x = v_{drift}/\Omega .$$

In the collisionless regime

$$D^{NC} \sim \nu_{90}(\Delta x)^2 \sim \nu_{90} \left(\frac{v_{drift}}{\Omega}\right)^2 . \tag{2.21}$$

For $D^{\delta} < D^{NC}$, that is,

$$\delta^{3/2} \frac{v_{drift}^2}{\nu_{90}} < \nu_{90}\left(\frac{v_{drift}}{\Omega}\right)^2$$

we find

$$\delta^{3/2} < (\nu/\Omega)^2$$

or

$$\delta < (\nu/\Omega)^{4/3} . \tag{2.22}$$

For $\nu/\Omega \sim 0.1$, the magnitude of the ripple well depth should be $\delta < 4.5\%$ in order for ripple losses not to be dominant. For very low collision frequencies ($\nu/\Omega \sim 0.01$), one requires $\delta < 0.2\%$. We see from this example that for the four-coil per corner case the ripple losses will dominate. However, for the eight-coil per corner case the overall enhanced losses due to ripple will have a negligible effect on plasma confinement.

REFERENCES

1. L. W. Owen, D. K. Lee, and C. L. Hedrick, "ELMO Bumpy Square," in Advanced Bumpy Torus Concepts: Proceedings of the Workshop, CONF-830758, Oak Ridge Natl. Lab., 1983, p. 55; also Sect. 1 of this report.

2. N. A. Uckan, L. W. Owen, D. A. Spong, R. L. Miller, W. B. Ard, J. F. Pipkins, and R. J. Schmidt, Reactor Assessments of Advanced Bumpy Torus Configurations, ORNL/TM-8985, Oak Ridge Natl. Lab., 1984; also Sect. 9 of this report.

3. N. A. Uckan, K. T. Tsang, and J. D. Callen, Effects of the Poloidal Variation of the Magnetic Field Ripple on Enhanced Heat Transport in Tokamaks, ORNL/TM-5438, Oak Ridge Natl. Lab., 1976.

4. N. A. Uckan, T. Uckan, and J. R. Moore, Calculation of Magnetic Field Ripple Effects in Circular and Noncircular Tokamaks, ORNL/TM-5603, Oak Ridge Natl. Lab., 1976.

5. D. E. Hastings, Oak Ridge National Laboratory, private communication, January 1984.

3. FIELD ERROR CALCULATIONS IN AN ELMO BUMPY SQUARE (EBS)

N. A. Uckan, D. K. Lee, and T. Uckan

A closed field line device, such as an ELMO Bumpy Torus (EBT) or an ELMO Bumpy Square (EBS), is very sensitive to small perturbations in the magnetic field. Numerical calculations of field errors due to single-coil misalignments indicate that the field line closure is most sensitive to angular misalignments of the coils in both EBT and EBS. Errors in absolute spatial positions are found to have very small effects, provided there is no corresponding angular misalignment. Statistical analysis of errors from N coils (where $N = N_s + N_c$, with N_s the total number of coils in straight sections and N_c the total number of coils in high-field curved corner sections), assuming the errors in all N coil alignments are randomly distributed in a Gaussian fashion, is found to be in reasonable agreement with the numerical calculations. A specific example for an EBS configuration is given. Each side of this EBS configuration consists of a linear array of five EBT-S coils, and the corners are formed by 90° sections having eight half-size (one-half number of turns) EBT-S coils with a ratio of currents $I_{corner}/I_{side} \simeq 1.2\text{-}1.4$. Calculations indicate that a misalignment of 1 cm in one coil yields an error $\delta B/B < 10^{-6}$, whereas a misalignment of 1° in one coil orientation results in an error $\delta B/B \sim 10^{-4}$. Corresponding errors in EBT-S are $\delta B/B < 10^{-10}$ for 1 cm misalignment of one coil and $\delta B/B \sim 10^{-4}$ for 1° misalignment of one coil orientation.

3.1 INTRODUCTION

An ideal ELMO Bumpy Square (EBS) is a closed field line system with zero rotational transform and no toroidal current, characteristic of an ideal ELMO Bumpy Torus (EBT). This current-free equilibrium configuration is sensitive to the system magnetic field asymmetrics (perturbations). If large enough, these field perturbations or field errors ($\delta B/B$) can cause[1-4] (1) field lines to spiral out of the confinement volume, thereby degrading confinement; (2) establishment of toroidal current and therefore enhanced fluctuations; and (3) distortion of equipotentials of the ambipolar potential well.

In practice, the field errors are unavoidable due to small coil misalignments during installation, imperfection in coil winding, etc.

Here, we (1) describe the numerical scheme used in the evaluation of both $\delta B/B$ and field line closure, (2) discuss which classes of perturbations (spatial or angular) are dominant, and (3) describe the statistical analysis of errors from all coils.

3.2 FIELD ERROR CALCULATION DUE TO SINGLE-COIL MISALIGNMENT

As pointed out, the field errors can arise from many different sources: coil misalignment, imperfect winding effects in a coil, magnetic fields from buswork and leads, and field perturbations due to the presence of magnetic materials. Although all these sources can cause significant error fields, we will discuss only the first effect in this paper. We will evaluate the amount δR that a field line centered at the magnetic axis (starting in the coil throat) misses connecting with itself when followed once around the torus. For perfect coils installed with no misalignment, this number should be zero. We note that the choices of magnetic axis and coil throat location for the starting point have to do with the fact that field errors will be more critical in regions of large magnetic field and large radii of curvature[1-5] $[(\delta B/B) \sim \rho/R_c \sim (BR_c)^{-1}$, where ρ is the gyroradius and R_c is the radius of curvature]. Shown in Fig. 3.1 is the geometry of an EBS configuration indicating the coil arrangements and coordinate system used. An EBS configuration has four symmetric planes and eight field periods. Specific coils involved in the calculations within one field period are designated by A through G in Fig. 3.1.

In our examples we will consider an EBS configuration whose sides are constructed from EBT-S mirror coils (five mirror coils per side — coils such as A, B, and C) and whose corners are 90° sections of a toroidal solenoid in which the field is produced by eight half-size EBT-S coils per corner. Figure 3.2 shows magnetic field lines in the equatorial plane (X-Y plane) with specific dimensions. The mirror sector length (or the coil spacing) in the sides is L_m = 40 cm, and the major radius of the corner sections is $R_{corner} \simeq 44$ cm, with the axis of each corner section displaced radially outward by $(\Delta \text{ shift})_{corner} \simeq$ 2.5 cm from the axis of the sides. This displacement and the length of the transition sector (L_{Tr}) are adjusted so that the rings in the transition sector (the sector connecting the simple mirror field to a 1/R varying toroidal field) form on the same flux lines as in the axisymmetric sectors. Depending on the ratio of the currents in the

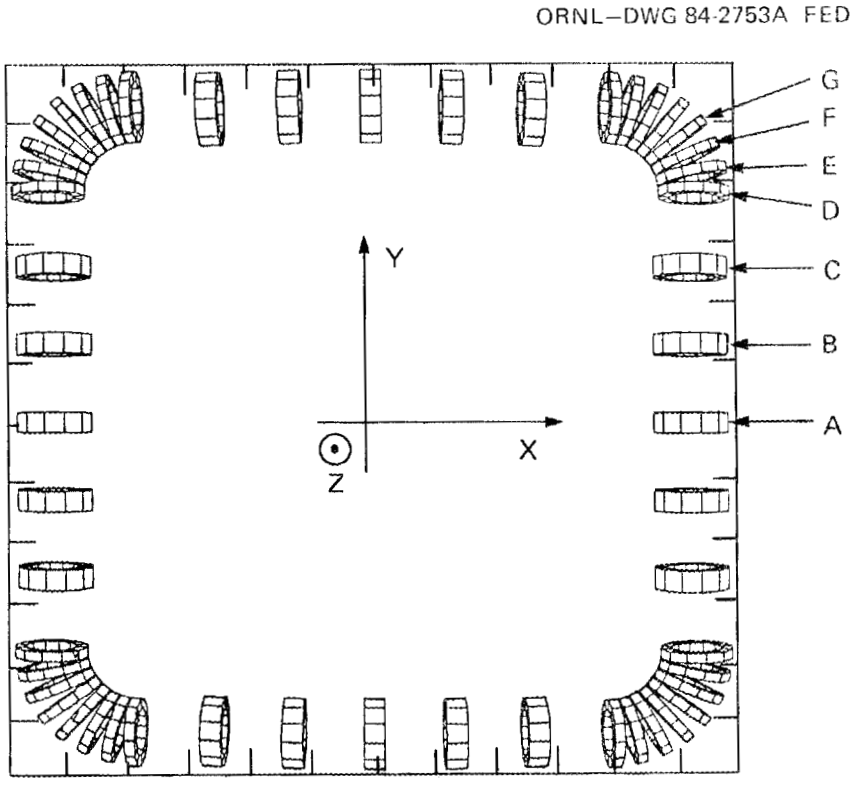

Fig. 3.1. Geometry of an EBS configuration indicating the coil arrangements (top view). Coordinate system used is shown (X and Y axes are indicated; Z-axis points out of the paper — right-hand coordinate system). Specific coils involved in the calculations A through G are indicated, which represent the coils in one field period. In an EBS there are four symmetry planes and eight field periods.

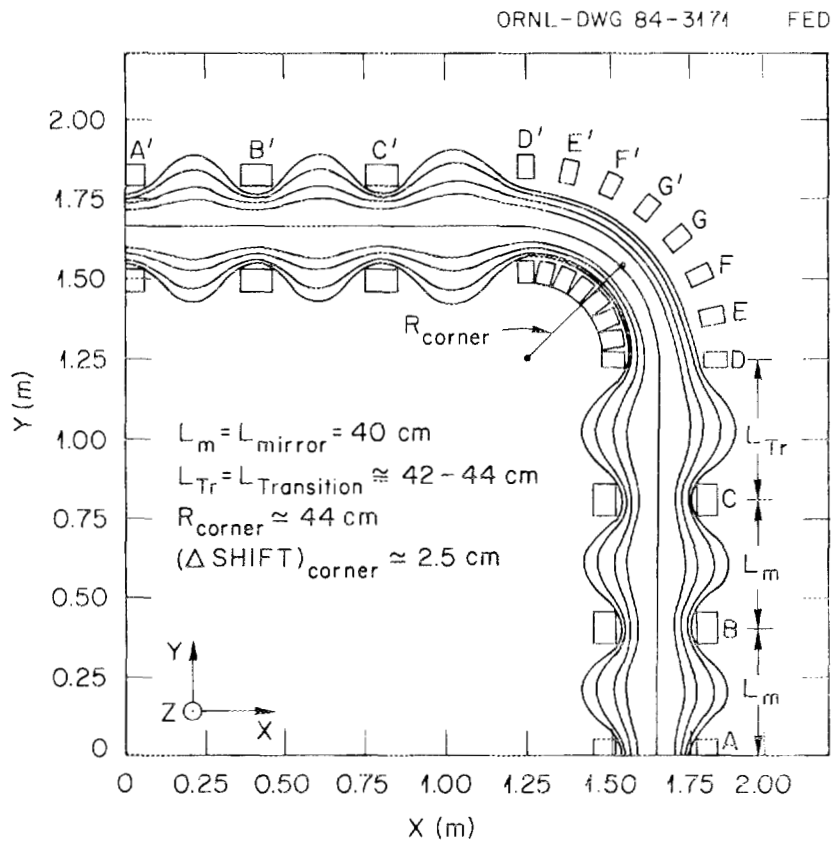

Fig. 3.2. Magnetic field lines in the equatorial plane (X–Y plane) of an EBS are shown for one quadrant. A through G coils and their mirror images G′ through A′ are shown along with specific dimensions used in the calculations. Here L_m = mirror sector length, L_{Tr} = transition sector length, R_{corner} = radius of the corner, and $(\Delta shift)_{corner}$ = (center of coil D − center of coil A) = $X_{Do} - X_{Ao}$.

corner coils to the currents in the straight section, the transition sector length is typically larger (~2 to 4 cm) than the length of the mirror sectors. For $I_{corner}/I_{side} \simeq 1.2\text{-}1.4$, $L_{Tr} \simeq 42\text{-}44$ cm. In our example, we have $I_{corner}/I_{side} \simeq 1.4$ and $L_{Tr} \simeq 42$ cm.

In numerical calculations, the mirror coils (i.e., coils A, B, and C) are approximated by two circular filaments, and the corner coils (i.e., coils D, E, F, and G) are approximated by a single circular filament. The field line geometry shown in Fig. 3.2 is calculated with finite coil dimensions from EFFI, which do not differ from those of circular filament approximation.[6] The code evaluates $\delta R(\delta X, \delta Y, \delta Z)$ in a coil plane by integrating the field line equations through one full period around the machine (360° in ϕ). Theoretically, δR vanishes for the ideal positions and orientations of the coils. Actual numerical results obtained from the code usually range from 10^{-9} to 10^{-10} cm for $|\delta R|$. Therefore, the accuracy of the code seems sufficient for the purpose of the present study.

There are five degrees of freedom associated with each coil: three for the position of the coil center and two for the angles of the coil plane. The five corresponding coil errors are denoted by ΔX, ΔY, ΔZ, $\Delta\theta$, and $\Delta\phi$, where θ is the angle between the Z-axis and the projection of the coil normal to the X-Y plane, and ϕ is the angle between the coil plane (which is coplanar with the Z-axis) and the X-axis in the X-Y plane (Fig. 3.3).

Table 3.1 lists the field line displacement δR obtained with only one coil perturbed and with only the error involved in coil position or orientation. The field line displacement is measured in the center of the coil plane of the A coil (X-Z plane with coil center at $X = X_{Ao}$, $Y = 0$, $Z = Z_{Ao} = 0$). Figures 3.4 and 3.5 show directions and relative magnitudes of field line displacement in a circle of radius 11 cm (radius of the clear bore under the coil) in the coil plane for $\Delta\theta = 1°$ and for $\Delta\phi = 1°$, respectively.

The results of the calculations indicate that the field line closure is most sensitive to angular misalignment of the coils ($\Delta\theta$ and $\Delta\phi$). In these cases, an <u>assumed</u> angular error of 1° causes $\delta B/B \simeq 2.22 \times 10^{-4}$. We note that in EBT-S a similar angular misalignment of 1° ($\Delta\theta$ or $\theta\phi$) causes similar error fields ($\delta B/B \simeq 2.2 \times 10^{-4}$).

Of equal significance is the effect of the errors in θ and ϕ, which are essentially orthogonal; $\Delta\theta$ causes a vertical displacement of

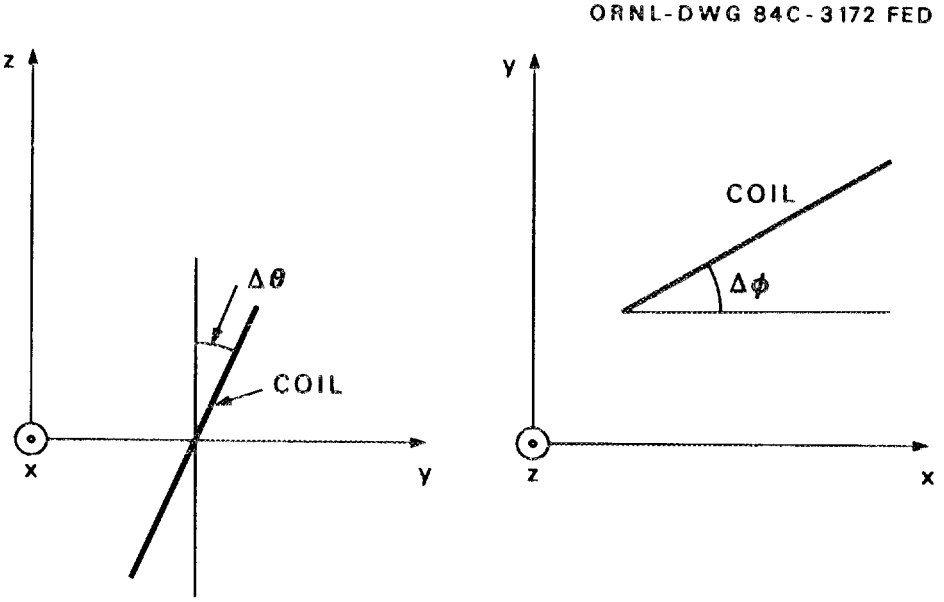

Fig. 3.3. Two angles of the coil plane. Orientation of X, Y, and Z coordinates are shown, with the same orientation as in Figs. 3.1 and 3.2.

Table 3.1. Results of perturbations to one coil[a]

Coil perturbed	Perturbation	Field line displacement δX (mm)	Field line displacement δZ (mm)	δB/B
A	$\Delta\theta = 1°$	≈ 0	-2.82	2.22×10^{-4}
A	$\Delta\phi = 1°$	-2.81	≈ 0	2.22×10^{-4}
G	$\Delta\theta = 1°$	≈ 0	-1.17	9.22×10^{-5}
G	$\Delta\phi = 1°$	-1.21	0	9.54×10^{-5}
B	$\Delta X = 1$ cm	1.1×10^{-2}	0	8.67×10^{-7}
B	$\Delta Y = 1$ cm	6.2×10^{-3}	0	4.89×10^{-7}
B	$\Delta Z = 1$ cm	0	1.7×10^{-2}	1.34×10^{-6}
B	$\Delta I/I = 10^{-3}$	3.4×10^{-4}	0	2.68×10^{-8}

[a] Field line displacement is measured in the center of the A coil plane (X-Z plane). Calculated lack of field line closure $\delta\mathfrak{R}(\delta X, \delta Z)$ and corresponding field error $\delta B/B = |\delta\mathfrak{R}|/C$, where C is the circumference (field line length)

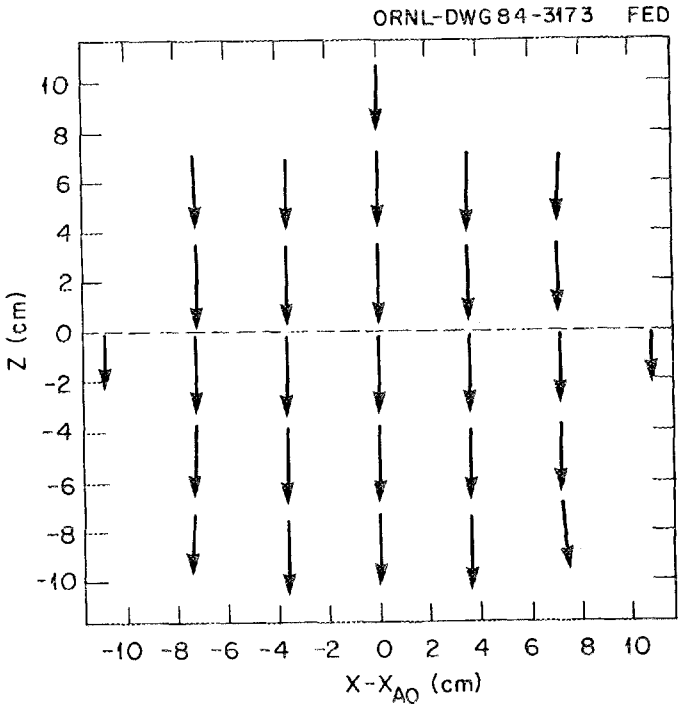

Fig. 3.4. Arrow plot showing the direction and relative magnitude of field line displacements in the plane of A coil for $\Delta\theta = 1°$. The largest magnitude is 2.82 mm at the coil center (0,0).

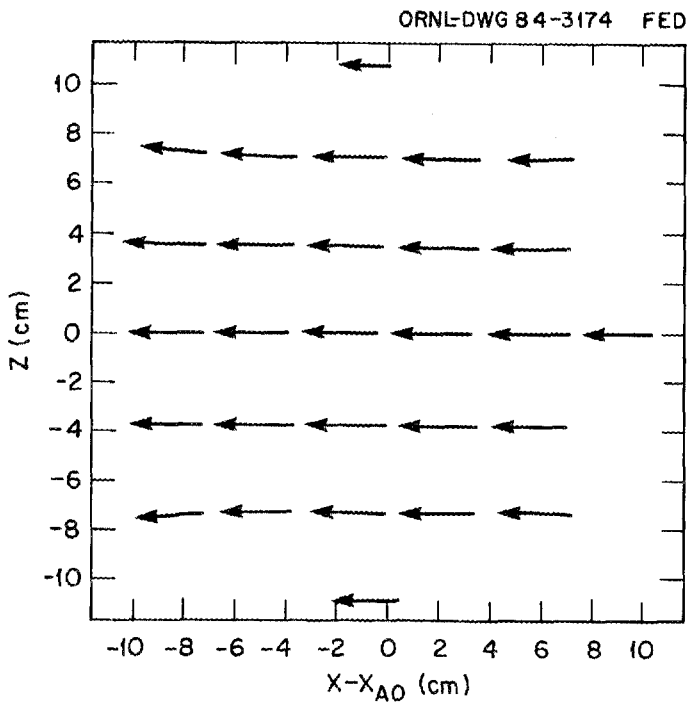

Fig. 3.5. Arrow plot showing the direction and relative magnitude of field line displacements in the plane of A coil for $\Delta\phi = 1°$. The largest magnitude is 2.81 mm at the coil center (0,0).

the field lines (Fig. 3.4), and $\Delta\phi$ causes a horizontal displacement of the field lines (Fig. 3.5).

Errors in absolute position are much less sensitive, provided there is no corresponding angular misalignment.

3.3 STATISTICAL ANALYSIS OF ERRORS

In the previous section, we determined that the dominant misalignment contributions to field errors were in the two angles θ and ϕ. Since the proper determination of angular alignment will require fairly stringent positional alignment also, we will discuss only the angular errors and assume that nonclosure of field lines arising from positioning errors is small relative to the angular ones.

First, we will consider only the variations in θ. The total number of coils in the sides is $N_s = 20$ (five coils per side) and in corners $N_c = 32$ (eight coils per corner). For one coil (side or corner), we have the expression

$$\delta B/B = C_\theta \Delta\theta \ .$$

If we assume that the errors in all 20 straight-side coils are distributed normally with one Gaussian distribution and that the errors in all 32 corner coils are distributed normally with another Gaussian distribution (both of which have a mean error of zero and an rms error of θ_{rms}), then the problem is exactly equivalent to the one-dimensional random walk problem. Each magnet error $\Delta\theta$ contributes a step-size $(\delta Z)_j$ to a field line, where $j = s(\text{side}), c(\text{corner})$. For small individual displacements, the problem can be treated as a linear superposition of steps of varying size and direction with an rms step-size determined by θ_{rms}. For N steps, the rms displacement

$$\delta Z_N = N^{1/2}\, \delta Z_1 \ ;$$

then,

$$\left(\frac{\delta B}{B}\right)_\theta = \left(\frac{\delta B}{B}\right)_{corner} + \left(\frac{\delta B}{B}\right)_{side} \ ,$$

$$\left(\frac{\delta B}{B}\right)_{corner} = N_c^{1/2} \left(C_\theta \theta_{rms}\right)_c \ ,$$

and

$$\left(\frac{\delta B}{B}\right)_{side} = N_s^{1/2}(C_\theta \theta_{rms})_s \ .$$

Thus,

$$\left(\frac{\delta B}{B}\right)_\theta = [(32)^{1/2}C_{\theta c} + (20)^{1/2}C_{\theta s}]\theta_{rms} \ ,$$

where $(\theta_{rms})_c = (\theta_{rms})_s$ is taken.

The same arguments apply for errors in the ϕ direction. Since the errors in ϕ and θ cause the same magnitude change in $\delta B/B$ (i.e., $C_\theta = C_\phi$, from Table 3.1) but are perpendicular in direction, the expression for the total field error is simply

$$\frac{\delta B}{B} = \left[\left(\frac{\delta B}{B}\right)_\theta^2 + \left(\frac{\delta B}{B}\right)_\phi^2\right]^{1/2} \ ,$$

which yields

$$\frac{\delta B}{B} = [(32)^{1/2}C_{\theta c} + (20)^{1/2}C_{\theta s}](\theta_{rms}^2 + \phi_{rms}^2)^{1/2} \ ,$$

where ϕ_{rms} is the rms error in ϕ. The above expession is valid if the errors in ϕ and θ are uncorrelated, which seems to be the most reasonable assumption to make. Finally, if we assume the rms errors in the ϕ and θ directions to be equal, then

$$\frac{\delta B}{B} = [8C_{\theta c} + (40)^{1/2}C_{\theta s}]\theta_{rms} \ .$$

From Table 3.1 we have

$$C_{\theta c} = 9.54 \times 10^{-5} \quad \text{and} \quad C_{\theta s} = 2.22 \times 10^{-4} \ .$$

Thus,

$$\frac{\delta B}{B} = 2.17 \times 10^{-3} \ \theta_{rms} \ ,$$

where θ_{rms} is expressed in degrees.

The question remains, "What is the inherent $\delta B/B$ that can be tolerated?" (That is, what is the field error inherent to the device construction without global correction?) In the EBT-S device the inherent field error is $\delta B/B \simeq 5 \times 10^{-4}$, which can be corrected to a level of $\delta B/B \simeq 10^{-4}$ with the global field error correction coils.[1,3,7] That is, the global field correction coils correct 80% of the inherent device field error in EBT-S. (We note this occurs only when the $\delta B/B \geq 7 \times 10^{-4}$ plasma properties start to degrade.[7]) Based on the EBT-S experience[1,7] and the fact that coil alignment errors produce fairly uniform field errors across the plasma (Figs. 3.4 and 3.5), we assume that similar levels of field errors ($\delta B/B \simeq 10^{-4}$) will be required in EBS and that the global field error correction coils can correct 80% of the inherent device field error. Thus, the inherent field error criterion (that is, five times that for the net field error $\delta B/B \simeq 5 \times 10^{-4}$) will yield the required values for θ_{rms}. Solving

$$\frac{\delta B}{B} = 2.17 \times 10^{-3} \theta_{rms} = 5 \times 10^{-4} \ ,$$

we have

$$\theta_{rms} = 0.23° \ .$$

Since the treatment here is statistical in nature (as is the alignment of the coils), the actual $\delta B/B$ is not specified exactly by a specification of θ_{rms}. Rather, it has a Gaussian distribution; the probability that $\delta B/B$ will be less than 5×10^{-4} is about 68%, and the probability that it will be less than 10^{-3} is over 95%. When corrected with global correction coils, the probability that $\delta B/B$ will be less

than 10^{-4} is about 68% and the probability that it will be less than 2×10^{-4} is more than 95%.

Because drift orbits in EBS are much better centered than those in EBT-S, the effect of field errors on particle orbit displacement might be expected to be more pronounced in EBS than in EBT-S. In this regard, if we choose to be more pessimistic in the field error criterion in EBS than in EBT-S, we can assume that the inherent field error should not exceed $\delta B/B \simeq 2 \times 10^{-4}$ (instead of $\delta B/B \simeq 5 \times 10^{-4}$). Under this pessimistic assumption,

$$\theta_{rms}(\text{pessimistic}) \simeq 0.1 \ .$$

With this value of θ_{rms}, the probability that inherent $\delta B/B$ will be less than 4×10^{-4} is greater than 95%, and when it is corrected, $\delta B/B$ is less than 8×10^{-5}.

REFERENCES

1. T. Uckan et al., "Field Errors in EBT and Their Effects on the Ambipolar Potential," in Ambipolar Potential Formation and Control in Bumpy Tori and Mirrors, CONF-810511, Oak Ridge Natl. Lab., 1981, p. 205.

2. J. D. Callen, "Magnetic Field Error Effects on the Ambipolar Potential in EBT," in Ambipolar Potential Formation and Control in Bumpy Tori and Mirrors, CONF-810511, Oak Ridge Natl. Lab., 1981, p. 203.

3. T. Uckan, "Field Error Measurements on EBT," Bull. Am. Phys. Soc. 27(8), 1115 (1982).

4. B. H. Quon et al., Influence of Global Magnetic Perturbations on Plasma Behavior in ELMO Bumpy Torus, ORNL/TM-6704, Oak Ridge Natl. Lab., 1980; T. Uckan, in Fusion Energy Division Annual Progress Report for Period Ending December 1979, ORNL-5645, Oak Ridge Natl. Lab., 1980, p. 10; T. Uckan et al., Field Errors in EBT and Their Effects on the Ambipolar Potential, ORNL/TM-7912, Oak Ridge Natl. Lab., 1981.

5. N. A. Uckan et al., "Analysis of Field Error Criteria in an EBT Reactor" in Engineering Problems of Fusion Research: Proceedings of the 9th Symposium, vol. I, IEEE, New York, 1981, p. 467.

6. R. T. Santoro and L. W. Owen, Oak Ridge National Laboratory, private communication, January 1984.

7. T. Uckan, Oak Ridge National Laboratory, private communication, January 1984.

4. INTRODUCTION TO MAGNETIC EQUILIBRIA AND SINGLE-PARTICLE ORBITS IN THE SQUARE CONFIGURATION OF EBT — A TUTORIAL

C. L. Hedrick and L. W. Owen

Here we discuss the ideal magnetohydrodynamic (MHD) magnetic equilibrium properties and single-particle orbit characteristics of the square configuration of ELMO Bumpy Torus (EBT). The intent is to make this aspect of the theory accessible to those unfamiliar with the general aspects of EBT theory. In particular, we attempt to include sufficient detail to enable the interested reader to reproduce the analytic development without excessive effort. Recognizing that many will not have the time or inclination for such an effort, most of the main features are discussed briefly in the introduction. The more formal developments, as well as what we have found to be useful interpretations of the mathematics, are contained in the body of the text. So as not to obscure the basic arguments unduly with algebraic detail, lengthy mathematical developments have been relegated to appendixes.

4.1 INTRODUCTION

For any magnetic containment configuration, one begins by examining its ideal MHD equilibrium and single-particle containment properties. Here we examine these properties for the square[1] configuration of EBT (see Fig. 4.1). The equilibrium and orbit properties form the basis for the "higher-order" calculations of transport, heating, and stability.

The starting point for our analysis is a calculation of the pressure surfaces. As is well known for closed line scalar pressure, the pressure surfaces are the same as surfaces of constant $\oint d\ell/B$ [ref. 2]. In Appendix 4A the Grad-Lortz algorithm[3-6] used to calculate finite-beta, tensor pressure equilibria for the hot electron rings is extended to permit finite core beta (assumed small compared to ring beta). It is again found that the core scalar pressure is constant on constant $\oint d\ell/B$ surfaces.

For vacuum magnetic fields, analytic approximations are developed for $\oint d\ell/B$ in detail. In a midplane of one of the mirror cells composing the sides of the square, the pressure contours are found to

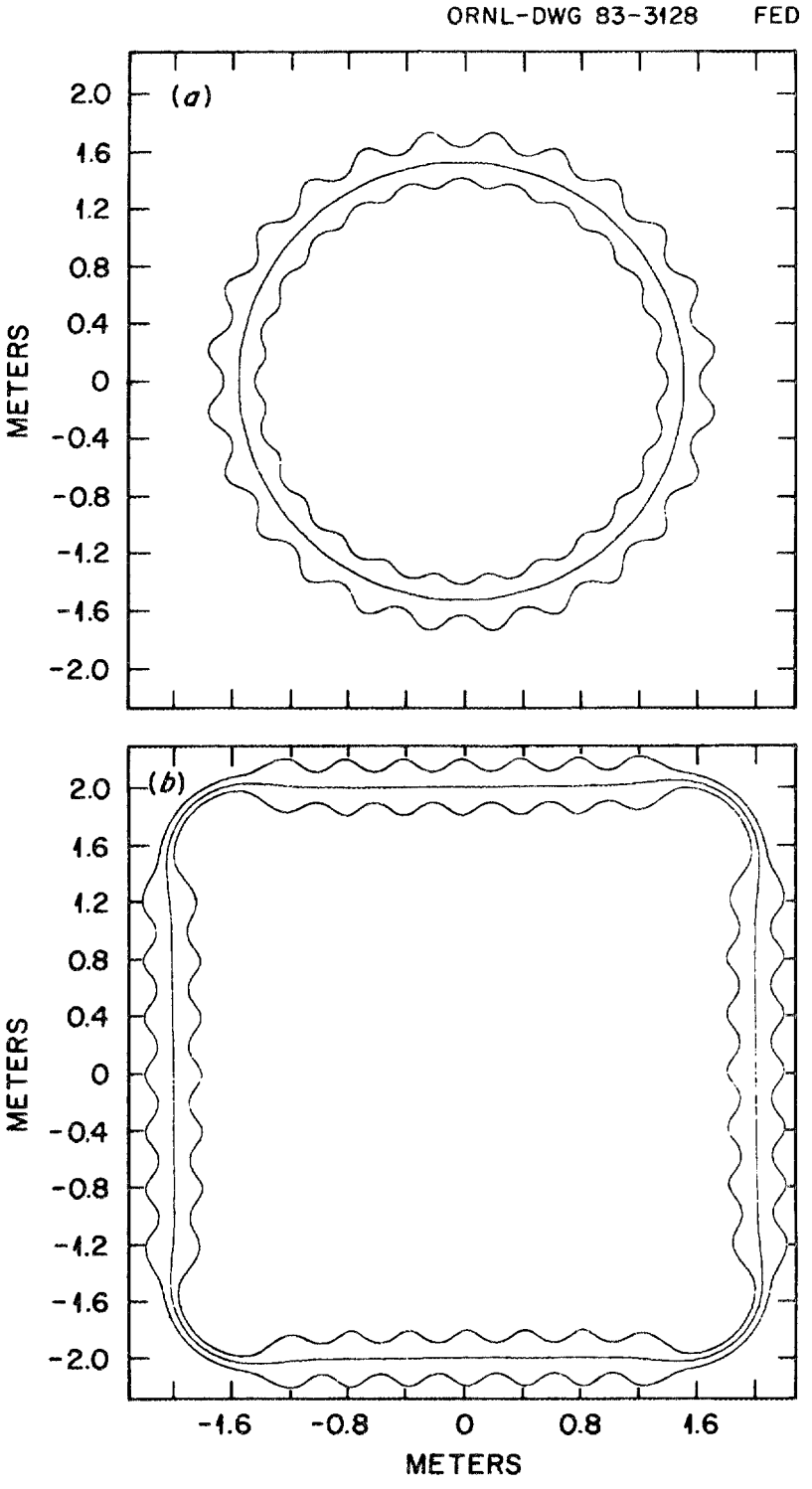

Fig. 4.1. Circular (EBT-I/S) and square (EBS) configurations of EBT.

be shifted circles (shifted toward the "major axis"). The pressure is, of course, constant along field lines, so that the entire pressure surface is shifted inward from the axis of the coil configuration.

The inward shift for the square configuration is qualitatively similar to that obtained for the circular EBT configuration. For both configurations the shift decreases with increasing local mirror ratio (or bumpiness) and number of mirror cells. The square configuration exhibits an additional inverse dependence on the global mirror ratio (ratio of the maximum B on-axis in the corners to the minimum B on-axis in the sides). This dependence of the square configuration on global mirror ratio is what is exploited in reducing the inward shift of the pressure surfaces (and the inward shift of passing and transitional particle orbits).

Having discussed the shift of the pressure surfaces in the absence of rings, we qualitatively discuss how $\oint d\ell/B$ (and hence the core pressure) is changed when the hot electron rings produce a substantial change in $\oint d\ell/B$.

Preparatory to considering single-particle orbits, we first make an estimate of the ratio of the parallel electric field to the perpendicular electric field. To do this we first use equilibrium considerations to determine the parallel current. Using Spitzer conductivity, we obtain an estimate of the parallel electric field. We find that $E_{\parallel}/E_{\perp}$ is proportional to ν_e/ω_{ce} and is inversely proportional to $e\Delta\Phi_{\perp}/T$. Since ν_e/ω_{ce} is so small (e.g., 10^{-6} to 10^{-5}), we conclude that the parallel electric field is negligible and that to a high level of approximation the potential is constant along field lines.

The connection between the MHD fluid equations and single-particle orbits is provided by the kinetic equation. In Sect. 4.4 the MHD relation between pressure and $\oint d\ell/B$ is redeveloped using the drift kinetic equation. The average over velocity space and a flux tube are shown to lead to $\hat{b} \times \nabla \oint d\ell/B$. Then $\oint d\ell/B$ is interpreted as a kind of average drift surface. This kinetic approach also permits a treatment of certain nonideal effects, which can usually be omitted for magnetic equilibria (but not for transport) because of quasi neutrality.

The treatment of orbits is divided into two major portions: (1) analytic and qualitative discussions and (2) discussion of numerical results. In the qualitative section we discuss the motion of low- and high-energy particles. The high-energy particles are further subdivided into trapped, passing, and transitional particles. For the

extreme limits of pitch angle ($v_{\parallel} = 0$ and $v_{\parallel} = v$), simple expressions are given for determining the drift orbits for all energies.

The trapped particles that exist in the nearly axisymmetric sides have drift orbits which are circular, with virtually no shift relative to the coil axis. Passing particle orbits are also circular in cross section but are shifted inward. The trick of introducing "reverse toroidal curvature" in the transition between the sides and the corners to further reduce this shift is discussed in a qualitative way. The qualitative behavior of high-energy transitional particles (the worst contained particles) is discussed. The analytic argument for neglecting a class of particles that have been found to be small numerically (for two decades) is discussed. (Their number is exponentially small.)

In Sect. 4.6 numerical results of orbit calculations are presented for both the square and circular EBT configurations. The nearly circular character of the orbits suggests an approximation that is equivalent to the standard aspect ratio expansion for a circular EBT. Using this approximation, numerical estimates of the step-size for diffusion as a function of energy and cosine of the pitch angle are given for both the square and circular configurations. Numerical estimates of the neoclassical lifetimes for both the square and circular configurations are given. The square lifetime is typically an order of magnitude larger than that of the circular configuration.

4.2 MHD EQUILIBRIUM CONSIDERATIONS

Fundamental to the analysis of any plasma is that charge be conserved:

$$\frac{\partial \rho}{\partial t} + \nabla \cdot \mathbf{j} = 0 \ . \tag{4.1}$$

As shown in Appendix 4A, this concept, together with the fluid pressure (or momentum) balance equation

$$\mathbf{j} \times \mathbf{B} = \nabla p \tag{4.2}$$

and $\nabla \cdot \mathbf{B} = 0$, leads in steady state to the requirement that the pressure p is a function of $\oint d\ell/B$. This means that the surfaces of constant pressure can be determined by determining the surfaces of constant $\oint d\ell/B$.

Since both the pressure and $\oint d\ell/B$ are constant along field lines [e.g., $\mathbf{B} \cdot \nabla p = 0$, which follows by dotting Eq.(4.2) with $\mathbf{B}$], it suffices to determine contours of constant $\oint d\ell/B$ in some surface which cuts all the field lines. For concreteness we will choose this surface to be a midplane of one of the approximately identical mirror cells that make up a side of the square configuration.

To calculate $\oint d\ell/B$ analytically we make use of approximations to the magnetic field of the square configuration of EBT. We assume that there are N mirror cells per side and that all these cells are identical except for those adjoining the corners. In the identical mirror cells the magnetic field on-axis is taken to be B_0 in the midplanes. Under the coils where the identical cells join, the magnetic field is given by $M_L B_0$, where M_L is the local mirror ratio.

For the mirror cells adjoining the corners, the magnetic field on-axis is again taken to be B_0 in the midplane. Where a side joins a corner, the magnetic field is taken to be $M_G B_0$, where M_G is the global mirror ratio. Within the corners we approximate the magnetic field by that of a toroidal solenoid (that is, constant along circular field lines and having a 1/R dependence across field lines).

As shown in Appendix 4B the contribution to $\oint d\ell/B$ from a single half-cell is

$$U_M \simeq \frac{(1-\delta)L}{B_0}\left\{1 + \frac{1}{2}\delta^2\left[1 + \left(\frac{\pi r_s}{L}\right)^2\right]\right\}, \tag{4.3}$$

where L is the distance between a midplane and an adjacent coil plane for a mirror cell and

$$\delta = \text{bumpiness parameter} = \frac{M-1}{M+1}$$

with

$$M = \text{mirror ratio}\ .$$

The radius in the midplane is denoted by r_s.

The contribution of all four sides to $\oint d\ell/B$ is given by

$$U_{side} = 4\left\{ \frac{2(N-1)(1-\delta_L)L}{B_0}\left[1 + \frac{1}{2}\delta_L^2\left(1 + \frac{\pi^2 r_s^2}{L^2}\right)\right] \right.$$

$$\left. + \frac{2(1-\delta_G)}{B_0} L\left[1 + \frac{1}{2}\delta_L^2\left(1 + \frac{\pi^2 r_s^2}{L^2}\right)\right]\right\} . \qquad (4.4)$$

The first term in Eq. (4.4) comes from the $2(N-1)$ identical half-cells per side, whereas the last term comes from the two half-cells per side that are adjacent to corners.

The contribution to $\oint d\ell/B$ from a single corner is given by

$$U_c = \int_0^{\pi/2} \frac{R\, d\ell}{B} = \frac{\pi}{2}\frac{R}{B} . \qquad (4.5)$$

In the corners,

$$B = M_G B_0\left(\frac{R_0}{R}\right) = M_G B_0\left(\frac{R_0}{R_0 + X_c}\right) \qquad (4.6)$$

so that for $X_c/R_0 \ll 1$,

$$U_c \simeq \frac{\pi}{2}\frac{R_0}{M_G B_0}\left(1 + 2\frac{X_c}{R_0}\right) . \qquad (4.7)$$

To relate X_c in a corner to r_0 in a side we make use of conservation of magnetic flux. The flux within a circle of radius r_s in the side is given approximately by $\pi r_s^2 B_0$. As this flux tube passes into the corner, its radius is reduced because of the stronger magnetic field. In the corner the flux is given approximately by $\pi r_c^2 M_G B_0$. Equating these expressions for the flux we find that $r_c = r_s/M_G^{1/2}$. In the equatorial plane, $r_c = X_c$ and $r_s = X_s$ such that

$$X_c = X_s/M_G^{1/2} \ , \tag{4.8}$$

where

$$r_s^2 = X_s^2 + y_s^2 \ . \tag{4.9}$$

Combining Eqs. (4.7) and (4.8), we find that the contribution to $\oint d\ell/B$ from all four sides is

$$4U_c \simeq \frac{2\pi R_0}{M_G B_0}\left(1 + \frac{2X_s}{M_G^{1/2} R_0}\right) . \tag{4.10}$$

From Eqs. (4.4) and (4.10) we find that

$$\oint \frac{d\ell}{B} = 4\left\{\frac{2(N-1)(1-\delta_L)L}{B_0}\left[1 + \frac{1}{2}\delta_L^2\left(1 + \frac{\pi^2 r_s^2}{L^2}\right)\right]\right.$$

$$\left. + \frac{2(1-\delta_G)L}{B_0}\left[1 + \frac{1}{2}\delta^2{}_G\left(1 + \frac{\pi^2 r_s^2}{L^2}\right)\right]\right\}$$

$$+ \frac{2\pi R_0}{M_G B_0}\left(1 + \frac{2X_s}{M_G^{1/2} R_0}\right) . \tag{4.11}$$

The contours of constant $\oint d\ell/B$ are readily obtained from Eq. (4.11) if we rewrite it in a form to emphasize $r_s^2 = X_s^2 + y_s^2$ and X_s. Thus,

$$X_s^2 + y_s^2 + 2\xi X_s = C_1 = \text{constant} \ , \tag{4.12}$$

or

$$(X_s + \xi)^2 + y_s^2 = C_1 + \xi^2 \ , \tag{4.13}$$

where

$$\xi \equiv \frac{L}{2\pi\delta_L^2(1-\delta_L)M_G^{3/2}NF}, \tag{4.14}$$

$$F \equiv 1 + \frac{1}{N}\left[\frac{\delta_G^2(1-\delta_G)}{\delta_L^2(1-\delta_L)} - 1\right]. \tag{4.15}$$

Equation (4.13) is the equation of a circle shifted inward (toward the major axis) by ξ (Fig. 4.2).

The inward shift of the pressure surfaces for the square configuration is qualitatively quite similar to that which occurs for the circular configuration of EBT. For example, the shift is reduced by having a larger number of mirror cells (aspect ratio in the circular configuration). The major difference is the appearance of the global mirror ratio M_G.

The additional dependence on global mirror ratio permits considerably better centering of the plasma. For example, if $M_L = 2$ so that $\delta_L = 1/3$, $N = 6$, and $M_G = 4$, then

$$\frac{\xi}{L} \simeq 0.05 . \tag{4.16}$$

For $M_L = 2$, L is approximately equal to the coil radius, which in turn is comparable to the plasma radius. Thus, ξ/L is approximately (by a factor of 2) the ratio of the shift to the radius.

To this point we have omitted the effect of the hot electron rings on $\oint d\ell/B$. We next consider the qualitative effects of a substantial hot electron ring on the pressure surfaces for the core plasma. As shown in Appendix 4A, the core pressure surfaces correspond (approximately) to the surfaces of constant $\oint d\ell/B$.

Because the magnetic field of a hot electron ring falls off rapidly with distance, the primary effect is on the field in the sides of the square configuration. The effect of the hot electron rings on $\int d\ell/B$ for a single mirror cell is illustrated in Fig. 4.3. For the substantial ring shown it will be noted that the slope of $\int d\ell/B$ is steepened for the inside half of the ring and reversed on the outer

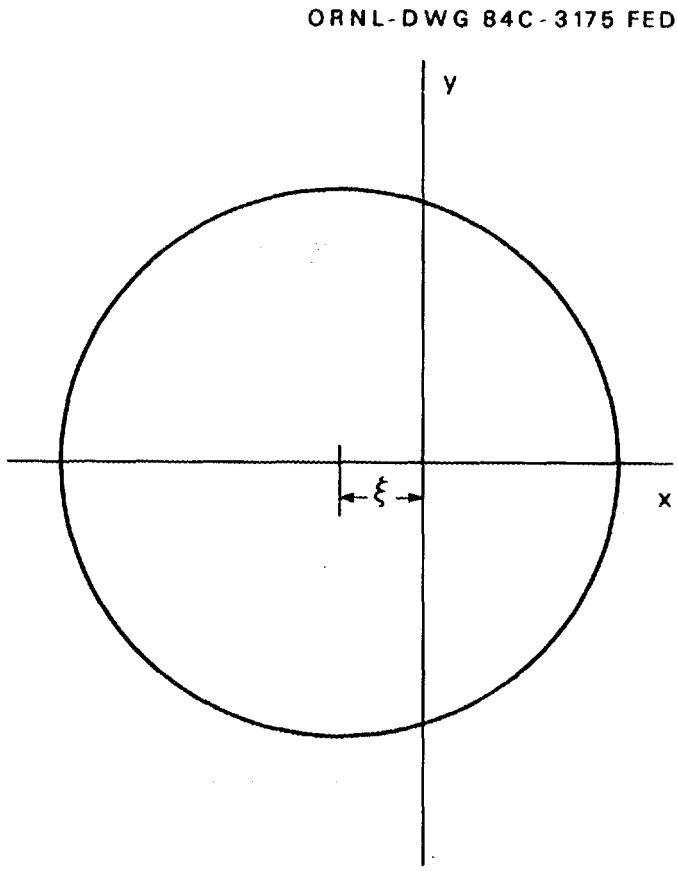

Fig. 4.2. Pressure surface in the midplane of one of the mirror cells composing the sides of the square configuration. Since pressure is constant along field lines, the pressure surface follows field lines, contracting in cross-sectional area in regions of higher magnetic field. For both circular and square configurations ξ is reduced with increasing local mirror ratio (bumpiness) and number of mirror cell. The additional dependence of ξ on global mirror ratio for the square configuration is exploited to reduce the inward shift of the pressure surface.

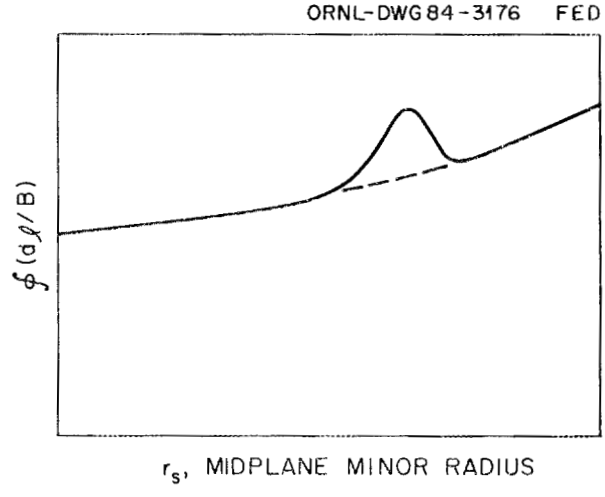

Fig. 4.3. $\oint d\ell/B$ vs minor radius in the midplane when substantial ring beta occurs. The departure from the vacuum curve (dashed) occurs at radii where ring pressure exists.

half of the ring. We can express this formally by expanding the contribution to $\oint d\ell/B$ from a single half mirror cell about some midplane radius r_0,

$$U_M \simeq U_M(r_0^2) + U_M'(r_0^2)(r_s^2 - r_0^2) , \tag{4.17}$$

and noting that $U_M'(r_0^2)$ is simply related to the slope (especially at the relatively large radii occupied by the ring).

To determine the contours of $\oint d\ell/B$ we could now proceed to repeat the type of analysis that led from Eq. (4.3) to Eq. (4.14). To gain a qualitative understanding we need only note that we would again obtain an expression for $\oint d\ell/B$ similar to Eq. (4.11) except that the coefficient of r_s^2 would involve $U_M'(r_0^2)$ instead of the factor arising from Eq. (4.3): $\left[\frac{\pi^2}{2}\frac{1}{B_0}\frac{\delta^2(1-\delta)}{L}\right]$. The equation for the pressure contour would again be that of a circle shifted by ξ. In place of Eq. (4.14) we would obtain

$$\xi \propto 1/U_M'(r_0^2) . \tag{4.18}$$

By referring to Fig. 4.3 we see that Eq. (4.18) indicates that the contours of pressure, while approximately circular, would not be concentric. Proceeding from small radius to large, the inward shift of the contours would be reduced as one encountered the steeper gradients in U_M associated with the inner half of the rings. On the outer half of the rings, where U_M' has the opposite sign from the vacuum value, the shift would be outward instead of inward.

Near the peak in the ring pressure, where $U_M'(r_0) \simeq 0$, the analysis leading to Eq. (4.18) fails since it is necessary to retain $U_M''(r_0^2)$ omitted in Eq. (4.17). However, the situation is a familiar one which produces banana- or crescent-shaped contours in $\oint d\ell/B$ (for an analysis of a similar topology see Appendix 4F). The simplest expectation for the core pressure across the separatrix (largest banana) is that it be constant. Thus, we expect that the core pressure will show a flat spot near the peak of a well-developed ring pressure.

4.3 PARALLEL CURRENT AND ELECTRIC FIELD

As indicated in Appendix 4A, the Lortz and modified Grad-Lortz algorithms for computing core scalar pressure equilibria (in the presence of anisotropic rings) use the relation

$$\mathbf{j} = \nabla\varsigma \times \nabla p \ , \tag{4.19}$$

where $\mathbf{j}$ and p are core plasma quantities and ς is defined as

$$\varsigma \equiv \int_0^{\ell} \frac{d\ell}{B} \ . \tag{4.20}$$

The zero in ℓ is conveniently taken to be one of the symmetry planes which passes through the center of a side or which passes through the center of a corner. The magnetic field is normal to these planes, and in these planes any parallel component of current vanishes.

It is convenient to first focus on a corner. We will take ς to be zero in the center of a corner. We will also take this as the zero in toroidal angle ϕ. Using the same approximations for the magnetic field used earlier (circular field lines, etc.), we find that

$$\varsigma = \int_0^{\phi} R \, d\phi'/B = \frac{R\phi}{B} \qquad -\frac{\pi}{4} \le \phi \le \frac{\pi}{4} \ . \tag{4.21}$$

Recalling that $B \propto 1/R$ we find that

$$\nabla\varsigma = \frac{1}{B}\left(2\phi\hat{e}_R + \hat{e}_\phi\right) \ . \tag{4.22}$$

Within a corner the pressure is a function of minor radius so that

$$\nabla p = \frac{\partial p}{\partial r}\,\hat{e}_r \ . \tag{4.23}$$

Inserting Eqs. (4.22) and (4.23) into (4.19) and making use of

$$\hat{e}_R \times \hat{e}_r = -\hat{e}_\phi \sin\theta = -\hat{b}\sin\theta \ , \qquad \hat{e}_\phi \times \hat{e}_r = -\hat{e}_\theta \ , \tag{4.24}$$

where θ is poloidal angle, we find that in a corner

$$\mathbf{j} = -\frac{1}{B}\frac{dp}{dr}\left(2\phi \sin\theta\, \hat{b} + \hat{e}_\theta\right) \ . \tag{4.25}$$

The parallel current appearing in Eq. (4.25) has a simple interpretation. In the center of a corner ($\phi = 0$), the current is purely poloidal and the lines of $\mathbf{j}$ are circles. As we move away from the central symmetry plane, the current is still a collection of approximately circular filaments, but the circles are no longer perpendicular to $\mathbf{B}$. These cocked circular filaments of current have components parallel to $\mathbf{B}$ which are largest in magnitude at the top and bottom ($\theta = \pm\pi/2$) and zero in the equatorial plane ($\theta = 0,\pi$). As ϕ is changed from zero to $\pm\pi/4$ (where the corners join the sides), this cocking of the current relative to the magnetic field increases. The maximum ratio of the magnitude of the parallel to perpendicular currents occurs at $\phi = \pm\pi/4$ and is

$$\text{MAX}\left(\frac{|j_\parallel|}{|j_\perp|}\right) = \frac{\pi}{2}|\sin\theta| \ .$$

Since the central plane of a side has $j_\parallel = 0$, it follows from continuity that the sides must undo the cocking that occurs in the ends. In other words, the increase in the magnitude of $j_\parallel$ that occurs in the corners as one moves away from the center of a side must be reversed somewhere in the sides.

It follows from Eq. (4.19) that the parallel current in the sides occurs because $\nabla\varsigma$ and ∇p are not coparallel (except at the central plane where $\varsigma = \frac{1}{8}\oint d\ell/B$). The reason they are not coparallel is that whereas ς is very nearly symmetric about the axis of the bumpy cylinder

the pressure surfaces are shifted away from the axis (e.g., inward toward the major axis). As indicated in Appendix 4C, this leads to two types of axial variation of the parallel current. One type of variation is sinusoidal and occurs in the circular EBT configuration. The second type of axial variation is approximately linear in arc length. This second type of variation is cancelled by distributed toroidal effects in the circular configuration. In the square configuration, the second type of axial variation continues to build up until the side joins the end. The two types of axial variation along the side, as well as the behavior in a corner, are illustrated in Fig. 4.4.

Because of finite resistivity there will be a parallel component of electric field associated with the parallel current. That is, the ambipolar potential will vary along the field lines. It is thus of some interest to estimate $E_{\parallel}/E_{\perp}$.

To estimate $E_{\parallel}$ we use the relation

$$j_{\parallel} = \sigma E_{\parallel} , \tag{4.26}$$

where the Spitzer conductivity is given by

$$\sigma = \frac{2}{\nu_e} \frac{n_e^2}{m_e} \tag{4.27}$$

and ν_e is the electron Coulomb collision frequency. To estimate $E_{\perp}$ we note that the radial variation in the potential in EBT-I/S (and many other toroidal devices) is comparable to T. That is,

$$E_{\perp} = h \frac{T_e}{ea} , \tag{4.28}$$

where a is the plasma radius and h is comparable to unity (e.g., within a few factors of 2).

From $\mathbf{j} \times \mathbf{B} = \nabla p$ we estimate that

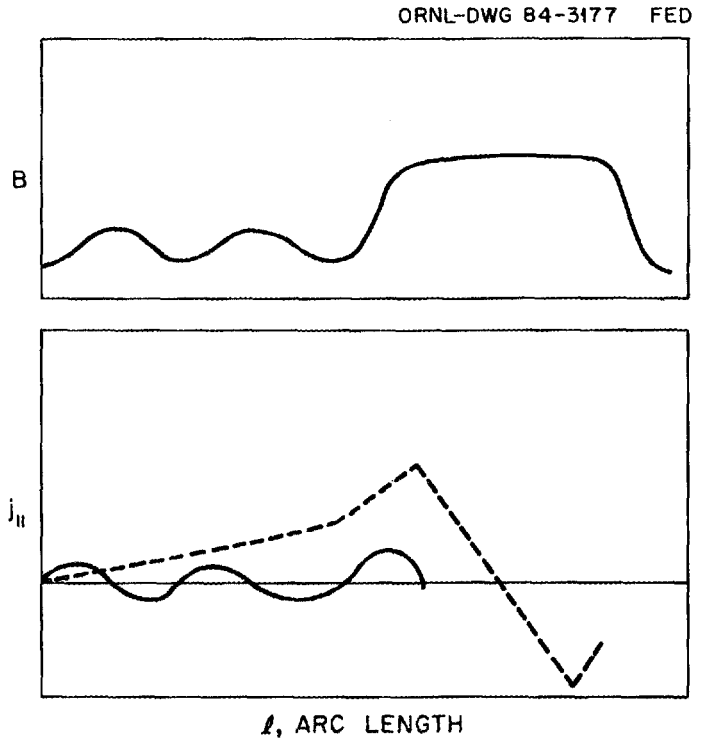

Fig. 4.4. Variation of B and $j_{\parallel}$ vs arc length ℓ. The oscillatory part of $j_{\parallel}$ (solid curve) also occurs for the circular configuration. The other part of $j_{\parallel}$ occurs in polygonal configurations such as the square. The zeros in $j_{\parallel}$ occur at symmetry planes.

$$j_\perp \simeq \frac{nT_e}{2aB} , \tag{4.29}$$

so that

$$j_\parallel = kk_\perp \simeq k \frac{nT_e}{2aB} , \tag{4.30}$$

where k is the ratio of $j_\parallel$ to $j_\perp$ (e.g., $|k| < \pi/2$). Combining Eq. (4.30) with Eqs. (4.28) and (4.29), we obtain

$$E_\parallel \simeq \frac{1}{4} k \frac{\nu_e}{\omega_{ce}} \frac{T_e}{ea} , \tag{4.31}$$

so that

$$\frac{E_\parallel}{E_\perp} \simeq \frac{1}{4} kh \frac{\nu_e}{\omega_{ce}}$$

or

$$\frac{E_\parallel}{E_\perp} \simeq \frac{1}{8\pi} (kh) \frac{\nu_e}{f_{ce}} . \tag{4.32}$$

Now ν_e/f_{ce} is a very small number. For example, using EBT-S-like parameters of $n = 10^{12}$ cm^{-3} and $T_e = 100$ eV, ν_e is tens to hundreds of kilohertz, whereas the electron cyclotron frequency is tens of gigahertz. Thus,

$$\frac{\nu_e}{f_{ce}} = O(10^{-5}) . \tag{4.33}$$

Since $\nu_e \propto n/T_e^{3/2}$, even for reactor conditions ν_e/f_{ce} is $O(10^{-5} - 10^{-6})$.

From the above we conclude (1) that the electron conductivity along field lines does not permit substantial variation of the potential along field lines and (2) that assuming the potential is constant along field lines is an excellent approximation.

As an aside we note that these parallel electric fields can lead to azimuthal components of the electric field. For the bumpy torus configuration this can lead to convection — called Pfirsch-Schlüter diffusion in tokamaks and stellarators. However, this particular form of transport applies primarily to very cold end-collisional plasma configurations in which the mean free path is small. For a density and temperature comparable to that found in EBT-I/S, the transit frequencies are such that $\nu_e \tau_b \gtrsim 2 \times 10^{-2}$. Thus, particles experience very few collisions per transit of a one-half field period. The tertiary $\mathbf{E}_\theta \times \mathbf{B}$ drifts from toroidicity are oppositely directed across symmetry planes and, hence, cancel over a full field period (e.g., two halves of a side or the two halves adjacent to a corner). Estimates of the displacement per transit of a half period are very small and considerably smaller when the cancellation over a full period is taken into account.

4.4 KINETIC TREATMENT

We now connect the foregoing fluid treatment with particle drift motion via the kinetic equation. Our starting point is the drift kinetic equation[7] for species j:

$$\frac{\partial f_j}{\partial t} + \mathbf{v}_\parallel \cdot \nabla f_j + \mathbf{v}_D \cdot \nabla f_j = C_j \ , \tag{4.34}$$

where C_j represents scattering by Coulomb collisions, microwave fields, etc., as well as the particle source (e.g., ionization of neutrals). The drift velocity is given by

$$\mathbf{v}_D = \frac{mv^2}{2e_j B} \hat{b} \times \left(\frac{v_\perp^2}{v^2} \nabla \ell n \, B + 2 \frac{v_\parallel^2}{v^2} \kappa \right) + \frac{\mathbf{E} \times \mathbf{B}}{B^2} \ . \tag{4.35}$$

Multiplying Eq. (4.34) by d^3v and integrating (see Appendix 4D) yields

$$\frac{\partial n_j}{\partial t} + \nabla \cdot (n_j \langle v_\parallel \rangle_j \hat{b})$$

$$+ \nabla p_j \cdot \left[\frac{\hat{b}}{e_j B} \times (\nabla \ell n\, B + \kappa) \right]$$

$$+ \frac{E \times B}{B^2} \cdot \left[\nabla n_j - n_j (\nabla \ell n\, B + \kappa) \right] = \int d^3v\, C_j \,, \qquad (4.36)$$

where we have assumed that f_j is isotropic to lowest order. The density, pressure, and velocity space average of $v_\parallel$ are denoted by n_j, p_j, and $\langle v_\parallel \rangle_j$. We note for future reference that the factor multiplying ∇p_j in Eq. (4.36) arises from the velocity space average of the ∇B and curvature drifts.

We notice that if we multiply Eq. (4.36) by e_j and sum over species, we obtain the charge-conservation equation [Eq. (4.1)]. The first term in Eq. (4.36) leads to the time derivative of the charge density, whereas the second term leads to the divergence of the parallel current. The remaining terms, which arise from $v_D \cdot \nabla f$, lead to the divergence of the perpendicular current.

Now the term involving $\langle v_\parallel \rangle$ in Eq. (4.36) can be written:

$$\nabla \cdot (n_j \langle v_\parallel \rangle_j \hat{b}) = B \frac{\partial}{\partial \ell} \left(\frac{n_j \langle v_\parallel \rangle_j}{B} \right) , \qquad (4.37)$$

where we have used $\hat{b} = B/B$ and $\nabla \cdot B = 0$. Since n_j, $\langle v_\parallel \rangle_j$, and B are single valued, this suggests that we divide Eq. (4.36) by B and integrate over ℓ. This yields

$$U \frac{\partial n_j}{\partial t} + \oint \frac{d\ell}{B} \left\{ \nabla p_j \cdot \left[\frac{\hat{b}}{e_j B} \times (\nabla \ell n\, B + \kappa) \right] \right.$$

$$\left. + \frac{E \times B}{B^2} \cdot \left[\nabla n_j - n_j (\nabla \ell n\, B + \kappa) \right] \right\} = \oint \frac{d\ell}{B} \int d^3v\, C_j \,, \qquad (4.38)$$

where

$$U \equiv \oint \frac{d\ell}{B} . \tag{4.39}$$

As shown in Appendix 4E, Eq. (4.38) can be written in the form

$$U \frac{\partial n_j}{\partial t} + \nabla p_j \cdot \left(\frac{\nabla U \times \hat{b}}{e_j B} \right)$$

$$+ \frac{\mathbf{E} \times \mathbf{B}}{B^2} \cdot \left(U \nabla n_j + n_j \nabla U \right) = \oint \frac{d\ell}{B} \int d^3v \, C_j . \tag{4.40}$$

We now multiply Eq. (4.40) by e_j and sum over species. Assuming steady state we obtain

$$\nabla p \cdot \left(\frac{\nabla U \times \hat{b}}{B} \right) = 0 , \tag{4.41}$$

where

$$p = \sum_j p_j , \tag{4.42}$$

and we have assumed quasi neutrality so that

$$\rho = \sum_j e_j n_j \simeq 0 \tag{4.43}$$

and the terms involving $\mathbf{E} \times \mathbf{B}$ vanish.

Equation (4.41) can be rewritten as

$$(\nabla p \times \nabla U) \cdot \hat{b} = 0 . \tag{4.44}$$

Since neither ∇p nor ∇U have components in the direction of $\hat{b}$, we can equally well write Eq. (4.44) as

$$\nabla p \times \nabla U = 0 \ , \tag{4.45}$$

which means that the gradient of p is in the direction of the gradient of U. That is, the pressure can be written as a function of $U \equiv \oint d\ell/B$. (As an aside we note that it is possible to estimate the size of the terms involving the charge density. For $e\Phi/T$ of order unity and aspect ratio of order 10, these terms are on the order 1% — if one includes bumpiness.)

Tracing the origin of Eq. (4.45) we see that the factor multiplying ∇p in Eq. (4.41) came from the flux tube average of the velocity space average of the curvature and ∇B drifts (but not the $E \times B$ drift). We are thus led to write Eq. (4.41) in the form

$$\mathbf{v}_D \cdot \nabla p = 0 \ , \tag{4.46}$$

where $\mathbf{v}_D$ is the average of the magnetic drifts. This formulation, that the pressure is constant on an average drift surface, is potentially useful for dealing with deviations from the assumptions made herein (e.g., an anisotropic pressure tensor).

Equation (4.46) also allows us to draw an analogy to toroidal systems with rotational transforms. For systems with a large fraction of passing particles and rotational transfer, the dominant motion perpendicular to the minor axis of the torus is provided by $\mathbf{v}_{\parallel} \cdot \nabla f$. The "average particle" then is, to lowest order, confined to a flux surface. For the closed line systems with no rotational transfer discussed here, the average drift surface plays the same role as the flux surface — both are the surfaces followed by an average particle.

Thus, in both cases, it is natural to assume that all macroscopic equilibrium quantities are, to lowest order, constant on the surfaces followed by the average particle. Determining the next-order effects (e.g., through transport calculations) demands that one consider the deviations from the average. That is, one must know the details of single-particle motion (discussed qualitatively in the next section).

4.5 SINGLE-PARTICLE ORBITS — BASIC ANALYIS AND IDEAS

In this section we discuss the qualitative behavior of certain limiting cases and give, where possible, simple formulas for calculating drift motion.

We begin with relatively cool particles. From the expression for the drift velocity given in Eq. (4.35), we see that if $mv^2/2$ is sufficiently small (e.g., $mv^2/2 \ll |e\Phi|$) then the dominant drift motion is provided by the $\mathbf{E} \times \mathbf{B}$ drift. These relatively cool particles drift on potential surfaces. This follows from

$$\nabla\Phi \cdot \mathbf{v}_D \simeq \nabla\Phi \cdot \frac{(\mathbf{E} \times \mathbf{B})}{B^2} = -\mathbf{E} \cdot \frac{(\mathbf{E} \times \mathbf{B})}{B^2} = 0 \ , \tag{4.47}$$

which states that $\mathbf{v}_D$ has no component perpendicular to the potential surface.

We next consider relatively hot trapped particles. We begin with deeply trapped particles — particles with $v_{\parallel} = 0$ in a midplane of one of the mirror cells making up the sides of the square configuration. For these deeply trapped hot particles, Eq. (4.35) reduces to

$$\mathbf{v}_D \simeq \frac{mv_{\perp}^2}{2e_j B} \hat{b} \times \nabla \ell n \ B \ . \tag{4.48}$$

To a high level of accuracy $\hat{b}$ is normal to the midplane and $\nabla \ell n \ B$ lies in the midplane. Thus, Eq. (4.48) states that $\mathbf{v}_D$ lies in the midplane, and by dotting Eq. (4.48) with ∇B we see that this type of particle follows a contour of constant B. Since the magnetic field is nearly axisymmetric in the sides, the contours of constant-B are nearly concentric circles and, hence, so are the orbits.

Hot particles which are not quite so deeply trapped are no longer confined to the midplane but bounce back and forth between turning points where $\epsilon/\mu = B$ (i.e., $v_{\parallel} = 0$). These particles again drift on surfaces which are nearly circular in cross section since the magnetic field is nearly axisymmetric. However, the net drift per bounce tends to be lower for less deeply trapped particles. This is most easily seen for low beta, where $\nabla_{\perp} \ell n \ B \simeq \kappa$. From Fig. 4.1 it is obvious that the curvature becomes less in magnitude as one moves away from the

midplane (it is of opposite sign under a coil in the sides). Consequently, the less deeply trapped particles must average the smaller values of local ∇B drifts (or even ones of opposite direction) along with those they encounter passing through the midplane.

Numerically the drift surfaces for any EBT configuration are readily determined from the longitudinal adiabatic invariant

$$J = \oint m v_{\parallel} d\ell \ , \tag{4.49}$$

where the limits of integration are between turning points ($v_{\parallel} = 0$) and $v_{\parallel}$ is given by

$$v_{\parallel} = (2/m)^{1/2} \ (\epsilon - e\Phi - \mu B)^{1/2} \tag{4.50}$$

with Φ the ambipolar potential, μ the magnetic moment, and ϵ the total energy (kinetic plus potential).

For deeply trapped particles in the circular or square configuration, one can take the limiting form of Eq. (4.49) to obtain a simple result which does not involve integration. This result is more simply obtained by setting $v_{\parallel} = 0$ in Eq. (4.50). Since the total energy ϵ is constant, we obtain

$$e\Phi + \mu B = \text{constant} \ . \tag{4.51}$$

Notice that for low kinetic energy (small μ) the drift contours are those of constant potential, whereas for large kinetic energy the drift contours are mod-B contours. For any known (or postulated) Φ one can use Eq. (4.51) to determine the drift contours for deeply trapped particles of any kinetic energy.

We next consider passing particles and begin with relatively hot particles with $\mu = 0$ (so $v = v_{\parallel}$). For these hot, passing particles, Eq. (4.35) reduces to

$$\mathbf{v}_D \simeq \frac{mv_{\parallel}^2}{e_j B}\,\hat{b} \times \boldsymbol{\kappa} \ . \tag{4.52}$$

As a passing particle traverses the mirror cells composing the sides of the square configuration, it sees the alternating curvature of the field lines. Thus, a particle that starts in a midplane first rotates about the axis of the side in one direction and then as it approaches the coil region rotates in the opposite direction. This rotation in the opposite direction continues until the particle begins to approach the next midplane region where the direction of rotation is again reversed.

The result, after traversing a field line between two adjacent midplanes (or two adjunct coil planes), is that the particle has rotated about the axis with the sign of rotation associated with the midplane. The reason that the midplane rotary drift dominates can be seen from Eq. (4.52). The velocity is proportional to B^{-1} so the angular speed is proportional to $(rB)^{-1}$. The magnetic flux is constant along a field line and in the axisymmetric sides is approximately proportional to r^2B. Thus, (rB) is proportional to $B^{1/2}$ and the angular speed is proportional to $B^{-1/2}$. Since B is smaller near the midplane than near the coil plane and the angular speed is proportional to $B^{-1/2}$, the midplane motion dominates.

As a hot passing particle traverses more mirror cells, this motion is repeated. After traversing N cells it has rotated through N times the angle it rotated through in one mirror cell. Eventually the particle reaches the side where its local drift is vertical. After the particle passes through the corner, it enters a second side and begins the rotary motion about the axis of the side and then enters a corner and drifts vertically.

If all this drift motion across field lines is projected into a single plane (via field lines), one obtains a picture something like that shown in Fig. 4.5 for an extremely large gyroradius particle. For a particle with a more typical gyroradius the length of the vertical and circular segments of drift are so short that the eye cannot distinguish the segments. This limiting case of a continuum is ideally handled through the use of longitudinal adiabatic invariant J.

For passing particles J can again be defined by Eqs. (4.49) and (4.50). The only difference is that integration follows a closed field line through one circuit (i.e., once around the "square torus"). Again, as in the case of trapped particles, the integrals are quite

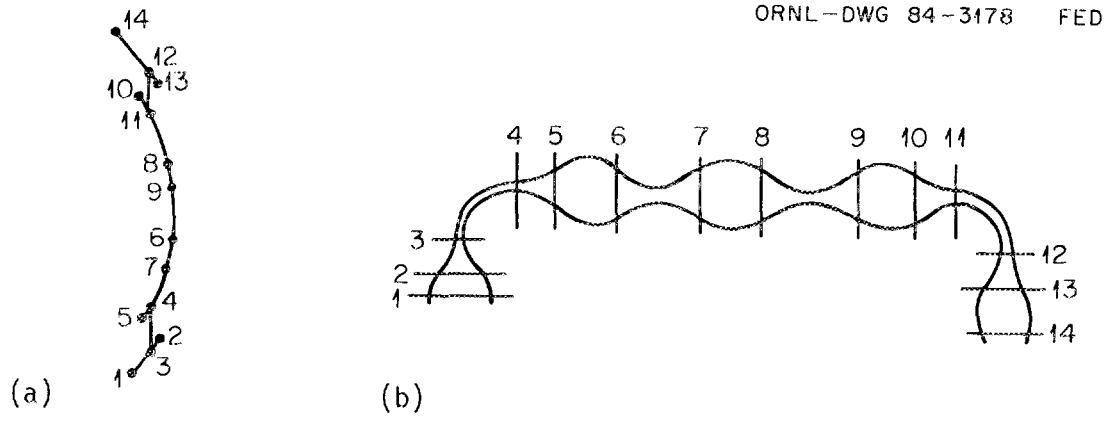

Fig. 4.5. (a) To depict the drift motion of a high energy passing particle, it is convenient to project the orbit into a single plane via field lines. (b) It is also helpful to simultaneously follow the motion parallel to the field lines. The numbers in (a) and (b) refer to times ($t_1 < t_2 <\cdots< t_{14}$). At the spatial points corresponding to these times the character of the curvature (b) and curvature drift changes. Between 3 and 4 the particle drifts vertically in a corner (and again between 11 and 12). Along the sides a passing particle rotates in opposite directions as it experiences different signs of curvature - indicated on the circular arcs in (a).

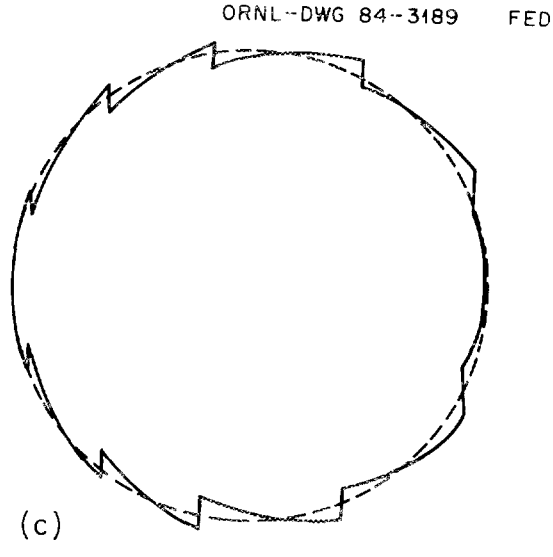

Fig. 4.5(c). The solid curve represents a more complete view of the orbit shown in 4.5(a). In order to make the detailed interaction of sides and corners visible, an exceedingly large gyro radius has been used in 4.5(a), (b), and (c). More typically, one complete toroidal circuit consists of thousands of line segments and circular arcs and is indistinguishable to the eye from the continuum limit described by the longitudinal adiabatic invariant J (dashed).

suitable for numerical integration. There is also a relatively simple limiting case from which the interplay of $\mathbf{E} \times \mathbf{B}$ and curvature drift can be studied.

For passing particles with $\mu = 0$ (i.e., the extreme limit), $v_{\parallel}$ is constant and, hence, Eqs. (4.49) and (4.50) reduce to

$$J = (2m)^{1/2}(\epsilon - e\Phi)^{1/2} \oint d\ell \ . \tag{4.53}$$

For high-energy particles ($\epsilon >> |e\Phi|$), the shape of the drift surfaces is dominated by $\oint d\ell$, which is associated with the transit average of curvature drift. For low kinetic energy, $\epsilon - e\Phi \simeq 0$ and the shape of the drift surfaces is dominated by the potential.

Using the same approximations used to evaluate $\oint d\ell/B$ earlier, one can also evaluate $\oint d\ell$. One again finds that the drift contours are shifted circles. The shift is found to be of the form

$$\hat{\xi} \propto \frac{L}{\delta_L^2 \, N M_G^{1/2}} \ . \tag{4.54}$$

The constant of proportionality is fairly sensitive to the transition between corners and sides, and the analytic approximations introduced here for field line shape inadequately model these details.

This sensitivity to the transition can be exploited by introducing some "reversed toroidal curvature" in the mirror cells adjacent to the corners. One can qualitatively understand the improvement in orbit centering this produces from either the standpoint of $\oint d\ell$ or from the drift motion. The inward shift in the contours of $\oint d\ell$ is caused by the fact that the outer field lines are longer than the inner field lines. By introducing "reversed toroidal curvature" one tends to overcome this effect. At first one might think this would be a negligible effect. It is the fact that the reversed toroidal curvature occurs in the lower magnetic field of the sides that produces the effect. This is most easily understood in terms of the drift motion.

The inward shift of $\oint d\ell$ is associated with the vertical drift produced by toroidal curvature in the corners. Equation (4.52) shows that this drift is proportional to B^{-1}. Introducing reversed toroidal curvature at lower B produces an oppositely directed vertical drift

that is larger in magnitude, thereby cancelling more of the undesirable drift of the corners.

In practice, it is relatively simple to produce reversed toroidal curvature. One simply increases the major radius of the corners slightly, keeping the coils for the sides fixed. The fringing field of the larger major radius corners automatically provides the reversed toroidal curvature in the adjacent mirror cells. The results of numerical calculations for such a coil configuration are shown in Fig. 4.5.

We next consider particles which are transitional between the purely trapped and purely passing populations. Here, we will primarily confine our discussion to hot transitional particles so that we can approximate $\epsilon - e\Phi \simeq \epsilon$ and concentrate on the magnetic drifts.

Along a given field line the maximum value of B, B_{MAX}, is attained half way through any of the corners. A particle on this field line is trapped if $\epsilon/\mu < B_{MAX}$ and passing if $\epsilon/\mu > B_{MAX}$. However, B_{MAX} varies inversely with major radius, so that as particles drift across field lines they can change from trapped to passing. Because the mod-B contours in the center of the corners are vertical lines, the trapped passing boundaries in configuration space are also vertical lines. To the inside of such a line a particle will be trapped and to the outside a particle with the same value of ϵ/μ will be passing.

On the basis of our previous discussion one might guess that a transitional particle drift orbit would be reasonably well centered and approximately circular on the inside (where it is trapped) and not as well centered on the outside (where it is passing). This is qualitatively correct except for an exponentially small class of particles which nearly stall in the center of a corner.

To stall, a particle must cross the vertical trapped-passing boundary <u>while in the corner</u>. Although it is true that the projection of their drift motion crosses this boundary, most transitional particles do not actually cross the boundary while in the corner because they have a finite displacement per transit.

To analyze nearly stalled particles we need to estimate how much time they spend nearly stalled in a corner. We begin by noting that the transit time

$$\tau_t = \oint \frac{d\ell}{v_{\parallel}} = \left(\frac{m}{2}\right)^{1/2} \oint \frac{d\ell}{(\epsilon - \mu B)^{1/2}} \tag{4.55}$$

is singular when $\epsilon/\mu = B_{MAX}$. Near the center of a corner

$$B = B_{MAX}\left(1 - \frac{\ell^2}{L_C^2}\right) . \tag{4.56}$$

The contribution to τ_t from points near $B = B_{MAX}$ is given by

$$\frac{1}{v_{\|0}} \int_0^{\ell} d\ell' \, \frac{1}{(\Delta + \ell'^2/L^2)^{1/2}}$$

$$= \frac{L}{v_{\|0}} \left\{ \log\left[\frac{\ell}{L} + \left(\Delta + \frac{\ell^2}{L^2}\right)^{1/2}\right] + \frac{1}{2} \log\left(\frac{1}{\Delta}\right) \right\} , \tag{4.57}$$

where

$$v_{\|0} = \left(\frac{2}{m}\epsilon\right)^{1/2} , \tag{4.58}$$

$$\Delta = 1 - \mu B_{MAX}/\epsilon , \tag{4.59}$$

and we have noted that $\mu B_{MAX}/\epsilon = 1 - \Delta \simeq 1$.

The singularity in the transit time for $\Delta = 0$ is due to the term proportional to $\log(1/\Delta)$ in Eq. (4.57). Physically this term arises from stalling. Hence we define

$$\tau_{stall} = \frac{L}{2v_{\|0}} \log\left(\frac{1}{\Delta}\right) . \tag{4.60}$$

While a particle is nearly stalled, it will drift vertically with the local drift velocity v_{Dc} and move a distance $v_{Dc}\tau_{stall}$. One way of gaging the importance of this behavior is to compare this distance with the circumference of a drift orbit in the absence of stalling, $2\pi r$. Thus, we define the ratio of distances

$$h = \frac{\text{distance traveled when stalled}}{\text{circumference of orbit}} \tag{4.61}$$

or

$$h = \frac{v_{Dc}\, \tau_{stall}}{2\pi r} \ . \tag{4.62}$$

For fixed h (e.g., 1/10) we can use Eqs. (4.60) and (4.62) to determine the value of Δ. This allows us to estimate how many particles are nearly stalled. We find that

$$\log\left(\frac{1}{\Delta}\right) = \frac{2\pi r h}{L}\,\frac{v_{\parallel}}{v_{Dc}} \ . \tag{4.63}$$

Now the local drift velocity is $v_{Dc} = mv_{\parallel}^2/eBR$ so that

$$\Delta = \exp\left[-4\pi\,\frac{R}{L}(r/\rho_{\parallel})h\right] \ , \tag{4.64}$$

where the parallel gyroradius is given by

$$\rho_{\parallel} = mv_{\parallel}/eB \ . \tag{4.65}$$

The ratio $r/\rho_{\parallel}$ tends to be very large. We can put a lower bound on it by recalling that the adiabatic invariant μ ceases to be conserved for

$$\frac{\rho_{\parallel}}{L} \lesssim \frac{1}{20} \ . \tag{4.66}$$

Thus, one should take the magnitude of the argument of the exponential in Eq. (4.64) to be greater than

$$80\pi\,\frac{R}{L}\,h \ . \tag{4.67}$$

Since R/L is of order unity we see that, except for very small h (which then has a minimal effect on the orbit), the argument of the exponential is quite large and the number of particles involved, Δ, is exponentially small. For example, if $h = 1/10$ and $R/L \simeq 1$, then $\Delta = \exp(-8\pi) \simeq \exp(-25)$.

Transitional particles have been studied numerically for both the circular and square EBT configurations using the time-dependent guiding center equations. These calculations, starting with Gibson et al. in 1964,[8] have consistently showed that one has to prepare a particle extremely carefully in order to observe nearly stalled behavior at all.

Gibson et al.[8] suggested a procedure using J for transitional particles that works very well for a circular EBT (but ignores the exponentially small class of nearly stalled particles). This procedure can be extended to the square configuration. One redefines the limits of integration for J for passing particles so that the integral extends for the central symmetry plane of a side to the central symmetry plane of a corner (this integral is then 1/8 of the original integral, which was for a full circuit). For particles which are not trapped in the local mirrors of the sides but are trapped between ends, one defines the limit of integration for J to be between the central symmetry plane and the turning point near the corner. In this way J is made to be continuous (although its derivatives are not) at the trapped-passing boundary, and standard numerical methods can then be used to determine the drift surfaces. The results of such a numerical calculation are shown in Fig. 4.6.

4.6 SINGLE-PARTICLE ORBITS – SOME NUMERICAL RESULTS

Here we consider the results of numerical calculations and those results that suggest approximations which permit still further numerical and analytic calculations.

Figure 4.7 shows the results of calculating drift surfaces for trapped, passing, and transitional particles for the circular configuration and square configuration. For reference purposes these orbits are for highly energetic particles for which the electric field can be neglected; $\oint d\ell/B$ is also shown. It will be noticed that all orbits are approximately circular. The trapped particles are shifted least while the passing and transitional orbits are shifted inward. It will be noticed that the square configuration gives better centering for all three classes of orbits. Perhaps most noticeable is that the

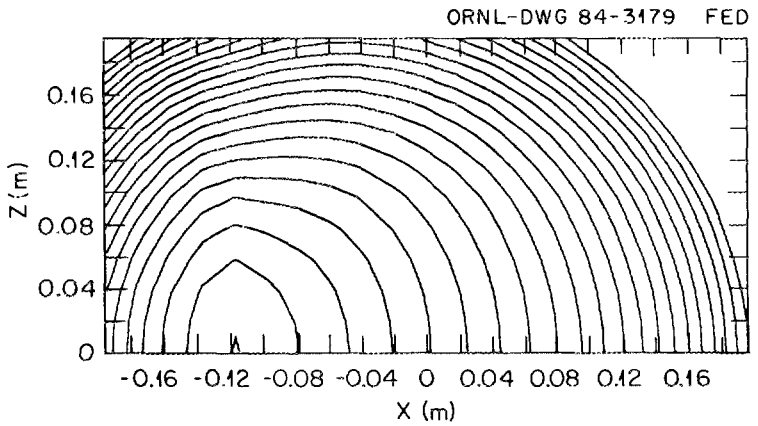

Fig. 4.6. Drift surfaces in a midplane for a high-energy transitional particle in a square configuration. The last closed contour within the volume passes close to the axis of the side. This is in contrast to the circular EBT-I/S configuration, which does not contain any high-energy transitional particles.

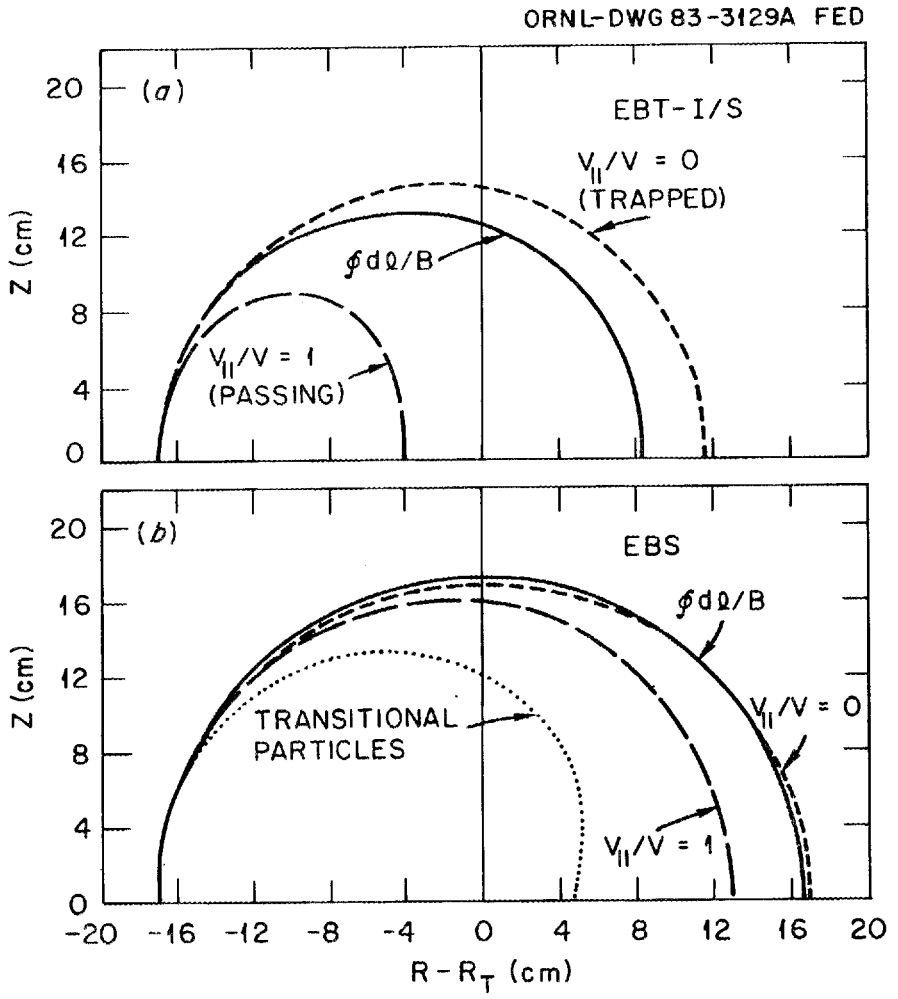

Fig. 4.7. Comparison of high-energy particle orbits for the circular (top) and square (bottom) configurations. Highly trapped particles ($v_{||} = 0$) and extreme passing particles ($v_{||} = v; \mu = 0$) are shown. For reference purposes, contours of $\oint d\ell/B$ are also shown.

circular configuration does not have any transitional orbits that close within the volume, whereas the square configuration does.

Since detailed orbit information for all velocity space, interesting as it may be, is difficult to convey or comprehend quickly, several different measures of orbit qualities have evolved over the years. One measure is simply the shift of an orbit from some reference point. Since the orbits for a given point in velocity space (ϵ and μ) are not always concentric, the convention has been to use the case of an orbit of zero radius. This is readily obtained by finding the minimum in the longitudinal adiabatic invariant J. This shift is commonly referred to as R_{JMIN}.

Figure 4.8 shows R_{JMIN} for both square and circular EBT configurations. Two features are noticeable. One is that the square configuration produces less of a shift for all pitch angles than does the circular configuration. The second is that because the global mirror ratio exceeds the local mirror ratio in the square configuration there are fewer transitional and passing particles for the square configuration. Thus, not only are the orbits better centered but also there are fewer of the particles whose shift is largest.

A second measure of orbit quality is the area of the last closed drift orbit. This area is often normalized to the area of the shadow of the limiter (coil throat) or to the area occupied by the hot electron rings. It is sometimes referred to as the volumetric efficiency and sometimes as the filling factor.

Figure 4.9 shows the area of the last closed drift surfaces (for both circular and square configurations) vs $(v_{\parallel}/v)_{midplane}$. Notice that the area of the trapped particles ($v_{\parallel}/v = 0$) is larger for the square configuration than for the circular one. This occurs because the trapped particles experience virtually no toroidal effects and, hence, are better centered in the square configuration than in the circular one. Also notice that the areas are larger for the square than for the circular configuration — consistent with the earlier figure for R_{JMIN}. (Here it should be noted that because the orbits are not concentric R_{JMIN} reflects the shift at small radii, and the area tends to reflect the better centering that usually occurs at larger radii.)

Because the volume element in velocity space is

$$\epsilon^{1/2} d\epsilon \; d\left(\frac{v_{\parallel}}{v}\right)_{midplane} ,$$

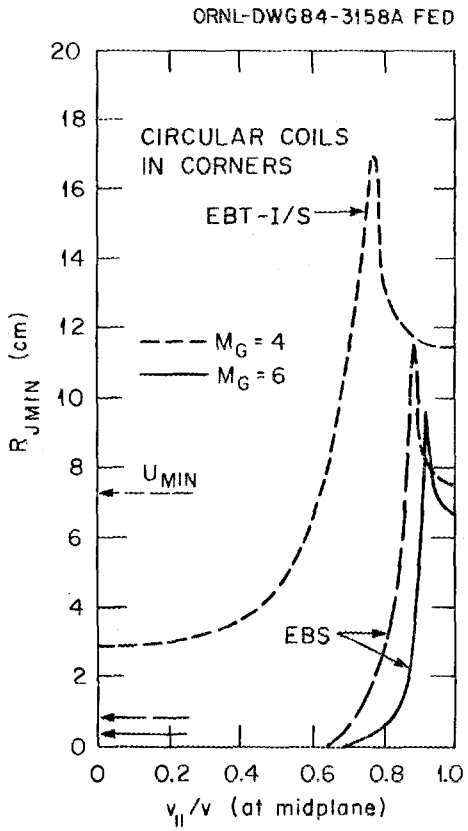

Fig. 4.8. Shift of small radius orbits, R_{JMIN}, vs $(v_{||}/v)_{midplane}$ for high-energy particles. The solid curve represents a square configuration with global mirror ratio $M_G \simeq 6$, whereas the long dashes indicate the same coils with less current in the corners ($M_G \simeq 4$). The higher curve (short dashes) is for EBT-I/S.

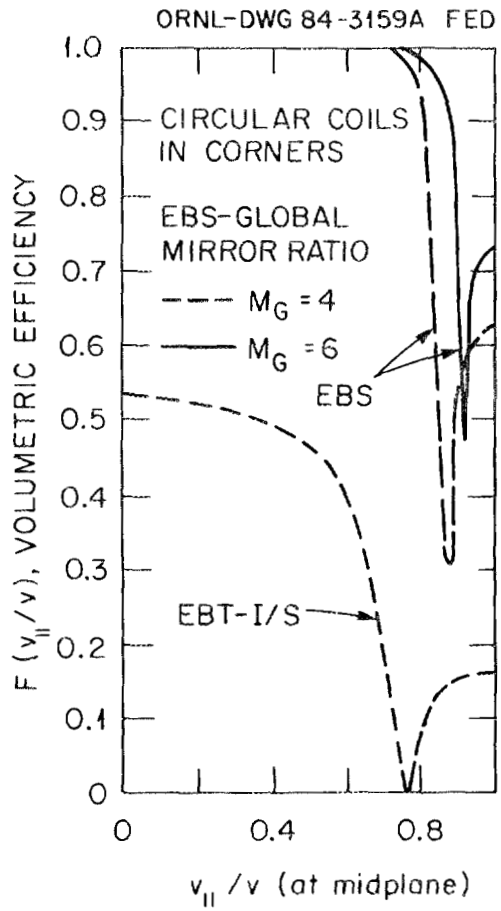

Fig. 4.9. Volumetric efficiency vs $(v_{||}/v)_{midplane}$ for circular EBT-I/S (short dashes) and square configuration (solid curve is for $M \simeq 6$ and long dashes for $M_G \simeq 4$). The normalization chosen is $F = (\text{drift orbit area})/(\pi r^2_{limiter})$ In all cases $r_{limiter} = 19.5$ cm.

we can use Fig. 4.9 to get a single scalar measure of orbit quality. In the absence of an electric field the orbits are independent of energy and we can simply visually integrate the area as a function of $(v_{\parallel}/v)_{midplane}$. One quickly verifies that the square configuration, in the absence of electric field, contains roughly 90% to 95% of the particles, whereas the circular configuration contains about 50%.

We now turn to obtaining measures of orbit quality in the presence of an electric field (or for particles with energies for which the electric field is significant). Here we shall be content with discussing the primary features.

We have already noted that the orbits at large energy are approximately shifted circles. This suggests that we express the longitudinal adiabatic invariant J as a part dependent only on minor radius and one dependent on r cos θ. (Recall how we obtained shifted circles for the contours of $\oint d\ell/B$ in a midplane.) On the other hand, we know[9] that the bounce- or transit-averaged drift velocity is given by $\langle \mathbf{v}_D \rangle = \nabla J \times \hat{b}/(eB\tau)$. The part dependent on minor radii only will lead to a poloidal-directed velocity (call it $r\Omega$). The part that depends on $X = r \cos\theta$ will lead to virtually directed velocity (call it v_y). We are thus led to write

$$\langle \mathbf{v}_D \rangle = r\Omega \hat{e}_\theta + v_y \hat{e}y \ . \tag{4.68}$$

This equation is a standard way of expressing the toroidal effects (aspect ratio expansion) for the circular EBT configuration. It is also a natural way to express orbits in the square configuration: the sides lead to Ω and the corners lead to v_y. If v_y and Ω can be regarded as constant, then the resultant motion is a circle. The center of the circle is at

$$\Delta X = v_y/\Omega \ . \tag{4.69}$$

To illustrate the effect of electric fields we write

$$\Omega = \Omega_B + \Omega_{E\times B} \tag{4.70}$$

and similarly for v_y. The part of Ω arising from curvature and grad-B drifts, Ω_B, has a simple dependence on energy: $\Omega_B \propto \epsilon$. The dependence on pitch angle, like R_{JMIN} and the area, is best determined numerically. The part of Ω arising from $\mathbf{E} \times \mathbf{B}$, Ω_{ExB}, is of course independent of velocity space.

Anticipating the role this measure of orbits plays in calculating diffusion coefficients, we note that typically one expects $D \sim \langle \nu (\Delta X)^2 \rangle$, where the average is over velocity space. Figure 4.10 shows $(\Delta X)^2$ vs energy and $(v_{\parallel}/v)_{midplane}$ for both the square and circular configurations. Notice that at low energy the step-size is small and that it becomes large at larger energy. (The assumed form of the electrostatic potential confines low-energy particles, as discussed in the previous section.) At higher energy the transitional and passing particles develop significant values of $(\Delta X)^2$.

The high values of $(\Delta X)^2$ can be somewhat misleading for two reasons. One reason is that the expression for the step-size given in Eq. (4.69) can break down. This expression assumes that Ω is relatively independent of position. However, it is often the case that Ω passes through zero as a function of r (especially at low to modest energy). One way to test whether Ω goes to zero locally or globally is to examine its derivative with respect to radius. Thus, one writes

$$\Omega = \Omega(r_0) + \Omega'(r - r_0) + \ldots \quad . \tag{4.71}$$

When $\Omega(r_0)$ is zero, then the topology of the orbits is no longer that of nested circles. Instead, a separatrix forms and crescent- or banana-shaped orbits form within this separatrix. The width of the separatrix (maximum banana width) then becomes the appropriate measure of step-size. In this case, Eq. (4.69) should be replaced by

$$\Delta X \propto (v_y/\Omega')^{1/2} \quad . \tag{4.72}$$

(See Appendix 4F for the development of this estimate.) Figure 4.10 has assumed that $\Omega' \simeq 0$ when $\Omega \simeq 0$, which is not necessarily the case.

The second reason that Fig. 4.10 can be misleading is that it obscures the fact that very few particles tend to be at the large

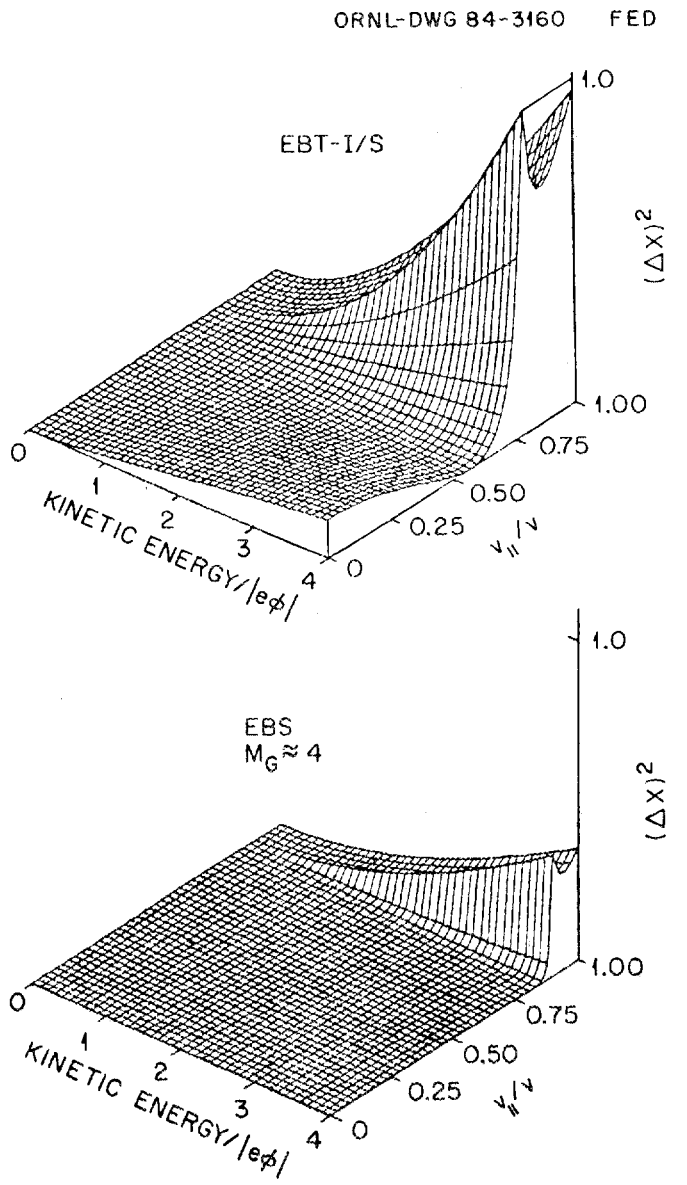

Fig. 4.10. Square of the displacement from the mean, $(\Delta X)^2$, vs kinetic energy and $(v_\parallel/v)_{midplane}$. The nonzero electrostatic potential was chosen to confine particles at low energy for both configurations. Note that the deviation from the mean is considerably suppressed by the square configuration.

energies where the large step-size occurs. Figure 4.11 illustrates this point by displaying $(\Delta X)^2 f(\epsilon)$, where $f(\epsilon)$ is a Maxwellian. Notice that the effect of the high-energy particles, when weighted by the number present, is not nearly so pronounced.

From Fig. 4.11 one could obtain a reasonable estimate of the diffusion coefficient (at low collisionality) by simply integrating $(\Delta X)^2 f$. Rather than do this we have chosen to use the formalism of Spong, Hedrick, and Hastings[10,11] to calculate the diffusion coefficient for both low ($D \sim \nu$) and high ($D \sim 1/\nu$) collisionality. Figure 4.12 shows the diffusion coefficient for both square and circular EBT configurations for electrons. Notice that there is about an order of magnitude difference in the two transport coefficients — leading to the conclusion that the neoclassical lifetime in the square configuration can be an order of magnitude larger than in a circular configuration of comparable size.

4.7 SUMMARY

A detailed exposition of the fundamental equilibrium and orbit ideas and formulas relevant to EBTs (especially the square configuration) has been given. The equation that governs the core scalar pressure surfaces has been developed from both an MHD and drift kinetic approach. Analytic approximations for the pressure surfaces have been developed which are in qualitative agreement with numerical calculation.

Simple expressions for orbits have been given where possible and approximations developed where the full expression requires numerical calculation. A brief survey of typical numerical orbit results has been given for both the square and circular configurations of EBT.

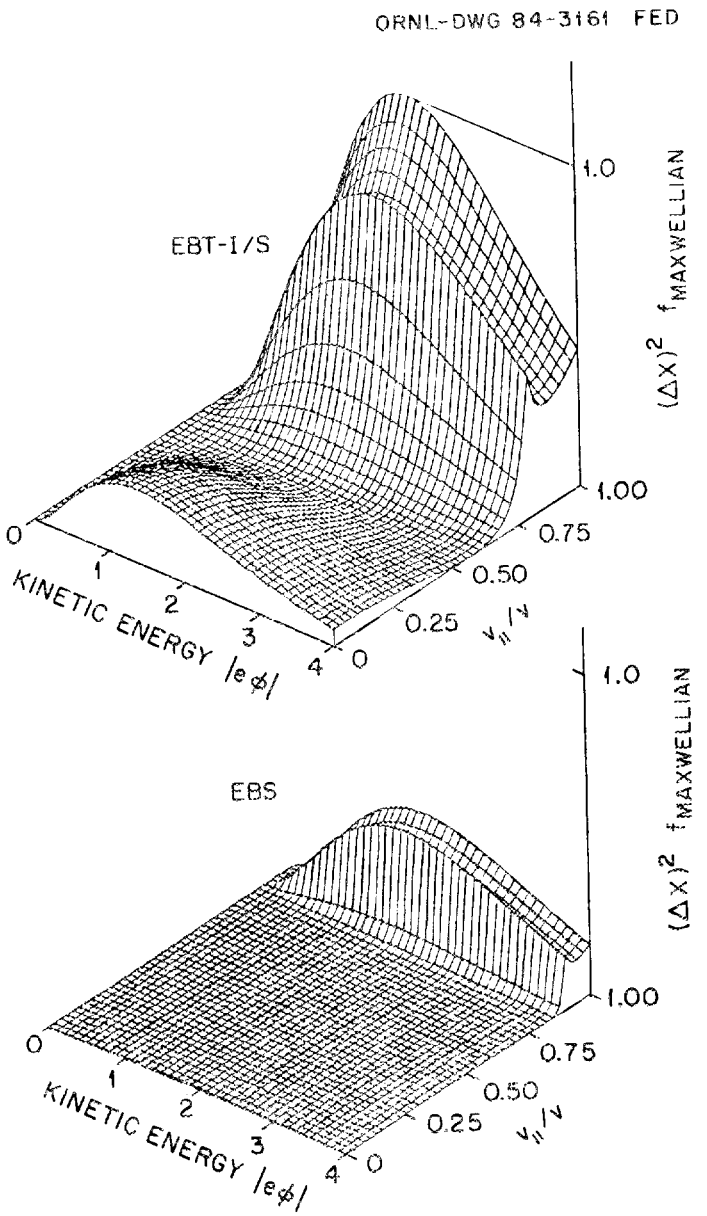

Fig. 4.11. Square of the displacement multiplied by a Maxwellian distribution. The figure indicates the importance of weighting the displacement by the number of particles having that displacement.

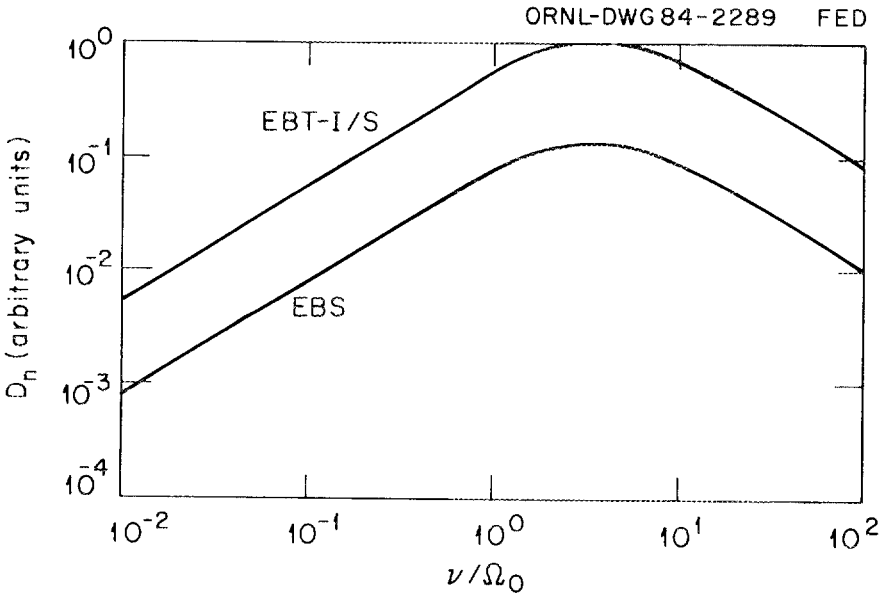

Fig. 4.12. Diffusion coefficient vs collisionality for circular and square configurations. Note that the diffusion is roughly an order of magnitude less for the square configuration. Thus, for similar assumptions for the ambipolar potential, the lifetime is an order of magnitude larger for the square configuration.

ACKNOWLEDGMENTS

We are pleased to acknowledge fruitful discussions with the entire EBT Theoretical and Experimental staff at Oak Ridge who have played a large role in honing our thoughts on equilibrium and particle orbits. The useful questions and comments of Jeff Harris, Jim Rome, and Harold Weitzner played a significant part in our choice of topics. One of us (CLH) performed part of this work while at JAYCOR, and he gratefully acknowledges the hospitality and interest of Nick Krall and John McBride. Discussions with a dozen colleagues at other institutions on equilibria and orbits which have helped mold our thinking pop instantly into our minds. In particular, Ray Dandl, Gareth Guest, and Harold Grad launched our interest in this area and have continued to offer sage and insightful remarks.

Finally, we should remark that our choice of references were ones with which we were most familiar and could easily cite. We are certain that in some instances earlier papers by the same and other authors preceded the cited work.

APPENDIX 4A

Here we develop an extension of the closed line magnetic equilibrium theories of Lortz (scalar pressure);[2] Grad;[3] Hedrick, Guest, and Nelson;[4] and Hall and McNamara.[5] This theory assumes that the magnetic field of the scalar pressure core plasma is sufficiently small that it is unnecessary to modify the fields and currents associated with the hot electron rings and the coils. In the limit of zero ring pressure this extension reduces to the theory of Lortz[2] and is then exact.

Since in many problems of interest the ring plasma pressure is considerably larger than that of the core plasma, we begin by reviewing the available theories for treating the ring magnetic equilibrium problem (without core). The ring plasma is highly anisotropic and thus should be described in terms of a tensor pressure. Grad[3] showed that by assuming the tensor pressure was separable (into a factor which was constant along field lines and a part which varied with B) a "constant of the motion" existed (analogous to $\oint d\ell/B$ for scalar pressure), which greatly facilitated the computation of magnetic equilibria. The algorithm of Grad has been used successfully to compute finite-beta, tensor pressure equilibria by Owen[6,12] for circular EBT configurations.

For nonseparable tensor pressure, algorithms exist[4,5] for computing magnetic equilibria. These algorithms would also permit simultaneous inclusion of nonseparable tensor pressure and core plasma (scalar or tensor pressure). The principal difference between Grad's separable case and the general case is that a simple constant of the motion does not exist (or at least has not been found), and one must solve a partial differential equation (in flux line coordinates: alpha, beta) or calculate the longitudinal adiabatic invariant J for a large number of variables. Since the constraints imposed by the constant of the motion in the separable case enter as a side condition, it seems likely to us that the more general case would not pose any insurmountable numerical problem. It also seems highly likely to us that the actual numerical implementation of these algorithms would require upward of two man-years for each distinctly different configuration.

In numerically implementing Grad's separable case for the circular EBT, heavy use was made of the symmetry properties to reduce the core storage requirements. The square EBT configuration has fewer symmetry planes and, hence, would require more core storage (e.g., by a factor

of 5). However, the square configuration does have an approximate symmetry that can be exploited.

Since the rings form in the nearly axisymmetric bumpy cylinders that make up the sides of the square, the magnetic field of the rings can be calculated quite accurately assuming axisymmetry. This two-dimensional problem in terms of an elliptic partial differential equation of a flux function[4,13] is much simpler numerically than the three-dimensional problem (by one to two orders of magnitude). Should asymmetric corrections prove necessary, they could be obtained using a variant of Grad's aspect ratio expansion for the circular EBT configuration.

To treat core plasma equilibria we write

$$\begin{aligned} \mathbf{B} &= \mathbf{B}_0 + \mathbf{B}_1 \ , \\ \mathbf{j} &= \mathbf{j}_0 + \mathbf{j}_1 \ , \end{aligned} \tag{4A.1}$$

where $\mathbf{B}_0$ is due to the coils and rings, $\mathbf{B}_1$ is due to the core plasma, and similarly for $\mathbf{j}$. We have in mind that the field of the rings comes from solving $\mathbf{j}_{ring} \times \mathbf{B} = \nabla \cdot \overleftrightarrow{P}_{ring}$ and that the core pressure does not change this relation. If the field of the core significantly modifies the magnetic field near the rings, then one would in principle need to recalculate the ring equilibrium to maintain the relation between ring current and pressure. This suggests that the theory developed here might form the basis for a larger iteration scheme that includes both ring and core — a point we do not wish to dwell on here.

The magnetic equilibrium equations to be solved for the core plasma are then

$$\mathbf{j}_1 \times \mathbf{B} = \nabla p \ , \tag{4A.2}$$

$$\nabla \times \mathbf{B}_1 = \mathbf{j}_1 \ , \tag{4A.3}$$

$$\nabla \cdot \mathbf{B}_1 = 0 \ , \tag{4A.4}$$

where p is the scalar pressure of the core.

It follows from Eq. (4A.3) that

$$\nabla \cdot \mathbf{j}_1 = 0 \ , \tag{4A.5}$$

which is charge conservation, in steady state, for the core plasma. Just as $\nabla \cdot \mathbf{B} = 0$ implies that a Clebsch representation exists for the magnetic field ($\mathbf{B} = \nabla\alpha \times \nabla\beta$), Eq. (4A.5) implies that

$$\mathbf{j}_1 = \nabla\zeta \times \nabla\eta \ . \tag{4A.6}$$

Since Eq. (4A.2) implies that

$$\mathbf{j}_1 \cdot \nabla p = 0 \ , \tag{4A.7}$$

a natural choice for either ζ or η in Eq. (4A.6) is p. Choosing $\eta = p$, Eq. (4A.6) becomes

$$\mathbf{j}_1 = \nabla\zeta \times \nabla p \ . \tag{4A.8}$$

We now note that

$$\mathbf{j}_{1,\perp} = \frac{1}{B^2}\mathbf{B} \times (\mathbf{j}_1 \times \mathbf{B}) \ . \tag{4A.9}$$

Inserting Eq. (4A.2) into Eq. (4A.9) yields

$$\mathbf{j}_{1,\perp} = \frac{1}{B^2}\mathbf{B} \times \nabla p \ . \tag{4A.10}$$

Inserting the other expression for $\mathbf{j}_1$, Eq. (4A.8), into Eq. (4A.9) yields

$$\mathbf{j}_{1,\perp} = \frac{1}{B^2}\mathbf{B} \times \left[(\nabla\varsigma \times \nabla p) \times \mathbf{B}\right] ,$$

or

$$\mathbf{j}_{1,\perp} = \frac{1}{B^2}\mathbf{B} \times \left[\nabla p(\mathbf{B} \cdot \nabla\varsigma) - \nabla\varsigma(\mathbf{B} \cdot \nabla p)\right] . \tag{4A.11}$$

However, from Eq. (4A.2) $\mathbf{B} \cdot \nabla p = 0$ so that

$$\mathbf{j}_{1,\perp} = \frac{1}{B^2}\mathbf{B} \times \nabla p(\mathbf{B} \cdot \nabla\varsigma) . \tag{4A.12}$$

Comparing Eq. (4A.10) and Eq. (4A.12) we see that

$$\mathbf{B} \cdot \nabla\varsigma = 1 . \tag{4A.13}$$

Introducing the arc length ℓ along a field line, Eq. (4A.13) can be written

$$\partial\varsigma/\partial\ell = 1/B \tag{4A.14}$$

with the solution

$$\varsigma(\alpha,\beta,\ell) = \varsigma_0(\alpha,\beta) + \int_{\ell_0}^{\ell} d\ell'/B(\alpha,\beta,\ell') , \tag{4A.15}$$

where we have introduced flux line coordinates α and β ($\nabla\alpha \times \nabla\beta = B$) which have the property that they are constant along field lines ($B \cdot \nabla\alpha = B \cdot \nabla\beta = 0$).

Notice that if L is the length of a closed field line then $\zeta(\alpha,\beta,\ell_0 + L)$ is not equal to $\zeta_0(\alpha,\beta)$. Physical quantities such as j_1 and p must, however, be single valued. Inserting Eq. (4A.15) into Eq. (4A.8) we find that

$$j_1(\alpha,\beta,\ell_0) = \nabla\zeta_0 \times \nabla p \tag{4A.16}$$

and

$$j_1(\alpha,\beta,\ell_0 + L) = \nabla\zeta_0 \times \nabla p + \left(\nabla\phi \frac{d\ell}{B}\right) \times \nabla p \ . \tag{4A.17}$$

Imposing $j_1(\alpha,\beta,\ell_0 + L) = j_1(\alpha,\beta,\ell_0)$ yields

$$\nabla p \times \nabla U = 0 \ , \tag{4A.18}$$

where

$$U \equiv \oint d\ell/B \ . \tag{4A.19}$$

Now p and U are only functions of α and β (they are constant along a field line) and are constant on surfaces formed by field lines. Equation (4A.18) implies that ∇p and ∇U are in the same direction so that the surfaces of constant pressure p are the same as the surfaces of U = constant. Thus, the pressure may be regarded as a function of $U \equiv \oint d\ell/B$.

We now express B_1 in terms of ζ. We can rewrite Eq. (4A.8) as

$$j_1 = \nabla \times (\zeta\nabla p) \ . \tag{4A.20}$$

However, from Eq. (4A.3) $j_1 = \nabla \times B$ so that

$$\nabla \times (B_1 - \varsigma \nabla p) = 0$$

from which it follows that $B_1 - \varsigma \nabla p = \nabla \Phi$ or

$$B_1 = \nabla \Phi + \varsigma \nabla p \ . \tag{4A.21}$$

From Eq. (4A.4), $\nabla \cdot B_1 = 0$, we see that Φ satisfies the Poisson equation

$$\nabla^2 \Phi = - \nabla \cdot (\varsigma \nabla p) \ . \tag{4A.22}$$

Now all EBT configurations are designed to make use of Grad's theorem[3] that symmetry across a plane guarantees closed field lines. In the circular EBT configuration the midplanes and coil planes are symmetry planes. In the square configuration the planes that cut the sides at their centers are symmetry planes. The planes that cut the corners at their centers are also symmetry planes. In a symmetry plane the magnetic field is normal to the plane, while the current and gradient of the pressure lie in the symmetry plane.

It is convenient to take $\ell = \ell_0 = 0$ to correspond to a symmetry plane and to set ς_0 of Eq. (4A.15) to be zero so that Eq. (4A.15) becomes

$$\varsigma(\alpha,\beta,\ell) = \int_0^{\ell} d\ell'/B(\alpha,\beta,\ell') \ . \tag{4A.23}$$

We are now in a position to describe an iteration procedure. Starting with an initial guess for B (like B_0) we calculate ς from Eq. (4A.23). This automatically yields $U \equiv \oint d\ell/B$. We then set up the pressure in the symmetry plane (consistent with $\nabla p \times \nabla U = 0$) and map the pressure along magnetic field lines to points off the symmetry plane. We next use p and ς to form the right side of the Poisson equation for Φ, Eq. (4A.22), and solve the Poisson equation for Φ. Using Eqs. (4A.1) and (4A.21) we calculate a new value of B. Using the

new value of B we can recalculate ς (and U) and the pressure and the driving term in the Poisson equation, solve the Poisson equation for Φ, and calculate still another value of B_1. This procedure is repeated until a sufficiently converged solution is obtained.

For many purposes (e.g., low-to-modest core beta), it is not necessary to compute the change in the magnetic field produced by the core plasma. For these cases all we may require is the fact that the pressure is a function of $\oint d\ell/B$ and, perhaps, the core plasma current. Equations (4A.8) and (4A.23) provide a convenient way of determining the parallel component of the current and can be used to determine the perpendicular component although Eq. (4A.10) may be more convenient in some instances.

Finally we should note that the iteration scheme suggested here, although probably adequate, is not necessarily the most efficient one. Alternative iteration schemes have been suggested for the Lortz problem (no ring present) by Grad[14] and McNamara.[15] These should be equally applicable to the approximate theory developed here for cases involving a significant ring beta.

APPENDIX 4B

Here, a small radius, vacuum magnetic field approximation is developed for the contribution to $\oint d\ell/B$ from a single-mirror one-half cell.

The distance between a midplane and an adjacent coil plane is taken to be L. The strength of the magnetic field in the center of the midplane ($r = z = 0$) is denoted by B_0. The mirror ratio on-axis ($r = 0$) is denoted by M, so that the magnetic field in the center of the coil plane ($r = 0; z = L$) is MB_0. It is convenient to define a bumpiness parameter δ by

$$\delta = \frac{M - 1}{M + 1} . \tag{4B.1}$$

For the field due to the coils alone there are no currents in the plasma volume, and **B** satisfies

$$\mathbf{B} = \nabla\Phi . \tag{4B.2}$$

Keeping only the two lowest harmonics, the magnetostatic potential is given by

$$\Phi = \frac{B_0}{1 - \delta}\left[z - \frac{\delta}{k}\sin kz\, I_0(kr)\right] , \tag{4B.3}$$

where

$$k = \pi/L . \tag{4B.4}$$

It is also useful to express the magnetic field in terms of a flux function ψ:

$$\mathbf{B} = \nabla\psi \times \nabla\theta . \tag{4B.5}$$

For vacuum fields ψ satisfies the equation

$$\nabla \times \nabla\psi \equiv \frac{\partial^2\psi}{\partial z^2} + \frac{\partial^2\psi}{\partial r^2} - \frac{1}{r}\frac{\partial\psi}{\partial r} = 0 \ . \tag{4B.6}$$

Although we could derive the general solution to Eq. (4B.6), here it is simpler to observe that

$$B_z = \frac{1}{r}\frac{\partial\psi}{\partial r} = \frac{\partial\Phi}{\partial z} \ , \tag{4B.7}$$

$$B_r = -\frac{1}{r}\frac{\partial\psi}{\partial z} = \frac{\partial\Phi}{\partial r} \ . \tag{4B.8}$$

From Eqs. (4B.7) and (4B.8) we see that $\Phi = z$ corresponds to $\psi = \frac{1}{2} r^2$ and that $\Phi = \sin kz\ I_0(kr)$ corresponds to $\psi = rI_1(kr)\cos kz$. Comparing to Eq. (4B.3) we find that

$$\Psi = \frac{B_0}{1-\delta}\left[\frac{1}{2} r^2 - \frac{\delta}{k} rI_1(kr)\ \cos kz\right] \ . \tag{4B.9}$$

The components of the magnetic field are

$$B_Z = \frac{B_0}{(1-\delta)}\left[1 - \delta\ \cos kz\ I_0(kr)\right] \ , \tag{4B.10}$$

$$B_r = -\left(\frac{B_0}{1-\delta}\right)\delta\ \sin kz\ I_1(kr) \ . \tag{4B.11}$$

Note that for $r = 0$

$$B = B_z = \frac{B_0}{1-\delta}\left(1 - \delta\ \cos kz\right) \ ,$$

so that $B = B_0$ at $r = z = 0$. At $r = 0$, $z = L$, $B = (1 + \delta)B_0/(1 - \delta) = MB_0$ so that the choice of parameters δ and B_0 is consistent with the specifications made earlier.

To obtain qualitative information we will use a small radius approximation and expand in the bumpiness parameter δ. For small r the modified Bessel functions in Eqs. (4B.10) and (4B.11) yield

$$B_z \simeq \frac{B_0}{(1 - \delta)} \left[1 - \delta \cos kz\left(1 + \frac{1}{4} k^2 r^2\right)\right], \tag{4B.12}$$

$$B_r \simeq - \frac{B_0}{(1 - \delta)} \delta \sin kz\left(\frac{1}{2} kr\right). \tag{4B.13}$$

Now, since $dz/d\ell = B_z/B$,

$$\frac{d\ell}{B} = \frac{dz}{B_z} \simeq \left(\frac{1 - \delta}{B_0}\right) \frac{dz}{[1 - \delta \cos kz(1 + \frac{1}{4} k^2 r^2)]}. \tag{4B.14}$$

To facilitate the integration of Eq. (4B.14) we next expand in δ:

$$\frac{d\ell}{B} \simeq dz\left(\frac{1 - \delta}{B_0}\right)\left[1 + d \cos kz\left(1 + \frac{1}{4} k^2 r^2\right) + \delta^2 \cos^2 kz\left(1 + \frac{1}{4} k^2 r^2\right)^2 + \ldots\right]. \tag{4B.15}$$

However, since we have neglected terms of order $k^4 r^4$ in Eqs. (4B.12) and (4B.14), we should not retain them in Eq. (4B.15). Thus,

$$\frac{d\ell}{B} \simeq dz \left(\frac{1 - \delta}{B_0}\right)\left[\left(1 + \delta \cos kz + \delta^2 \cos^2 kz\right) + k^2 r^2\left(\frac{1}{4} \delta \cos kz + \frac{1}{2} \delta^2 \cos^2 kz\right)\right]. \tag{4B.16}$$

Note that the field lines are "bumpy" so that r varies with z. However, from Eq. (4B.5) we see that the flux function ψ is constant along field lines since

$$\mathbf{B} \cdot \nabla\psi = 0 \ .$$

Thus, if we express r^2 [in Eq. (4B.16)] in terms of ψ and z, we will have the desired result.

We begin by noting that we only require r^2 in Eq. (4B.16) to first order in δ and ψ (formally, ψ or r^2 may be replaced by k^2 as the expansion parameter here). Thus, we only need the leading term of $I_1(kr)$, and Eq. (4B.9) becomes

$$\psi \simeq \frac{B_0}{1 - \delta}\left(\frac{1}{2} r^2 - \frac{\delta}{2} r^2 \cos kz\right),$$

$$r^2 \simeq \frac{2\psi(1 - \delta)}{B_0} \frac{1}{1 - \delta \cos kz} , \tag{4B.17}$$

or

$$r^2 \simeq \frac{2\psi(1 - \delta)}{B_0}\left(1 + \delta \cos kz\right) . \tag{4B.18}$$

Now the field line labeled by ψ could equally well be labeled by its value of r in the midplane, r_s. Now, from Eq. (4B.17)

$$r_s^2 = \frac{2\psi}{B_0} , \tag{4B.19}$$

so that Eq. (4B.18) becomes

$$r^2 \simeq r_s^2(1 - \delta)(1 + \delta \cos kz) \ . \tag{4B.20}$$

Inserting Eq. (4B.20) into Eq. (4B.16) we obtain

$$\frac{d\ell}{B} \simeq dz \left(\frac{1-\delta}{B_0}\right)\left[\left(1 + \delta \cos kz + \delta^2 \cos^2 kz\right)\right.$$
$$\left. + (1-\delta)k^2 r_s^2 \left(\frac{1}{4}\delta \cos kz + \frac{3}{4}\delta^2 \cos^2 kz\right)\right] . \qquad (4B.21)$$

We notice that since $\cos^2 kz = \frac{1}{2}(1 + \cos 2kz)$, we should omit the $\cos 2kz$ terms to be consistent with omitting second and higher harmonics in Φ, ψ, and **B**. Thus,

$$\int_0^{\ell} \frac{d\ell'}{B} \simeq \int_0^{z} dz' \left(\frac{1-\delta}{B_0}\right)\left[\left(1 + \frac{1}{2}\delta^2\right) + \delta \cos kz'\right.$$
$$\left. + \frac{1}{4}\delta(1-\delta)k^2 r_s^2 \left(\cos kz' + \frac{3}{2}\delta\right)\right] , \qquad (4B.22)$$

or

$$\int_0^{\ell} \frac{d\ell'}{B} \simeq L\left(\frac{1-\delta}{B_0}\right)\left\{\frac{z}{L}\left(1 + \frac{1}{2}\delta^2\right) + \frac{\delta}{\pi}\sin\left(\frac{\pi z}{L}\right)\right.$$
$$\left. + \frac{1}{4}\delta(1-\delta)\left(\frac{\pi r_s}{L}\right)^2\left[\frac{1}{\pi}\sin\left(\frac{\pi z}{L}\right) + \frac{3}{2}\delta\frac{z}{L}\right]\right\} . \qquad (4B.23)$$

Thus, the contribution of a one-half cell to $\oint d\ell'/B$ is given by

$$\int_0^{L} \frac{d\ell'}{B} \simeq L\left[\left(\frac{1-\delta}{B_0}\right)\left(1 + \frac{1}{2}\delta^2\right) + \frac{3}{8}\delta^2(1-\delta)\left(\frac{\pi r_s}{L}\right)^2\right] . \qquad (4B.24)$$

APPENDIX 4C

Here we develop the contribution to the parallel current from a single-mirror one-half cell for low beta. The parallel current arises because the pressure surfaces are displaced inward from the axis of the (vacuum) magnetic field.

We may formally obtain the required MHD equations from Appendix 4A by noting that if the field of the rings is negligible then we need not split **B** into zeroth and first-order parts. Instead, the field due to the coils may be incorporated into the potential function Φ appearing in Eq. (4A.21). When this is done, one obtains the equations

$$\mathbf{B} = \nabla\Phi + \varsigma\nabla p \ , \tag{4C.1}$$

$$\varsigma = \int_0^{\ell} \frac{d\ell'}{B} + \varsigma_0 \ , \tag{4C.2}$$

$$\mathbf{j} = \nabla\varsigma \times \nabla p \ . \tag{4C.3}$$

For low core beta

$$\mathbf{B} \simeq \nabla\Phi \simeq \nabla\Phi_{coil} \simeq \mathbf{B}_{coil} \ , \tag{4C.4}$$

and

$$\varsigma \simeq \int_0^{\ell} \frac{d\ell'}{B_{coil}} + \varsigma_0 \ . \tag{4C.5}$$

A few remarks are in order at this point concerning the zero of ℓ. If we are dealing with a one-half cell whose midplane is also a symmetry plane (center of a side), then we are free to set $\varsigma_0 = 0$. If this is not the case, we will follow the convention here that $\ell = 0$ corresponds to the midplane of the one-half cell in question, but we must retain ς_0. (ς_0 is calculated by adding up the contributions from

all the one-half cells between the one in question and the central symmetry plane of the side.) This convention allows us to use the indefinite integral given in Appendix 4B for $\int d\ell/B$ [Eq. (4B.23)]. This same convention will be followed in calculating $\mathbf{j}$ from Eq. (4C.3).

Since the vacuum magnetic field is axisymmetric, so is our approximation to ζ. That is, $\zeta = \zeta(\psi,\ell)$. However, the pressure is shifted inward so that it depends on the angle θ as well as ψ. Thus, from Eq. (4C.3)

$$j_{\parallel} = \hat{b} \cdot (\nabla\zeta \times \nabla p) ,$$

or

$$j_{\parallel} = B \frac{\partial\zeta}{\partial\psi} \frac{\partial p}{\partial\theta} . \tag{4C.6}$$

As in Appendix 4B, instead of labeling field lines by ψ (and θ), we replace ψ by the radius for which the field line pierces the midplane r_s. From Eq. (4B.19) we have $\psi = 2B_0 r_s^2$, so that Eq. (4C.6) becomes

$$j_{\parallel} = \frac{B}{B_0} r_s \frac{\partial\zeta}{\partial r_s} \frac{\partial p}{\partial\theta} . \tag{4C.7}$$

We have seen [Eq. (4.12)] that p is constant on contours of

$$(X_s + \xi)^2 + y_s^2 = \text{constant} ,$$

where $\xi = r_s\cos\theta$, $y_s = r_s\sin\theta$. We are thus led to define a new field line label by

$$r_p^2 = (r_s\cos\theta + \xi)^2 + r_s^2\sin^2\theta \qquad (4C.8)$$

$$= r_s^2 + 2\xi r_s\cos\theta + \xi^2 ,$$

and

$$p = p(r_p) . \qquad (4C.9)$$

For the devotees of α,β coordinates this is equivalent to writing $p = p(\alpha)$ with α as a function of ψ and θ.

Now the partial derivative in Eq. (4C.7), $(\partial p/\partial\theta)$, is to be taken at fixed ψ or fixed r_s. Thus,

$$\frac{\partial p}{\partial\theta} = \frac{dp}{dr_p}\frac{\partial r_p}{\partial\theta}\Big|_{r_s} . \qquad (4C.10)$$

However, from Eq. (4C.8),

$$\frac{\partial r_p}{\partial\theta}\Big|_{r_s} = -\xi\frac{r_s}{r_p}\sin\theta . \qquad (4C.11)$$

Provided we are not too close to $r_s = 0$, we can approximate r_s/r_p by unity in Eq. (4C.11) so that

$$\frac{\partial r_p}{\partial\theta}\Big|_{r_s} \simeq -\xi\sin\theta . \qquad (4C.12)$$

Combining Eqs. (4C.7), (4C.10), and (4C.12) we obtain

$$j_{\parallel} \simeq -\xi\frac{B}{B_0}r_s\frac{\partial\zeta}{\partial r_s}\frac{dp}{dr_s}\sin\theta , \qquad (4C.13)$$

where we have used $dp/dr_p \simeq dp/dr_s$ (which fails for $r_s < |\xi|$).

From Eq. (4C.5)

$$\frac{\partial \zeta}{\partial r_s} = \frac{\partial \zeta_0}{\partial r_s} + \frac{\partial}{\partial r_s}\left(\int_0^{\ell} \frac{d\ell'}{B}\right) . \tag{4C.14}$$

Differentiating Eq. (4B.23) yields

$$\frac{\partial}{\partial r_s}\left(\int_0^{\ell} \frac{d\ell'}{B}\right) = \frac{\pi^2}{2} \frac{\delta(1-\delta)^2}{B_0} \frac{r_s}{L^3} \left(\frac{1}{\pi} \sin \frac{\pi z}{L} + \frac{3}{2} \delta \frac{z}{L}\right) . \tag{4C.15}$$

Combining Eqs. (4C.13), (4C.14), and (4C.15), we see that the contribution to $j_{\parallel}$ from this one-half cell is

$$\Delta j_{\parallel} \simeq -\frac{\pi^2}{2} \frac{\delta}{B_0} \frac{dp}{dr_s} \frac{\xi r_s^2}{L^3} \left(\frac{1}{\pi} \sin \frac{\pi z}{L} + \frac{3}{2} \frac{\delta z}{L}\right) \sin \theta , \tag{4C.16}$$

where we have used $(1 - \delta)^2 \simeq 1$.

Equation (4C.16) consists of two parts: an oscillatory part and a part that is linear in z. The oscillatory part occurs in the circular configuration. In a circular EBT configuration, the term linearly proportional to z is cancelled by distributed toroidal effects. In the square configuration, the term proportional to z is cancelled again by toroidal effects, but this time these toroidal effects all occur in the corner.

APPENDIX 4D

Here we develop the first moment of the drift kinetic equation, Eq. (4.35), which we reproduce here:

$$\frac{\partial f_j}{\partial t} + \mathbf{v}_{\parallel} \cdot \nabla f + \mathbf{v}_D \cdot \nabla f_j = C_j \ . \tag{4D.1}$$

Implicit here is that f_j is a function of the total energy, $\epsilon = e\Phi + mv^2/2$ and the diamagnetic moment $\mu = mv_{\perp}^2/2B$. We are primarily concerned with scalar pressure here, which corresponds to an isotropic distribution, f_j independent of μ.

The moment of $\partial f_j/\partial t$ is clearly $\partial n_j/\partial t$, where

$$n_j = \int d^3v \ f_j \ . \tag{4D.2}$$

The next term in Eq. (4D.1) can be rewritten

$$\mathbf{v}_{\parallel} \cdot \nabla f = \frac{v_{\parallel}}{B} \mathbf{B} \cdot \nabla f = \frac{v_{\parallel}}{B} \nabla \cdot (\mathbf{B} f) \ , \tag{4D.3}$$

where we have used $\nabla \cdot \mathbf{B} = 0$. The moment of this term is most conveniently obtained by writing the velocity space integral in terms of ϵ and μ. The element of volume in velocity space is

$$d^3v = C \frac{B}{v_{\parallel}} d\epsilon \ d\mu \ , \tag{4D.4}$$

so that Eq. (4D.3) can be integrated:

$$\int d^3v \ \mathbf{v}_{\parallel} \cdot \nabla f_j = C_j \int d\epsilon \ d\mu \frac{B}{v_{\parallel}} \left[\frac{v_{\parallel}}{B} \nabla \cdot (\mathbf{B} f_j) \right] \ . \tag{4D.5}$$

Because the divergence is at fixed ϵ and μ, it can safely be passed through the integrand in Eq. (4D.5), and we obtain

$$\int d^3v \, \mathbf{v}_{\parallel} \cdot \nabla f_j = \nabla \cdot \left(C_j \int d\epsilon \, d\mu \, \mathbf{B} f_j \right) \tag{4D.6}$$

or

$$\int d^3v \, \mathbf{v}_{\parallel} \cdot \nabla f = \nabla \cdot \left(\hat{b} C_j \int d\epsilon \, d\mu \, B f_j \right) . \tag{4D.7}$$

Now,

$$C_j \int d\epsilon \, d\mu \, B f_j = C_j \int d\epsilon \, d\mu \, \frac{B}{v_{\parallel}} \cdot v_{\parallel} f_j$$

$$= \int d^3v \, v_{\parallel} f_j \, . \tag{4D.8}$$

By definition

$$n_j \langle v_{\parallel} \rangle_j = \int d^3v \, v_{\parallel} f_j \tag{4D.9}$$

so that by combining Eqs. (4D.7), (4D.8), and (4D.9) we obtain

$$\int d\epsilon \, v \, \mathbf{v}_{\parallel} \cdot \nabla f_j = \nabla \cdot \left(n_j \langle v_{\parallel} \rangle_j \hat{b} \right) . \tag{4D.10}$$

For the remaining term on the left side of the drift kinetic equation, Eq. (4D.1), it is more convenient to use the velocity space components rather than ϵ and μ when performing the integration. Recalling that we are most interested in isotropic distributions here, we write

$$f_j(\epsilon,\mathbf{x}) = F_j\left(\frac{1}{2}mv^2,\mathbf{x}\right). \tag{4D.11}$$

However, $mv^2/2 = \epsilon - e\Phi$, so that

$$f_j(\epsilon,\mathbf{x}) = F_j(\epsilon - e\Phi,\mathbf{x}) \tag{4D.12}$$

Then (at fixed ϵ),

$$\begin{aligned}\nabla f_j &= \nabla F_j + \frac{\partial F_j}{\partial\left(\frac{1}{2}mv^2\right)}\left(-e\nabla\Phi\right)\\ &= \nabla F_j + e\,\mathbf{E}\,\frac{\partial F_j}{\partial\left(\frac{1}{2}mv^2\right)}.\end{aligned} \tag{4D.13}$$

The drift velocity, Eq. (4.36), is

$$\mathbf{v}_D = \frac{\mathbf{E}\times\mathbf{B}}{B^2} + \frac{\frac{1}{2}mv^2}{e_jB}\,\hat{b}\times\left(\frac{v_\perp^2}{v^2}\nabla\,\ell n\,B + 2\,\frac{v_\parallel^2}{v^2}\kappa\right). \tag{4D.14}$$

Combining Eqs. (4D.13) and (4D.14), we find that

$$\begin{aligned}\mathbf{v}_D\cdot\nabla f_j &= \frac{\mathbf{E}\times\mathbf{B}}{B^2}\cdot\nabla F_j\\ &+ \frac{\frac{1}{2}mv^2}{e_jB}\left[\hat{b}\times\left(\frac{v_\perp^2}{v^2}\nabla\,\ell n\,B + \frac{2v_\parallel^2}{v^2}\kappa\right)\right]\cdot\nabla F_j\\ &+ \frac{1}{2}mv^2\,\frac{\partial F_j}{\partial(\frac{1}{2}mv^2)}\,\frac{\mathbf{E}\times\mathbf{B}}{B^2}\cdot\left(\frac{v_\perp^2}{v^2}\nabla\,\ell n\,B + 2\,\frac{v_\parallel^2}{v^2}\kappa\right)\end{aligned} \tag{4D.15}$$

where we have noted that $\mathbf{E} \cdot (\mathbf{E} \times \mathbf{B}) = 0$. The integral of the first term on the right side of Eq. (4D.15) is trivial:

$$\int d^3v \left(\frac{\mathbf{E} \times \mathbf{B}}{B^2}\right) \cdot \nabla F_j = \frac{\mathbf{E} \times \mathbf{B}}{B^2} \cdot \nabla n_j \ . \tag{4D.16}$$

The integration of the other terms in Eq. (4D.15) can be carried out if we notice that since F_j is isotropic the only pitch angle dependence occurs in the factor

$$\frac{v_\perp^2}{v^2} \nabla \ell n \, B + 2 \frac{v_\parallel^2}{v^2} \kappa \ .$$

It is convenient to introduce the variables

$$K = \frac{1}{2} mv^2 \ , \tag{4D.17}$$

$$\varsigma = v_\parallel / v \ , \tag{4D.18}$$

so that

$$d^3v = 2\pi K^{1/2} dK \, d\varsigma \tag{4D.19}$$

and

$$\frac{v_\perp^2}{v^2} = 1 - \varsigma^2 \ . \tag{4D.20}$$

We find that

$$\frac{\int_{-1}^{1} d\zeta \left(\frac{v_\perp^2}{v^2} \nabla \ell n\, B + 2 \frac{v_\parallel^2}{v^2} \kappa^2 \right)}{\int_{-1}^{1} d\zeta} = \frac{2}{3} (\nabla \ell n\, B + \kappa) \quad . \tag{4D.21}$$

Since

$$\int d^3v \, \frac{1}{2} m v^2 F_j = \frac{3}{2} p_j \quad , \tag{4D.22}$$

$$\int d^3v \, \frac{1}{2} m v^2 \nabla F_j = \frac{3}{2} \nabla p_j \quad . \tag{4D.23}$$

The one remaining integral in Eq. (4D.15) is

$$\begin{aligned} \int d^3v \, \frac{1}{2} m v^2 \, \frac{\partial F_j}{\partial \left(\frac{1}{2} m v^2 \right)} &= 2\pi \int_{-1}^{1} K^{1/2} \, dK - \left(K \frac{\partial F_j}{\partial K} \right) \\ &= -\frac{3}{2} \cdot \left(2\pi \int_{-1}^{1} d\zeta K^{1/2} dK F_j \right) \\ &= -\frac{3}{2} \int d^3v \, F_j \\ &= -\frac{3}{2} n_j \quad . \end{aligned} \tag{4D.24}$$

Inserting Eqs. (4D.16), (4D.21), (4D.23), and (4D.24) into Eq. (4D.15) yields

$$\begin{aligned} \int d^3v \, v_D \cdot \nabla f_j = \nabla p_j \cdot \left[\frac{\hat{b}}{e_j B} \times (\nabla \ell n\, B + \kappa) \right] \\ + \frac{E \times B}{B^2} \cdot \left[\nabla n_j - n_j (\nabla \ell n\, B + \kappa) \right] \end{aligned} \tag{4D.25}$$

Combining Eqs. (4D.2), (4D.10), and (4D.25) yields the left side of Eq. (4.37).

APPENDIX 4E

Here we develop expressions for the perpendicular derivatives of closed-line integrals. These generally useful expressions are then applied to $\oint d\ell/B$. The resultant expressions are then used to express the integrals appearing in Eq. (4.38) in terms of $\oint d\ell/B$ and its gradient.

We begin with the Clebsch representation for the magnetic field:

$$\mathbf{B} = \nabla\alpha \times \nabla\beta \ . \tag{4E.1}$$

Since $\nabla\alpha$ and ∇B are not necessarily orthogonal, we define the two vectors

$$\mathbf{U}_\alpha \equiv \frac{\nabla\beta \times \mathbf{B}}{B^2} \ , \tag{4E.2}$$

$$\mathbf{U}_\beta = \frac{\mathbf{B} \times \nabla\alpha}{B^2} \ , \tag{4E.3}$$

which have the properties:

$$\mathbf{U}_\alpha \cdot \nabla\alpha = 1 \ ; \ \mathbf{U}_\alpha \cdot \nabla\beta = 0$$
$$\tag{4E.4}$$
$$\mathbf{U}_\beta \cdot \nabla\alpha = 0 \ ; \ \mathbf{U}_\beta \cdot \nabla\beta = 1$$

(These properties can be easily verified. For example, $\mathbf{U}_\alpha \cdot \nabla\alpha = \nabla\alpha \cdot (\nabla\beta \times \mathbf{B})/B^2 = (\nabla\alpha \times \nabla\beta) \cdot \mathbf{B}/B^2 = \mathbf{B} \cdot \mathbf{B}/B^2 = 1.$) The utility of $\mathbf{U}_\alpha$ and $\mathbf{U}_\beta$ becomes apparent if we write

$$\nabla\Phi = \frac{\partial\Phi}{\partial\alpha}\nabla\alpha + \frac{\partial\Phi}{\partial\beta}\nabla\beta + \frac{\partial\Phi}{\partial\ell}\hat{b} \ . \tag{4E.5}$$

Using Eq. (4E.4) [and (4E.1), which implies $\hat{b} \cdot \nabla\alpha = \hat{b} \cdot \nabla\beta = 0$], we find that

$$\partial\Phi/\partial\alpha = \mathbf{U}_\alpha \cdot \nabla\Phi \ ,$$

$$\partial\Phi/\partial\beta = \mathbf{U}_\beta \cdot \nabla\Phi \ , \tag{4E.6}$$

$$\partial\Phi/\partial\ell = \hat{b} \cdot \nabla\Phi \ .$$

The vectors $\mathbf{U}_\alpha$ and $\mathbf{U}_\beta$ have a simple interpretation in terms of displacement. A small change in α (at fixed β) yields

$$\Delta\mathbf{x}_\perp|_\beta = \mathbf{U}_\alpha \Delta\alpha \ . \tag{4E.7}$$

Similarly,

$$\Delta\mathbf{x}_\perp|_\alpha = \mathbf{U}_\beta \Delta\beta \ . \tag{4E.8}$$

This interpretation allows us to compute volume and surface elements. For example,

$$d^3\chi = \mathbf{U}_\alpha \times \mathbf{U}_\beta \cdot \hat{b} \ d\alpha \ d\beta \ d\ell \ . \tag{4E.9}$$

(One can verify that this gives the general expression for the Jacobian in three dimensions.) However,

$$\mathbf{U}_\alpha \times \mathbf{U}_\beta \cdot \hat{\mathbf{b}} = (\hat{\mathbf{b}} \times \mathbf{U}_\alpha) \cdot \mathbf{U}_\beta$$

$$= \left[\frac{\mathbf{B} \times (\nabla\beta \times \mathbf{B})}{B^3}\right] \cdot \mathbf{U}_\beta$$

$$= \frac{\nabla\beta}{B} \cdot \mathbf{U}_\beta = 1/B \ , \qquad (4E.10)$$

so that

$$d^3x = \frac{d\ell}{B}\, d\alpha\, d\beta \ . \qquad (4E.11)$$

We now consider integrals of the form

$$I(\alpha,\beta) = \oint d\boldsymbol{\ell} \cdot \mathbf{V}(\alpha,\beta,\ell) \ , \qquad (4E.12)$$

$$\frac{\partial I}{\partial \alpha} = \lim_{\Delta\alpha \to 0} \frac{1}{\Delta\alpha}\left[\frac{I(\alpha + \Delta\alpha,\beta) - I(\alpha,\beta)}{\Delta\alpha}\right] . \qquad (4E.13)$$

We apply Stoke's theorem to (4E.13) and obtain

$$\frac{\partial I}{\partial \alpha} = \lim_{\Delta\alpha \to 0} \frac{1}{\Delta\alpha} \int d\mathbf{S} \cdot (\nabla \times \mathbf{V}) \ , \qquad (4E.14)$$

where the surface element $d\mathbf{S}$ is given by

$$d\mathbf{S} = \Delta\mathbf{x}\big|_\beta \times d\boldsymbol{\ell} \ , \qquad (4E.15)$$

$$d\mathbf{S} = \Delta\alpha(\mathbf{U}_\alpha \times \hat{\mathbf{b}}\, d\ell) \ . \qquad (4E.16)$$

However,

$$\mathbf{U}_\alpha \times \mathbf{b} = \frac{(\nabla\beta \times \mathbf{B}) \times \mathbf{B}}{B^3}$$

$$= -\frac{\nabla\beta}{B} ,$$

so that

$$d\mathbf{S} = -\delta\alpha\left(\frac{\nabla\beta}{B}\right) d\ell , \tag{4E.17}$$

and Eq. (4D.14) becomes

$$\frac{\partial I}{\partial \alpha} = -\oint \frac{d\ell}{B} \nabla\beta \cdot (\nabla \times \mathbf{V}) . \tag{4E.18}$$

Similarly,

$$\frac{\partial I}{\partial \beta} = \oint \frac{d\ell}{B} \nabla\alpha \cdot (\nabla \times \mathbf{V}) . \tag{4E.19}$$

Equations (4E.18) and (4E.19) are useful as they stand in the study of small magnetic field errors.

For the special (but common) case

$$\mathbf{V} = S\hat{\mathbf{b}} , \tag{4E.20}$$

Eq. (4E.12) reduces to

$$I = \oint d\ell \; S , \tag{4E.21}$$

while

$$\nabla \times \mathbf{V} = \nabla S \times \hat{b} + S \nabla \times \hat{b} \ . \tag{4E.22}$$

Using the vector identity of $\nabla(\mathbf{A} \cdot \mathbf{C})$ with $\mathbf{A} = \mathbf{C} = \hat{b}$, we obtain

$$0 = \hat{b} \times (\nabla \times \hat{b}) + (\hat{b} \cdot \nabla)\hat{b}$$

or

$$\hat{b} \times (\nabla \times \hat{b}) = -\kappa \ . \tag{4E.23}$$

We notice that since $\nabla\alpha$ and $\nabla\beta$ are perpendicular to $\hat{b}$ we only require the perpendicular component of $\nabla \times \hat{b}$ [from Eq. (4E.22)] in Eqs. (4E.18) and (4E.19). From Eq. (4E.23)

$$\hat{b} \times (\nabla \times \hat{b}) \times \hat{b} = (\nabla \times \hat{b})_{\perp} = -\kappa \times \hat{b} \ . \tag{4E.24}$$

Now,

$$\nabla S \times \hat{b} = \left(\frac{\partial S}{\partial \alpha}\nabla\alpha + \frac{\partial \hat{S}}{\partial \beta}\nabla\beta\right) \times \hat{b}$$

$$= -B\frac{\partial S}{\partial \alpha}\mathbf{U}_{\beta} + B\frac{\partial S}{\partial \beta}\mathbf{U}_{\alpha} \ , \tag{4E.25}$$

and

$$\nabla\alpha \cdot (\kappa \times \hat{b}) = \kappa \cdot (\hat{b} \times \nabla\alpha) = B\,\kappa \cdot \mathbf{U}_{\beta} \ , \tag{4E.26}$$

$$\nabla\beta \cdot (\kappa \times \hat{b}) = \kappa \cdot (\hat{b} \times \nabla\beta) = -B\,\kappa \cdot \mathbf{U}_{\alpha} \ . \tag{4E.27}$$

Combining Eqs. (4E.22) through (4E.27) yields

$$\nabla\beta \cdot (\nabla \times \mathbf{V}) = -B\left(\frac{\partial S}{\partial \alpha} - S\,\boldsymbol{\kappa} \cdot \mathbf{U}_\alpha\right), \tag{4E.28}$$

$$\nabla\alpha \cdot (\nabla \times \mathbf{V}) = B\left(\frac{\partial S}{\partial \beta} - S\,\boldsymbol{\kappa} \cdot \mathbf{U}_\beta\right). \tag{4E.29}$$

Inserting Eq. (4E.28) into (4E.18) and Eq. (4E.29) into (4E.19), we obtain

$$\frac{\partial}{\partial \alpha}\oint d\ell\, S = \oint d\ell\left(\frac{\partial S}{\partial \alpha} - S\,\boldsymbol{\kappa} \cdot \mathbf{U}_\alpha\right), \tag{4E.30}$$

$$\frac{\partial}{\partial \beta}\oint d\ell\, S = \oint d\ell\left(\frac{\partial S}{\partial \beta} - S\,\boldsymbol{\kappa} \cdot \mathbf{U}_\beta\right). \tag{4E.31}$$

Here we should remark that although Eqs. (4E.30) and (4E.31) are derived for closed-line integrals they apply to integrals where S vanishes at the end-points of integration (e.g., the longitudinal adiabatic invariant for trapped particles). The contour of integration and the surface integral must be altered somewhat in going from Eq. (4E.13) to (4E.14), but the short segments which connect the end points of integration contribute nothing since S vanishes there.

If we set $S = 1/B$, then

$$I = U \equiv \oint d\ell/B\,, \tag{4E.32}$$

and Eqs. (4E.30) and (4E.31) yield

$$\frac{\partial U}{\partial \alpha} = -\frac{d\ell}{B}\left(\frac{\partial\, \ell n\, B}{\partial \alpha} + \boldsymbol{\kappa} \cdot \mathbf{U}_\alpha\right), \tag{4E.33}$$

$$\frac{\partial U}{\partial \beta} = -\oint \frac{d\ell}{B}\left(\frac{\partial\, \ell n\, B}{\partial \beta} + \boldsymbol{\kappa} \cdot \mathbf{U}_\beta\right). \tag{4E.34}$$

We now apply the above to the terms involving $\nabla\, \ell n\, B + \boldsymbol{\kappa}$ appearing in Eq. (4.38):

$$Q \equiv \oint \frac{d\ell}{B^2} \left(\frac{\nabla p_j}{e_j} - E n_j \right) \cdot \left[\hat{b} \times (\nabla \ell n\, B + \kappa) \right] . \tag{4E.35}$$

Since

$$E = - \nabla \Phi = - \frac{\partial \Phi}{\partial \alpha} \nabla \alpha - \frac{\partial \Phi}{\partial \beta} \nabla \beta \tag{4E.36}$$

and

$$\nabla p_j = \frac{\partial p_j}{\partial \alpha} \nabla \alpha + \frac{\partial p_j}{\partial \beta} \nabla \beta ,$$

$$Q = \left(\frac{1}{e_j} \frac{\partial p_j}{\partial \alpha} + n_j \frac{\partial \Phi}{\partial \alpha} \right) \oint \frac{\delta \ell}{B^2} \nabla \alpha \cdot \left[\hat{b} \times (\nabla \ell n\, B + \kappa) \right]$$

$$+ \left(\frac{1}{e_j} \frac{\partial p_j}{\partial \beta} + n_j \frac{\partial \Phi}{\partial \beta} \right) \oint \frac{d\ell}{B^2} \nabla \beta \cdot \left[\hat{b} \times (\nabla \ell n\, B + \kappa) \right] . \tag{4E.37}$$

Now,

$$\nabla \alpha \cdot \left[\hat{b} \times (\nabla \ell n\, B + \kappa) \right] = (\nabla \alpha \times \hat{b}) \cdot (\nabla \ell n\, B + \kappa)$$

$$= - B U_\beta \cdot (\nabla \ell n\, B + \kappa) , \tag{4E.38}$$

$$\nabla \beta \cdot \left[\hat{b} \times (\nabla \ell n\, B + \kappa) \right] = (\nabla \beta \times \hat{b}) \cdot (\nabla \ell n\, B + \kappa)$$

$$= B U_\alpha \cdot (\nabla \ell n\, B + \kappa) , \tag{4E.39}$$

so that

$$\oint \frac{d\ell}{B^2} \nabla\alpha \cdot \left[\hat{b} \times (\nabla\, \ell n\, B + \kappa)\right]$$

$$= -\oint \frac{d\ell}{B} \left(\frac{\partial\, \ell n\, B}{\partial\beta} + \mathbf{U}_\beta \cdot \kappa\right)$$

$$= \frac{\partial}{\partial\beta} \oint \frac{d\ell}{B} = \frac{\partial U}{\partial\beta}\,, \tag{4E.40}$$

where we have used Eq. (4E.34). Similarly,

$$\oint \frac{d\ell}{B^2} \nabla\beta \cdot \left[\hat{b} \times (\nabla\, \ell n\, B + \kappa)\right] = -\frac{\partial}{\partial\alpha} \oint \frac{d\ell}{B} = -\frac{\partial U}{\partial\alpha}\,. \tag{4E.41}$$

Inserting Eqs. (4E.40) and (4E.41) into Eq. (4E.37), we find

$$Q = \left(\frac{1}{e_j} \frac{\partial p_j}{\partial\alpha} + n_j \frac{\partial\Phi}{\partial\alpha}\right) \frac{\partial U}{\partial\beta} - \left(\frac{1}{e_j} \frac{\partial p_j}{\partial\beta} + n_j \frac{\partial\Phi}{\partial\beta}\right) \frac{\partial U}{\partial\alpha}\,. \tag{4E.42}$$

We notice that Eq. (4E.42) looks something like a cross-product. Accordingly, we consider

$$\nabla\psi \times \nabla U = \left(\frac{\partial\psi}{\partial\alpha} \nabla\alpha + \frac{\partial\psi}{\partial\beta} \nabla\beta\right) \times \left(\frac{\partial U}{\partial\alpha} \nabla\alpha + \frac{\partial U}{\partial\beta} \nabla\beta\right), \tag{4E.43}$$

where ψ is a function of α and β only. Using Eq. (4E.1) we find that

$$\nabla\psi \times \nabla U = \mathbf{B} \left(\frac{\partial\psi}{\partial\alpha} \frac{\partial U}{\partial\beta} - \frac{\partial\psi}{\partial\beta} \frac{\partial U}{\partial\alpha}\right), \tag{4E.44}$$

so that

$$\frac{\partial\psi}{\partial\alpha} \frac{\partial U}{\partial\beta} - \frac{\partial\psi}{\partial\beta} \frac{\partial U}{\partial\alpha} = \frac{1}{B}\, \hat{b} \cdot (\nabla\psi \times \nabla U)\,. \tag{4E.45}$$

Setting $\psi = p_j$ and $\psi = \Phi$ in Eq. (4E.45) we find that

$$Q = \frac{1}{e_j B}\hat{b} \cdot (\nabla p_j \times \nabla U) + n_j \frac{\hat{b}}{B} \cdot (\nabla \Phi \times \nabla U)$$

or

$$Q = \nabla p_j \cdot \left(\frac{\nabla U \times \hat{b}}{e_j B}\right) + n_j \nabla U \cdot \frac{(\hat{b} \times \nabla \Phi)}{B} . \tag{4E.46}$$

Using $\mathbf{E} = -\nabla\Phi$ we finally obtain

$$Q = \nabla p_j \cdot \left(\frac{\nabla U \times \hat{b}}{e_j B}\right) + \left[\left(\frac{\mathbf{E} \times \mathbf{B}}{B^2}\right) \cdot \nabla U\right] n_j . \tag{4E.47}$$

The remaining integral in Eq. (4.38) is

$$L \equiv \oint \frac{d\ell}{B} \left(\frac{\mathbf{E} \times \mathbf{B}}{B^2}\right) \cdot \nabla n_j . \tag{4E.48}$$

Using Eq. (4E.36), this becomes

$$L = -\oint \frac{d\ell}{B} \left[\left(\frac{\partial \Phi}{\partial \alpha}\nabla\alpha + \frac{\partial \Phi}{\partial \beta}\nabla\beta\right) \times \mathbf{B}\right] \cdot \nabla n_j$$

$$= -\oint \frac{d\ell}{B} \left(-\frac{\partial \Phi}{\partial \alpha}\mathbf{U}_\beta + \frac{\partial \Phi}{\partial \beta}\mathbf{U}_\alpha\right) \cdot \left(\frac{\partial n_j}{\partial \alpha}\nabla\alpha + \frac{\partial n_j}{\partial \beta}\nabla\beta\right), \tag{4E.49}$$

$$L = -\oint \frac{d\ell}{B} \left(-\frac{\partial \Phi}{\partial \alpha}\frac{\partial n_j}{\partial \beta} + \frac{\partial \Phi}{\partial \beta}\frac{\partial n_j}{\partial \alpha}\right) . \tag{4E.50}$$

Since Φ and n_j are independent of ℓ, we may take these outside the integral and obtain

$$L = -\left(-\frac{\partial\Phi}{\partial\alpha}\frac{\partial n_j}{\partial\beta} + \frac{\partial\Phi}{\partial\beta}\frac{\partial n_j}{\partial\alpha}\right) U \ . \tag{4E.51}$$

In exactly the same way that we obtained Eq. (4E.45), we obtain

$$-\frac{\partial\Phi}{\partial\alpha}\frac{\partial n_j}{\partial\beta} + \frac{\partial\Phi}{\partial\beta}\frac{\partial n_j}{\partial\alpha} = -\frac{(\nabla\Phi \times \nabla n_j) \cdot \hat{b}}{B} \ . \tag{4E.52}$$

Using Eqs. (4E.36) and (4E.51) we obtain

$$L = \left[\left(\frac{E \times B}{B^2}\right) \cdot \nabla n_j\right] U \ . \tag{4E.53}$$

APPENDIX 4F

Here we develop a simple estimate of the maximum banana width based on the formalism employing Ω and V_y. We are particularly interested in considering the case where Ω passes through zero at some radius r_0. Thus, we write

$$r = r_0 + \Delta r \tag{4F.1}$$

and

$$\Omega = \Omega_0 + \Omega'(\Delta r) \ . \tag{4F.2}$$

The longitudinal adiabatic invariant J can be expressed in terms of Ω and v_y by

$$J \propto \hat{J} = \Omega_0(\Delta r) + \frac{1}{2}\Omega'(\Delta r)^2 + v_y \cos\theta \ , \tag{4F.3}$$

where we have assumed that $\Delta r/r_0 << 1$. One can verify that Eq. (4F.3) leads to the correct drift motion (and determine the constant of proportionality between J and $\hat{J}$) by inserting Eq. (4F.3) into

$$\langle \mathbf{V}_D \rangle = \frac{\nabla \hat{J} \times \hat{b}}{eB\tau} \tag{4F.4}$$

and taking $\hat{b}$ to be in the z-direction.

Since we are primarily interested in the case $\Omega \simeq 0$, we set Ω_0 to zero in Eq. (4F.3) and obtain the simple quadratic equation

$$\frac{1}{2}\Omega'(\Delta r)^2 + v_y \cos\theta - \hat{J} = 0 \tag{4F.5a}$$

with the solution

$$\Delta r = \pm\left[\frac{2(\hat{J} - v_y \cos\theta)}{\Omega'}\right]^{1/2} . \qquad (4F.5b)$$

We see that for $\hat{J} > v_y$ (with the convention that $\hat{J}$, v_y, and Ω' are positive) we can expand the dependence on cos θ and obtain

$$\Delta r \simeq \pm(2\hat{J}/\Omega')^{1/2}\left(1 - \frac{1}{2} v_y \cos\theta/\hat{J}\right) . \qquad (4F.6)$$

Both signs of Eq. (4F.6) lead to (approximate) shifted circles. The upper sign (larger $r = r_0 + \Delta r$) is shifted inward since the cos θ term is negative. The lower sign (smaller $r = r_0 + \Delta r$) is shifted outward since the cosine term is positive.

When $\hat{J} \leq v_y$ we see that only certain angles ($\cos\theta < \hat{J}/v_y$) are allowed. These orbits are crescent or banana shaped. The maximum banana (separatrix) occurs when $\hat{J} = v_y$ and the tips of the maximum size banana (x-point) occur at $\cos\theta = 1$. We can calculate the maximum banana width by setting $\hat{J} = v_y$ and $\cos\theta = -1$ in Eq. (4F.5b). We obtain

$$\Delta r = \pm 2(v_y/\Omega')^{1/2} . \qquad (4F.7)$$

Thus, the maximum distance from one leg of the banana- or crescent-shaped orbit to the other leg is

$$2|\Delta r| = 4(v_y/\Omega')^{1/2} . \qquad (4F.8)$$

REFERENCES

1. L. W. Owen and D. K. Lee, "ELMO Bumpy Square," presented at the 1983 Sherwood Theory Meeting, Annual Controlled Fusion Theory Conference, Arlington, Va., March 21-23, 1983.

2. D. Lortz, "The Existence of Toroidal Magnetohydrostatic Equilibrium Without Rotation Transformation," Z. Angew. Math. Phys. 21, 196 (1970).

3. H. Grad, "Plasma Containment in Closed Line Systems," in Proceedings of the 4th International Conference on Plasma Physics and Nuclear Fusion Research, vol. 3, Madison, Wisconsin, June 17-23, 1971, p. 229.

4. C. L. Hedrick, G. E. Guest, and D. B. Nelson, Some Techniques for Determining Tensor Pressure Equilibria, ORNL/TM-4076, Oak Ridge Natl. Lab., 1973.

5. L. S. Hall and B. McNamara, "Three-Dimensional Equilibrium of the Anisotropic, Finite-Pressure Guiding Center Plasma: Theory of the Magnetic Plasma," Phys. Fluids 18, 552 (1975).

6. L. W. Owen and C. L. Hedrick, "Tensor Pressure, 3D Equilibria for EBT," Bull. Am. Phys. Soc. 20, 1351 (1975).

7. G. Gibson, W. C. Jordan, E. J. Laner, and C. H. Woods, "Guiding Center Motion and Plasma Behavior in the Bumpy Torus," Phys. Fluids 7, 548-56 (1964).

8. R. D. Hazeltine, "Recursive Derivation of Drift Kinetic Equation," Plasma Phys. 15, 77-80 (1973).

9. T. G. Northrup and E. Teller, "Stability of Adiabatic Motion of Charged Particles in the Earth's Field," Phys. Rev. 117, 215-25 (1960).

10. D. A. Spong and C. L. Hedrick, "Variational Corrections to ELMO Bumpy Torus Neoclassical Ion Plateau Transport," Phys. Fluids 23, 1903 (1980).

11. D. E. Hastings and D. A. Spong, "Nonresonant Electron Transport in the ELMO Bumpy Torus Experiment Using a BKG Operator," Phys. Fluids 26, 1551 (1983).

12. L. W. Owen, "3-D MHD Tensor Pressure Equilibria for EBT," in U.S.-JAPAN Theory Workshop on 3-D MHD Studies for Toroidal Devices, CONF-8110101, Oak Ridge Natl. Lab., 1981.

13. D. B. Nelson and C. L. Hedrick, "Macroscopic Stability and Beta Limit in the ELMO Bumpy Torus," Nucl. Fusion 19, 283 (1979).

14. H. Grad, Courant Institute, personal communication, 1983 and 1984.

15. B. McNamara, Lawrence Livermore National Laboratory, personal communication, 1984.

5. STABILITY OF THE ELMO BUMPY SQUARE

D. A. Spong

The ELMO Bumpy Square (EBS) will offer an interesting and flexible test bed for the stabilization of a connected core plasma in a closed-field-line geometry using energetic hot electron rings. The basic rationale behind the EBS device is that locating all the toroidal curvature in the corner sections where the magnetic field is highest significantly reduces neoclassical transport and improves the overall plasma centering. Bumps in the side sections are necessary to provide an azimuthal particle precession, which is essential for confinement. The average unfavorable curvature introduced by the bumps is counteracted by the diamagnetic well dug by the localized hot electron rings (which act as an uncoupled species provided core beta, β_c, is not too large and the hot electron energy is sufficiently high). Analogous hot species stabilization schemes have been proposed in recent years for tokamaks,[1] helical axis stellarators,[2] and tandem mirrors.[3] Because certain of the characteristic instability modes reappear among these different confinement geometries and the theoretical analysis methods are common, research into hot electron stabilization on the EBS can be of significant benefit to the remainder of the fusion community. In addition, hot particle instabilities have some parallels to modes observed in tokamaks[4] with neutral injection and modes predicted in future tokamaks[5] where alpha particles will be present. By forming hot electron rings in the straight axisymmetric bumpy sections, the EBS will ensure the greatest possible control and diagnoses of hot electron ring parameters of any device where hot electron stabilization has been considered. In addition, more efficient ring production is possible in this device than in other geometries, ensuring the production of deep diamagnetic wells - a condition which may be somewhat marginal in ELMO Bumpy Torus-Scale (EBT-S).

The EBS does, however, allow the possibility of several new types of instabilities that would not be present to the same extent in the EBT-S, since the toroidal curvature is being concentrated in the corners instead of evenly distributed around the torus. A preliminary examination has been made of some of the possible modes, and none of them at this time appear to be overly limiting, although more detailed quantitative work needs to be done and is presently under way. If one considers simple interchange modes, which are constant along a field

line, they are driven only by field-line- averaged unfavorable curvature and thus should be roughly the same in the square as in the torus. Actually, they will be slightly less limiting in the square because part of the bad curvature is localized in regions of higher magnetic field than in the torus. The modes that one would clearly expect to be different in the square are those that balloon somewhat in the corners. An analysis of these modes has recently been made[6] using the ideal MHD variational principle and the generalized kinetic energy principle,[7,8] where the sides and corners have been characterized by piecewise constant equilibrium properties.

This analysis[6,9] has indicated that the dominant effect determining the β_c limit is still the ring-core interaction in the sides and not ballooning in the corner sections. Such a result can be understood by noting that the curvature in the corners is a factor of 2 weaker than that in the bad curvature sections of the sides, and the magnetic field is typically a factor of 4 higher in the corners. Because it will be possible experimentally to vary the magnetic field of the corners, one can check if the bad curvature regions in the corners begin to be important below some critical global mirror ratio ($M_G = B_{corner}/B_{midplane}$). The dependence of calculated stability boundaries on ring beta $\tilde{\beta}_H$ and M_G using the generalized kinetic energy principle is plotted in Fig. 5.1. Here both $\tilde{\beta}_c$ and $\tilde{\beta}_H$ are normalized betas (normalized to $\beta_{LVDN} = 2\Delta/R_c$). As may be seen, there is a lower stability boundary that corresponds to diamagnetic well stabilization (modified here by finite β_c) and an upper boundary that is analogous to the β_c limit of Van Dam-Lee[10] and Nelson.[11] This upper limit drops with increasing β_H as was the case in the earlier work[10,11] [$\beta_c < (2\Delta/R_c)(1 + \beta_H)^{-1}$] due to the destabilizing effect of the ring pressure gradient on modes that have some degree of ballooning. As Fig. 5.1 shows, the stability boundaries do not significantly degrade until $M_G = 2$ (this is probably a lower limit on the global mirror ratio that could be tried experimentally). At typical mirror ratios of $M_G = 4$, there is no substantial difference from $M_G = \infty$ (which corresponds to a bumpy cylinder). This analysis[9] using the generalized kinetic energy principle is based on a number of approximations: for example, piecewise constant parameters for the sides and corners are used, large radial and azimuthal mode numbers are assumed, no hot electron FLR effects are considered, core plasma compressibility is neglected, N_{Hot} effects are neglected, and low-frequency ($\omega \ll \omega_{d,Hot}$ or ω_{ci}) modes are considered. Some of these, such as keeping the

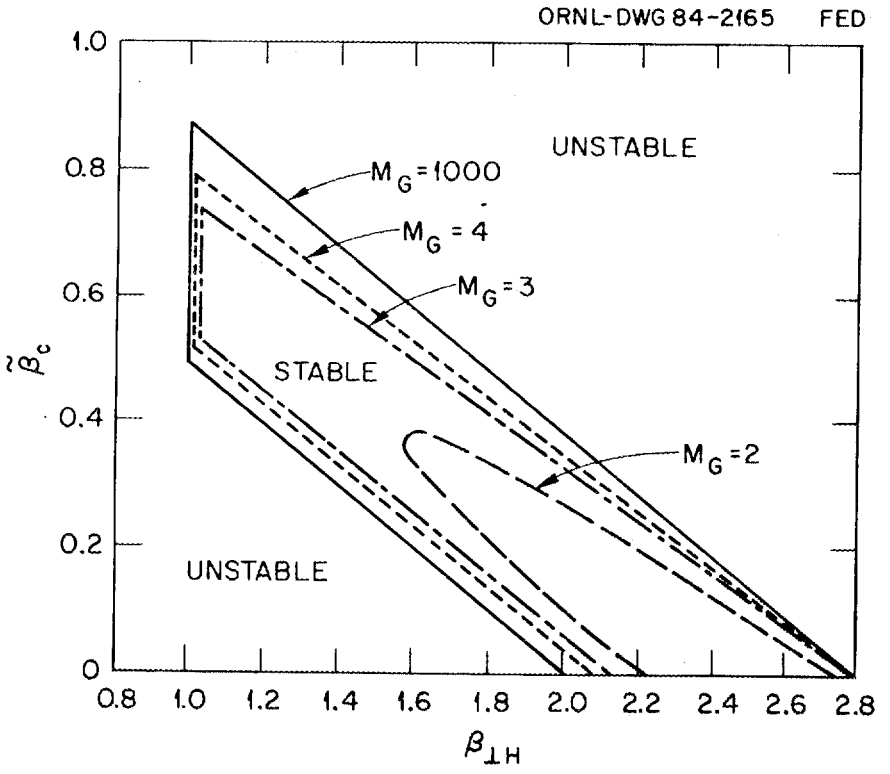

Fig. 5.1. Stability boundaries in the ELMO Bumpy Square vs $\tilde{\beta}_{\perp H}$ and for several values of M_G (= $B_{corner}/B_{midplane}$).

detailed dependences of parameters along the field lines in the side sections, can be improved by further calculations, and work is presently under way in this area.

In addition to the ideal MHD modes, resistive modes can also be present in the bad curvature regions of the corners. It is often possible for such modes to still be unstable when the ideal modes are stable. However, such modes are present in almost all plasma confinement devices, and the effective bad curvature seen by a resistive mode localized in the corner of an EBS is not significantly worse than that seen by equivalent resistive modes present in small tokamaks. Although the tokamak does have shear, which helps to stabilize these modes, the bumpy square has a low density in the corner and good coupling to the sides. Resistive modes typically grow on a much slower timescale than ideal modes, and, as a result, their nonlinear effects are of more importance in determining their consequences than for the ideal MHD instabilities. The analysis and classification of resistive modes in an EBS will require a sustained effort, and it is probably not possible to say anything definitive about them in the near term.

Several instability modes under study in tandem mirror systems have been discussed as possible candidates in EBS systems. These are the passing particle interchange mode,[12,13] the shear Alfvén wave — hot electron precessional drift mode,[14] and possibly the Alfvén ion cyclotron mode.[15,16] The passing particle interchange[12,13] is an electrostatic drift wave (potential, ϕ, varies along the field line), which is localized in, and feeds off, bad curvature regions. In the tandem such a mode is possible due to the very weak coupling between the central cell and end plug regions. In the EBS the coupling between a side and corner is expected to be much stronger due to the good field line connection and the fact that the equilibrium ambipolar potential is not being forced to vary strongly along a field line, as it is in the tandem. The shear Alfvén wave coupled to hot electron drift[11] is not expected to be a significant problem in an EBS because the hot electron drift frequency is above the ion cyclotron frequency and the shear Alfvén wave cannot propagate in this frequency range. Such a mode can exist in a larger size EBS device, where $\omega_{d,Hot}$ is less than ω_{ci}, and warrants further study. The approximate stability criterion is given[14] as

$$\frac{2\pi V_A}{L_c} > \ell\omega_{KH} \quad \text{or} \quad n_i < \frac{2\pi B^2}{m_i \mu_o \ell \omega_{KH}} ,$$

where

V_A = Alfvén velocity ,

ω_{KH} = hot electron curvature drift frequency ,

ℓ = azimuthal mode number ,

L_c = toroidal circumference .

One aspect of the square that may make it more resilient than a conventional bumpy torus against such modes is the fact that they must propagate through the high magnetic field corners. As can be seen from the above inequality, the high-B field raises the critical ion density and helps extinguish the instability. The ion cyclotron[15,16] mode is driven by ion anisotropy and has been of interest in the tandem mirrors due to the presence of sloshing ion distributions, perpendicular neutral injection, and loss cones. Such modes are no more likely to be prevalent in EBS than in EBT-S (where there is no strong evidence of them) and may be even less prevalent due to the smaller fraction of the distribution affected by loss cones in EBS. They may be of interest, though, with respect to certain configurations of ion cyclotron heating.

In addition to the above questions concerning new modes that can be present in the EBS, it is also of interest to consider modifications of modes that are thought to determine the operating window in EBT-S. These are the hot electron interchange mode and the stabilization of low-frequency, low-β_c flute modes. Both calculations and experiments are under way to further understand these effects; the T-M transition has been correlated with the appearance of the hot electron interchange,[17] but its cause has not been definitively linked to this instability. The C-T transition is thought to be caused by some combination of ring effects (well stabilization and/or charge uncovering effects) and possibly core profile effects (compressibility, hollow temperature profiles). One might expect that for similar values

of magnetic field and field line curvature as EBT-S, these operational modes should be the same as in the present experiment. The EBS will be similar in these respects for the side sections, and the the mode transitions should occur at roughly the same values of β_{Hot} and n_{Hot}/n_{core} as in EBT-S. One significant difference will be that the maximum attainable value of β_{Hot} will be higher due to the more efficient production of rings in the straight axisymmetric sections. On the one hand, this will help ensure the diamagnetic well stabilization of the core plasma, but it could also lead to a T-M transition at higher pressures than in EBT-S if the core density does not rise in proportion to n_{Hot}. However, since the core confinement is improved in EBS, it is expected that n_{core} should be larger, resulting in values of n_{Hot}/n_{core}, which will not induce the hot electron interchange mode except at very low pressures.

REFERENCES

1. M. N. Rosenbluth, S. T. Tsai, J. W. Van Dam, M. G. Engquist, "Energetic Particle Stabilization of Ballooning Modes in Tokamaks," Phys. Rev. Lett. 51, 1967 (1983).

2. A. Boozer, "The ELMO Snakey Torus," in Advanced Bumpy Torus Concepts: Proceedings of the Workshop, CONF-830758, Oak Ridge Natl. Lab., 1983, p. 161.

3. J. Kesner et al., "Tandem Mirror Hot Electron Anchor," Nucl. Fusion 22, 577 (1982).

4. K. McGuire et al., "Study of High-Beta Magnetohydrodynamic Modes and Fast-Ion Losses in PDX," Phys. Rev. Lett. 50, 891 (1983).

5. K. T. Tsang et al., "Destabilization of Low Mode Number Alfvén Modes in a Tokamak by Energetic or Alpha Particles," Phys. Fluids 24, 1508 (1981).

6. C. L. Hedrick, "Comparison of Magnetic Equilibria and Low Frequency Stability for EBT and EBS," in Advanced Bumpy Torus Concepts: Proceedings of the Workshop, CONF-830758, Oak Ridge Natl. Lab., 1983, p. 217.

7. J. W. Van Dam et al., "A Generalized Kinetic Energy Principle," Phys. Fluids 25, 1349 (1982).

8. T. M. Antonsen et al., "Electrostatic Modification of Variational Principles for Anisotropic Plasmas," Phys. Fluids 25, 132 (1982).

9. D. A. Spong, "Ballooning Modes in the ELMO Bumpy Square Configuration Using the Generalized Kinetic Energy Principle," Sect. 7 of this report.

10. J. W. Van Dam and Y. C. Lee, "Stability Analysis of a Hot Electron EBT Plasma," in EBT Ring Physics: Proceedings of the Workshop, CONF-791228, Oak Ridge Natl. Lab., 1979, p. 471.

11. D. B. Nelson, "Effects of Hot Electrons on Magnetohydrodynamic Modes in ELMO Bumpy Torus," Phys. Fluids 23, 1950 (1980).

12. M. N. Rosenbluth et al., Fast Growing Trapped-Particle Modes in Tandem Mirrors, DOE/ET/53088-59, Institute for Fusion Studies, University of Texas, Austin, June 1982.

13. M. N. Rosenbluth et al., Topics in Plasma Instabilities: Trapped-Particle Modes and MHD, DOE/ET/53088-62, Institute for Fusion Studies, University of Texas, Austin, June 1982.

14. D. E. Baldwin and H. L. Berk, "Destabilization of the Hot Electron Precessional Mode in Tandem Mirrors and Bumpy Tori," Phys. Fluids 26, 3595 (1983).

15. R. C. Davidson et al., "Electromagnetic Ion Cyclotron Instability Driven by Ion Energy Anisotropy in High-Beta Plasmas," Phys. Fluids 18, 1045 (1975).

16. D. C. Watson, "Alfvén-Ion-Cyclotron Instability in Mirror Machines," Phys. Fluids 23, 2485 (1980).

17. S. Hiroe et al., Observations of Hot Electron Ring Instabilities in ELMO Bumpy Torus, ORNL/TM-8874, Oak Ridge Natl. Lab., 1983.

6. MHD BALLOONING MODES IN THE ELMO BUMPY TORUS

C. L. Hedrick

The MHD stability properties of the square configuration are analyzed here. In particular, limitations on core plasma beta due to ballooning modes are developed. The restrictions on core plasma beta are found to be comparable to those of the Lee-Van Dam-Nelson limit.

6.1 INTRODUCTION

Here we compare the MHD stability of the square configuration of ELMO Bumpy Torus (EBT) with the existing circular configuration. The most obvious difference between the two configurations is that all the toroidal curvature is localized in the "corners" of the square configuration, whereas in the circular configuration the toroidal curvature is, to lowest order, uniformly distributed. Whether the toroidal curvature is localized or uniformly distributed should have little effect on the stability properties of pure flute modes. However, ballooning modes should have a tendency to concentrate in the corners — especially along the outer field lines where the curvature and pressure gradients promote instability.

To make the problem tractable, we will make the assumption of localizability so that we can neglect radial and azimuthal couplings. (This assumption should be pessimistic insofar as stability is concerned since these couplings tend to be stabilizing.) We will use an energy principle to develop the stability criteria. Again, in the interest of simplicity, we confine ourselves to the so-called universal term and neglect the effects of compressibility, etc., of the so-called kinetic term. In particular, for these initial calculations, we confine ourselves to the so-called rigid ring model.

In Sect. 6.2, approximations based on the energy principle are developed. In Sect. 6.3, flute modes are analyzed for the square configuration of EBT since this information is useful in analyzing ballooning modes. In Sect. 6.4, a number of analytic estimates are developed for the various scale factors (magnetic field, curvature, etc.) appearing in the energy principle. A knowledge of the relative size of quantities in the sides and corners of the square configuration facilitates further approximations made in the analysis of the Euler equation developed in Sect. 6.5.

The stability criterion developed in Sect. 6.5 is reduced to a limitation on core beta in Sect. 6.6. This limitation is found to be no more restrictive than that of Lee-Van Dam-Nelson, provided the hot electron rings do not dig too deep a magnetic well.

6.2 A PESSIMISTIC ENERGY PRINCIPLE

From Nelson and Hedrick[1] we find that the energy principle can be written in the form

$$\delta W = \delta W_u + \delta W_k \ , \tag{6.1}$$

where the universal term is given by

$$\delta W_u = \frac{1}{2} \int d^3x \left[Q^2 + \left(\nabla \times \mathbf{B} - \mathbf{j}_e \right) \times \xi \cdot \mathbf{Q} + \xi \cdot \nabla p (\nabla \cdot \xi) \right] \ , \tag{6.2}$$

and, in the scalar pressure (MHD) limit, the kinetic term is given by

$$\delta W_k = \frac{1}{2} \int d^3x \left[\gamma p (\nabla \cdot \xi)^2 \right] \ . \tag{6.3}$$

Here $\mathbf{Q}$ is the perturbed magnetic field and ξ is the displacement. Except for the current produced by the hot electron rings, $\mathbf{j}_e$, the form of Eq. (6.2) is that of the more familiar single fluid. The fluid in this case is the core plasma characterized by the scalar pressure p.

It is convenient to write Eq. (6.2) in the form

$$\delta W_u = \frac{1}{2} \int d^3x (Q^2 + L) \ , \tag{6.4}$$

where

$$L \equiv \left(\nabla \times \mathbf{B} - \mathbf{j}_e \right) \times \xi \cdot \mathbf{Q} + \xi \cdot \nabla p (\nabla \cdot \xi) \ . \tag{6.5}$$

Using the equilibrium relation

$$\nabla \times \mathbf{B} = \mathbf{j}_e + \mathbf{j}_{core} \tag{6.6}$$

and

$$\nabla \cdot \xi = -\left[\frac{Q_{\parallel}}{B} + \xi \cdot (\kappa + \nabla \ell n\, B) \right] , \tag{6.7}$$

L can be rewritten in the form

$$L = j_{\parallel} \hat{b} \cdot (\xi \times Q) - \xi \cdot \nabla p \left[2 \frac{Q_{\parallel}}{B} + \xi \cdot (\kappa + \nabla \ell n\, B) \right] . \tag{6.8}$$

To make further progress in analyzing L, we introduce α,β coordinates through the Clebsch representation of the magnetic field:

$$\mathbf{B} = \nabla\alpha \times \nabla\beta . \tag{6.9}$$

It is convenient to define

$$\mathbf{V}_\alpha = \nabla\beta \times \mathbf{B}/B^2 \; ; \; \mathbf{V}_\beta = -\nabla\alpha \times \mathbf{B}/B^2 , \tag{6.10}$$

since these vectors have the properties that

$$\begin{aligned} &\mathbf{V}_\alpha \cdot \nabla\alpha = 1 \; ; \; \mathbf{V}_\alpha \cdot \nabla\beta = 0 , \\ &\mathbf{V}_\beta \cdot \nabla\alpha = 0 \; ; \; \mathbf{V}_\beta \cdot \nabla\beta = 1 , \end{aligned} \tag{6.11}$$

and

$$\mathbf{V}_\alpha \times \mathbf{B} = -\nabla\beta \; ; \quad \mathbf{V}_\beta \times \mathbf{B} = \nabla\alpha \; . \tag{6.12}$$

The displacement is then conveniently written as

$$\xi = X\,\mathbf{V}_\alpha + Y\,\mathbf{V}_\beta \; , \tag{6.13}$$

where

$$X = \nabla\alpha \cdot \xi \; ; \quad Y = \nabla\beta \cdot \xi \; . \tag{6.14}$$

Utilizing

$$\mathbf{Q} = \nabla \times (\xi \times \mathbf{B}) \; , \tag{6.15}$$

one finds that

$$\frac{Q_{\parallel}}{B} = \frac{\partial X}{\partial \alpha} + \frac{\partial Y}{\partial \beta} \; , \tag{6.16}$$

$$\frac{\mathbf{Q}_{\perp}}{B} = -\left(\frac{\partial X}{\partial \ell}\mathbf{V}_\alpha + \frac{\partial Y}{\partial \ell}\mathbf{V}_\beta \right) . \tag{6.17}$$

We now choose α such that

$$\nabla p = \frac{\partial p}{\partial \alpha}\nabla\alpha \; ; \tag{6.18}$$

α has the interpretation that it is the magnetic flux (modulo 2π) contained with the pressure surface and β is an angular-like coordinate.

By use of Eqs. (6.11) and (6.13), we see that the choice of α given by Eq. (6.18) yields

$$\xi \cdot \nabla p = X \frac{\partial p}{\partial \alpha} . \tag{6.19}$$

If we write κ and $\nabla_\perp \ell n\ B$ in component form,

$$\kappa = \kappa_\alpha \nabla\alpha + \kappa_\beta \nabla\beta , \tag{6.20}$$

$$\nabla_\perp \ell n\ B = \frac{\partial\ \ell n\ B}{\partial\alpha} \nabla\alpha + \frac{\partial\ \ell n\ B}{\partial\beta} \nabla\beta , \tag{6.21}$$

we can utilize Eq. (6.8) to write the integral of δW_u in the form

$$Q^2 + L = Q_\perp^2 - X^2 \frac{\partial p}{\partial \alpha} \left(\frac{1}{B^2} \frac{\partial p}{\partial \alpha} + \kappa_\alpha + \frac{\partial\ \ell n\ B}{\partial \alpha} \right)$$

$$+ \left[j_\parallel\ \hat{b} \cdot (\xi \times Q) + \left(Q_\parallel - \frac{1}{B} \frac{\partial p}{\partial \alpha} X \right)^2 \right.$$

$$\left. - X\ Y \frac{\partial p}{\partial \alpha} \left(\kappa_\beta + \frac{\partial\ \ell n\ B}{\partial \beta} \right) \right] , \tag{6.22}$$

where

$$Q_\perp^2 = B^2 \left| \frac{\partial X}{\partial \ell} \mathbf{v}_\alpha + \frac{\partial Y}{\partial \beta} \mathbf{v}_\beta \right|^2 , \tag{6.23}$$

and we note that in α,β coordinates $d^3x = d\alpha\ d\beta\ d\ell/B$ so that

$$\delta W_u = \int \frac{d\alpha\ d\beta\ d\ell}{B} \left(Q^2 + L \right) . \tag{6.24}$$

Since we expect that the drive for instability in the corners of the square configuration of EBT will be strongest on the outer field lines that lie in the equatorial plane, we now confine our attention to that plane. The up-down symmetry of the equatorial plane implies that

$$j_{\parallel} = \kappa_{\beta} = \frac{\partial \ell n\, B}{\partial \beta} = 0 \ . \tag{6.25}$$

It is also the case that in the equatorial plane $\nabla\alpha \cdot \nabla\beta = 0$ and

$$\mathbf{v}_{\alpha} \cdot \mathbf{v}_{\beta} = 0 \ . \tag{6.26}$$

Utilizing Eqs. (6.23), (6.25), and (6.26), we find that Eq. (6.22) reduces to

$$\begin{aligned} Q^2 + L = B^2 & \left[\left(\frac{\partial \chi}{\partial \ell} \right)^2 |\mathbf{v}_{\alpha}|^2 + \left(\frac{\partial \gamma}{\partial \ell} \right)^2 |\mathbf{v}_{\beta}|^2 \right] \\ & - \chi^2 \frac{\partial p}{\partial \alpha} \left(\frac{1}{B^2} \frac{\partial p}{\partial \alpha} + \kappa_{\alpha} + \frac{\partial \ell n\, B}{\partial \alpha} \right) \\ & + \left(Q_{\parallel} - \frac{1}{B} \frac{\partial p}{\partial \alpha} \chi \right)^2 \ . \end{aligned} \tag{6.27}$$

We now note that if we neglect two positive (stabilizing) terms then the expression for $Q^2 + L$ simplifies considerably. That is,

$$Q^2 + L \geq |\nabla\beta|^2 \left(\frac{\partial \chi}{\partial \ell} \right)^2 + D\chi^2 \ , \tag{6.28}$$

where

$$D = - \frac{\partial p}{\partial \alpha} \left(\frac{1}{B^2} \frac{\partial p}{\partial \alpha} + \kappa_{\alpha} + \frac{\partial \ell n\, B}{\partial \alpha} \right) , \tag{6.29}$$

and we have noted that $\nabla\alpha$, $\nabla\beta$, and $\mathbf{B}$ are mutually orthogonal in the equatorial plane so that Eq. (6.10) yields $B^2|\nabla_\alpha|^2 = |\nabla\beta|^2$.

The form of D given in Eq. (6.29) is useful for estimating flute-like perturbations ($\partial X/\partial \ell = 0$). For $\partial X/\partial \ell \neq 0$, an alternative expression for D is also useful. The development of the alternative expression begins with the vector identity

$$\frac{1}{2}\nabla_\perp \ell n\, B = \boldsymbol{\kappa} + \mathbf{B} \times (\nabla \times \mathbf{B})/B^2 \ . \tag{6.30}$$

If we utilize Eq. (6.6) and

$$\mathbf{j}_{core} \times \mathbf{B} = \nabla p = \nabla\alpha \frac{\partial p}{\partial \alpha} \ , \tag{6.31}$$

we find that in the equatorial plane

$$\frac{\partial\, \ell n\, B}{\partial \alpha} = \kappa_\alpha - \frac{1}{B^2}\frac{\partial p}{\partial \alpha} - \frac{\mathbf{j}_e \cdot \nabla\beta}{B^2} \ , \tag{6.32}$$

so that Eq. (6.29) becomes

$$D = -\frac{\partial p}{\partial \alpha}\left(2\kappa_\alpha - \frac{1}{B^2}\mathbf{j}_e \cdot \nabla\beta\right) . \tag{6.33}$$

In what follows it will be convenient to focus on the part of our underestimate of the integrand of δW, which is integrated along a field line:

$$\delta W_E \equiv \int \frac{d\ell}{B}\left[|\nabla\beta|^2\left(\frac{\partial X}{\partial \ell}\right)^2 + DX^2\right] . \tag{6.34}$$

6.3 FLUTE MODES

It will prove useful in analyzing ballooning modes to have first analyzed the case of pure flutes. Thus, suppose that X is constant along a field line so that Eq. (6.34) reduces to

$$\delta W_E = X^2 \int \frac{d\ell}{B} D \ . \tag{6.35}$$

We now express the integrand in terms of the gradients of

$$V \equiv \oint \frac{d\ell}{B} \ . \tag{6.36}$$

To do this we make use of the fact that if $I \equiv \oint d\ell \ S$, then

$$\frac{\partial I}{\partial \alpha} = \oint d\ell \left(\frac{\partial S}{\partial \alpha} - S \, U_\alpha \cdot \kappa \right) , \tag{6.37}$$

$$\frac{\partial I}{\partial \beta} = \oint d\ell \left(\frac{\partial S}{\partial \beta} - S \, U_\alpha \cdot \kappa \right) . \tag{6.38}$$

(This relation is valid for closed-field-line systems and for cases where S vanishes at the limits of integration, such as that encountered in a mirror-confined population of particles.)

Setting $S = 1/B$ in Eq. (6.37), we obtain

$$\frac{\partial U}{\partial \alpha} = - \int \frac{d\ell}{B} \left(\frac{\partial \ \ell n \ B}{\partial \alpha} + \kappa_\alpha \right) . \tag{6.39}$$

Comparing Eq. (6.39) to Eq. (6.29) and noting that $\partial p/\partial \alpha$ = constant along a field line (since $\nabla p = \nabla \alpha \ \partial p/\partial \alpha = j_{core} \times B$), we find that

$$\delta W_E = X^2 \frac{\partial p}{\partial \alpha} \left(\frac{\partial U}{\partial \alpha} - \frac{\partial}{\partial \alpha} \int \frac{d\ell}{B^3} \right) . \tag{6.40}$$

This leads to the condition for stability

$$\frac{\partial p}{\partial \alpha}\left(\frac{\partial U}{\partial \alpha} - \frac{\partial p}{\partial \alpha}\int \frac{d\ell}{B^3}\right) > 0 \ . \tag{6.41}$$

Because we have neglected the kinetic term that involves the compressibility γ, we have not recovered the oft-quoted result:

$$\left(\frac{\partial p}{\partial \alpha} + \gamma p \frac{1}{U}\frac{\partial U}{\partial \alpha}\right)\left(\frac{\partial U}{\partial \alpha} - \frac{\partial p}{\partial \alpha}\int \frac{d\ell}{B^3}\right) > 0 \ . \tag{6.42}$$

6.4 ESTIMATE OF GEOMETRICAL FACTORS

We now make some estimates of the quantities κ_α/B and $|\nabla\beta|^2/B$, which appear in the integrand of our underestimate for δW. We are particularly interested in comparing characteristic values in the sides of the square EBT configuration with the values in the corners. Following the conventions for the circular EBT configuration, we characterize the behavior in the sides of the square configuration by midplane values.

To lowest order in one of the mirror cells that constitute a side,

$$\alpha = \psi = \int_0^r r'\, dr'\, B(r',z) \ , \tag{6.43}$$

$$\beta = 0 \ , \tag{6.44}$$

and

$$\nabla\beta = \frac{1}{r}\hat{e}_\theta \ . \tag{6.45}$$

The quantity $|\nabla\beta|^2/B$ then is given approximately by

$$\frac{|\nabla\beta|^1}{B} = \frac{1}{r^2 B} \ . \tag{6.46}$$

Now, in the paraxial approximation [e.g., $B \simeq B_0(1 - \delta \cos kz)$],

$$\psi \simeq \frac{1}{2} B_0(1 - \delta \cos kz) r^2 \ ,$$

so that

$$\psi \simeq \frac{1}{2} r^2 B \ , \tag{6.47}$$

and we see that in the sides

$$\frac{|\nabla\beta|^2}{B} \simeq \frac{2}{\psi} \ . \tag{6.48}$$

Since ψ is constant along a field line, we see that $|\nabla\beta|^2/B$ is constant along a field line in the sides of the square.

To obtain the behavior of $|\nabla\beta|^2/B$ in the corners, we now suppose that the transition between side and corner occurs in the side. (This is possible though not necessary. Indeed it may be more desirable to have at least some of the transition occur in the corner. Nevertheless, our assumption facilitates the analytic approach used here, and any deviation from this assumption should have little effect on the results obtained here.) With this assumption, the field lines in the corners are segments of perfect circles. Consequently, the magnitudes of $\Delta\alpha$ and $\Delta\beta$ will remain unchanged as one traverses a corner since the distance between field lines (labeled by α and β) remains unchanged. Consequently,

$$\frac{|\nabla\beta|^2}{B} \simeq \text{constant along a field line} \ , \tag{6.49}$$

both in the sides and in the corners.

To calculate κ_α, we use Eqs. (6.20) and (6.11) to obtain

$$\kappa_\alpha = U_\alpha \cdot \boldsymbol{\kappa} \ . \tag{6.50}$$

In the equatorial plane, where $\nabla\alpha$ and $\nabla\beta$ are orthogonal,

$$U_\alpha = \frac{1}{B} |\nabla\beta| \frac{\nabla\alpha}{|\nabla\alpha|} \ . \tag{6.51}$$

In the sides where $\alpha \simeq \psi$

$$U_\alpha \simeq \frac{1}{rB} \frac{\nabla\psi}{|\nabla\psi|} \ . \tag{6.52}$$

In a midplane of a mirror cell in a side, the curvature is roughly given by

$$\boldsymbol{\kappa} = \frac{\hat{e}_r}{R_{coil}} \ , \tag{6.53}$$

where R_{coil} is a coil radius. In a midplane, it is also the case that $\nabla\psi = |\nabla\psi|\hat{e}_r$, so that a characteristic value of κ_α in a side is given by

$$\kappa_\alpha|_{midplane} = \left(\frac{1}{rB} \frac{1}{R_{coil}}\right)_{midplane} \ . \tag{6.54}$$

In a corner the magnitude of the curvature is simply the reciprocal of the radius of toroidal solenoid segmented to form the corner:

$$|\boldsymbol{\kappa}| = \frac{1}{R_{toroidal}} \simeq \frac{1}{2R_{coil}} \ , \tag{6.55}$$

where we have noted that in designing a square one tries to minimize the volume of the corners by using the minimum toroidal radius consistent with the placement of finite-size coils. To obtain the magnitude of κ_α, we note that in the equatorial plane $\boldsymbol{\kappa}$ and $\mathbf{U}_\alpha$ are in the same direction and that the magnitude of $\mathbf{U}_\alpha$ is obtained from Eqs. (6.51) and (6.49):

$$|U_\alpha|_{corner} = \frac{|\nabla\beta|}{B}\bigg|_{corner} = \frac{|\nabla B|}{B}\bigg|_{midplane} \left(\frac{B_{midplane}}{B_{side}}\right)^{1/2} .$$

Defining a global mirror ratio by

$$M_G = \frac{B_{corner}}{B_{midplane}} , \tag{6.56}$$

we have

$$|U_\alpha|_{corner} = \frac{1}{M_G^{1/2}} \left(\frac{|\nabla B|}{B}\right)\bigg|_{midplane} \tag{6.57}$$

$$= \frac{1}{M_G^{1/2}} \left(\frac{1}{rB}\right)_{midplane} .$$

Combining Eqs. (6.55) and (6.57) we obtain

$$\kappa_\alpha|_{corner} = \frac{1}{M_G^{1/2}} \frac{1}{2R_{coil}} \left(\frac{1}{rB}\right)_{midplane} . \tag{6.58}$$

Comparing Eqs. (6.44) and (6.48) we see that

$$\frac{\kappa_{\alpha,corner}}{\kappa_{\alpha,midplane}} = \frac{1}{2M_G^{1/2}} . \tag{6.59}$$

We also see that the quantity occurring in the integral of δW scales as

$$\frac{(\kappa_\alpha/B)_{corner}}{(\kappa_\alpha/B)_{midplane}} = \frac{1}{2M_G^{3/2}} . \tag{6.60}$$

6.5 BALLOONING MODE ANALYSIS

To treat nonconstant X we introduce an eigenvalue Λ (proportional to ω^2) so that we can write an approximate energy principle in the form

$$\Lambda \oint d\ell\, X^2 = \delta W_E = \oint \frac{d\ell}{B} \left[|\nabla\beta|^2 \left(\frac{\partial X}{\partial \ell}\right)^2 + DX^2 \right] . \tag{6.61}$$

Integrating by parts yields

$$\int d\ell \left[\frac{\partial}{\partial \ell} \left(\frac{|\nabla\beta|^2}{B} \frac{\partial X}{\partial \ell} \right) + \left(\Lambda - \frac{D}{B} \right) X \right] X = 0 , \tag{6.62}$$

from which we immediately obtain the Euler equation

$$\frac{\partial}{\partial \ell} \left(\frac{|\nabla\beta|^2}{B} \frac{\partial X}{\partial \ell} \right) + \left(\Lambda - \frac{D}{B} \right) X = 0 . \tag{6.63}$$

From Eq. (6.49) we see that $|\nabla\beta|^2/B$ is approximately constant along field lines so that Eq. (6.63) can be written

$$\frac{\partial^2 X}{\partial \ell^2} + \frac{B_o}{|\nabla\beta|_o^2} \left(\Lambda - \frac{D}{B} \right) X = 0 , \tag{6.64}$$

where the subscripted quantities are to be evaluated at some convenient point on the field line (e.g., at a midplane of a mirror segment in a side).

At this juncture we note that both the center of a side and the center of a corner are reflection symmetry points (planes, if one considers all field lines) for the equilibrium quantities. Thus, we introduce the distance L between the center of a side and the center of an adjacent corner and define

$$S = \ell/L \ , \tag{6.65}$$

where $S = 0$ corresponds to the center of a side and $S = 1$ corresponds to the center of the adjacent corner. With this definition we can rewrite Eq. (6.64) in the dimensionless form

$$\frac{\partial^2 X}{\partial S^2} + (\hat{\Lambda} - \hat{D})X = 0 \ , \tag{6.66}$$

where

$$\hat{\Lambda} = L^2 \frac{B_o}{|\nabla \beta_o|^2} \Lambda \ , \tag{6.67}$$

$$\hat{D} = L^2 \frac{B_o}{|\nabla \beta_o|^2} \frac{D}{B} \ . \tag{6.68}$$

We now make explicit approximations for $\hat{D}$ appearing in Eq. (6.66). Since $\hat{D}$ is approximately constant along a field line in the corner, we are led to treat the behavior of $\hat{D}$ in the sides in a similar fashion (particularly since here we are interested in the new features introduced by the corners). Thus, we treat $\hat{D}$ as being piecewise constant:

$$\hat{D} = \begin{cases} D_s \ , & 0 \le S < 1 - \epsilon \\ D_c \ , & 1 - \epsilon < S \le 1 \end{cases} \ , \tag{6.69}$$

and

$$\hat{D}(-S) = \hat{D}(S) \ , \tag{6.70}$$

$$\hat{D}(1 + S) = \hat{D}(1 - S) \ , \tag{6.71}$$

where the transition between side and corner occurs at $S = 1 - \epsilon$ ($\epsilon \ll 1$).

We now assume that the equilibrium is stable to flute modes (since if it is not it will also be unstable to the wider class that includes ballooning modes). In terms of the present notation this means that

$$\bar{D} \equiv (1 - \epsilon)D_s + \epsilon D_c > 0 \ . \tag{6.72}$$

[Comparison of Eq. (6.72) with Eq. (6.40) reveals a way to calculate $\bar{D}$, D_s, and D_c.]

The piecewise constant approximation to $\hat{D}$ implies that the solutions to Eq. (6.66) are simple sinusoids or exponents. Thus, we introduce wave numbers for the side and corner regions by

$$k_s^2 = \hat{\Lambda} - D_s \ , \tag{6.73}$$

$$k_c^2 = \hat{\Lambda} - D_c \ . \tag{6.74}$$

We are most interested in the lowest eigenvalues (Λ) of Eq. (6.66), which is Sturmian. Accordingly, we focus on modes that are symmetric at $S = 0$ and $S = 1$:

$$X = \begin{cases} \cos k_s S \ ; & 0 \le S < 1 - \epsilon \\ \\ a \cos [k_c(S-1)] \ , & 1 - \epsilon < S \le 1 \end{cases} \ . \tag{6.75}$$

Here we have noted that since Eq. (6.66) is linear and homogeneous the overall amplitude of X is unimportant and we can (arbitrarily) set $X(0) = 1$. We also note that k_c and/or k_s may be imaginary so that one or more of the cosines in Eq. (6.75) may be a hyperbolic cosine of a real quantity.

If we impose continuity of X at $S = 1 - \epsilon$, we obtain

$$\cos\left[k_s(1-\epsilon)\right] = a\cos k_c\epsilon \ , \tag{6.76}$$

whereas continuity of $\partial X/\partial s$ yields

$$k_s \sin\left[k_s(1-\epsilon)\right] = -ak_c \sin k_c\epsilon \ . \tag{6.77}$$

Eliminating a from Eqs. (6.76) and (6.77), we obtain the dispersion relation

$$k_s \tan\left[k_s(1-\epsilon)\right] = -k_c \tan k_c\epsilon \ . \tag{6.78}$$

To progress further analytically we assume that the arguments of the tangent functions in Eq. (6.78) are small (certainly justifiable at sufficiently low beta) so that

$$\tan x \simeq x\left(1 + \frac{1}{3}x^2\right) \ . \tag{6.79}$$

With this approximation Eq. (6.78) reduces to

$$(1-\epsilon)(\hat{\Lambda} - D_s)\left[1 + \frac{1}{3}(1-\epsilon)^2\ (\hat{\Lambda} - D_s)\right]$$

$$= -\epsilon(\hat{\Lambda} - D_c)\ \left[1 + \frac{1}{3}\epsilon^2(\hat{\Lambda} - D_c)\right] \ , \tag{6.80}$$

where we have used Eqs. (6.73) and (6.74) for k_c and k_s.

Equation (6.80) can be rewritten in the form

$$\hat{\Lambda} - \bar{D} = -\frac{1}{3}\left[(1-\epsilon)^3(\hat{\Lambda} - D_s)^2 + \epsilon^3(\hat{\Lambda} - D_c)^2\right] . \tag{6.81}$$

We now recall that (for small or modest beta) D_c, $D_s \ll 1$, and $\epsilon \ll 1$. For approximately flute-like modes, Eq. (6.81) gives $\hat{\Lambda} = \bar{D} + O(D^2)$. Formally, there is another root that is $\hat{\Lambda} = -3$ in the limit as ϵ, D_c, D_s, $\bar{D}$ tend to zero. However, this root clearly violates our approximation for the tangent functions appearing in Eq. (6.78) and, hence, should be discarded.

We are thus led to solve Eq. (6.81) for the root "near" $\hat{\Lambda} = \bar{D}$ by iteration [rather than by formally solving Eq. (6.81) as a quadratic]. We obtain

$$\hat{\Lambda} \simeq \bar{D}\left[1 - \frac{\epsilon^2}{3}\bar{D}\left(1 - \frac{D_c}{\bar{D}}\right)^2\right] , \tag{6.82}$$

where we have used the definition of $\bar{D}$ to eliminate D_s.

We now suppose that we are not too close to marginal stability for flute modes, so that we can write

$$|D_c/\bar{D}| \ll 1 . \tag{6.83}$$

Under these circumstances stability obtains, provided

$$\frac{\epsilon^2}{3}\bar{D} < 1 . \tag{6.84}$$

6.6 ESTIMATE OF BETA LIMIT

We now express our stability limit Eq. (6.84) in terms of more intuitive or readily evaluated quantities. From Eqs. (6.68), (6.69), and (6.72),

$$\frac{1}{3}\epsilon^2\bar{D} = \frac{1}{3}\epsilon^2 L^2 \left(\frac{B_o}{|\nabla\beta_o|^2}\right)\left(\int \frac{D}{B}\frac{d\ell}{L}\right) . \tag{6.85}$$

The combination ϵL is simply the distance along a field line from the start of a corner to the center of a corner. Thus,

$$\epsilon L = \frac{\pi}{4} R_{corner} \cdot \tag{6.86}$$

The combination $B_o/|\nabla\beta_o|^2$ has been taken to be constant along a field line. It is conveniently evaluated in the midplane of one of the mirror cells using Eq. (6.46):

$$B_o/|\nabla\beta_o|^2 = B_o r_o^2 \cdot \tag{6.87}$$

To estimate the final factor occurring in Eq. (6.85), we make use of Eqs. (6.35) and (6.41) and the assumption that we are not too near the marginal stability point for pure flute modes to write

$$\int \frac{D}{B}\frac{d\ell}{L} = \frac{\partial p}{\partial \alpha}\frac{\partial}{\partial \alpha}\left(\int \frac{d\ell}{BL}\right) \cdot \tag{6.88}$$

As we have already noted, the contribution of the sides to the integral in Eq. (6.88) is small [Eq. (6.60)], and the length of a corner is small compared to a side.

Thus we can approximate

$$\frac{1}{L}\int \frac{d\ell}{B} \simeq \left(\frac{1}{L_{side}}\int \frac{d\ell}{B}\right)\Bigg|_{\text{side only}} \cdot \tag{6.89}$$

We further approximate the integral in Eq. (6.89) by

$$\frac{1}{L}\int \frac{d\ell}{B} \simeq \frac{1}{L_{\text{single cell}}}\left(\int \frac{d\ell}{B}\right)_{\text{single cell}} \cdot \tag{6.90}$$

In the midplane of a single mirror cell,

$$\frac{\partial}{\partial\alpha}\left(\int\frac{d\ell}{B}\right)_{\text{single cell}} = \frac{\partial}{\partial\psi}\left(\int\frac{d\ell}{B}\right)_{\text{single cell}}$$

$$= \left[\frac{\partial}{\partial r_o}\left(\int\frac{d\ell}{B}\right)_{\text{single cell}}\right]/(\partial\psi/\partial r_o)$$

$$= \frac{1}{r_o B_o}\left[\frac{\partial}{\partial r_o}\left(\int\frac{d\ell}{B}\right)_{\text{single cell}}\right] . \qquad (6.91)$$

We now introduce a scale length R_U for the derivative of $\int d\ell/B$ by

$$\frac{\partial}{\partial r_o}\left(\int\frac{d\ell}{B}\right)\Bigg|_{\text{single cell}} = -\frac{1}{R_U}\left(\int\frac{d\ell}{B}\right)_{\text{single cell}} \qquad (6.92)$$

and note that (see Sect. 4)

$$\frac{1}{L_{\text{single cell}}}\left(\int\frac{d\ell}{B}\right)_{\text{single cell}} \cong -\frac{1}{R_U}\frac{(1-\delta)}{B_o} , \qquad (6.93)$$

where

$$\delta = \text{bumpiness parameter} = (M-1)/(M+1) \qquad (6.94)$$

with M = mirror ratio.

We next introduce a scale length for the pressure gradient by

$$\frac{\partial p}{\partial\alpha} = \frac{1}{r_o B_o}\frac{\partial p}{\partial r_o} = \frac{P}{r_o B_o}\left(-\frac{1}{R_p}\right) . \qquad (6.95)$$

Combining Eqs. (6.95), (6.93), (6.91), and (6.88) yields

$$\int\frac{D}{B}\frac{d\ell}{L} \simeq \frac{(1-\delta)}{r_o^2 B_o^3}\frac{P}{R_p R_U} , \qquad (6.96)$$

or, using the definition of core beta,

$$\beta_c = 2p/B_o^2 \ , \tag{6.97}$$

$$\int \frac{D}{B}\frac{d\ell}{L} \simeq \frac{(1-\delta)}{2r_o^2 B_o}\frac{\beta_c}{R_p R_U} \ . \tag{6.98}$$

Inserting Eqs. (6.86), (6.87), and (6.98) into Eq. (6.85) yields

$$\frac{1}{3}\epsilon^2 \bar{D} \simeq \frac{\pi^2(1-\delta)}{96}\frac{(R_{corner})^2}{R_p R_U}\beta_c \ , \tag{6.99}$$

so that the stability criterion given by Eq. (6.84) becomes

$$\beta_c < \frac{96}{\pi^2}\frac{1}{(1-\delta)}\left(\frac{R_p R_U}{R_{corner}^2}\right) . \tag{6.100}$$

We have already noted in developing Eq. (6.53) that

$$R_{corner} \simeq 2R_{coil} \ , \tag{6.101}$$

so that Eq. (6.100) becomes

$$\beta_c < \frac{24}{\pi^2}\frac{1}{(1-\delta)}\frac{R_p R_U}{R_{coil}^2} \ . \tag{6.102}$$

It is now convenient to relate R_U (which involves the effects of the hot electron rings) to the vacuum value of $|R_U|$ since (see Sect. 4)

$$|R_{Uo}|^{-1} \equiv \lim_{\beta_{ring}\to 0} |R_U|^{-1} \simeq \delta\left|\frac{\partial\, \ell n\, B_{o,vac}}{\partial r}\right| \simeq \frac{2\delta}{R_{coil}} \ , \tag{6.103}$$

so that

$$\beta < \frac{12}{\pi^2} \frac{1}{\delta(1-\delta)} \left(\frac{R_p}{R_{coil}}\right) \left(\frac{R_U}{R_{Uo}}\right) . \tag{6.104}$$

For a nominal local mirror ratio of M = 2, δ = 1/3, Eq. (6.104) becomes

$$\beta < \frac{54}{\pi^2} \left(\frac{R_p}{R_{coil}}\right) \left(\frac{R_U}{|R_{Uo}|}\right) . \tag{6.105}$$

Finally, we note that in terms of the present notation an approximate Lee-Van Dam-Nelson limit on beta is given by

$$\beta_{LVDN} = \frac{2R_p}{R_{coil}} ,$$

so that Eq. (6.105) becomes

$$\beta < \frac{27}{\pi^2} \left(\frac{R_U}{|R_{Uo}|}\right) \beta_{LVDN} . \tag{6.106}$$

Thus, for ring beta sufficiently small that $R_U/|R_{Uo}| \leq 1/3$, this stability limit is comparable to or less restrictive than the Lee-Van Dam-Nelson limit. This is not a very restrictive limit on ring beta.

6.7 SUMMARY

Here we have used a simplified formalism to estimate the potential limitations on core plasma beta imposed by MHD ballooning modes in the square configuration of an EBT. Anticipating that it will be desirable to include more kinetic effects than seemed advisable for an initial examination of the problem, a great many details have been made explicit. For example, the curvature, connection length, and universal term of δW can all be expected to play a role in more detailed kinetic formalism.

Within the MHD model employed, an attempt has been made to err on the side of pessimism at each point. Even so, we find that the limitations on core plasma beta imposed by the MHD ballooning modes are no more restrictive than the Lee-Van Dam-Nelson criterion, provided that the hot electron rings do not produce too deep a magnetic well.

REFERENCE

1. D. B. Nelson and C. L. Hedrick, "Macroscopic Stability and Beta Limit in the ELMO Bumpy Torus," Nucl. Fusion 19, 283 (1979).

7. BALLOONING MODES IN THE ELMO BUMPY SQUARE CONFIGURATION USING THE GENERALIZED KINETIC ENERGY PRINCIPLE

D. A. Spong

In the bumpy square configuration, toroidal curvature is localized in the corner sections rather than uniformly distributed, as is the case in the existing circular ELMO Bumpy Torus (EBT) configuration. This feature, coupled with the fact that the magnetic field is higher in the corner sections, results in a number of distinct advantages with respect to particle confinement, heating, and transport. It might be expected, however, that ballooning modes should have some tendency to concentrate in the corner sections — especially along the outer field lines where the curvature and pressure gradients are unfavorable. Here we examine the stability of such a configuration using a ballooning mode equation[1] derived from the generalized kinetic energy principle. The side and corner sections of the square are treated with a piecewise constant approximation and matched at a transition boundary to obtain the stability condition. This retains the ring-core coupling and yields both the low β_c diamagnetic well stabilization condition and a high-β_c stability limit analogous to the Lee-Van Dam-Nelson β_c limit, where β_c is the core plasma beta. Due to the high magnetic field in the corners and the relatively weak curvature there ($\simeq$1/2 of the curvature in the bumpy sections), this upper β_c limit is not significantly changed from that which would be present in the conventional circular bumpy torus configuration.

7.1 INTRODUCTION

Hot-species stabilization schemes have recently been proposed in tokamaks,[1] helical axis stellarators,[2] and tandem mirrors.[3] Instability modes connected with the presence of a superthermal component have also been discussed in relation to tokamaks with neutral injection[4] and for future devices where alpha particles will be present.[5] In this paper, we analyze the stability properties of the bumpy square configuration,[6] which is stabilized by hot electron rings produced near the second harmonic cyclotron resonance by microwave heating. Of the various toroidal configurations in which hot species stabilization has been proposed, this geometry is at present the only one in which ring formation is experimentally proven. In addition, by forming the rings

in straight mirror sectors rather than in regions where distributed toroidal curvature is present, the bumpy square geometry offers the highest possible ring formation efficiency and confinement. This will help to ensure the production of deep diamagnetic wells at the ring locations without excessive microwave power requirements, a condition which is necessary to stably support steep core plasma gradients. The main stability question of interest relative to the bumpy square is how the isolated toroidal curvature in the high-field corner sections will influence overall stability properties. For example, at what values of core beta do ballooning modes localize in the corner sectors and go unstable? Also, a related question is whether the unfavorable curvature in the corners will degrade existing stability limits[7,8] in the side sections, resulting from consideration of the core-hot electron ring coupling.

To address these stability questions, we examine low-frequency modes using an energy principle analysis. Of the various possible approaches, this method allows the most complete description of the magnetic field line topology, which is of primary importance here in comparing the square geometry against an ideal straight bumpy cylinder. A number of different energy principles have been formulated that can be applied to magnetically confined plasmas in closed field line devices. The earliest of these is that of Bernstein et al.[9] (and generalized in ref. 10 to the case of tensor pressure), referred to in the following as the conventional magnetohydrodynamic (MHD) limit. This energy principle may be written as

$$\delta W = \delta W_f + \delta W_k \quad , \tag{7.1}$$

where

$$\delta W_f = \frac{1}{2} \int d^3x \left[\sigma Q_\perp^2 + \tau Q_\parallel^2 + \sigma j_\parallel \hat{b} \cdot (\xi \times Q) \right.$$

$$\left. + Q\xi \times \tilde{\nabla} P_\parallel - \frac{1}{B}(2Q_\parallel + \xi \cdot \nabla B)(\xi \cdot \tilde{\nabla} P_\perp) \right] \tag{7.2}$$

and

$$\delta W_k = -\frac{1}{2}\int d\alpha\, d\beta\, d\mu\, dJ \left(\frac{\partial F}{\partial \epsilon}\right)_\alpha H^2 \quad , \tag{7.3}$$

with

H = gyro-averaged change in the particle kinetic energy due to field displacement ξ,

$$\sigma = 1 + \frac{P_\perp - P_\parallel}{B^2} \quad ,$$

$$\tau = 1 - \frac{1}{B}\frac{\partial P_\perp}{\partial B} \quad ,$$

$Q_\perp$ = Lagrangian perturbed magnetic field perpendicular to the equilibrium **B** field,

$Q_\parallel$ = Lagrangian perturbed magnetic field parallel to the equilibrium **B** field,

ξ = field line displacement vector,

$j_\parallel$ = plasma current parallel to **B**,

$$q = \hat{b}\hat{b} : \nabla\xi \quad ,$$

$P_\parallel, P_\perp$ = parallel and perpendicular plasma pressure components, respectively,

$$\tilde{\nabla} = \nabla - \nabla B \frac{\partial}{\partial B} \quad ,$$

α,β = radial and angle-like Clebsch variables used to represent the magnetic field $\mathbf{B} = \nabla\alpha \times \nabla\beta$,

μ = magnetic moment = $MV_\perp^2/2B$,

J = longitudinal invariant = $M \oint d\ell\, V_\parallel$,

ϵ = particle energy = $MV_\parallel^2/2 + \mu B$,

F = gyro-averaged distribution function.

This form of δW assumes that the instability growth rate is small compared to the cyclotron frequency and large compared to the bounce and drift frequencies. That is, particles are taken as being tied to field lines and having no motion along or across (except for gyromotion) field lines over the time scale of the instability.

A somewhat more general form of the energy principle for an anisotropic, guiding-center plasma was next derived by Kruskal and Oberman.[11] Their energy principle has the same form as given in Eq. (7.1) with δW_f given in Eq. (7.2). However, now the kinetic portion δW_k is changed to the form given below:

$$\delta W_k = -\frac{1}{2} \int d\alpha\, d\beta\, d\mu\, dJ \left(\frac{\partial F}{\partial \epsilon}\right)_\alpha \langle H \rangle^2 \quad , \tag{7.4}$$

where

$\langle \ldots \rangle$ = bounce average = $\dfrac{1}{\partial J/\partial \epsilon} \oint \dfrac{d\ell}{V_\parallel} (\ldots)$,

F = gyro- and bounce-averaged guiding-center distribution function.

Here it is assumed that the instability growth rate is small compared to the bounce and gyration frequencies but large compared to the cross-field drift frequency. This corresponds to a physical picture of particles tied to magnetic field lines (like beads) with gyration perpendicular to field lines and parallel motion along them for the time scale of the instability but with no drift across them.

Finally, the most recent derivation of the energy principle, the generalized kinetic energy principle,[12,13] retains the cross-field drift motion, and its kinetic portion is written as follows:

$$\delta W_k = -\frac{1}{2}\int d\alpha\, d\beta\, d\mu\, dJ \left[\left(\frac{\partial F}{\partial \epsilon}\right)_\alpha \langle\langle H\rangle\rangle^2 + \frac{(\partial F/\partial \alpha)_\epsilon}{(\partial \epsilon/\partial \alpha)_J}\left(\langle H\rangle^2 - \langle\langle H\rangle\rangle^2\right)\right] , \tag{7.5}$$

where

$\langle\langle \ldots \rangle\rangle$ = double average over both the bounce and drift motion

$$= \frac{1}{\tau_D}\oint d\beta \frac{1}{\langle d\beta/dt\rangle}\langle \ldots \rangle ,$$

with τ_D = precessional drift period,

$\left\langle \frac{d\beta}{dt} \right\rangle$ = bounce-averaged rate of precession.

This version of energy principle then treats the drift frequency, bounce frequency, and gyration frequency all as being large compared to the growth rate of the instability.

Consideration of the assumptions underlying the various kinetic parts of δW given in Eqs. (7.3), (7.4), and (7.5) then indicates that these should apply to increasingly energetic plasma components. In examining the stability of a hot electron stabilized bumpy square configuration, we consequently use the generalized kinetic energy principle of Eq. (7.5) to describe the hot electron component and the conventional MHD form of Eq. (7.3) for the lower temperature core plasma. The fluid portion of δW given in Eq. (7.2) will apply to both components. This is justified as long as we examine instabilities whose growth rate is much less than the core ion or electron cyclotron frequencies but much greater than the core drift or bounce frequencies. On the other hand, the hot electron component must be sufficiently

energetic that its cross-field drift frequency is much greater than the instability growth rate. Such frequency orderings should be appropriate to low-frequency MHD modes in the near-term bumpy square geometry.

Inherent in using such an approach to examine bumpy square stability are a number of assumptions: finite Larmor radius effects are neglected, only low-frequency modes ($\omega << \omega_{d,Hot}$ or ω_{ci}) are considered, relativistic effects are not included, and effects that depend on n_{Hot} (as separate form β_{Hot}) are neglected. Hot electron finite Larmor radius effects have been examined recently[14,15] for a number of modes that can occur in bumpy field devices and found to be strongly stabilizing for even moderate values of m, the azimuthal mode number. However, at low m the zero Larmor radius theory[16] still appears to establish the β_c limitation. The low-frequency limitation will prevent us from considering the full impact of the ring-core decoupling.[16] This is not apt to be of too much importance in near-term experimental devices where the hot electron drift frequency is significantly larger than typical MHD growth rates, but requires further analysis in possible future devices where the ratio $\omega_{D,Hot}/\gamma_{MHD}$ does not remain as large. The neglect of n_{Hot} effects precludes charge uncovering stabilization which can stabilize certain classes of modes[17] before diamagnetic well stabilization is established. Also, it prevents examination of the hot electron interchange stability boundaries; however, since the hot interchange mode is not unstable in this model (due to the assumption that $\omega << \omega_{d,Hot}$), this is of no interest here anyway.

In addition to the above assumptions, which are inherent to the energy principle analysis, we make a few other approximations only to simplify the present calculation, most of which can be improved with straightforward extensions. In fact, work on this in some areas is already under way. We do not include the full three-dimensional effects for the core or ring plasmas. This is probably quite good for the hot electron rings in the sides of the bumpy square since they should be very close to azimuthally symmetric but may not be as good for the core plasma. Finally, we will neglect the radial mode structure and will treat the sides and corner sections in a piecewise continuous fashion. These last two approximations can easily be avoided by treating the radial wave number as an independent parameter and by going to a more elaborate numerical solution of the eigenvalue

equation. However, as a first cut, we do not include this degree of detail.

The outline of the remainder of this section is as follows. First, we revisit the derivation of the ballooning equation for a hot electron plasma immersed in a cooler core plasma (as given by Rosenbluth, Tsai, Van Dam, et al.[1]) and discuss the differences and similarities of this equation with that obtained using conventional MHD. Second, we discuss approximations that can be made to this equation appropriate to the ELMO Bumpy Square (EBS) device. Finally, a solution and dispersion relation for the bumpy square are presented, and results for stability boundaries as a function of β_{core}, β_{Hot}, and global mirror ratio (= $B_{corner}/B_{midplane}$) are given.

7.2 KINETIC BALLOONING EQUATION DERIVATION REVISITED

As mentioned in the previous section, we will use the conventional MHD fluid portion of δW for the core plus ring component and the generalized kinetic energy principle for δW_k, which in this case will apply only to the hot electron ring. Using Φ and $Q_{\parallel}$ as variables (the perturbed electrostatic potential and the Lagrangian magnetic field perturbation parallel to the equilibrium magnetic field, respectively) instead of the displacement ξ (with $\xi_{\parallel}$ set equal to zero), the following results have been given in ref. 1 for δW_f and δW_k:

$$\delta W_f = \frac{1}{2}\int \frac{d\ell}{B}\left[\sigma\,|\nabla S|^2\,(\hat{b}\cdot\nabla\Phi)^2 + \tau\left(Q_{\parallel} - \frac{\sigma}{\tau}\,Be\cdot\kappa\Phi\right)^2\right.$$

$$\left. - (e\cdot\kappa)\left(e\cdot\tilde{\nabla}P_{\parallel} + \frac{\sigma}{\tau}\,e\cdot\tilde{\nabla}P_{\perp}\right)\Phi^2\right] , \qquad (7.6)$$

$$\delta W_K = -\frac{1}{2}\int dE\,d\mu\left(\frac{\partial F}{\partial\alpha}\right)_{\epsilon}\frac{\langle H\rangle^2}{(\partial\epsilon/\partial\alpha)_J}$$

$$= \frac{1}{2}\int dE\,d\mu\,(e\cdot\nabla F)\,\frac{\left[\int\frac{d\ell}{V_{\parallel}}\left(\mu Q_{\parallel} + V_{\parallel}^2\,e\cdot\kappa\Phi\right)\right]^2}{\langle\omega_D\rangle} , \qquad (7.7)$$

where $\mathbf{e} = \mathbf{B} \times \nabla S/B^2$, S = eikonal function, and $\langle\omega_D\rangle$ = bounce-averaged drift frequency. Here we have used an eikonal ansatz to decouple the α and β dependences from the ℓ dependence (i.e., we assume that the variations in α and β are much more rapid than the ℓ variation). We have also assumed that the β (azimuthal angle) dependence in $\langle H\rangle$ and $\langle\omega_D\rangle$ is negligible except through the $e^{im\beta}$ of perturbed fields. This is equivalent to assuming axisymmetry about the minor axis. This should be a reasonable approximation for hot electron rings in the side sections of a bumpy square since they are in straight bumpy cylinders and do not experience any toroidal curvature. The assumption that $\langle H\rangle/\langle\omega_D\rangle \propto e^{im\beta}$ then results in $\langle\langle H\rangle\rangle = \tau_D^{-1} \oint d\beta\, \langle H\rangle/\langle\omega_D\rangle = 0$, which reduces Eq. (7.5) to the form given in Eq. (7.7).

It is now desirable to express δW_k in terms of moments of the hot electron distribution F. This will be especially useful in being able to factor the equilibrium force balance relation into the energy principle at a later point. Actually, this could be done along with the minimization with respect to Φ and $Q_{||}$ in terms of the distribution F itself, but the algebra would probably become much more obscure. Expressing δW_k in terms of moments of F can be achieved by using a Schwartz inequality. This will allow us to write δW_k as a ratio of two velocity space integrals instead of as a velocity space integral of a ratio of two functions. The Schwartz inequality gives the following relationship:

$$\int dE\, d\mu\, A^2 \geq \frac{\left(\int dE\, d\mu\, AD\right)^2}{\int dE\, d\mu\, D^2} \quad . \tag{7.8}$$

If we then identify A^2, AD, and D^2 as

$$A^2 = \mathbf{e} \cdot \nabla F\, \frac{\langle H\rangle^2}{\langle\omega_D\rangle} \quad ,$$

$$AD = \mathbf{e} \cdot \nabla F\, \langle H\rangle \quad ,$$

$$D^2 = \mathbf{e} \cdot \nabla F\, \langle\omega_D\rangle \quad ,$$

then the inequality of Eq. (7.8) yields

$$\delta W_k \geq \frac{\left[\int dE\, d\mu\, \mathbf{e}\cdot\nabla F \int \frac{d\ell}{V_\parallel}\left(\mu Q_\parallel + V_\parallel^2\, \mathbf{e}\cdot\kappa\Phi\right)\right]^2}{2\int dE\, d\mu\, \mathbf{e}\cdot\nabla F \int \frac{d\ell}{V_\parallel}\left(\mu\mathbf{e}\cdot\nabla B + V_\parallel^2 \mathbf{e}\cdot\kappa\right)} \quad . \tag{7.9}$$

That is, the right side represents a lower bound on δW_k such that this should result in a pessimistic estimate of stability. This application of the Schwartz inequality, of course, depends on the above quantities (A^2, D^2, and AD) having the same sign over the range of integration. Changes in their overall sign should not influence the argument, but a change in sign with respect to pitch angle or energy variations can invalidate it. For example, the bounce-averaged drift frequency in the hot electron ring region is plotted in Fig. 7.1 vs ς equal to cosine of the pitch angle and for three different values of β_{Hot}. In the first case, β_{Hot} is zero; second, it is just enough to cancel the curvature drift, but not form a well; and third, in the bottom figure, β_{Hot} is large enough to reverse ∇B and the overall direction of $\langle\omega_D\rangle$. As may be seen, there is generally a region near $\varsigma \simeq 0.8$ where $\langle\omega_D\rangle$ reverses sign. Normally, this would prevent the use of a Schwartz inequality. However, since the kinetic portion of δW here is only applied to the hot electron ring, which is highly anisotropic ($P_{\perp H} > P_{\parallel H}$), it is expected that the hot electron distribution will not significantly populate the range of pitch angles where $\langle\omega_D\rangle$ reverses sign. In fact, in the present calculation we assume $P_{\parallel H} = 0$, which ensures the validity of the Schwartz inequality. However, even if one allows a finite $P_{\parallel H}$, it is expected that this procedure should be valid for typical ring electron distributions. In earlier work,[12] where the ring pressure was taken as isotropic, the stability window was observed to vanish, and this possibly can be related to the above difficulty.

Using the form of δW_k given in Eq. (7.9), one can now interchange orders of integration on the numerator and denominator velocity integrals, that is,

$$\int dE\, d\mu(\ldots) \int \frac{d\ell}{V_\parallel}(\ldots) \rightarrow \int \frac{d\ell}{B}(\ldots) \int \frac{dE\, d\mu\, B}{V_\parallel}(\ldots) \quad ,$$

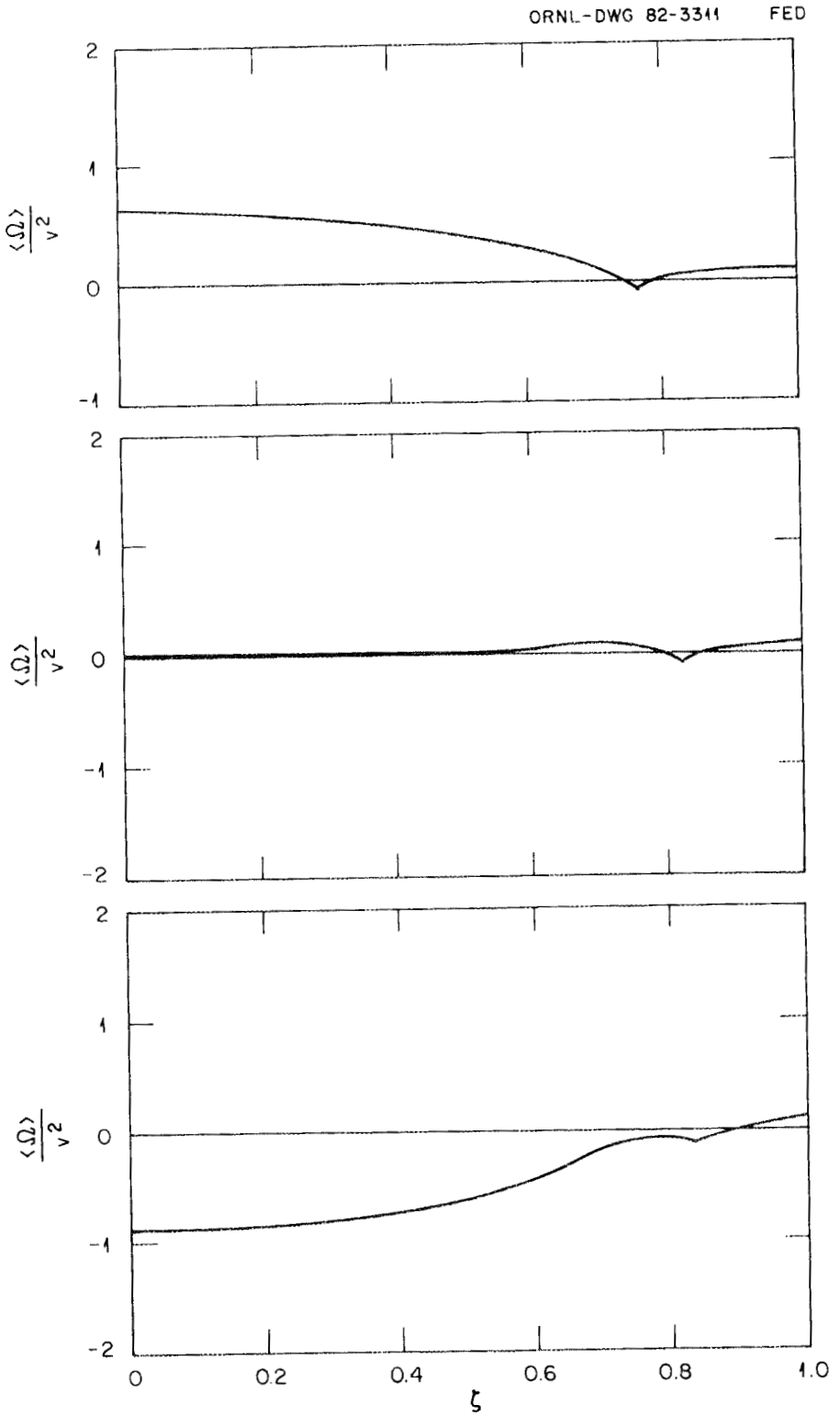

Fig. 7.1. Bounce-averaged drift frequency vs pitch angle ($\zeta = \cos V_{\parallel}/V$) for three different values of ring beta, β_{Hot}. $\beta_{Hot} = 0$ (top), small β_{Hot} (middle), and large β_{Hot} (bottom).

and express these integrals in terms of pressure moments of the hot electron distribution function:

$$\text{Top integral} = \int \frac{d\ell}{B} \int \frac{dE\, d\mu\, B}{V_\parallel} (\mathbf{e}\cdot\nabla F)(\mu Q_\parallel + V_\parallel^2 \mathbf{e}\cdot\kappa\Phi)$$

$$= \int \frac{d\ell}{B} \left[(\mathbf{e}\cdot\tilde{\nabla}P_\perp)\frac{Q_\parallel}{B} + (\mathbf{e}\cdot\tilde{\nabla}P_\parallel)(\mathbf{e}\cdot\kappa)\Phi \right]^2 \quad ;$$

$$\text{Bottom integral} = \int \frac{d\ell}{B} \int \frac{dE\, d\mu\, B}{V_\parallel} (\mathbf{e}\cdot\nabla F)(\mu \mathbf{e}\cdot\nabla B + V_\parallel^2\, \mathbf{e}\cdot\kappa)$$

$$= \int \frac{d\ell}{B} \left[\frac{1}{B} (\mathbf{e}\cdot\tilde{\nabla}P_\perp)(\mathbf{e}\cdot\nabla B) + (\mathbf{e}\cdot\tilde{\nabla}P_\parallel)(\mathbf{e}\cdot\kappa) \right] .$$

Here, the operator $\tilde{\nabla} = \nabla - \nabla B\, \partial/\partial B$ and arises from moving the gradient operator from inside the velocity integrals ($\int dE\, d\mu\, B/V_\parallel$) to outside. The kinetic portion of δW then becomes[1]

$$\delta W_k = \frac{\left\{ \int \frac{d\ell}{B} \left[\left(\frac{Q_\parallel}{B}\right) \mathbf{e}\cdot\tilde{\nabla}P_{\perp H} + (\mathbf{e}\cdot\kappa)(\mathbf{e}\cdot\tilde{\nabla}P_{\parallel H})\Phi \right] \right\}^2}{2 \int \frac{d\ell}{B} \left[\frac{1}{B} (\mathbf{e}\cdot\nabla B)(\mathbf{e}\cdot\tilde{\nabla}P_{\perp H}) + (\mathbf{e}\cdot\kappa)(\mathbf{e}\cdot\tilde{\nabla}P_{\parallel H}) \right]} . \qquad (7.10)$$

Separating out the components of δW_f and W_k, which involve $Q_\parallel$, we can now minimize with respect to $Q_\parallel$, resulting in the following integral equation for $Q_\parallel$:

$$Q_\parallel = \frac{\sigma}{\tau} B(\mathbf{e}\cdot\kappa)\Phi - \frac{(\mathbf{e}\cdot\tilde{\nabla}P_{\perp H})}{AB\tau}(X + Y) \quad , \qquad (7.11)$$

where

$$X = \int \frac{d\ell}{B} (\mathbf{e}\cdot\kappa)(\mathbf{e}\cdot\tilde{\nabla}P_{\parallel H})\Phi \quad ,$$

$$Y = \int \frac{d\ell}{B} (\mathbf{e} \cdot \tilde{\nabla} P_{\perp H}) \frac{Q_{\parallel}}{B} \quad ,$$

$$A = \int \frac{d\ell}{B} \left[\frac{1}{B} (\mathbf{e} \cdot \nabla B)(\mathbf{e} \cdot \tilde{\nabla} P_{\perp H}) + (\mathbf{e} \cdot \kappa)(\mathbf{e} \cdot \tilde{\nabla} P_{\parallel H}) \right] \quad .$$

This can easily be solved by taking a $\int d\ell (\mathbf{e} \cdot \tilde{\nabla} P_{\perp H})/B^2$ moment and gives the following solution[1] for $Q_{\parallel}$:

$$Q_{\parallel} = \frac{\sigma}{\tau} B\Phi (\mathbf{e} \cdot \kappa) - \frac{1}{\tau B} (\mathbf{e} \cdot \tilde{\nabla} P_{\perp H}) \Lambda \quad , \tag{7.12}$$

where

$$\Lambda = \frac{\int \frac{d\ell}{B} (\mathbf{e} \cdot \kappa)(\mathbf{e} \cdot \tilde{\nabla} P_{\parallel H} + \frac{\sigma}{\tau} \mathbf{e} \cdot \tilde{\nabla} P_{\perp H}) \Phi}{\int \frac{d\ell}{B} \left[(\mathbf{e} \cdot \kappa)(\mathbf{e} \cdot \tilde{\nabla} P_{\parallel H} + \frac{\sigma}{\tau} \mathbf{e} \cdot \tilde{\nabla} P_{\perp H}) - \frac{1}{\tau B^2} (\mathbf{e} \cdot \tilde{\nabla} P_{\perp H})(\mathbf{e} \cdot \nabla p_c) \right]} \quad .$$

In deriving this we have incorporated the equilibrium pressure balance relation $\nabla_{\perp} B = B\kappa - 1/B \nabla_{\perp} P_{\perp}$ to eliminate the $\mathbf{e} \cdot \nabla B$ term appearing in A above [Eq. (7.11)]. This will avoid sensitivities to the equilibrium model, which would otherwise exist in the resulting ballooning equation.

Substituting $Q_{\parallel}$ from Eq. (7.11) into Eq. (7.10) and minimizing with respect to Φ leads to the ballooning equation, given in ref. 1:

$$\mathbf{B} \cdot \nabla \left(\frac{\sigma |\nabla S|^2}{B^2} \mathbf{B} \cdot \nabla \Phi \right) + (\mathbf{e} \cdot \kappa)(\mathbf{e} \cdot \tilde{\nabla} P_{\parallel} + \frac{\sigma}{\tau} \mathbf{e} \cdot \tilde{\nabla} P_{\perp}) \Phi + \Gamma \Phi$$

$$= (\mathbf{e} \cdot \kappa)(\mathbf{e} \cdot \tilde{\nabla} P_{\parallel H} + \frac{\sigma}{\tau} \mathbf{e} \cdot \tilde{\nabla} P_{\perp H}) \Lambda \quad , \tag{7.13}$$

where Γ is proportional to ω^2,

$$\nabla S = \mathbf{k}_{\perp} \quad ,$$

$$\sigma = 1 + \frac{P_\perp - P_\parallel}{B^2} ,$$

$$\tau = 1 + \frac{1}{B}\frac{\partial P_\perp}{\partial B} ,$$

$$\kappa = (\hat{b} \cdot \nabla)\hat{b} ,$$

$$\mathbf{e} = \mathbf{B} \times \nabla S/B^2 ,$$

$$\tilde{\nabla} = \nabla - \nabla B \frac{\partial}{\partial B} .$$

This is an integro-differential equation of the Fredholm type with a symmetric kernel and may be solved by the prescription given in ref. 1. That is, we can break Φ up into a homogeneous solution and a particular solution: $\Phi = \Phi_0 + c\Phi_1$, where Φ_0 is a solution of Eq. (7.13) with the right side set equal to zero and Φ_1 is a solution with $\Lambda = 1$. The constant c is then determined by substituting this solution back into Eq. (7.13). We use this method with a very simplified equilibrium model for the bumpy square. At this point, Eq. (7.13) could be applied to numerically calculated bumpy square equilibrium fields and solved using shooting techniques. Work on this type of calculation is presently under way, but only the simplified analytic model will be discussed here.

7.3 SIMPLIFICATION OF THE BALLOONING EQUATION AND RELATION TO CONVENTIONAL MHD

In order to reduce Eq. (7.13) to a readily tractable form, we make a number of approximations. First, we consider the high-m limit where the radial mode structure can be neglected and S can be taken as $m\beta$. Second, the azimuthal mode number m cancels from the ballooning equation. Third, we take $P_{\parallel H} \equiv 0$ and assume that $\beta_{\perp H}$ and β_{core} are sufficiently small such that $\sigma \approx 1$ and $\tau \approx 1$. Finally, as mentioned in ref. 18, the quantity $|\nabla\beta|^2/B$ can be related to magnetic flux and should be fairly constant along a field line. Invoking these approximations results in the following:

$$\mathbf{e} = \frac{\mathbf{B} \times \nabla\beta}{B^2} = \mathbf{U}_\alpha = \text{contravariant basis vector in } \nabla\alpha \text{ direction,}$$

$$\mathbf{B} \cdot \nabla\left(\frac{\sigma|\nabla S|^2}{B^2}\mathbf{B} \cdot \nabla\Phi\right) \simeq |\nabla\beta|^2 \frac{d^2\Phi}{d\ell^2}\frac{B}{B_0} \quad ,$$

$$\mathbf{e} \cdot \boldsymbol{\kappa} = \kappa_\alpha = \text{contravariant curvature } \alpha \text{ component,}$$

$$\mathbf{e} \cdot \tilde{\nabla} = \frac{d}{d\alpha} \quad .$$

We then define the following quantities to simplify the appearance of the ballooning equation:

$$D_c = -\frac{2L^2B_0}{|\nabla\beta_0|^2}\frac{\kappa_\alpha}{B}\frac{dp_c}{d\alpha} \quad ,$$

$$D_H = -\frac{L^2B_0}{|\nabla\beta_0|^2}\frac{\kappa_\alpha}{B}\frac{\partial P_{\perp H}}{\partial\alpha} \quad ,$$

$$D_{CH} = \frac{L^2B_0}{|\nabla\beta_0|^2}\frac{1}{B^3}\frac{\partial P_{\perp H}}{\partial\alpha}\frac{dp_c}{d\alpha} \quad ,$$

where L = typical field line length, we normalize ℓ as $s = \ell/L$, and "0" subscripts denote evaluation at the midplane. The ballooning equation can then be written as

$$\frac{d^2\Phi}{ds^2} + (\Gamma - D_c - D_H)\Phi = -\frac{D_H \int ds\, D_H\Phi}{\int ds\, D_H(1 - \beta_c/\beta_{LVDN})} \quad , \tag{7.14}$$

where we have noted that

$$\frac{D_{CH}}{D_H} = \frac{1}{B^2\kappa_\alpha}\frac{dp_c}{d\alpha} \simeq \frac{R_c}{2L_n}\beta_c = \frac{\beta_c}{\beta_{LVDN}} \quad ,$$

with

$$\beta_{LVDN} = \frac{2L_n}{R_c} \quad ,$$

$$L_n = \left(\frac{1}{p_c}\frac{dp_c}{dr}\right)^{-1} \quad .$$

An analogous equation from conventional MHD (using a rigid ring model) would be[19]

$$\frac{d^2\Phi}{ds^2} + (\Gamma - D_c - D_{CH})\Phi = \frac{\gamma\tilde{D}_c p_c q}{1 + \gamma p I/q}\int ds\, \tilde{D}_c\Phi \quad , \tag{7.15}$$

with

$$\tilde{D}_c = D_c/p_c' \quad ,$$

$$q = \oint \frac{d\ell}{B} \quad ,$$

$$I = \oint \frac{d\ell}{B^3} \quad ,$$

γ = ratio of specific heats.

Here we have retained compressibility effects which enter in through the integral term on the right side of the equation. Comparison of Eqs. (7.14) and (7.15) indicates that the effect of the hot species enters in through a term which is very similar to the compressibility term in conventional MHD. Since D_H is negative on the outside half of a hot electron ring located in an unfavorable curvature region, the right side of Eq. (7.14) will add positive "compressibility" (which is stabilizing for $\beta_c < \beta_{LVDN}$) and negative "compressibility" (which is destabilizing for $\beta_c > \beta_{LVDN}$). The latter effect gives rise to the β_c limit at $\beta_c = \beta_{LVDN}$.

One difference between Eqs. (7.14) and (7.15) on the left side is that $\Gamma - D_c - D_H$ in the kinetic ballooning equation is replaced by $\Gamma - D_c - D_{CH}$ in the conventional MHD equation. Setting this coefficient to zero and requiring $\Gamma \geq 0$ results in a stability condition for flute mode, at least in a local sense. [A line-averaged condition can be obtained by going a few steps back in the derivation of the ballooning equation and retaining the line averages of $\delta W(\ell)$.] For conventional MHD, the D_{CH} term gives rise to diamagnetic well stabilization (in the rigid ring sense) since

$$-D_c < D_{CH} \text{ implies that } \beta_{\perp H} > \frac{4L_{nH}}{R_c} \quad ,$$

where

$$L_{nH} = \left(\frac{1}{P_{\perp H}} \frac{dP_{\perp H}}{dr}\right)^{-1} \quad ,$$

R_c = radius of curvature at the midplane.

In the case of the kinetic ballooning equation, D_{CH} is replaced by D_H (proportional to $\kappa\, dP_{\perp H}/dr$), which would appear to add to the instability drive of the core plasma occurring in the D_c term (proportional to $\kappa\, dp_c/dr$). However, if we take the flute limit in Eq. (7.14) and take D_{CH} and D_H to be constants along a field line [actually such strong approximations are not necessary if we go back to the line-averaged version of $\delta W_k(\ell)$], the right side of Eq. (7.14) becomes

$$-\frac{D_H \int ds\, D_H \Phi}{\int ds\, D_H (1 - \beta_c/\beta_{LVDN})} \simeq \frac{-D_H \Phi}{1 + D_{CH}/D_H} \simeq -\Phi(D_H - D_{CH}) \quad ,$$

where we have also expanded in powers of β_c/β_{LVDN}. In this limit, the $D_H\Phi$ term on the left side of Eq. (7.14) is cancelled by a similar term from the right side and replaced by exactly the term required to give rigid ring conventional MHD.

However, for instability modes that have some finite degree of ballooning, the hot electron pressure gradient term will not completely cancel, resulting in a nonrigid ring response that can be

destabilizing. This is especially apparent if we use the identity $(A + B)^{-1} = A^{-1} - (B/A)(A + B)^{-1}$ to rewrite Eq. (7.14) as follows:

$$\frac{d^2\Phi}{ds^2} + (\Gamma - D_c)\Phi = D_H\Phi - \frac{D_H \int ds\, D_H\Phi}{\int ds\, D_H}$$

$$+ D_H \frac{\int ds\, D_{CH} \int ds\, D_H\Phi}{\int ds\, D_H \int ds\, D_H(1 - \beta_c/\beta_{LVDN})} \quad . \qquad (7.16)$$

7.4 APPLICATION OF THE KINETIC BALLOONING EQUATION TO A BUMPY SQUARE CONFIGURATION

The hot-electron-stabilized, bumpy square device is discussed extensively in ref. 6. In this geometry there are eight symmetry planes, so it will only be necessary to consider one-eighth of the device. A diagram of a one-eighth sector is shown in Fig. 7.2 with some typical dimensions indicated. Here, as in ref. 18, we assume that the transition from a side to a corner section occurs in the corner and that $s = 1 - \epsilon$ represents the boundary between a side and a corner, $s = 0$ is the middle of a side, and $s = 1$ is the middle of a corner. Here $\epsilon = \pi R_{coil}/L$ and L is given by

$$L = \left(6 + \frac{\pi}{2}\right) R_{coil} \quad .$$

If we then convert κ_α and $dp/d\alpha$ to the normal cylindrical radial variable, we have

$$\kappa_\alpha = -\frac{1}{rBR_c} \quad ,$$

$$\frac{dp}{d\alpha} = -\frac{P}{rBL_n} \quad .$$

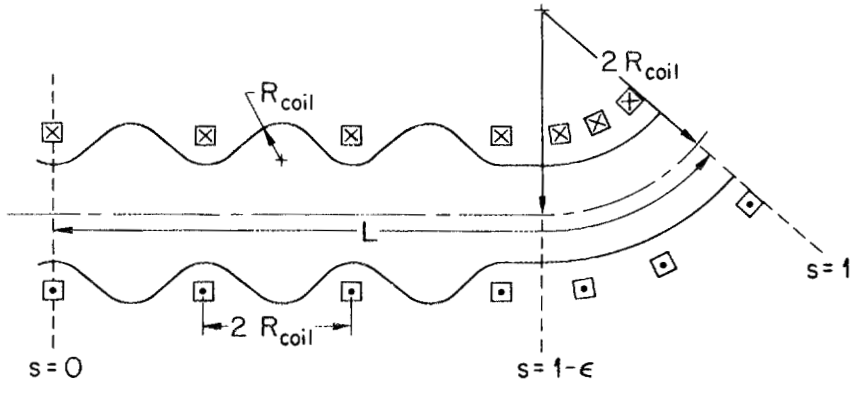

Fig. 7.2. Schematic diagram of a one-eighth sector of an EBS with some typical dimensions.

As mentioned, the quantity $B_0/|\nabla\beta_0|^2 (= r_0^2 B_0)$ is related to the magnetic flux ($\psi \simeq r^2 B$) which is constant along a field line. If we further use the constancy of $r^2 B$ in examining the dependence of D_H and D_c in the side section, we find that these terms are left with a $R_c^{-1} B^{-2}$ scaling. This tends to weight them heavily toward the midplanes of the side sections. As a first approximation, we then simply evaluate these terms at the midplane and take them as constants. Since there are presumably no hot electrons in the corner sections, we only need to evaluate D_c there. Assuming that magnetic field lines in the corner are one-quarter arcs of perfect circles (of radius $2R_{coil}$) with a magnetic field strength M_G times larger than that in the midplanes of the sides, $D_{c,corner}$ can be approximated in a simple manner (as was done in ref. 18). The resulting values of D_c and D_H are given below:

$$D_{c,side} \simeq -\frac{(12+\pi)^2}{2}\frac{\beta_c}{\beta_{LVDN}}, \tag{7.17}$$

$$D_H \simeq -\frac{(12+\pi)^2}{4}\frac{\beta_{\perp H}}{\beta_{LVDN}}, \tag{7.18}$$

$$D_{c,corner} \simeq -\frac{(12+\pi)^2}{4M_G^{3/2}}\frac{\beta_c}{\beta_{LVDN}}. \tag{7.19}$$

We can then write down separate ballooning equations for the side and corner sections:

$$\frac{d^2\Phi}{ds^2} + (\Gamma - D_{c,corner})\Phi = 0 \tag{7.20}$$

(corner equation — no hot species)

$$\frac{d^2\Phi}{ds^2} + (\Gamma - D_{c,side} - D_H)\Phi = -\frac{D_H \int ds\, D_H\Phi}{\int ds\, D_H(1 - \beta_c/\beta_{LVDN})} \tag{7.21}$$

(side equation — hot species present at midplane) .

As mentioned in the previous section (Sect. 7.3), the side equation may be solved by decomposing the solution ($\Phi = \Phi_0 + c\Phi_1$) into a homogeneous part Φ_0 [with the right side of Eq. (7.21) set to zero] and a particular solution Φ_1 that is a solution of

$$\frac{d^2\Phi_1}{ds^2} + (\Gamma - D_{c,side} - D_H)\Phi_1 = -D_H \ . \tag{7.22}$$

Substitution back into the original Eq. (7.21) then gives the constant c as

$$c = \frac{f(\Phi_0)}{1 - f(\Phi_1)} \ , \tag{7.23}$$

where

$$f(\Phi) = \frac{\int ds\ D_H\Phi}{\int ds\ D_H(1 - \beta_c/\beta_{LVDN})} \ .$$

The boundary conditions that will be applied to Φ are

(a) $\frac{d\Phi}{ds} = 0$ at $s = 0$ and $s = 1$ since these are symmetry planes;

(b) $\Phi(s = 1) = 1$ (since the equation is homogeneous, we can specify the value of Φ at one point);

(c) Φ and $d\Phi/ds$ are continuous at $s = 1 - \epsilon$.

The solution in the corner section subject to these boundary conditions is:

$$\Phi_{corner} = \cos k_c(s - 1) \ , \tag{7.24}$$

where

$$k_c^2 = \Gamma - D_{c,corner} \cdot$$

The solution in the sides can be constructed using a Green's function to give

$$\Phi_{side} = \cos k_s s + \frac{c}{k_s \cos k_s(1-\epsilon)} \left\{ \frac{k_s \cos k_s s}{c} \left[\cos k_c \epsilon - \cos k_s(1-\epsilon) \right] \right.$$

$$+ \int_0^s D_H \cos k_s y \sin k_s(1-\epsilon-s)\, dy$$

$$\left. + \int_s^{1-\epsilon} D_H \cos k_s s \sin k_s(1-\epsilon-y)\, dy \right\}, \qquad (7.25)$$

where

$$k_s^2 = \Gamma - D_{c,side} - D_H \cdot$$

Since in our case D_H is independent of s, this reduces to

$$\Phi_{side} = \left[\cos k_c \epsilon + c \frac{D_H}{k_s^2} \right] \frac{\cos k_s s}{\cos k_s(1-\epsilon)} - c \frac{D_H}{k_s^2} . \qquad (7.26)$$

Substituting back into Eq. (7.21) or using Eq. (7.23) then gives the constant c as

$$c = \frac{k_s \tan k_s(1-\epsilon) \cos k_c \epsilon}{k_s^2 \frac{Q}{D_H} + D_H \left[1 - \epsilon - \frac{1}{k_s} \tan k_s(1-\epsilon) \right]} , \qquad (7.27)$$

where

$$Q = \int ds\ (D_H + D_{CH}) = D_H(1-\epsilon)\left(1 - \frac{\beta_c}{\beta_{LVDN}}\right) .$$

The solutions of Eqs. (7.24) and (7.25) now satisfy continuity of Φ at $s = 1 - \epsilon$ (side-corner interface), but we have not made their derivatives continuous. This requirement leads to the dispersion relation given below:

$$k_c \tan k_c \epsilon = -k_s \tan k_s (1 - \epsilon)$$

$$-\frac{D_H}{k_s^2} \frac{\tan^2 k_s (1 - \epsilon)}{(1 - \epsilon)\left(1 - \frac{\beta_c}{\beta_{LVDN}}\right) + \frac{D_H}{k_s^2}\left[1 - \epsilon - \frac{1}{k_s} \tan k_s (1 - \epsilon)\right]}, \quad (7.28)$$

where

$$k_s^2 = \Gamma - D_{c,side} - D_H ,$$

$$k_c^2 = \Gamma - D_{c,corner} .$$

Stability is determined by solving this equation for Γ, with $\Gamma < 0$ implying instability and $\Gamma > 0$ implying stability.

7.5 RESULTS

In order to solve the dispersion relation given in Eq. (7.28), we have used a numerical root-finding technique. The equation was rewritten in a form that does not have any singularities; also, it was necessary to properly continue the trigonometric functions so that they became hyperbolic functions in cases where k_c^2 and k_s^2 were negative. It was observed that there is always a root at $\Gamma = 0$ for $\beta_c = 0$, independent of $\beta_{\perp H}$. This particular root was followed as β_c was changed in small increments. Typical results are plotted in Fig. 7.3 for Γ vs β_c/β_{LVDN} for several different values of $\tilde{\beta}_{\perp H}$ $(= \beta_{\perp H}/\beta_{LVDN})$. As may be seen, the root is always unstable ($\Gamma < 0$) for $\tilde{\beta}_{\perp H} = 0$. Then, as $\tilde{\beta}_{\perp H}$ is increased, there begins to be a stable window in β_c. At $\tilde{\beta}_{\perp H} = 2$ (which is the diamagnetic well stabilization condition), the

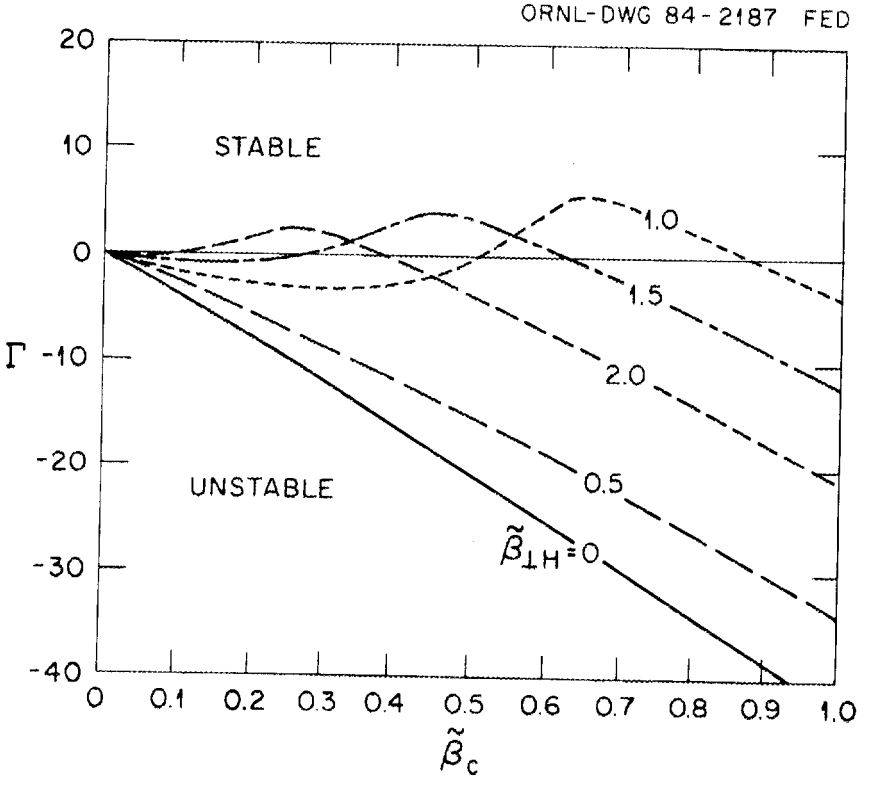

Fig. 7.3. Γ vs normalized core beta $\tilde{\beta}_c = \beta_c/\beta_{LVDN}$ for several different values of ring beta $\beta_{\perp H}$. Note $\tilde{\beta}_{\perp H} = \beta_{\perp H}/\beta_{LVDN}$.

lower end of the stable window in β_c extends all the way to $\beta_c = 0$, as would be expected.

Next, in Fig. 7.4 we have plotted the stability boundaries in the $\tilde{\beta}_c (= \beta_c/\beta_{LVDN})$ vs $\tilde{\beta}_{\perp H}$ plane for several values of M_G. Several interesting features can be seen here which relate to the discussion of Sect. 7.3. First of all, there is a diamagnetic well stabilization boundary at $\tilde{\beta}_{\perp H} = 2$ and $\tilde{\beta}_c = 0$. However, as $\tilde{\beta}_c$ is made finite, proportionally less $\tilde{\beta}_{\perp H}$ is required for stability. This effect is expected to be due to the positive "compressibility" aspect of the kinetic term on the right side of Eq. (7.14) for $\beta_c < \beta_{LVDN}$. However, this is only observed to extend to $\tilde{\beta}_{\perp H} = 1$ (left edge of the figure); past this point stability does not seem to be possible at any value of $\tilde{\beta}_c$. Another effect present in Fig. 7.4 is the dropoff in the upper β_c limit as $\tilde{\beta}_{\perp H}$ is raised. This is expected to be related to a lack of cancellation in the hot electron pressure gradient term (nonrigid ring response), discussed prior to Eq. (7.16), as the mode structure develops a significant degree of ballooning.

The scaling of the stability boundaries with M_G $(= B_{corner}/B_{midplane})$ indicates that both the upper and lower boundaries begin to deteriorate slightly as M_G is lowered. This would be expected since decreasing M_G changes the weighting of the unfavorable curvature in the corner sections. However, M_G must be lowered a good bit to see any effect since the corner curvature is 50% weaker than the curvature in the midplanes. Also, the length of the field lines through the corner section is significantly shorter than through the side section. As a result, no significant change occurs until $M_G = 2$. For the bumpy square device presently under consideration, M_G is nominally equal to 4; an M_G of 2 is probably a lower limit to the variation that could realistically be made in this parameter. As may be seen, there is no substantial difference between the $M_G = 4$ and $M_G = 1000$ cases. The latter should correspond to a bumpy cylinder limit.

7.6 CONCLUSIONS

The generalized kinetic energy principle (for the hot electrons), coupled with the conventional MHD energy principle for the core plasma, has been applied to the ballooning stability of a bumpy square plasma with hot electron rings. A very simplified model of the vacuum magnetic field and plasma properties is used here. However, the two

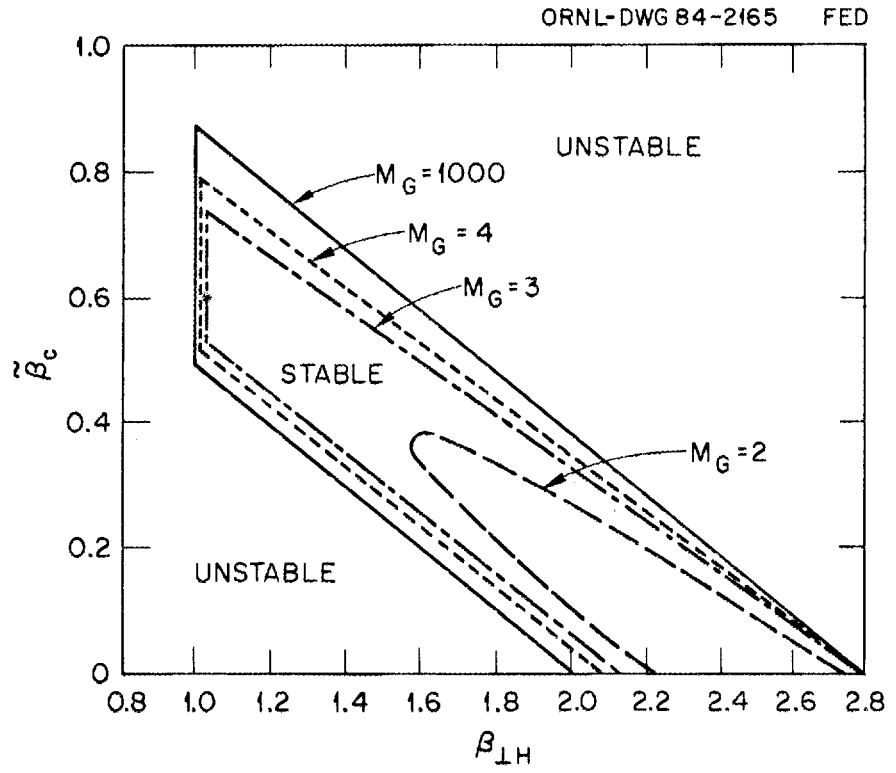

Fig. 7.4. Stability boundaries in the $\tilde{\beta}_c$ vs $\tilde{\beta}_{\perp H}$ plane for several values of global mirror ratio M_G.

lower-frequency stability boundaries (diamagnetic well stabilization and upper β_c limit with $\beta_c \simeq \beta_{LVDN}$) that would be expected in such a configuration are readily apparent in the results; this leads one to conclude that the ballooning equation is not highly sensitive to the equilibrium model. Further refinements are desirable at this point and would probably involve using realistic vacuum magnetic fields (which are available now[6] for the bumpy square), with finite-beta corrections, and using numerical shooting techniques to solve for the stability condition. Work is presently under way on this type of calculation.

The results obtained in the present, simplified model indicate that β_c limits in a bumpy square with $M_G = 4$ are not drastically different from those present in an infinite bumpy cylinder. Two effects of interest are that for finite values of β_c stability can be achieved with $\beta_{\perp H} < 4\Delta/R_c$ (i.e., below the critical value for diamagnetic well stabilization) and that the upper β_c limit drops off as $\beta_{\perp H}$ is increased above the minimum required for stability. The first feature is thought to be caused by the positive "compressibility" aspect of the kinetic term in the ballooning equation for $\beta_c < \beta_{LVDN}$. The second has been related to an enhancement in the ring–core interaction as ballooning becomes stronger. Both effects encourage operation at as low a value of $\beta_{\perp H}$ as possible while maintaining core plasma stabilization. Fortunately, this is also the regime in which one would like to operate to minimize ring power requirements.

REFERENCES

1. M. N. Rosenbluth, S. T. Tsai, J. W. Van Dam, and M. G. Engquist, "Energetic Particle Stabilization of Ballooning Modes in Tokamaks," Phys. Rev. Lett. 51, 1967 (1983).
2. A. Boozer, "The ELMO Snakey Torus," in Advanced Bumpy Torus Concepts: Proceedings of the Workshop, CONF-830758, Oak Ridge Natl. Lab., 1983, p. 161.
3. J. Kesner et al., Tandem Mirror Hot Electron Anchor, PFC/JA-81-17, Massachusetts Institute of Technology, Cambridge, 1981.
4. K. McGuire et al., "Study of High-Beta Magnetohydrodynamic Modes and Fast-Ion Losses in PDX," Phys. Rev. Lett. 50, 891 (1983).
5. K. T. Tsang et al., "Destabilization of Low Mode Number Alfvén Modes in a Tokamak by Energetic or Alpha Particles," Phys. Fluids 24, 1508 (1981).
6. N. A. Uckan, comp., ELMO Bumpy Square Status Report, January 1984 (unpublished).
7. D. B. Nelson, "Effects of Hot Electrons on Magnetohydrodynamic Modes in ELMO Bumpy Torus," Phys. Fluids 23, 1950 (1980).
8. J. W. Van Dam and Y. C. Lee, "Stability Analysis of a Hot Electron EBT Plasma," in EBT Ring Physics: Proceedings of the Workshop, CONF-791228, Oak Ridge Natl. Lab., 1979, p. 471.
9. I. B. Bernstein et al., "An Energy Principle for Hydromagnetic Stability Problems," Proc. R. Soc. London Ser. A 244, 17 (1958).
10. G. F. Chew, M. L. Goldberger, and F. E. Low, "The Boltzmann Equation and the One-Fluid Hydromagnetic Equations in the Absence of Particle Collisions," Proc. R. Soc. A 236, 112 (1956).
11. M. D. Kruskal and C. R. Oberman, "On the Stability of Plasma in Static Equilibrium," Phys. Fluids 1, 275 (1958).
12. J. W. Van Dam et al., "A Generalized Kinetic Energy Principle," Phys. Fluids 25, 1349 (1982).
13. T. M. Antonsen and Y. C. Lee, "Electrostatic Modification of Variational Principles for Anisotropic Plasmas," Phys. Fluids 25, 132 (1982).
14. H. L. Berk et al., "Finite Larmor Radius Stability Theory of ELMO Bumpy Torus Plasmas," Phys. Fluids 26, 2642 (1983).
15. K. T. Tsang and P. J. Catto, "Stability of Low-Frequency Modes in Tandem Mirrors and Bumpy Tori," Phys. Fluids 25, 1260 (1982).

16. H. L. Berk, J. W. Van Dam, and D. A. Spong, "Hot Plasma Decoupling Condition for Long Wavelength Modes," Phys. Fluids 26, 606 (1983).
17. D. A. Spong et al., "Profile Effects on EBT Stability Boundaries," Bull. Am. Phys. Soc. 28 (1983).
18. C. L. Hedrick, Sect. 6 of this report.
19. D. B. Nelson and C. L. Hedrick, "Macroscopic Stability and Beta Limit in the ELMO Bumpy Torus," Nucl. Fusion 19, 283 (1979).

Appendix 8

CONCEPTUAL DESIGN REPORT FOR ELMO BUMPY SQUARE

Abstract

A conceptual design was prepared for the EBS project, providing for the complete disassembly of the EBT device, demolition of its substructure, and assembly of new and existing components. This report presents a brief physical description of the project; a statement of the project purpose and justification; the system definition and baseline requirements; a discussion of the concept and some alternatives; preliminary assessments of safety, quality assurance, environment, and energy conservation; a description of the method for accomplishing the project; a schedule and cost estimate; a review of the specifications and existing systems; and a number of engineering drawings.

1. INTRODUCTION

This document contains the conceptual design for use by Martin Marietta Energy Systems, Inc., in preparing construction drawings and equipment specifications for changing the Fusion Energy Division ELMO Bumpy Torus (EBT) device from a toroidal configuration to a square configuration.

2. BRIEF PHYSICAL DESCRIPTION OF PROJECT

This project provides for the complete disassembly of the existing EBT device, demolition of the substructure, and reassembly of new and existing components to form a square configured device as shown on drawing SK10. Sixteen of the existing mirror coils will be salvaged and reinstalled between new cavity sections, four coils on a side. The connecting corner sections forming the vacuum vessel will be toroidal sectors, each with eight new half-size EBT mirror coils. A new device substructure and a new microwave manifold will be provided. Each set of eight corner coils will be powered by a 3-MW generator, requiring an additional 12 MW of power not previously supplied to the device. The power distribution system and cooling water system will be modified to accommodate the additional needs.

The instrumentation and control systems and the microwave waveguide network will be removed from the existing device and will be reinstalled essentially unchanged, except as required to adapt to the new configuration. The biological shield will remain unchanged.

3. PROJECT PURPOSE AND JUSTIFICATION

3.1 PURPOSE

This project is an advancement of the existing ELMO Bumpy Torus (EBT) research program sponsored by the U.S. Department of Energy (DOE), Office of Energy Research, Office of Fusion Energy. The purposes of this project are (1) to enhance and extend the technical data base of the program and (2) to provide challenge and stimulation to the overall fusion program through exploration of novel approaches in the areas of physics, technology, and fusion reactor engineering.

3.2 JUSTIFICATION OF NEED AND SCOPE

The EBT is a toroidal confinement system with a number of features that make it attractive as a reactor concept. These include steady-state operation with good accessibility for maintenance, modularity, and relatively simple magnetic coil system and engineering design requirements. In the years that these virtues of EBT were identified, the other fusion devices have recognized and tried to incorporate these advantages. This attempt led to, for example, the emphasis on current drive in tokamaks to approach steady state and to the modular tokamak and stellarator designs to get some of the maintainability/availability advantages of EBT. Historically, the EBT program has contributed to the development of fusion in a much broader sense than just its reactor attractiveness. These contributions include (1) microwave [electron cyclotron heating (ECH)] physics and technology, (2) physics of non-axisymmetric transport, (3) steady-state plasma-wall interactions,

(4) physics of very high temperature plasmas, and (5) several novel plasma diagnostics (i.e., heavy ion beam probe, etc.). These physics and technology contributions are expected to continue and to be further advanced with this new proposed project — the ELMO Bumpy Square (EBS).

Recently, several advanced bumpy torus configurations were studied in detail to identify those concepts that offer potential for significantly enhanced performance in the present EBT geometry and that offer favorable reactor extrapolations. Among the various possibilities considered, the reconfiguration of the present device from a torus into a square, with stronger magnetic fields in the corners, has been shown to be feasible and is a logical step in the program.

The EBS is formed by four linear arrays of simple magnetic mirrors linked by four high-field toroidal solenoids (corners). The configuration is such that the straight sides of the square are constructed from the EBT-I/S mirror coils (four coils per side), and each corner is formed by eight new half-size EBT-I/S coils that generate high field with negligible field ripple in the corners.

The EBS configuration offers a number of distinct advantages over a conventional EBT with respect to particle confinement, heating, transport, ring production, and stability. In EBS the particle drift orbits are better centered for all classes of particles. The velocity space loss region is greatly reduced, leading to improved volume utilization, significantly reduced direct particle losses, and increased microwave heating efficiency. For an isotropic distribution, more than 95% of the particles are confined in EBS, as compared to $\sim$50% confinement in EBT-I/S. The combination of nearly concentric particle drift orbits and

the small radial displacements in the high-field corners gives an order-of-magnitude reduction in neoclassical diffusive losses. The orbits of the deeply trapped particles and core plasma pressure surfaces almost coincide and are centered on the minor axis. There being no shift, hot electron rings will be exceedingly well centered in EBS. For the same anisotropy in EBS there should be little or none of the radial broadening of the ring that occurs in EBT. This should make it easier to form an average magnetic well in EBS than in EBT. Detailed calculations in the areas of equilibrium and stability indicate that equilibria exist (shifts are smaller in a square configuration than in a torus), and the stability limits (especially those associated with the corners) are no more restrictive than those studied for a conventional EBT. Reactor projections for EBS indicate the possibility of a substantial reduction in reactor physical size (a factor of 2 to 3) as compared to past EBT designs.

3.3 ECONOMIC CONSIDERATIONS

Because EBS is a reconfiguration of the existing EBT-I/S device, there is a minimal capital investment involved for the physics program.

As discussed in the previous section, EBS not only will extend the knowledge of EBT physics, but it will also advance the EBT in a favorable direction in terms of reactor desirability and will continue to contribute to the physics and technology of fusion in general.

4. SYSTEM DEFINITION AND BASELINE REQUIREMENTS

4.1 FUNCTIONAL REQUIREMENT

The device is designed to be a physics experiment wherein an environment is created to permit certain physical phenomena to occur and where precise observations and determinations can be made of their occurrences. The basic machine parameters that must be measured continuously are vacuum pressure, magnetic field intensity, rate of heat removal, and microwave power level. The measurement and control of these parameters is within the scope of this project.

4.2 PERFORMANCE REQUIREMENTS (RELIABILITY, AVAILABILITY, AND MAINTAINABILITY)

The operation of this device requires a staff of professional research physicists and an array of sophisticated diagnostic hardware. As a consequence of the high overhead, reliability (and congruent machine availability) is an overriding factor in the design of the machine. The machine will be designed to maximize the ease and speed of replacing a component (e.g., a burned O-ring, a shorted coil, a ruptured water-cooled electrical cable, etc.).

The reliability of building support systems is of concern, and continuing maintenance programs are in place. The dc motor-generator sets have scheduled maintenance, the demineralized water system and cooling tower operation is continually monitored, and cooling oil in the gyrotron power supplies required for microwave power generation is analyzed on a routine programmed basis.

4.3 PRELIMINARY ASSESSMENT OF INTERFACE REQUIREMENTS

The device will interface with building utilities — primarily the demineralized water cooling system and the motor-generator dc power network.

Approximately 2500 gal/min of cooling water will be required during operating periods. The pumping system has an automatic flow sensor currently operating on line, and additional pumps are automatically started or stopped as the load demand varies. The demands for cooling water for this project are adequately met by the building system now in place.

The motor-generator dc power output is shared by other experiments located in the building. This device interfaces to the power network through an assignment panel that dictates which experiment has control of the generator output. This system is in place also and requires no modifications to accommodate the new device configuration. The project needs for power interface consist of new generator control panels for the four additional generators required for the four sets of corner coils. The aluminum bus and necessary disconnect switches are in place and are available to the project.

4.4 CRITICAL ELEMENTS

There are no critical elements required by the device (in the sense that new or ongoing component research and development must be successfully completed). Design, fabrication, and assembly require only

presently developed technology, and no particular element can be considered more critical than another.

4.5 CONSTRAINTS

The device constraints are those imposed by the support system limitations. The magnet characteristics must be compatible with the generator voltage and current limits, the water cooling passage must withstand 250 psig, and the microwave power level introduced into the machine is constrained by the gyrotrons and their power supply limitations. The device will be designed to the limits of the support systems; no arbitrary constraints will be imposed.

4.6 PLANS FOR SYSTEM TESTS

All new and renovated water piping will be leak checked at system operating pressure. All vacuum piping will be leak checked in accordance with generally accepted high-vacuum procedures and standards. New coils will be tested by operating at full current before installation. After device assembly, all systems will be tested in strict accordance with a startup procedure to be generated by the Fusion Energy Division. The test will generally conform to established precedent set by tests on prior EBT configurations.

5. CONCEPT AND ALTERNATIVES

5.1 IDENTIFICATION OF ALTERNATIVES

The device is conceived as an experimental research device for exploring a particular plasma regime and, by its nature, is an alternative concept in that it is in constant competition for funding and technical support with other devices proposed for studying plasma regimes of interest in achieving controlled fusion reactions.

5.2 EVALUATION OF ALTERNATIVES

As stated in Sect. 3.2, several bumpy torus configurations have been studied in some detail. For a more detailed analysis of alternatives to the proposal described herein, refer to the *ELMO Bumpy Square Status Report* (January 1984) compiled by N. A. Uckan.

5.3 IDENTIFICATION OF RECOMMENDED CONCEPT

This report describes the recommended concept as determined by experimental results to date on the present EBT device and detailed physics calculations, as well as by detailed cost analysis and sound engineering practice.

6. UNCERTAINTIES

6.1 TECHNOLOGY/DEVELOPMENT

There are no unknown technology areas, and no research or development need be finished to construct the machine.

6.2 OPERATION

There are no uncertainties associated with operating the machine.

6.3 PROJECT

There are no known uncertainties associated with related project costs, schedule, or participants.

7. PRELIMINARY ASSESSMENTS

7.1 SAFETY, FIRE, AND HEALTH

No special hazards will be encountered, other than those normally associated with high-voltage equipment. The work area now has a sprinkler system in place. No harmful effluent will be generated by the project. High-intensity X rays are generated during device operation, but the biological shield around the existing device is calculated to be adequate for personnel safety. Radiation will be monitored in the personnel work area. Access into the device enclosure during operation is positively prevented by electro-mechanical devices interlocked with the X-ray-producing power supplies.

7.2 QUALITY ASSURANCE

Upon receipt by the Engineering Division of instructions to proceed with the project, a quality assurance (QA) plan/assessment for the device will be generated that will be applicable to the design, procurement, and construction phases of the project. This QA plan will be in effect before any drawings are issued for construction or any procurement is initiated. The QA plan will be in accordance with Engineering procedures.

7.3 ENVIRONMENT

All work on this project will be within an existing building and will not be visible within the surrounding area. No waste or residue

will be produced. The waste heat dissipated in the cooling tower may result in some increase of visible indication of water evaporation under certain climatic conditions.

7.4 ENERGY CONSERVATION

This project, by its nature, is a consumer of energy. The energy conservation concept is not applicable to this project.

8. METHOD OF ACCOMPLISHMENT

It is proposed that the project be accomplished for the U.S. Department of Energy in the manner outlined in the following subsections.

8.1 DEPARTMENT OF ENERGY

DOE will furnish overall project coordination and review and will approve all required documents, administer all prime contracts, and direct and administer all aspects of the project, including specific approval of work assignments and approval of work performed.

8.2 OAK RIDGE NATIONAL LABORATORY

The Operating Contractor will provide all design documents and materials specifications. Title III services will be provided as required. The Maintenance Division will disassemble the existing machine and will rebuild the device as described herein. New components will be fabricated in area shops or will be procured from an outside vendor.

8.3 COST-PLUS-ADJUSTED-FEE CONTRACTOR

To the extent feasible, a cost-plus-adjusted-fee (CPAF) contractor will procure material and provide labor to modify the demineralized water system from the building headers to pipe flanges near the device.

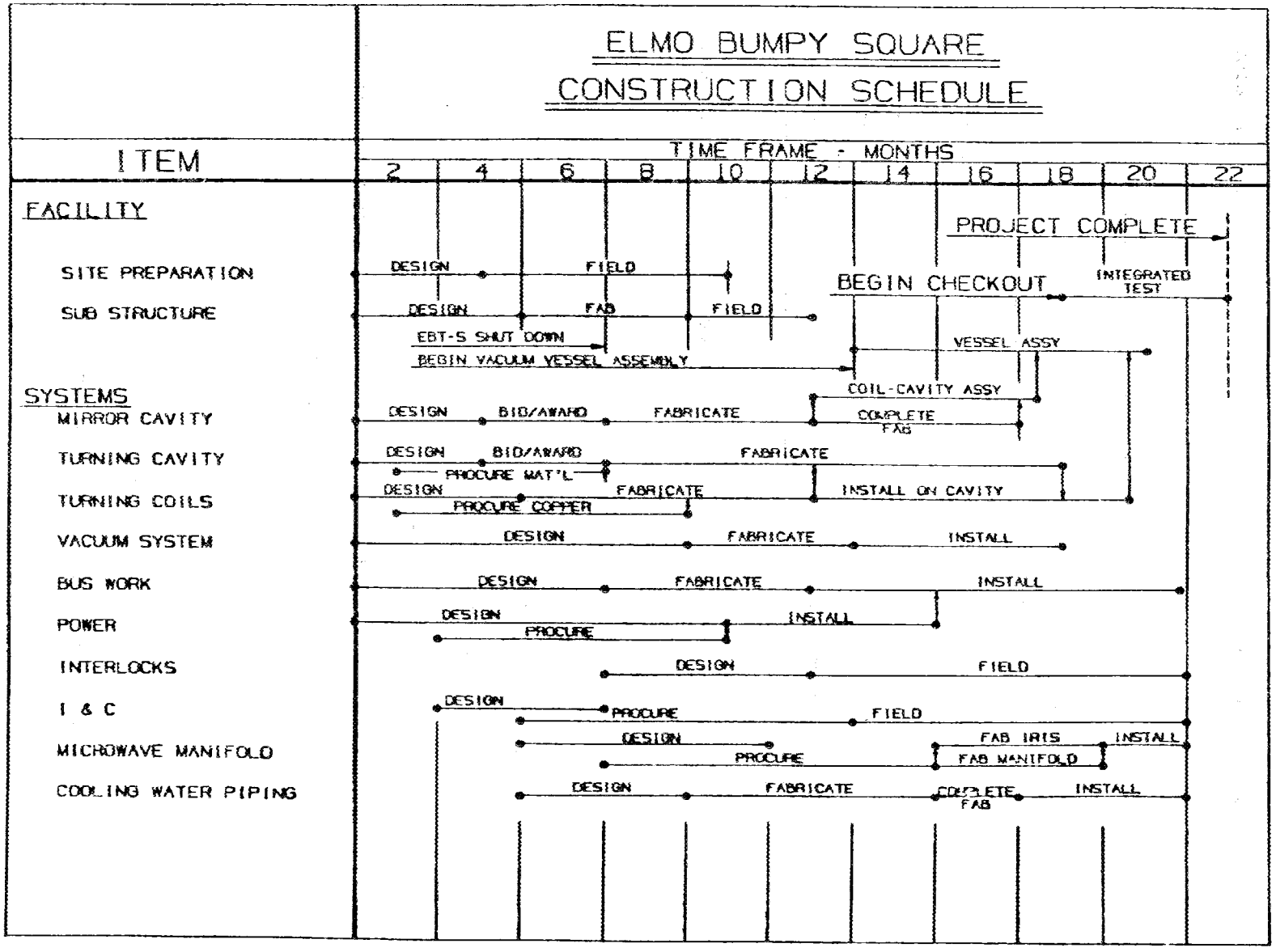
ELMO BUMPY SQUARE
CONSTRUCTION SCHEDULE
ITEM
TIME FRAME - MONTHS
2
4
6
8
10
12
14
16
18
20
22
FACILITY
PROJECT COMPLETE
SITE PREPARATION
DESIGN
FIELD
BEGIN CHECKOUT
INTEGRATED TEST
SUB STRUCTURE
DESIGN
FAB
FIELD
EBT-S SHUT DOWN
BEGIN VACUUM VESSEL ASSEMBLY
VESSEL ASSY
SYSTEMS
COIL-CAVITY ASSY
MIRROR CAVITY
DESIGN
BID/AWARD
FABRICATE
COMPLETE FAB
TURNING CAVITY
DESIGN
BID/AWARD
FABRICATE
PROCURE MAT'L
TURNING COILS
DESIGN
FABRICATE
INSTALL ON CAVITY
PROCURE COPPER
VACUUM SYSTEM
DESIGN
FABRICATE
INSTALL
BUS WORK
DESIGN
FABRICATE
INSTALL
POWER
DESIGN
INSTALL
PROCURE
INTERLOCKS
DESIGN
FIELD
I & C
DESIGN
PROCURE
FIELD
MICROWAVE MANIFOLD
DESIGN
FAB IRIS
INSTALL
PROCURE
FAB MANIFOLD
COOLING WATER PIPING
DESIGN
FABRICATE
COMPLETE FAB
INSTALL

10. COST ESTIMATE

The EBS cost estimate (in thousands of dollars) is listed below.

Engineering		$ 719
Titles I and II design	$464	
Project integration	$255	
Construction		$2709
Subtotal		$3428
Contingency		$ 808
TOTAL PROJECT COST		$4236

This cost estimate is based on the following lists of assumptions.

In scope

1. QA plan (including prerequisite Safety Analysis)
2. Removal of existing support structure
3. Design and construction of basic device
4. Title III support as required to establish as operational the vacuum and cooling systems and the coil power supplies

Out of scope

1. Removal of existing diagnostics
2. Removal of obsolete microwave components

3. Installation of diagnostics
4. Modification of biological shield to accommodate diagnostics or operations
5. Work on gyrotrons, their power supplies, rf supplies, and output power distribution networks
6. Modifications to blank cavity cover plates
7. Operational procedures (other than interlock logic)
8. Utilities around the machine associated with specialty operations and diagnostics

11. OUTLINE SPECIFICATIONS

11.1 GENERAL CODES, STANDARDS, AND SPECIFICATIONS

The applicable portions of the latest edition of the following codes, standards, and specifications will govern the work performed on this project.

11.1.1 DOE Manuals and Orders

2250.1 Cost and Schedule Control Systems Criteria for Contract Performance Measurement

5480.1A Environmental Protection, Safety, and Health Protection Program for DOE Operations

- Chapter I Environmental Protection, Safety, and Health Protection Standards
- Chapter VII Fire Protection
- Chapter XI Requirements for Radiation Protection
- Chapter XII Prevention, Control, and Abatement of Air and Water Pollution

5481.1A Safety Analysis and Review System (OR 5481.1A)

5484.1 Environmental Protection, Safety, and Health Protection Information Reporting Requirements

5484.2 Unusual Occurrence Reporting System

5700.4 Project Management System

5700.6A Quality Assurance (OR 5700.6)

6301 General Design Criteria

6430 Facilities General Design Criteria

11.1.2 Operating Contractor Engineering Procedures

Y/EF-538/R4, General Design Criteria for UCC-ND Projects

Engineering Standards

Safety and Fire Protection Standards

Welding Manual

11.1.3 Nationally Recognized Codes and Standards

American Society of Mechanical Engineers — Code

American Society for Testing and Materials — Standards

American Concrete Institute

American National Standards Institute

American Welding Society Standards

Concrete Reinforcing Steel Institute

Federal Aviation Administration Grounding, Bonding, and Shielding Practices for Electronic Equipment and Facilities (especially for diagnostics grounds)

Institute of Electrical and Electronics Engineers Standards

Instrument Society of America Standards

Insulated Power Cable Engineers Association

International Conference of Building Officials Uniform Building Code (Seismic Criteria)

Joint Industrial Council

National Electrical Code

National Electrical Safety Code — Handbook 81

National Fire Code, National Fire Protection Association

National Electrical Manufacturers Association Standards

Occupational Safety and Health Administration Standards

Underwriters Laboratory

Uniform Building Code

11.2 DEVICE MECHANICAL SYSTEMS

11.2.1 Vacuum System

The vacuum pumping system for the square configuration will consist of four pumps, each attached to one cavity section at the end of each side. Three existing turbomolecular pumps and one cryogenic pump will comprise the four pump complement mechanical foreline and tank roughing pumps will remain unchanged.

New cavity sections will be required that, with the existing mirror coil cases, constitute the plasma vacuum chamber. Six new "special" cavities will be required. Each is made of aluminum, is welded-plate constructed, and has a microwave port. These will have large cover plates on four sides, which will enhance diagnostic interfacing flexibility. The remaining fourteen cavities will have a simplified design to reduce costs and are flanged cylinders with one port for a microwave feed. Four cavities will have a vacuum pumping port, in addition.

11.2.2 Cooling System

The existing cooling system between the existing building headers and the EBS will be modified to accommodate the added heat load imposed by the corner coils. The cooling requirements for the magnet system

will increase from about 1200 gal/min to about 1750 gal/min (from 288 to 438 water paths at 4 gal/min). In addition to the magnet system, the vacuum vessel requires cooling to remove about 500 kW of heat deposited from ion cyclotron resonance heating (ICRH) and electron cyclotron resonance heating (ECRH).

The existing cooling water manifolds for the mirror coils will be modified and reinstalled. New manifolds will be fabricated for the turning coils. The manifolds around the machine will have connections for power bus cooling and cavity cooling and will have spares for diagnostic cooling, as well as for the mirror coil needs. Two gyrotrons for 28-GHz, 200-kW, continuous wave (cw), microwave power generation are now in place, and no changes will be required for their cooling systems, which are independent of the mirror coil cooling system.

11.2.3 Vacuum Vessel Support Structure

The existing support structure will be completely demolished down to the second floor level at elevation 289 m (949 ft).

The case of each mirror coil will be directly supported by a stand bolted to the floor. Each corner assembly will likewise be supported by a stand bolted to the floor. The individual stands will then be coupled by a concrete collar to distribute all centering and out-of-plane magnetic forces over the centerline span of the machine.

11.3 DEVICE ELECTRICAL SYSTEMS

11.3.1 Magnet System

Sixteen of the existing EBT mirror coils will be installed on this device — four each on each straight side. Four of the existing split mirror coils will be used, one on each side, and each in a different relative position. The coils on each side of the square are in series and in series with the opposite side of the square; they are powered by two dc generators in series with a combined rating of 700 V and 7140 A. Each corner has eight coils, each of which is physically half of the straight side mirror coils (two pancake coils instead of four); they are series connected and are in series with the opposite corner; they are powered by two dc generators in series with a combined rating of 700 V and 8570 A. The positive and negative solid copper bus around the machine is in close parallel alignment to cancel stray field effects.

Error field correction coils are not within the scope of this project, but adequate space consideration for their use is incorporated. Four continuous vertical and four continuous horizontal field coils will be located (one each) on the 45° planes out from the machine centerline.

Trim coils adjacent to the four turning coil assemblies are also provided for but are not part of the scope of this project. One circular coil, twice the diameter of a mirror coil, can be mounted inside each of the eight transition cavities. This location optimizes the function of the trim coils while removing space conflicts with other machine systems.

11.3.2 Microwave System

The microwave manifold will be a 10-cm-diam (4-in.-diam) copper duct square configured to match the coil-cavity arrangement. The manifold will connect to each straight-side cavity section through a 10-cm-diam (4-in.-diam) port, each port having an adjustable iris to control power distribution. Input power from one or both 28-GHz, 200-kW (cw) gyrotrons will be fed into the square manifold at a single point and split for a symmetric distribution at iris areas.

11.3.3 Device rf Sources

No changes to the radio frequency (rf) sources will be effected by the new configuration, other than a minor rerouting of ducts to fit the square geometry. New duct flanges will be required at the cavity interfaces, but these modifications are outside the scope of this project. Sources of rf power are listed here for information:

1. Gyrotrons — two each (28 GHz, 200 kW, cw). A power supply consisting of stacked, variable-voltage, regulated supplies will be used to drive either one or both of the gyrotrons. The beam supply has a rating of 100 kV at 10 A, and the gun supply is rated at 40 kV at 1.0 A.
2. Klystrons — Existing power supplies, oscillators, and amplifiers will be utilized for auxiliary heating in special experiments.
3. Transmitters — one each 2–30 MHz, 100 kW, cw; one each 2–30 MHz, 200 kW, cw; one each 175–215 MHz, 50 kW, cw; one each 2–30 MHz, 20 kW, cw; and one each 30–60 MHz, 20 kW, cw.

All of the sources listed are in place and are operational.

11.3.4 Instrumentation and Controls

The majority of the instrumentation and controls already exists. Additions will be made primarily in the cooling and generator control systems.

The vacuum and instrumentation systems exist and will be installed on the square configured device without change.

1. For vacuum instrumentation and control, the vacuum in each of the 20 cavities will be monitored by ion gauges. Line-pressure sensing and control-valve interlocks are provided for each of the three turbopumps to protect machine vacuum and to prevent damage to the pumps. Heated, interlocked molecular sieves are also provided for each turbopump. The turbopump foreline is instrumented with thermocouple gauges. The west quadrant utilizes a cryopump whose header is instrumented with ion and thermocouple gauges. Valving and interlocks are provided to adequately protect and isolate the cryopump.
2. All instrumentation for monitoring and controlling the sector coils already exists and need only be reconfigured to accommodate the new geometry. Valving interlocks and flow monitoring for the supply and return lines feeding the new corner coils will be added, along with 16 flow sensors for the coils themselves. A hose-break detector to be supplied by the Fusion Energy Division will be incorporated into the corner coil cooling-system instrumentation.
3. The controls for the west-end motor-generator (MG) sets currently in use are 18 years old and utilize obsolete components, some of which are now difficult to obtain. The circuit topology will remain

unchanged, but new controls utilizing components that reflect the state of the art will be supplied by the Fusion Energy Division. The control system for the east-end MG sets now in place has been developed from scratch, utilizing a high-gain, high-precision error amplifier incorporating excess di/dt sensing and protection, which drives an amplidyne generator to achieve precision closed-loop current regulation.

12. REFERENCE DATA

MECHANICAL	Dwg. No.
1. Plan View — Facility	SK10
2. Plan View — Machine	SK31
3. Elevation — Machine	SK30
4. Typical Elevation Cross Section	SK34
5. Flux Surface/Vacuum Vessel Interaction	SK32
6. Reference Configuration	SK36
7. Water piping	SK16
8. Water Manifolds & Support Structure	SK37
9. Circular Cavity	SK33
10. Square Cavity	SK19
11. Corner Assembly	SK35 (SHT. 1 & 2)
ELECTRICAL	
12. Plan View — Bus Work	SK21

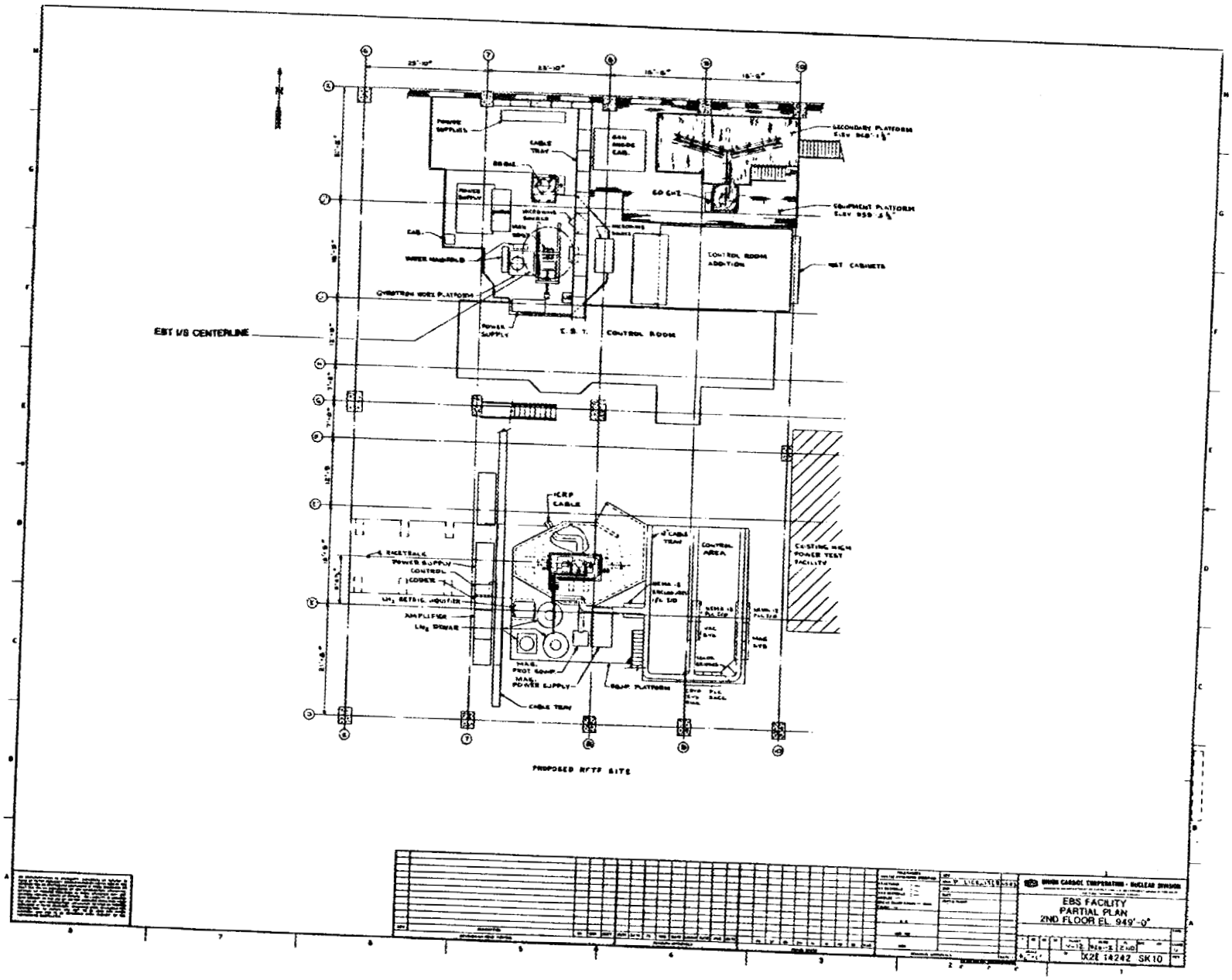
EBS I/S CENTERLINE
SECONDARY PLATFORM
EQUIPMENT PLATFORM
CONTROL ROOM ADDITION
MET CABINETS
POWER SUPPLY
C. S. T. CONTROL ROOM
CRP CABLE
CONTROL AREA
EXISTING HIGH POWER TEST FACILITY
MAG. POT SUMP
MAG. POWER SUPPLY
RAMP PLATFORM
CABLE TRAY
PROPOSED RFTF SITE
EBS FACILITY
PARTIAL PLAN
2ND FLOOR EL 949'-0"
X2E 14242 SK10

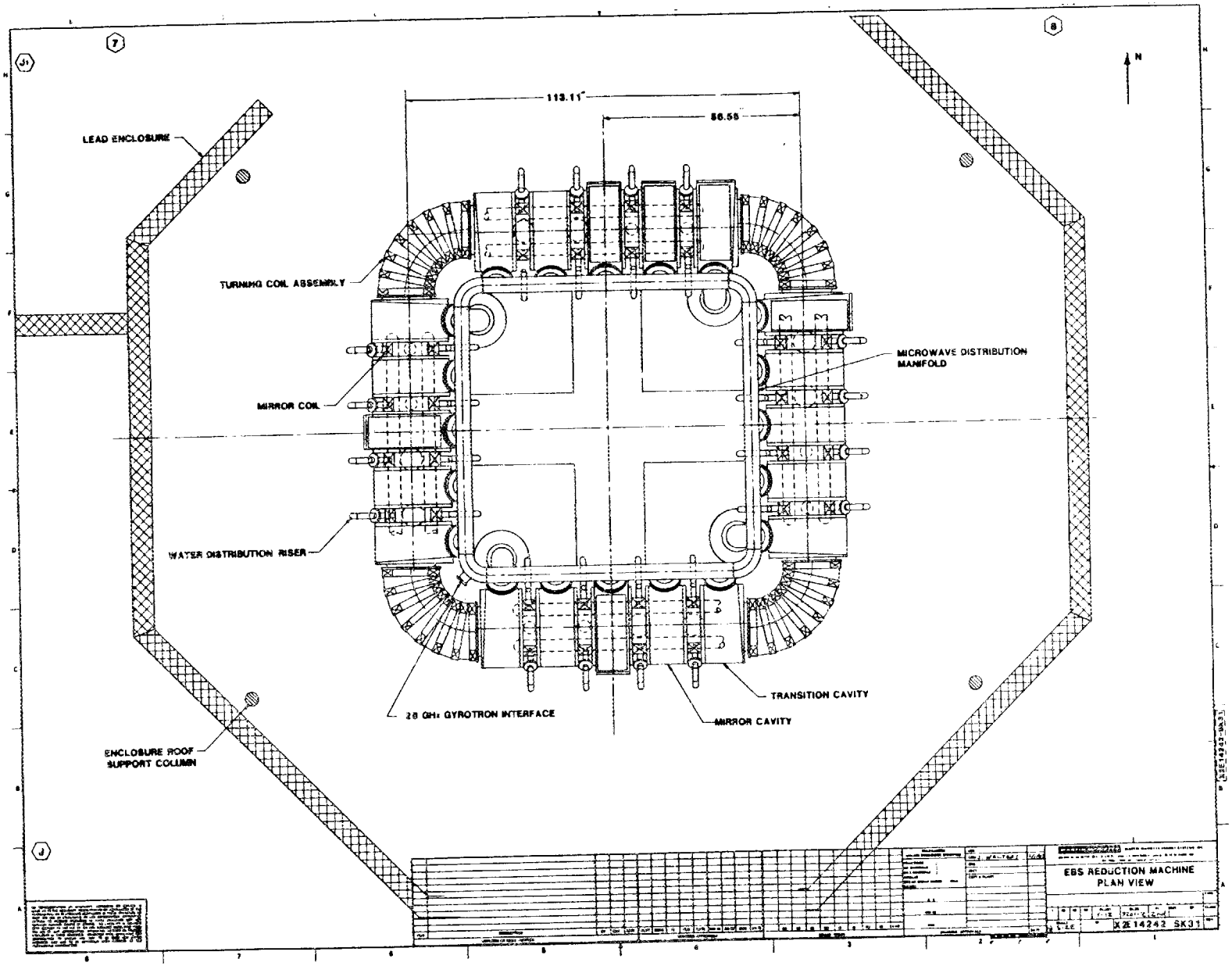
113.11"
56.55
N
LEAD ENCLOSURE
TURNING COIL ASSEMBLY
MICROWAVE DISTRIBUTION MANIFOLD
MIRROR COIL
WATER DISTRIBUTION RISER
28 GHz GYROTRON INTERFACE
TRANSITION CAVITY
MIRROR CAVITY
ENCLOSURE ROOF SUPPORT COLUMN
EBS REDUCTION MACHINE
PLAN VIEW
XE14242 SK31

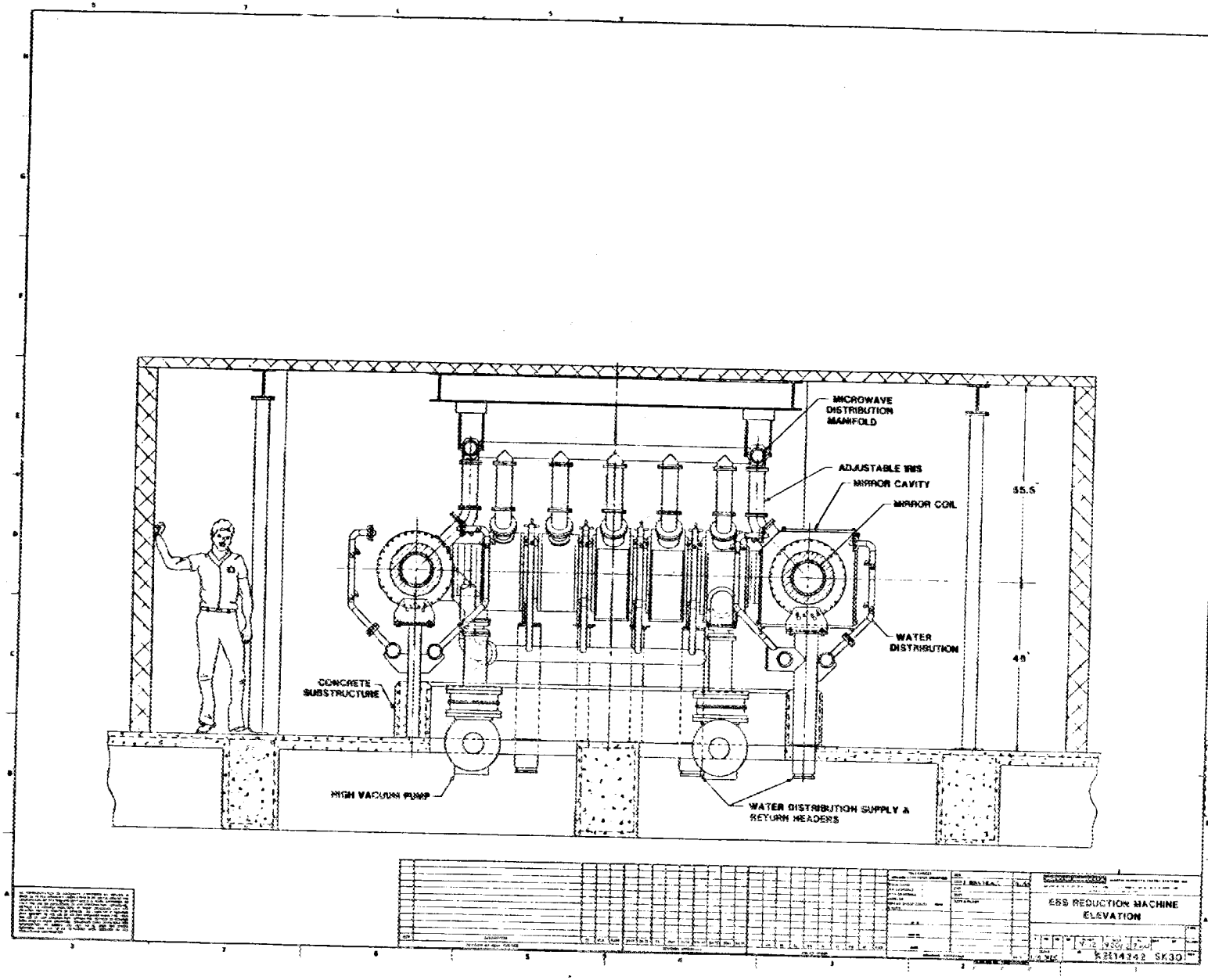
MICROWAVE DISTRIBUTION MANIFOLD
ADJUSTABLE IRIS
MIRROR CAVITY
MIRROR COIL
55.5'
48'
WATER DISTRIBUTION
CONCRETE SUBSTRUCTURE
HIGH VACUUM PUMP
WATER DISTRIBUTION SUPPLY & RETURN HEADERS
ESS REDUCTION MACHINE ELEVATION
5211242 SK30

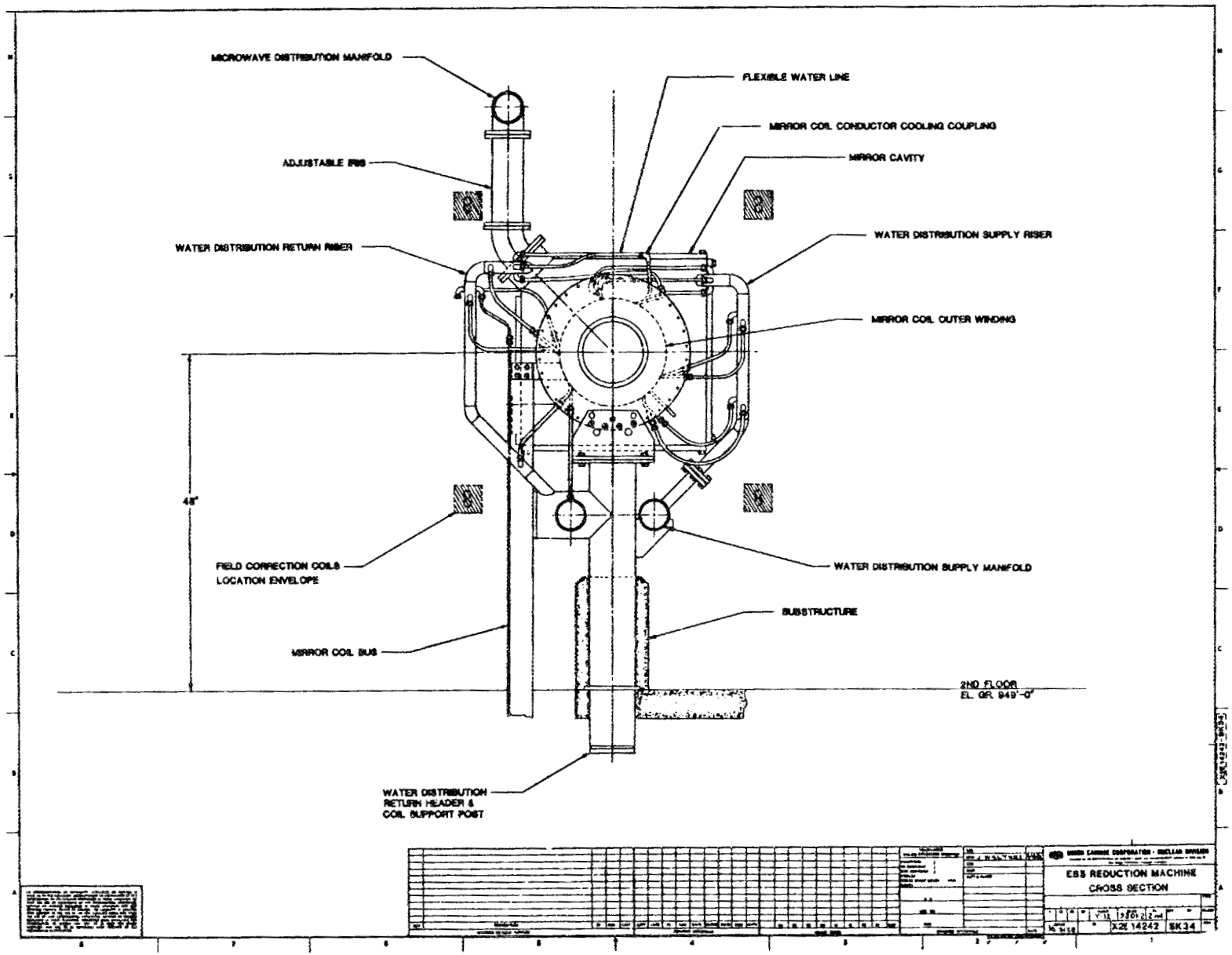
MICROWAVE DISTRIBUTION MANIFOLD
FLEXIBLE WATER LINE
MIRROR COIL CONDUCTOR COOLING COUPLING
MIRROR CAVITY
ADJUSTABLE RING
WATER DISTRIBUTION RETURN RISER
WATER DISTRIBUTION SUPPLY RISER
MIRROR COIL OUTER WINDING
48"
FIELD CORRECTION COILS
LOCATION ENVELOPE
WATER DISTRIBUTION SUPPLY MANIFOLD
SUBSTRUCTURE
MIRROR COIL BUS
2ND FLOOR
EL. GR. 949'-0"
WATER DISTRIBUTION
RETURN HEADER &
COIL SUPPORT POST
ESS REDUCTION MACHINE
CROSS SECTION
X2E 14242 SK34

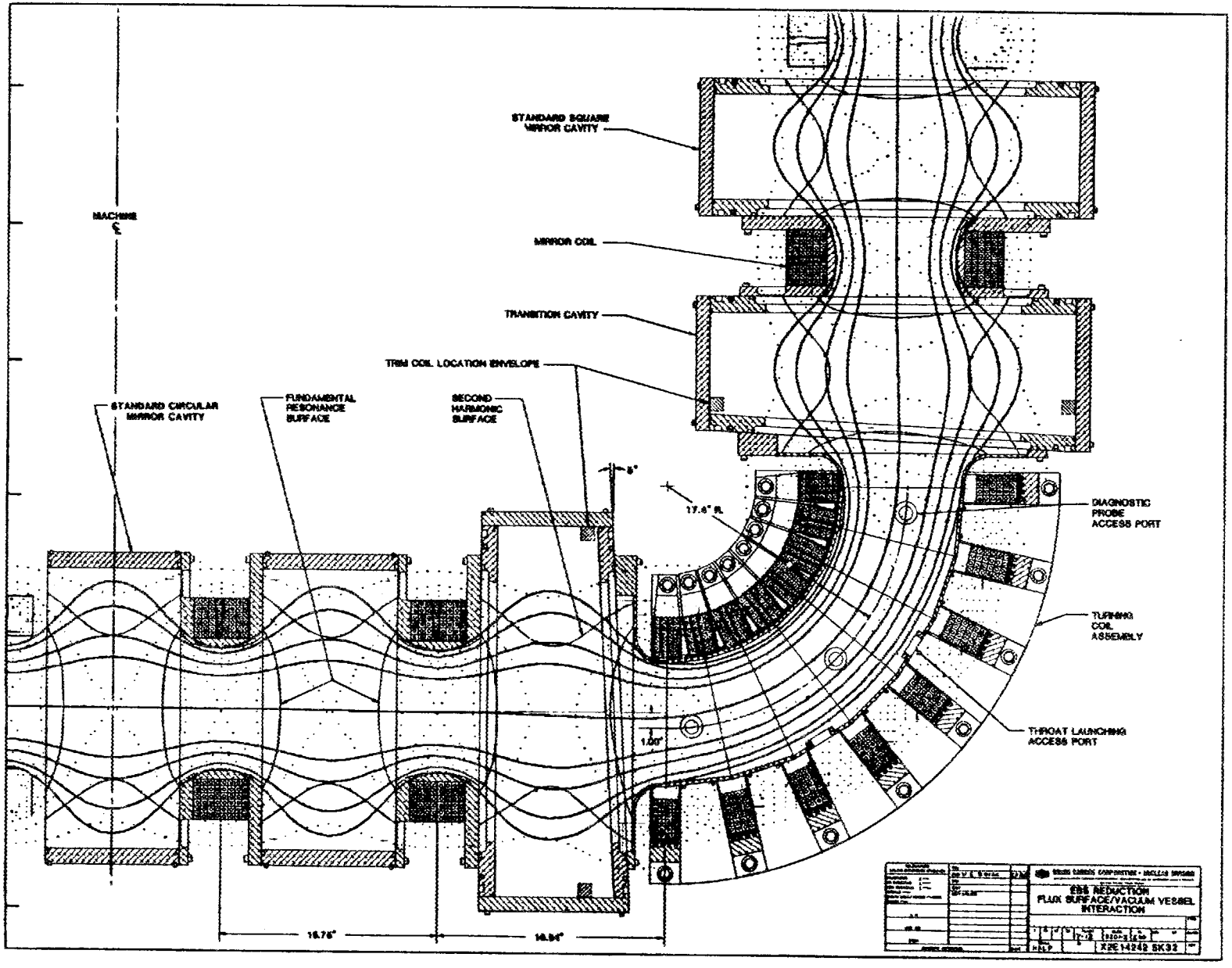
STANDARD SQUARE MIRROR CAVITY
MACHINE ℄
MIRROR COIL
TRANSITION CAVITY
TRIM COIL LOCATION ENVELOPE
STANDARD CIRCULAR MIRROR CAVITY
FUNDAMENTAL RESONANCE SURFACE
SECOND HARMONIC SURFACE
17.6" R.
DIAGNOSTIC PROBE ACCESS PORT
TURNING COIL ASSEMBLY
THROAT LAUNCHING ACCESS PORT
16.76"
16.94"
EBS REDUCTION
FLUX SURFACE/VACUUM VESSEL INTERACTION
X2E14248 SK32

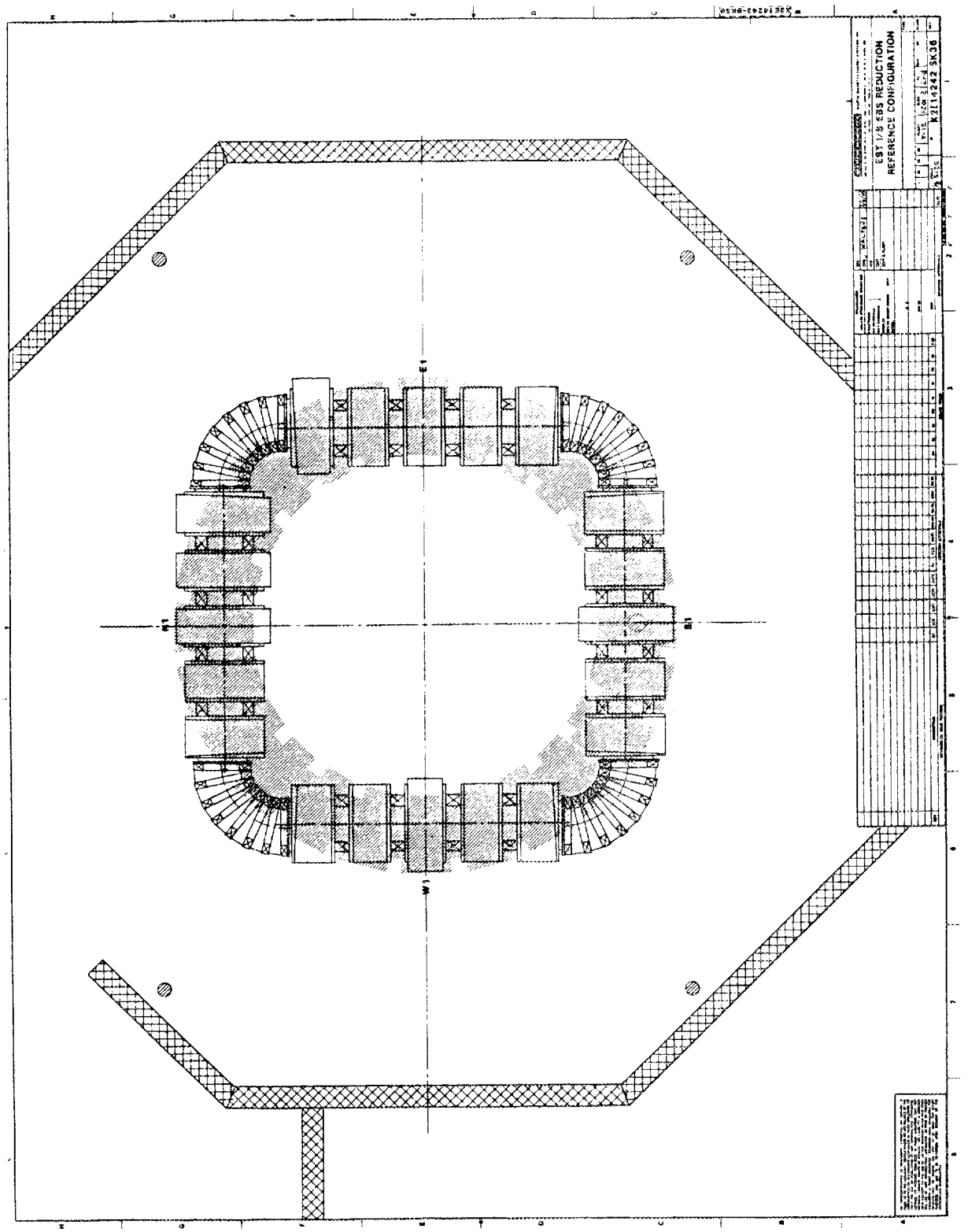
EST 1/4 SS REDUCTION
REFERENCE CONFIGURATION

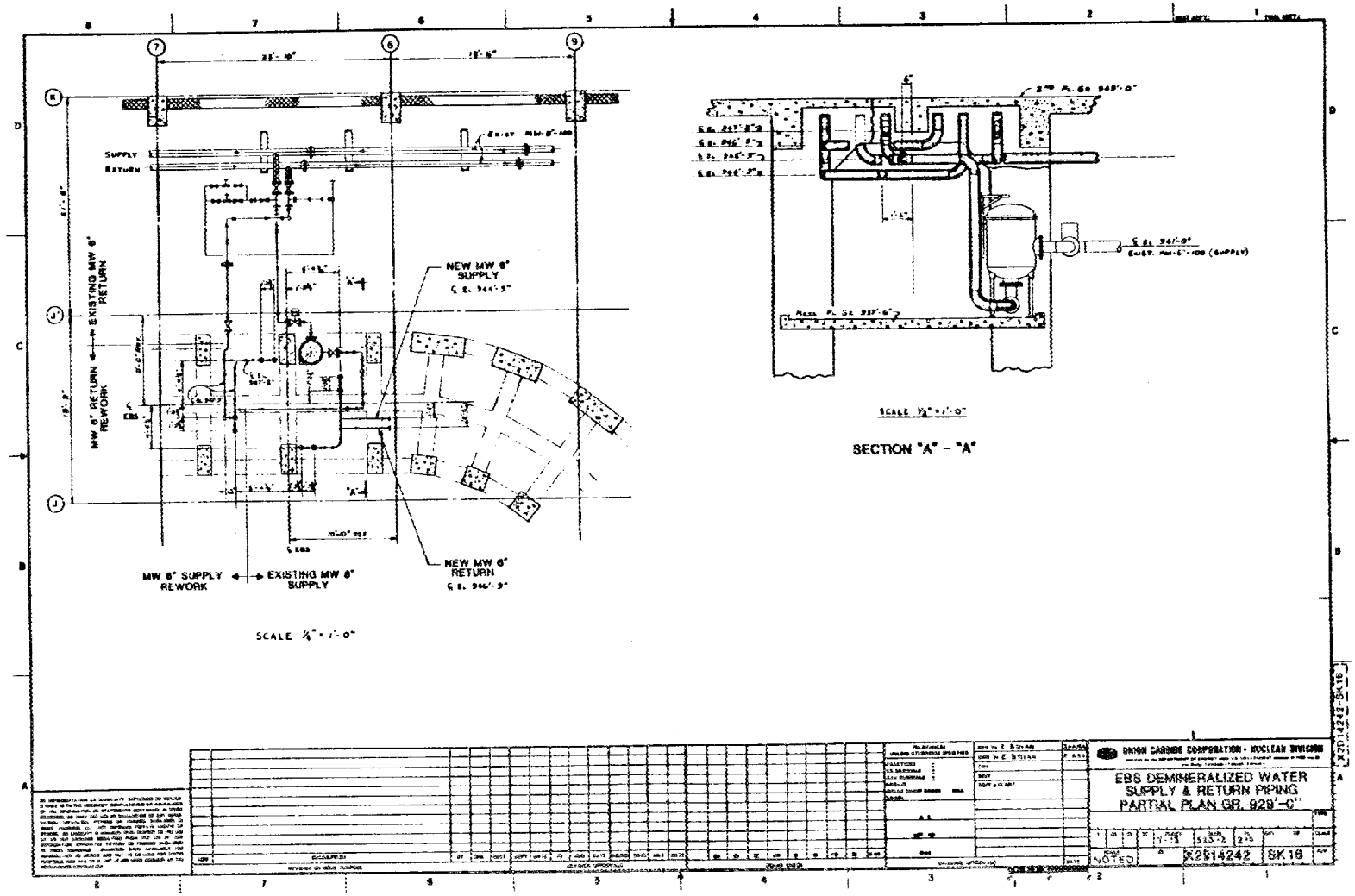
SUPPLY
RETURN
NEW MW 6" SUPPLY
NEW MW 6" RETURN
MW 6" RETURN REWORK
EXISTING MW 6" RETURN
MW 6" SUPPLY REWORK
EXISTING MW 6" SUPPLY
SCALE ¼" = 1'-0"
SECTION "A" – "A"
UNION CARBIDE CORPORATION - NUCLEAR DIVISION
EBS DEMINERALIZED WATER SUPPLY & RETURN PIPING PARTIAL PLAN GR. 929'-0"
X2914242
SK16

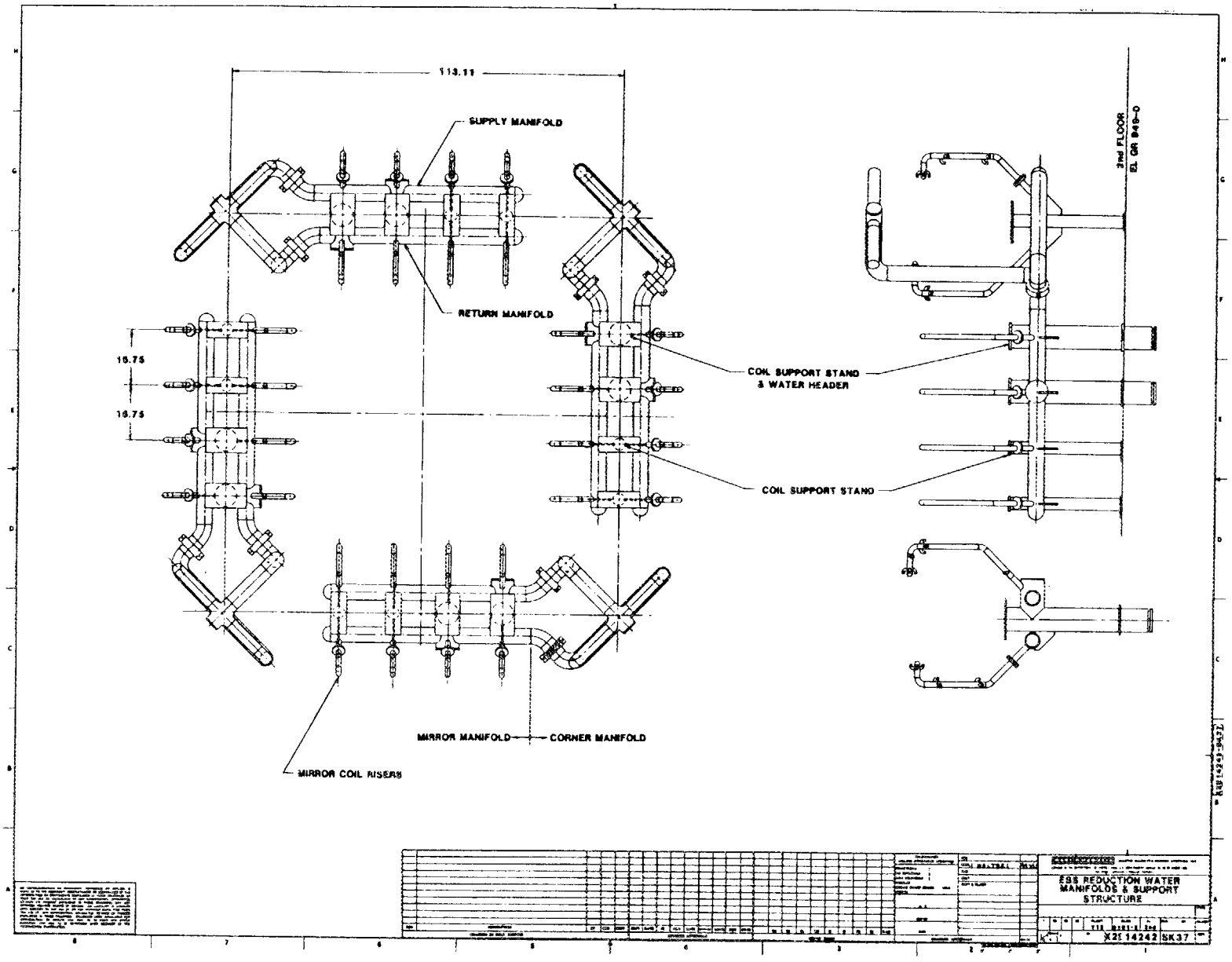
113.11
SUPPLY MANIFOLD
RETURN MANIFOLD
18.75
18.75
COIL SUPPORT STAND & WATER HEADER
COIL SUPPORT STAND
3rd FLOOR EL GR 849-0
MIRROR MANIFOLD
CORNER MANIFOLD
MIRROR COIL RISERS
ESS REDUCTION WATER MANIFOLDS & SUPPORT STRUCTURE
X25 14242 SK37

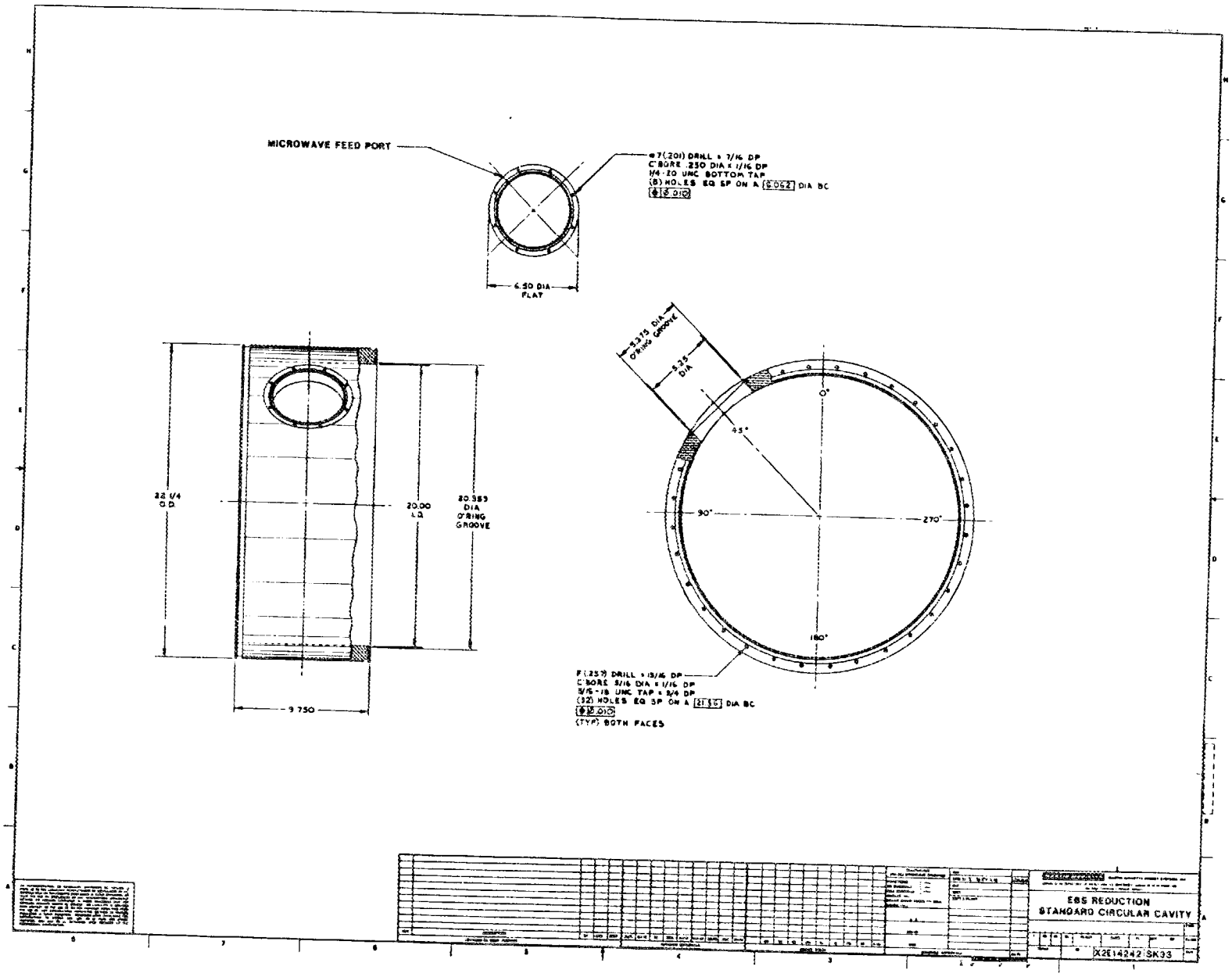
MICROWAVE FEED PORT
#7(.201) DRILL x 7/16 DP
C'BORE .250 DIA x 1/16 DP
1/4-20 UNC BOTTOM TAP
(8) HOLES EQ SP ON A .0062 DIA BC
.010
6.30 DIA FLAT
5.375 DIA O'RING GROOVE
5.25 DIA
0°
45°
90°
270°
180°
22 1/4 O.D.
20.00 I.D.
20.353 DIA O'RING GROOVE
9.750
F(.257) DRILL x 15/16 DP
C'BORE 5/16 DIA x 1/16 DP
5/8-18 UNC TAP x 5/8 DP
(32) HOLES EQ SP ON A 21.55 DIA BC
.010
(TYP) BOTH FACES
E&S REDUCTION
STANDARD CIRCULAR CAVITY
X2E14242 SK93

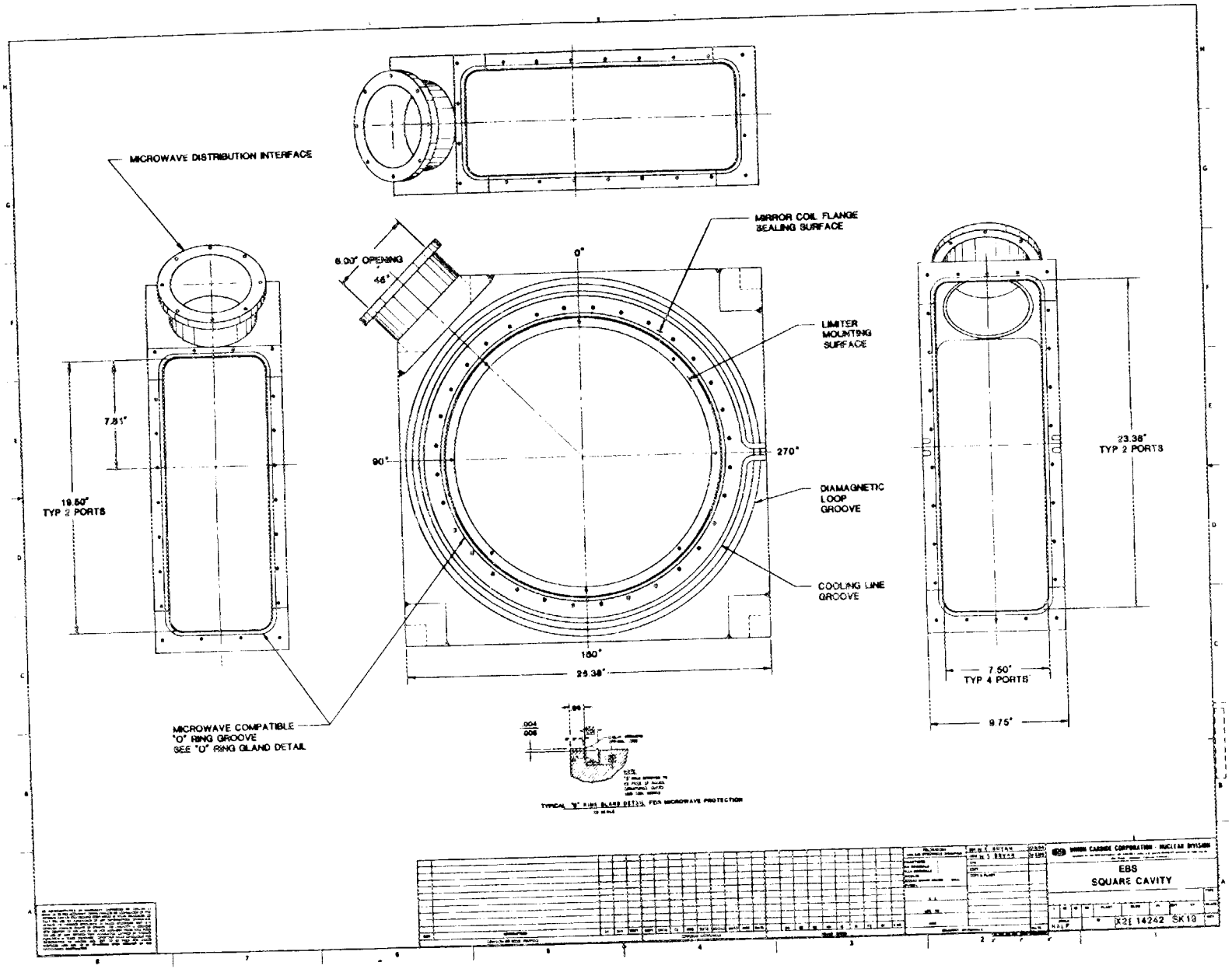
MICROWAVE DISTRIBUTION INTERFACE
MIRROR COIL FLANGE SEALING SURFACE
8.00" OPENING
46°
0°
LIMITER MOUNTING SURFACE
7.81"
19.80" TYP 2 PORTS
90°
270°
DIAMAGNETIC LOOP GROOVE
COOLING LINE GROOVE
180°
29.38"
23.38" TYP 2 PORTS
7.50" TYP 4 PORTS
9.75"
MICROWAVE COMPATIBLE "O" RING GROOVE SEE "O" RING GLAND DETAIL
EBS
SQUARE CAVITY
X21 14242 SK13

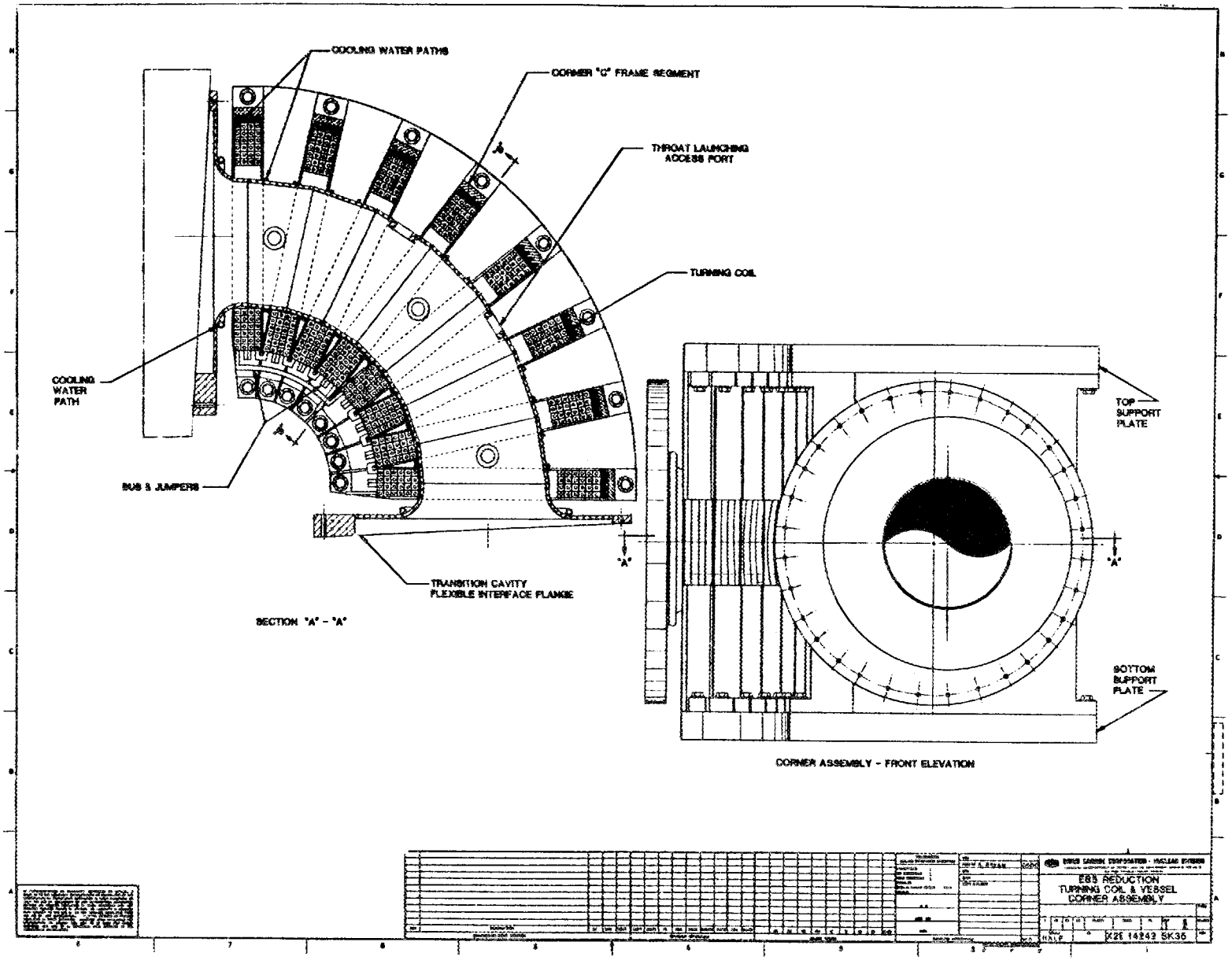
COOLING WATER PATHS
CORNER "C" FRAME SEGMENT
THROAT LAUNCHING ACCESS PORT
TURNING COIL
COOLING WATER PATH
BUS & JUMPERS
TRANSITION CAVITY FLEXIBLE INTERFACE FLANGE
SECTION "A" - "A"
"A"
"A"
TOP SUPPORT PLATE
BOTTOM SUPPORT PLATE
CORNER ASSEMBLY - FRONT ELEVATION
ESS REDUCTION
TURNING COIL & VESSEL
CORNER ASSEMBLY
X25 14242 SK35

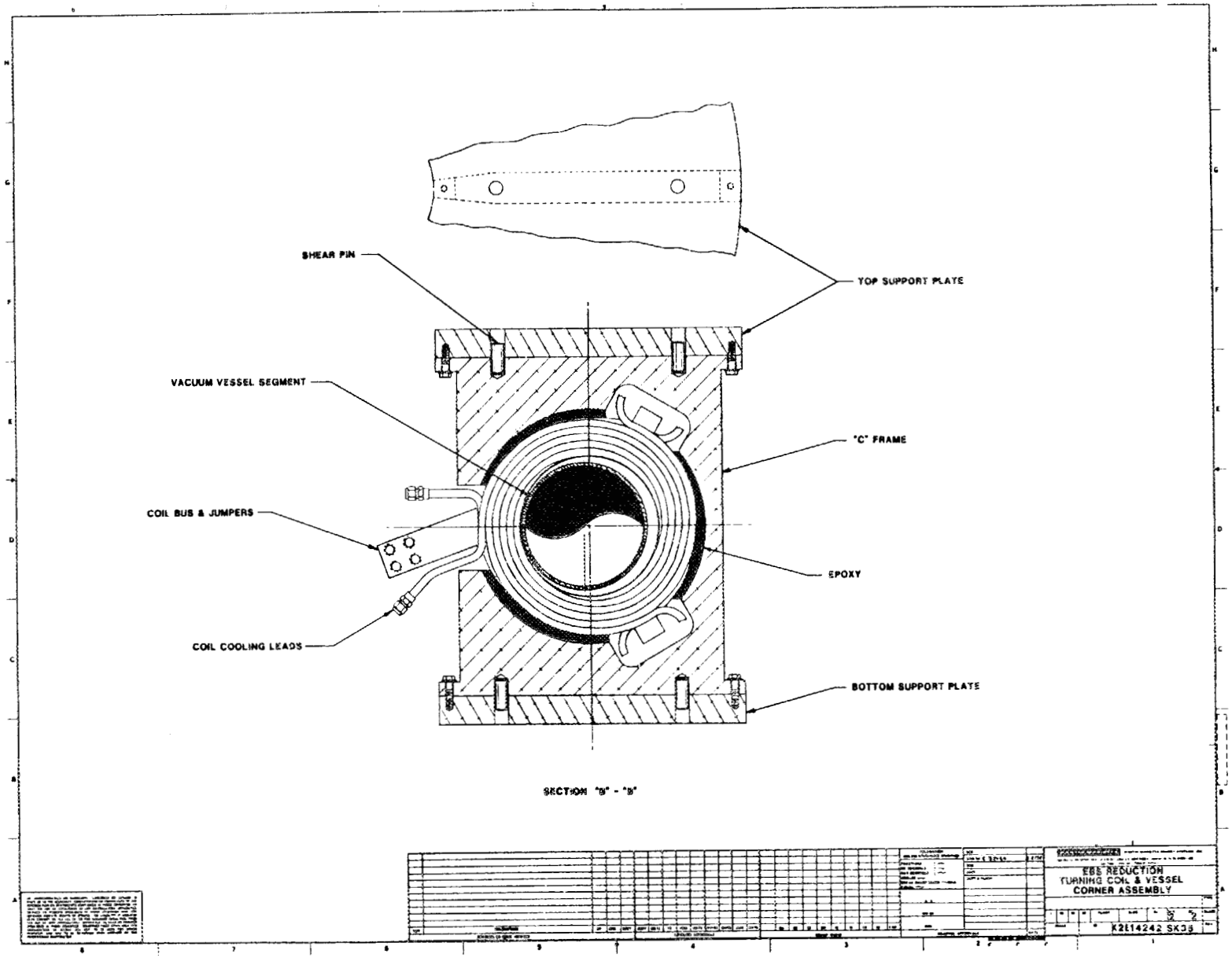
SHEAR PIN
TOP SUPPORT PLATE
VACUUM VESSEL SEGMENT
"C" FRAME
COIL BUS & JUMPERS
EPOXY
COIL COOLING LEADS
BOTTOM SUPPORT PLATE
SECTION "B" - "B"
EBS REDUCTION
TURNING COIL & VESSEL
CORNER ASSEMBLY
K2E14242 SK38

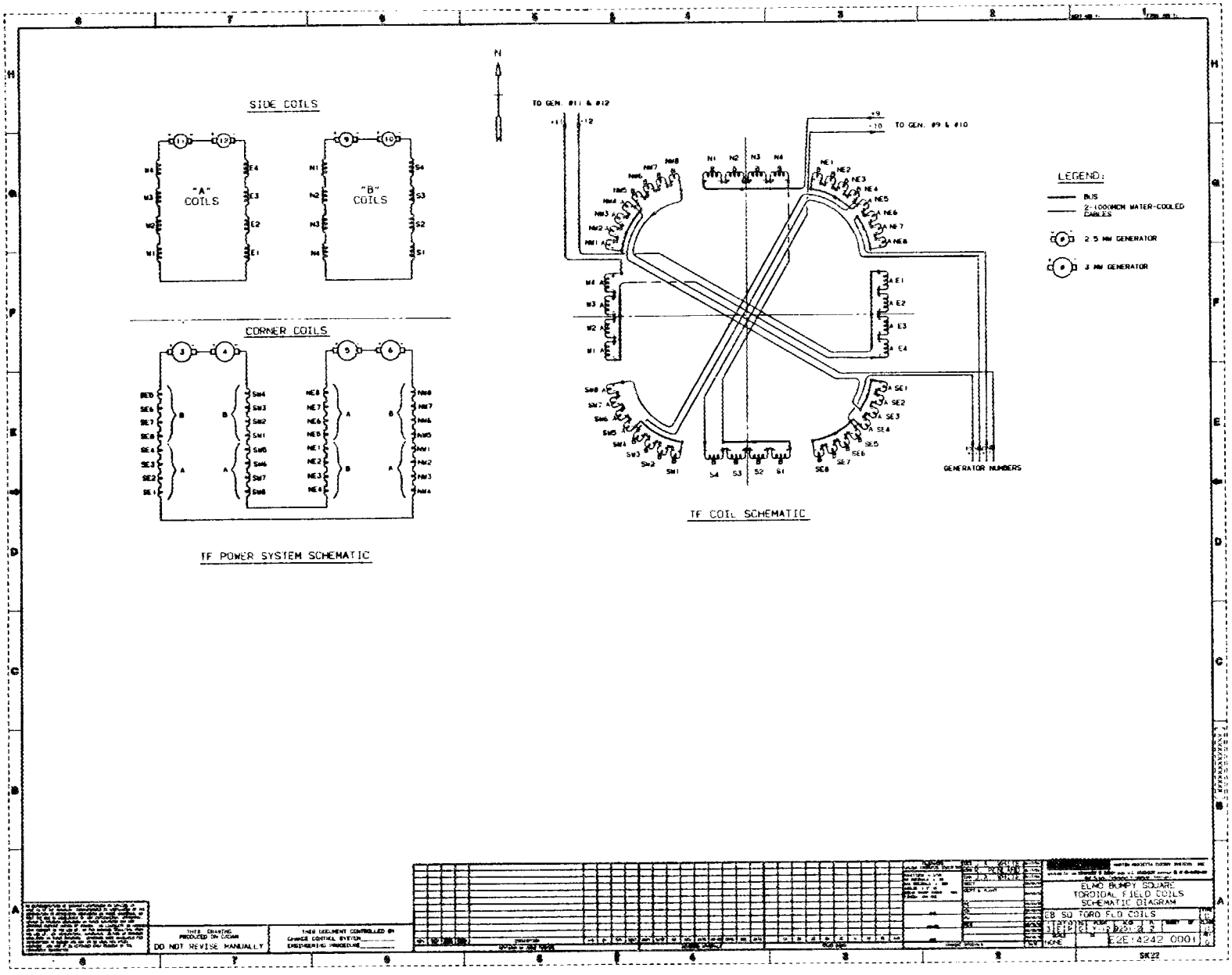
SIDE COILS
"A" COILS
"B" COILS
CORNER COILS
TF POWER SYSTEM SCHEMATIC
N
TO GEN. #11 & #12
TO GEN. #9 & #10
LEGEND:
BUS
2-1000MCM WATER-COOLED CABLES
2.5 MW GENERATOR
3 MW GENERATOR
GENERATOR NUMBERS
TF COIL SCHEMATIC
ELMO BUMPY SQUARE
TOROIDAL FIELD COILS
SCHEMATIC DIAGRAM
EB SQ TORO FLD COILS
DO NOT REVISE MANUALLY
SK22

9. REACTOR ASSESSMENTS OF ADVANCED BUMPY TORUS CONFIGURATIONS

N. A. Uckan, L. W. Owen, D. A. Spong, R. L. Miller,*
W. B. Ard,** J. F. Pipkins,** and R. J. Schmitt**

Here we summarize the results from refs. 1 and 2. Recently, several innovative approaches were introduced for enhancing the performance of the basic ELMO Bumpy Torus (EBT) concept and for improving its reactor potential.[3,4] These include planar racetrack and square geometries, Andreoletti coil systems, and bumpy torus-stellarator hybrids (which include the twisted racetrack and helical axis stellarator — snakey torus). Preliminary evaluations of reactor implications of each approach have been carried out based on magnetics (vacuum) calculations, transport and scaling relationships, and stability properties deduced from provisional configurations that implement the approach but are not necessarily optimized.[1,2] Further optimization is needed in all cases to evaluate the full potential of each approach.

Results of these studies[1,2] indicate favorable reactor projections with a significant reduction in reactor physical size as compared to conventional EBT reactor design[3] carried out in the past. Specifically, with these advanced configurations, reactors with $R \simeq 20 \pm 3$ m are found to be possible; this is almost a factor of 2 reduction in size compared to recent EBT reactor design points with $R \simeq 40 \pm 5$ m (which utilizes symmetrizing coils for an aspect ratio enhancement) for comparable power outputs. (Here R is defined as $2\pi R$-equivalent major radius.) This makes it possible to operate at high wall loadings (~2 to 4 MW/m^2 instead of ~1 to 1.5 MW/m^2) and increased engineering fusion power density.

---

*Applied Microwave Plasma Concepts, Inc., Encinitas, California 92024.
**McDonnell Douglas Astronautics Company, St. Louis, Missouri 63166.

9.1 INTRODUCTION

Several aspects of the ELMO Bumpy Torus (EBT) concept make it attractive as a fusion reactor: the large aspect ratio; simple, noninterlocking circular coils with modest field; modularity; and, above all, the steady-state operation. There have been several EBT reactor studies demonstrating the advantages resulting from these aspects of the EBT concept, the most recent of which is discussed in ref. 3.

During the recent U.S.-Japan Workshop on Advanced Bumpy Torus Concepts, several configurational approaches and concept improvement schemes emerged for enhancing the performance of the basic EBT concept and for improving its reactor potential.[4] These include (but are not limited to) configurations with (1) noncircular magnetic coils — Andreoletti coil systems;[5] (2) square or racetrack geometries without[6] or with[7] rotational transform; and (3) stellarator-bumpy torus hybrids — snakey torus.[8] In all cases EBT-like hot electron rings are used to stabilize the interchange modes driven by the unfavorable magnetic field curvature either on a continuous, steady-state basis [for cases (1) and (2) above] or on a transient basis during startup to access the "second stability regime" [for case (3) above].

The results of recent preliminary reactor assessments of these advanced bumpy torus configurations are summarized in the following sections.[1,2]

9.2 COMMENTS ON BASIC EBT CONFIGURATION

The toroidal curvature of the magnetic field in EBT results in an inward shift of particle drift orbits toward the major axis. The relative amount of shift, however, depends on the pitch angle ($V_{\parallel}/V$). This shift is largest for the transitional (resonant) and toroidally passing particles (i.e., those having $V_{\parallel}/V$), and it is smallest for particles trapped near the midplane of each sector (i.e., those having small $V_{\parallel}/V$). This dispersion in the displacement of particle drift orbits plays a major role in diffusive and direct particle losses.

The drift orbits are determined by contours of constant J, the longitudinal adiabatic invariant ($J = \oint V_{\parallel} d\ell$). The shift in drift orbit centers is then determined from R_{JMIN} — the radial position of the minimum of J. The volumetric efficiency $F(V_{\parallel}/V) = A(V_{\parallel}/V)/A(V_{\parallel} = 0)$ is defined as the ratio of the last closed drift orbit area

of a particle with a given pitch angle to that of $V_{\parallel} = 0$ (purely trapped particle).

In a simple bumpy torus, an increase in aspect ratio reduces the dispersion in drift orbits and improves the confinement of all classes of particles. The need for better confinement characteristics and efficient utilization of magnetic fields has led in the past to reactors with large physical size and power output. Through the use of low-current supplementary coils (i.e., ARE and SYM coils[9]) or inverse-D coils,[3] however, it was possible to reduce the reactor sizes from about $R_T \simeq 60$ m (ref. 10) to about $R_T \simeq 35$ m (ref. 3) for a fusion power output of $P \sim 1200$–1500 MWe. Results of the recent reactor studies with SYM and inverse-D coils are given in ref. 3. With the new advanced configurations, further reduction in reactor physical size has been shown to be possible. In all cases, unless otherwise specified, the following parameters are used: average plasma radius $\bar{a} \simeq 1.5$ m ($a = 1$ m under the coil); $B_{oo} = B_{min} \simeq 2.5$ T and $B_{max} \simeq 5.5$ T for mirror fields on-axis; the blanket and shield thickness under the mirror coil $\simeq 1.0$ m and is distributed nonuniformly between the coils; and the mirror coil half thickness $\simeq 0.35$ m.

9.3 EBT WITH ANDREOLETTI COILS (EBTEC)

The EBTEC (EBT with enhanced confinement) configuration consists of a toroidal array of racetrack-shaped coils — "Andreoletti coils" — whose major axes are alternately oriented vertically and horizontally.[5] By adjusting the elongation of the coils (H/W, height-to-width ratio) and the relative shifts in the centers of alternate coils, it has been shown that it is possible to obtain nearly concentric trapped and passing particle drift surfaces, thus greatly reducing the random-walk step-size for diffusion. As in EBT, the core plasma is stabilized by the hot electron rings which form near mod-B contours in the midplane. Here we present preliminary results for a reactor-size device.

Among the various sizes studied for a reactor, we present two cases here: (1) greatly enhanced confinement for a device comparable in size to the latest circular coil EBT reactor design, which uses SYM coils for aspect ratio enhancement,[3] that is, for $R_T \simeq 35$ m, and (2) a reduced major radius device, $R_T \simeq 20$–25 m, with confinement comparable to a circular coil reactor ($R_T \simeq 35$ m). In the calculations, the blanket and shield thickness is assumed to be 1.0 m at the limiting

coil throat in the shortest direction, and it has a nonuniform (>1 m) distribution between the coils (as well as under the coil in the longest direction).

For the enhanced confinement case ($R_T \simeq 35$ m, $M = 2.25$, and $a \simeq 1.25$ m under the coil), Fig. 9.1 shows the dispersion in drift orbit centers of trapped and passing particles, $\Delta R_{JMIN} = [R_{JMIN}(V_{\parallel}/V) = 0)] - [R_{JMIN}(V_{\parallel}/V) = 1)]$, vs the outward shift of the vertical coils relative to the horizontal coils. Because of less shift requirement, $H/W = 3$ has been chosen for the coils. To have $\Delta R_{JMIN} \simeq 0$, about a 7.5-m shift of coil centers is required. One quadrant of the equatorial plane of the configuration for this case is shown in Fig. 9.2.

A plot of volumetric efficiency (percent of area enclosed by a drift surface) in the midplane vs $V_{\parallel}/V$ is shown in Fig. 9.3 for an EBTEC reactor and for a circular coil EBT reactor without and with SYM coils for the same R, a, and M. Note that the EBTEC has nearly concentric orbits for all $V_{\parallel}/V$; however, the area for the resonance particles is small due to shielding scrape-off. It may be possible to alleviate this scrape-off by proper shaping or parameter optimization. In any case, a very significant improvement in resonance particle behavior over the circular coil case is evident from Fig. 9.3.

For the reduced major radius case ($R_T \simeq 20$–25 m), Fig. 9.4 (a plot of ΔR_{JMIN} vs R_T) indicates that drift orbit centering becomes poorer as R_T decreases. The coil shift is about 10 m; however, a larger shift could be used to reduce ΔR_{JMIN} further.

Figure 9.5 shows a 14-sector device with $R_T = 26.5$ m for the vertical coils and $R_T = 16.5$ m for the horizontal coils. The plasma in the midplane is centered at $R_T = 23$ m. Figure 9.6 shows the limiting field lines in the equatorial plane and the mod-B contours. Note that the distortion from the shift has moved the minimum in mod-B contours off of the midplane. Nevertheless, a drift surface analysis was carried out in the "geometric midplane." Figure 9.7 shows the trapped and passing particle drift orbits in this midplane. $\Delta R_{JMIN} \simeq 0.6$ m is lower than the value deduced from Fig. 9.4, but the plasma radius a is smaller here. Volumetric efficiency corresponding to this case is also shown in Fig. 9.3. Comparison with the circular coil EBT reactor still indicates significant improvement.

To summarize the results, we see that for the $R_T \simeq 35$ m case, trapped and passing particle orbits can be made to nearly coincide. A very narrow resonance region results (see Fig. 9.3), which can perhaps

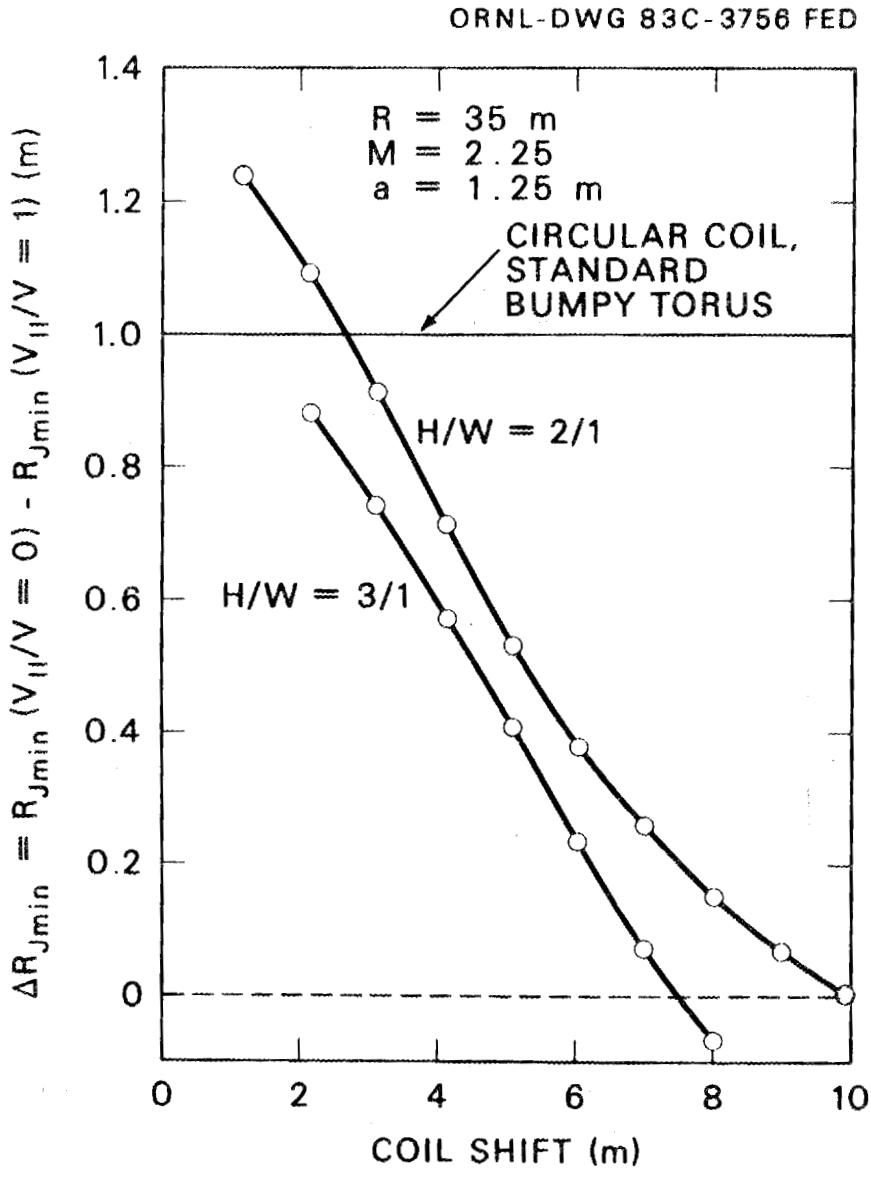

Fig. 9.1. Dispersion in drift orbit centers of trapped and passing particles, ΔR_{JMIN}, vs coil shift for an R_T = 35 m EBTEC.

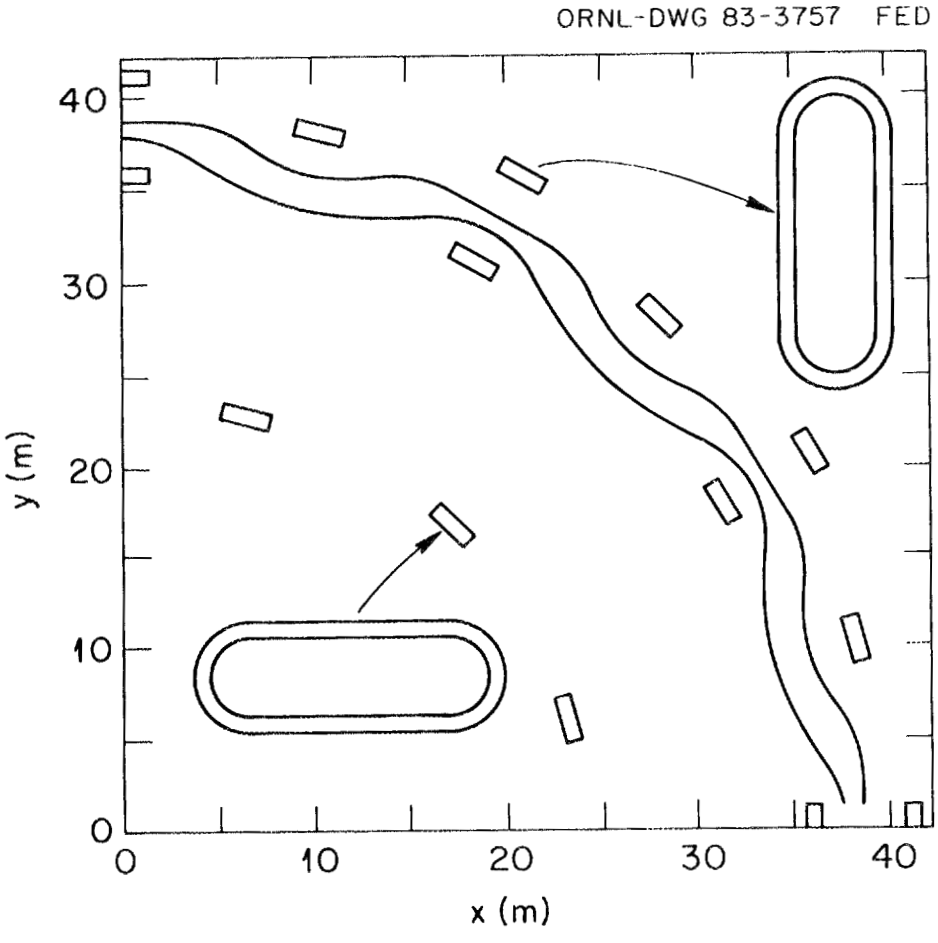

Fig. 9.2. One quadrant of an R_T = 35 m EBTEC projected onto the equatorial plane, with two magnetic lines of force and orientation of coils shown.

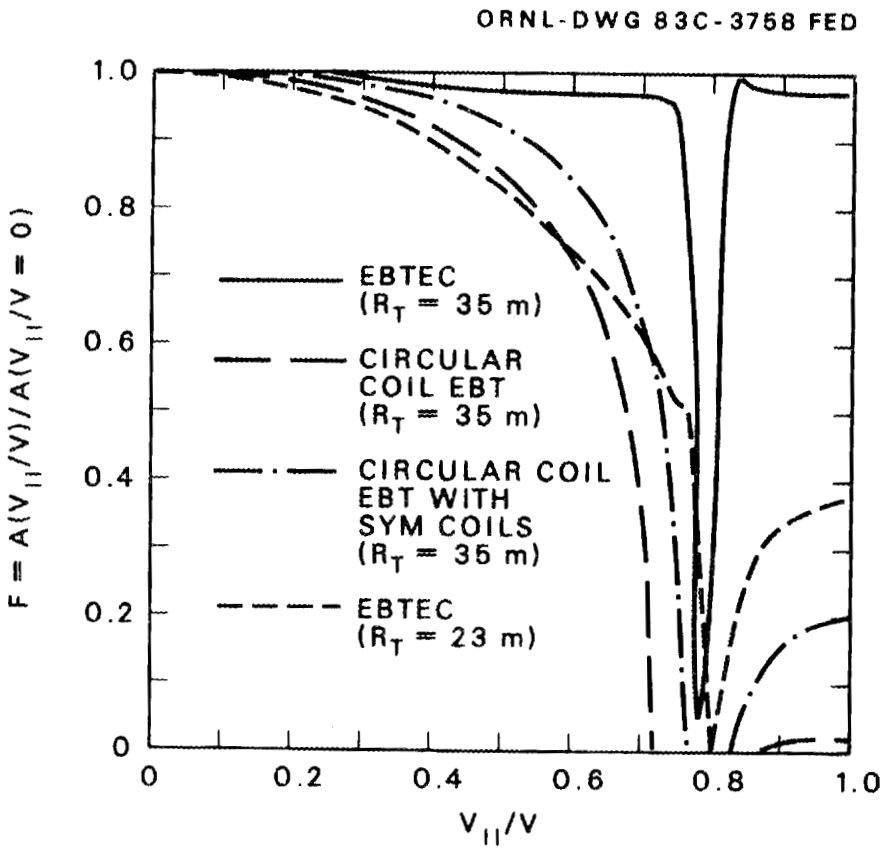

Fig. 9.3. Volumetric efficiency vs pitch angle for an EBTEC reactor (R_T = 35 m and 23 m) and for a circular coil EBT reactor (R_T = 35 m) with and without SYM coils.

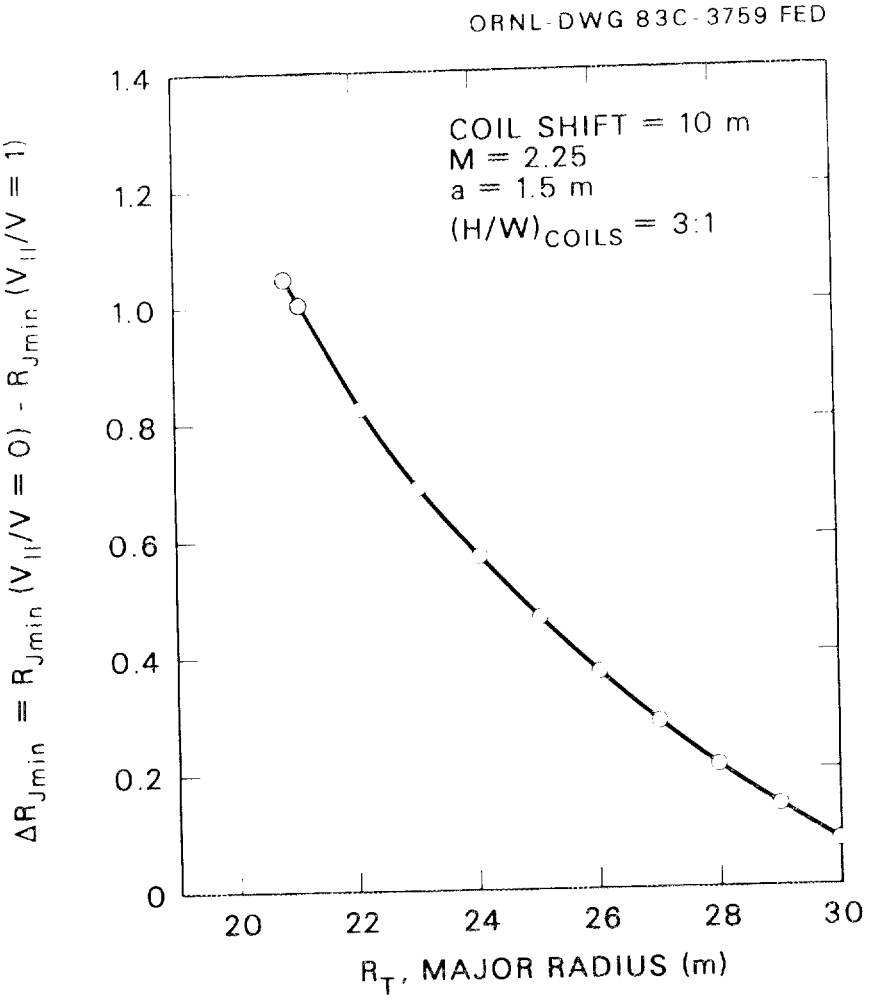

Fig. 9.4. Dispersion in drift orbit centers vs major radius for an EBTEC.

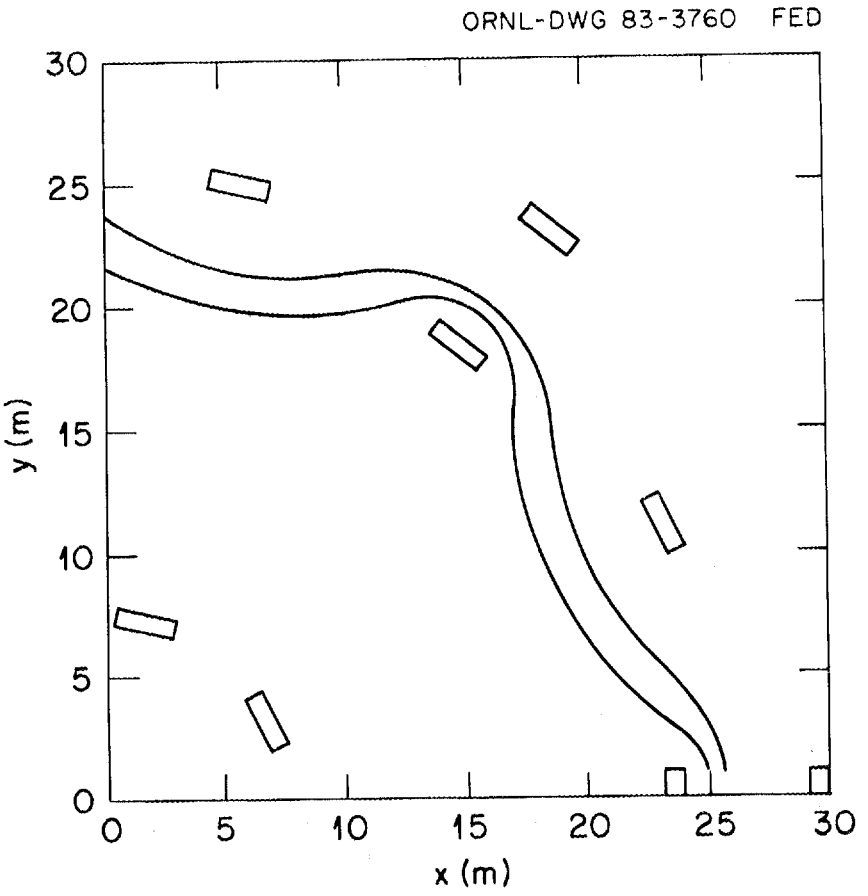

Fig. 9.5. One quadrant of a 14-sector EBTEC reactor.

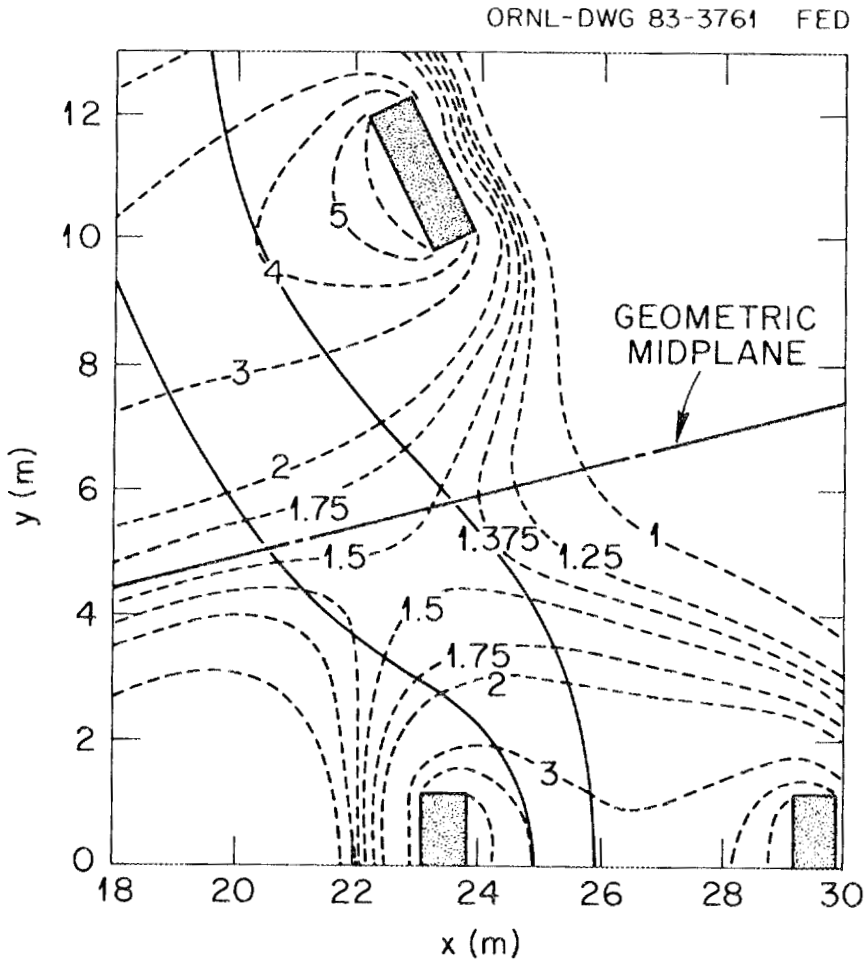

Fig. 9.6. Mod-B contours (dashed) and limiting field lines (solid) in the equatorial plane for an R_T = 23 m EBTEC.

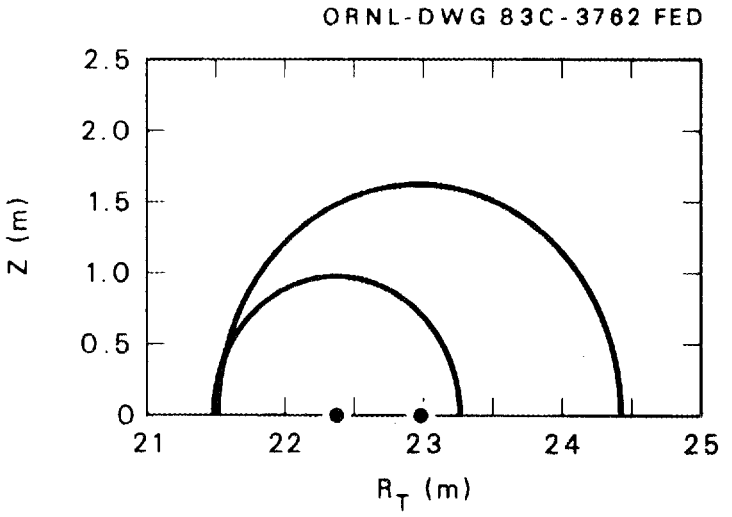

Fig. 9.7. Shape of the trapped (outer curve) and passing (inner curve) particle drift orbits in the "geometric midplane" (only upper half portions are shown).

be eliminated with further optimization; in particular, if R_T is increased, the resonant particles become circular at large plasma radius. For R_T = 23 m, the 14-coil case, the confinement is significantly better than for the R_T = 35 m circular coil reactor. To simplify the coils it may be possible to design alternative, smaller coils which produce the same magnetic field geometry as the shifted Andreoletti coils.

9.4 ELMO BUMPY SQUARE

The ELMO Bumpy Polygon geometry, in which the magnetic axis is not circular but is shaped like a racetrack, triangle, square, pentagon, etc., consists of linear segments of simple mirrors (made of circular or elliptical coils) that are linked by sections of high-field toroidal solenoids. In these configurations, the toroidal effects are localized in regions of high magnetic field, thereby minimizing the effect of toroidal curvature on single particle drift orbits, volumetric efficiency, etc. As in EBT, the core plasma is stabilized by the presence of hot electron rings in the linear mirror sections. For a near-term, experimental-size device (such as EBT-S), EBS has been shown to have single particle confinement properties and plasma volume utilization that are distinctly superior to those of a standard EBT of comparable size (see Sect. 1 of this report).

High-field solenoid sections (corners) can be circular or elliptical in cross section. It is also possible to replace the coils in the straight sections with the Andreoletti coils discussed previously. Reactor characteristics of the bumpy square (as well as the racetrack) are analyzed for both circular and Andreoletti coils. Significant improvements (similar to the results discussed previously) in orbit centering and volumetric efficiency over those of the circular coil EBT are found.

Figure 9.8 shows the variation of the normalized magnetic field strength as a function of arc length along the magnetic axis for one quadrant (straight section plus two half-corners) of a typical reactor case, which consists of three linear mirror sectors per side (total of 12 mirrors plus 4 corners). The on-axis mirror ratio in the sides is ~2.2 and the "global" mirror ratio (B at the corners/B at the reference midplane, B_{oo}) for this particular case is 3.6. The mirror coils on the sides are 8-T magnets, and the corner coils are 12 T. From the shape of the curve in Fig. 9.8, one can see that there are

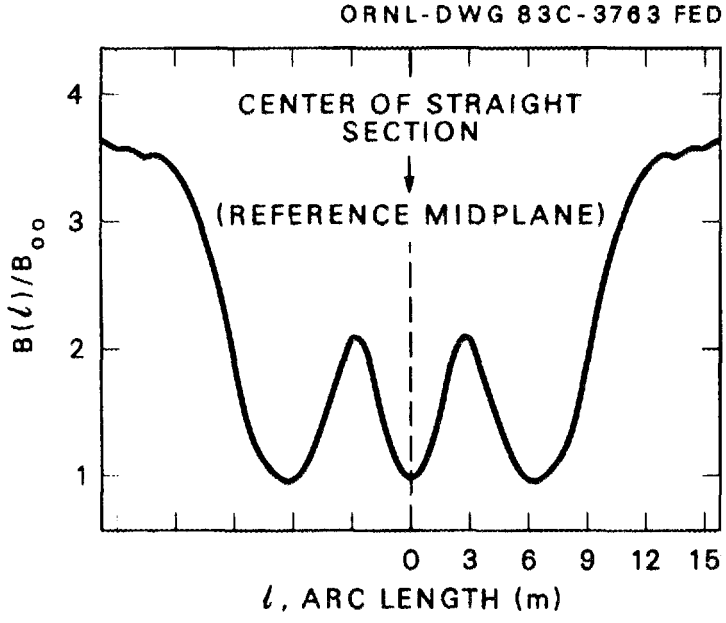

Fig. 9.8. Variation of the magnetic field as a function of arc length along the magnetic axis for one quadrant (straight section plus two half-corners) of an R_T = 20.5 m EBS.

mirror-trapped particles in a single sector, mirror-trapped particles between the high-field corners, and passing particles. There are also transitional particles that turn or barely pass near the various field maxima. The equivalent major radius of the device (circumference/2π) shown in Fig. 9.8 is about $R_T \simeq 20.5$ m, which has drift orbit characteristics much better than the $R_T = 35$ m circular coil EBT (Fig. 9.3). Transitional and passing particle orbit characteristics are similar to and the trapped particle orbits are significantly better than the $R_T = 35$ m EBT with SYM coils.

Simple scaling calculations indicate that diffusive step-size $\Delta\chi (= \Delta R_{JMIN})$ is inversely proportional to the global mirror ratio (B_{corner}/B_{oo}) and the ratio of the length of the straight section to the curved section,

$$\Delta\chi \propto \left[\frac{B_{corner}}{B_{oo}}\right]^{-1}\left[\frac{NL_m}{2\pi R_{cor}}\right]^{-1} \propto \left[\frac{B_{corner}}{B_{oo}}\right]^{-1}\left[\frac{N}{2\pi}\right]^{-1} ,$$

where N is the number of mirrors (in straight sections), L_m is the mirror sector length, and R_{cor} is the radius of the corner (toroidal solenoid) in which $R_{cor} \simeq (1\text{-}1.2)\ L_m$. We note that confinement time scales with $1/(\Delta\chi)^2$ and thus with the square of the global mirror ratio.

Figure 9.9 shows a field line drawing (in the equatorial plane) of a hybrid configuration, a bumpy square with Andreoletti coils. Here each straight section (side) consists of two mirror sectors with one horizontal Andreoletti coil ($H/W = 2$). Among the configurations studied, this one (though not optimized) gives the smallest bumpy square geometry for a reactor with an equivalent major radius of $R_T = 17.5$ m. The volumetric efficiency and drift orbit characteristics are much better than the $R_T = 20.5$ m bumpy square case discussed previously. Figure 9.10 shows the volumetric efficiency for the $R_T = 17.5$ m EBS. As we see, the orbit characteristics for all classes of particles for the $R_T = 17.5$ m EBS are significantly better than the $R_T = 35$ m EBT with SYM coils (Fig. 9.10).

Figure 9.11 shows a field line drawing of another hybrid configuration — a bumpy square with horizontal "teardrop" coils in which the shape of the coil is shown in Fig. 9.12. This is similar to the case discussed previously (see Fig. 9.9); however, in this case the plasma occupies a large fraction of the coil volume. The teardrop

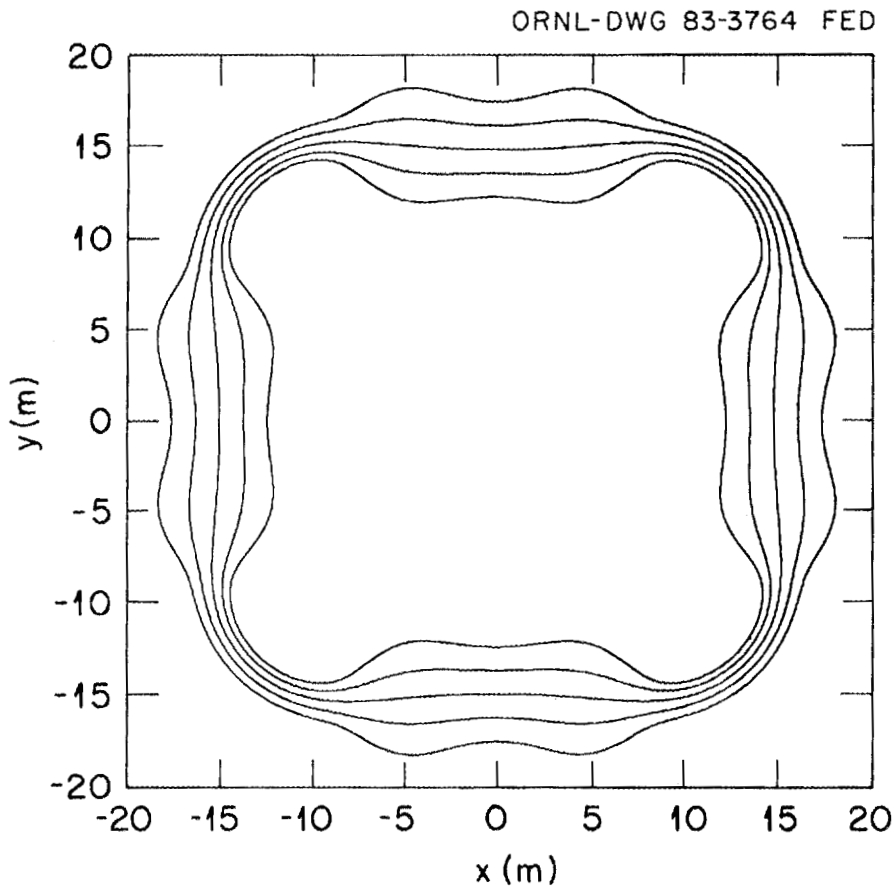

Fig. 9.9. Equatorial plane, field line drawing of an R_T = 17.5 m bumpy square with horizontal Andreoletti coils in straight sections.

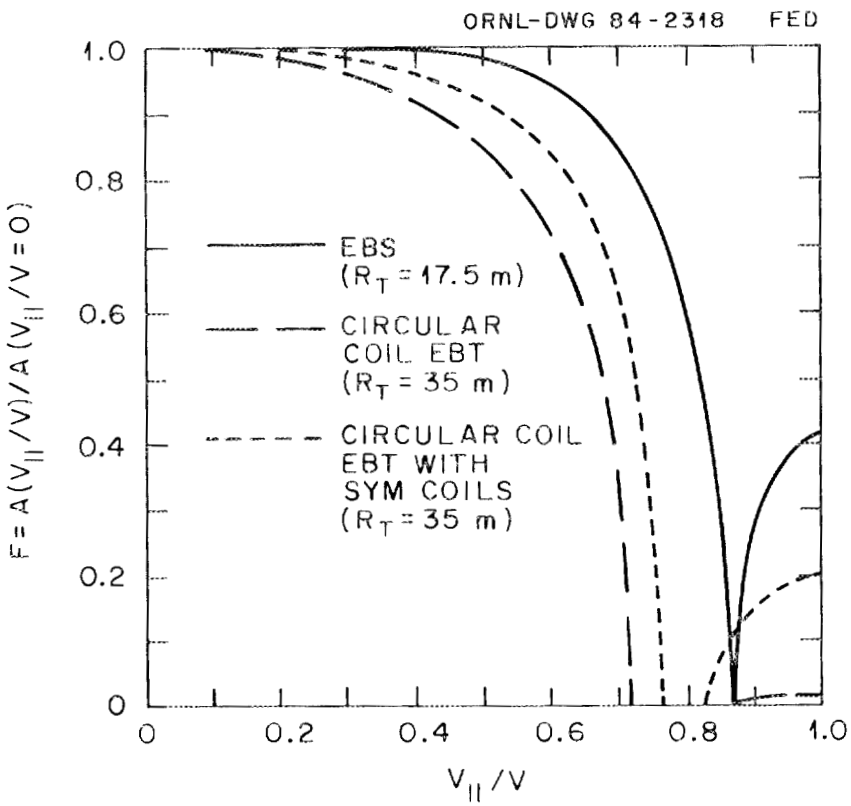

Fig. 9.10. Volumetric efficiency vs pitch angle for an EBS reactor (R_T = 17.5 m) and for a circular coil EBT reactor (R_T = 35 m) with and without SYM coils.

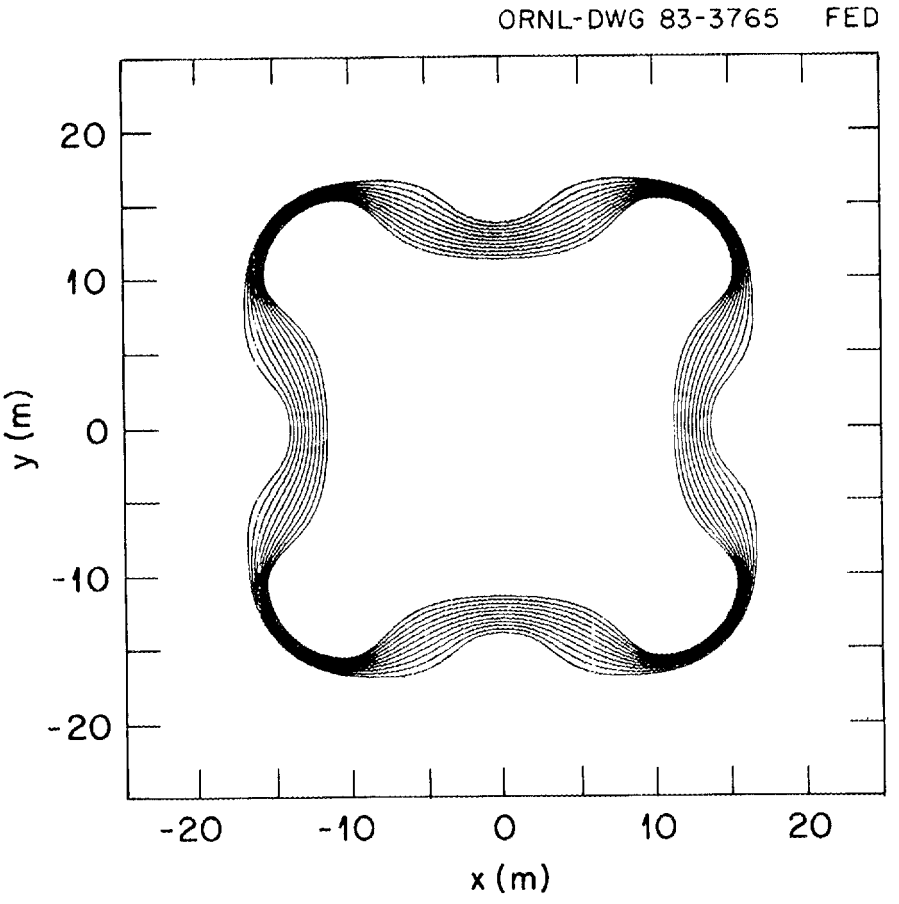

Fig. 9.11. A field line drawing of a bumpy square with horizontal "teardrop" coils in straight sections. Equivalent major radius $R_T \simeq 19.5$ m.

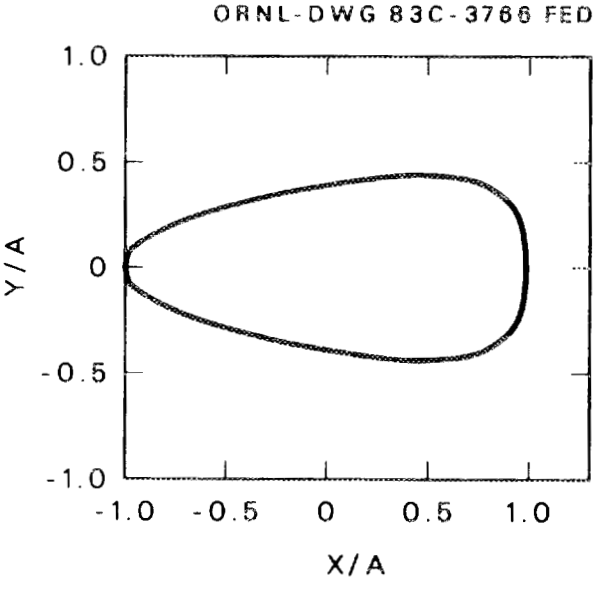

Fig. 9.12. Shape of the "teardrop" coil.

coils (one on each side) are shifted inward relative to the corners. Figure 9.13 shows the variation of the normalized magnetic field strength as a function of arc length along the magnetic axis for one quadrant, where $B_{oo} \simeq 2.2$ T, $L_m \simeq 10$ m, and $R_{cor} \simeq 6.5$ m. The global mirror ratio is about 5. The teardrop coils are 10-T magnets with modest current density and the corner coils are 15 T. The corner coils are of a much smaller cross section, and the total weight of all the coils in one corner is comparable to that of one teardrop coil. A plot of volumetric efficiency is given in Fig. 9.14, which compares very favorably with Figs. 9.3 and 9.10.

Because there are a finite number of coils that can be placed in corners, field ripple effects may play an important role. Ballooning modes associated with the corners and the effect of parallel currents on equilibrium and confinement properties are considered in Sects. 4 through 7 of this report.

9.5 TWISTED RACETRACK

The twisted racetrack (TRT) EBT is a type of "figure 8" stellarator with two straight sections composed of axisymmetric mirror sectors. In this configuration (Fig. 9.15), as in EBT, the "bumpiness" of the field provides favorable poloidal drifts and equilibrium, and the hot electron rings (in the straight sections) provide the stability. Rotational transform is introduced (by twisting the racetrack) to improve the confinement. The curved solenoid sections do not contain rings (as in the planar bumpy racetrack or bumpy square configurations) and have an on-axis field approximately equal to the magnetic field in the coil throats of straight sections. The flux surfaces are nearly concentric circles with essentially no shear. Thus the objective of TRT is to obtain a configuration with favorable EBT stability and equilibrium properties that has the stellarator-like favorable transport at modest aspect ratio.

Preliminary calculations carried out for a TRT reactor also indicate considerable improvement (similar to EBTEC and EBS) over a standard EBT configuration. The example looked at is for $R_T \simeq 20$ m, equivalent circumference major radius. It consists of six axisymmetric mirrors per straight section (with a mirror ratio $M = 2.25$ and mirror length $L_m \simeq 6.5$ m) — a total of 12 mirrors — and curved solenoid end connectors with a radius of $R_{cor} \simeq 8$ m. The rotational transform is $q(\text{axis}) \simeq 1.7$ and $q(\text{limiter}) \simeq 2.3$.

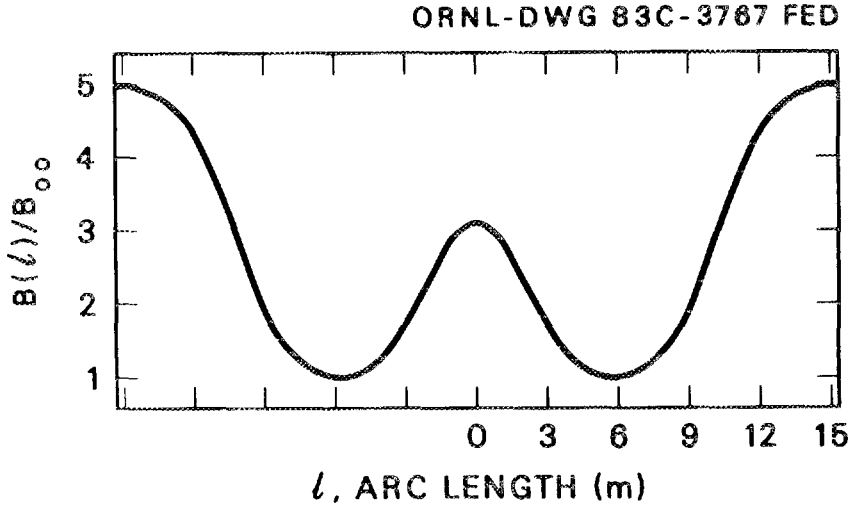

Fig. 9.13. Variation of the magnetic field as a function of arc length along the magnetic axis for one quadrant of a bumpy square configuration shown in Fig. 9.11.

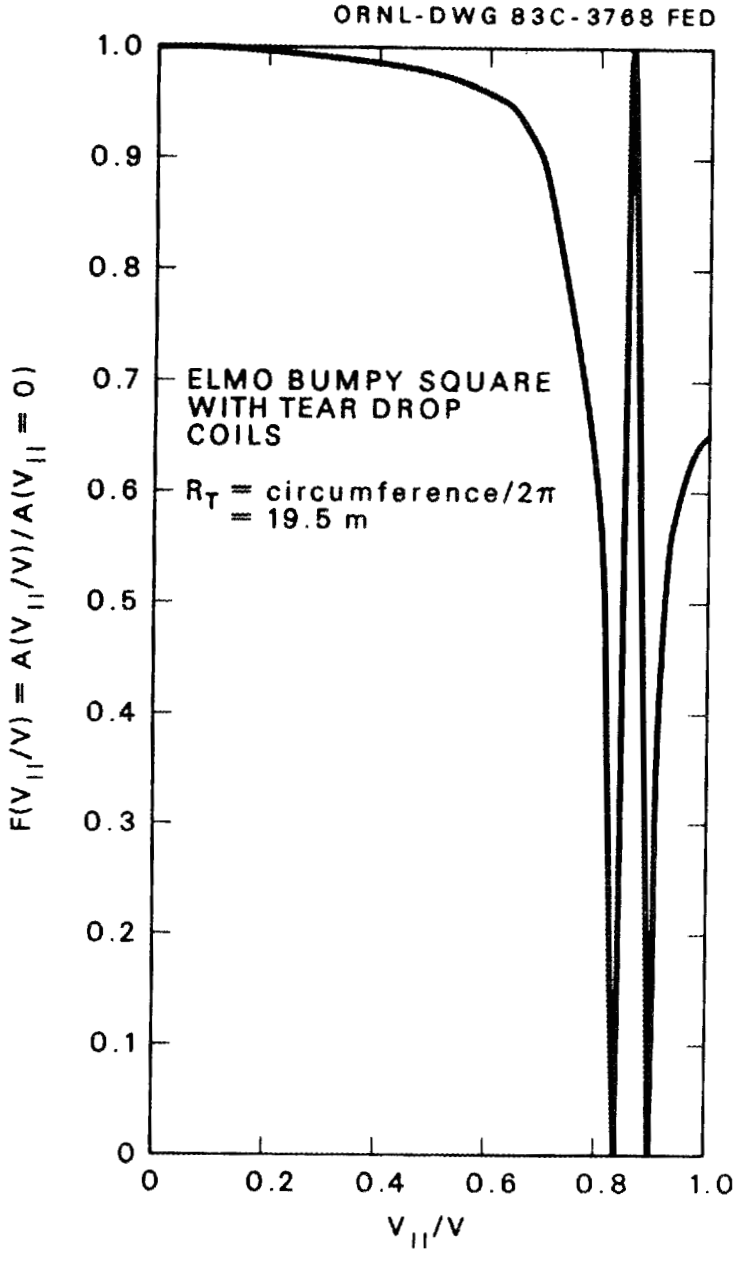

Fig. 9.14. Volumetric efficiency vs pitch angle for a bumpy square configuration shown in Fig. 9.11.

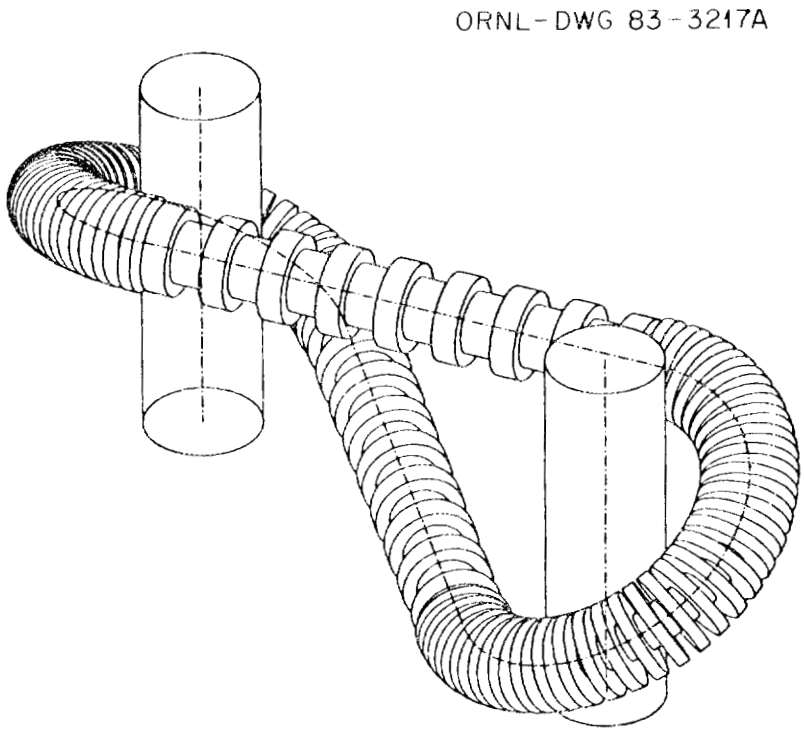

Fig. 9.15. Twisted racetrack configuration.

At reactor temperatures ($T_i \sim 20$ keV), the ion collision frequency is lower than the bounce time for ions trapped in the 1/R variation in the toroidal curved sections of the racetrack. In this regime the dominant thermal conductivity is due to these trapped ions, which are in banana orbits. The diffusion coefficient is given roughly by

$$D \sim \nu_{90}\rho_i^2\left[\frac{q^2}{\epsilon} f_T \nu^*\right],$$

where $q\rho_i/\epsilon^{1/2}$ is the banana width, f_T is the fraction of distribution trapped in the banana orbits, $\nu^*\nu_{90}$ is the effective collision frequency for untrapping the ions, and $\epsilon = a/R_{cor}$ is the inverse aspect ratio. The banana width in the TRT is the same as in a tokamak or stellarator with the same toroidal curvature. However, the fraction of trapped particles and the effective collision frequency in the straight section with mirrors are different from those in the toroidal section. Therefore, to evaluate the transport in TRT, the parameters must be integrated around the device. Calculations are carried out by approximating the mirror sectors as square magnetic wells with a field $B_{min} = B_{max}/M$ for half the length of the sector ($L_m/2$) and a field B_{max} for the other half of the length. For a density of $\sim 10^{20}$ m^{-3}, a temperature of ~20 keV, and $q \simeq 1.7$, we find $n\tau \simeq 3.5 \times 10^{20}$ $m^{-3}\cdot s$ for this TRT reactor.

This preliminary result of $n\tau$ indicates some margin of ignition that is approximately equal to that in a circular EBT reactor with SYM coils for $R_T \simeq 35$ m (ref. 3).

9.6 SUMMARY

Reactor projections for the advanced bumpy torus concepts indicate the possibility of a substantial reduction in reactor physical size (a factor of 2 of more) compared to past EBT designs. The trend to smaller EBT reactor systems is summarized nicely in Fig. 9.16. Further reductions are anticipated as the concepts continue to develop.

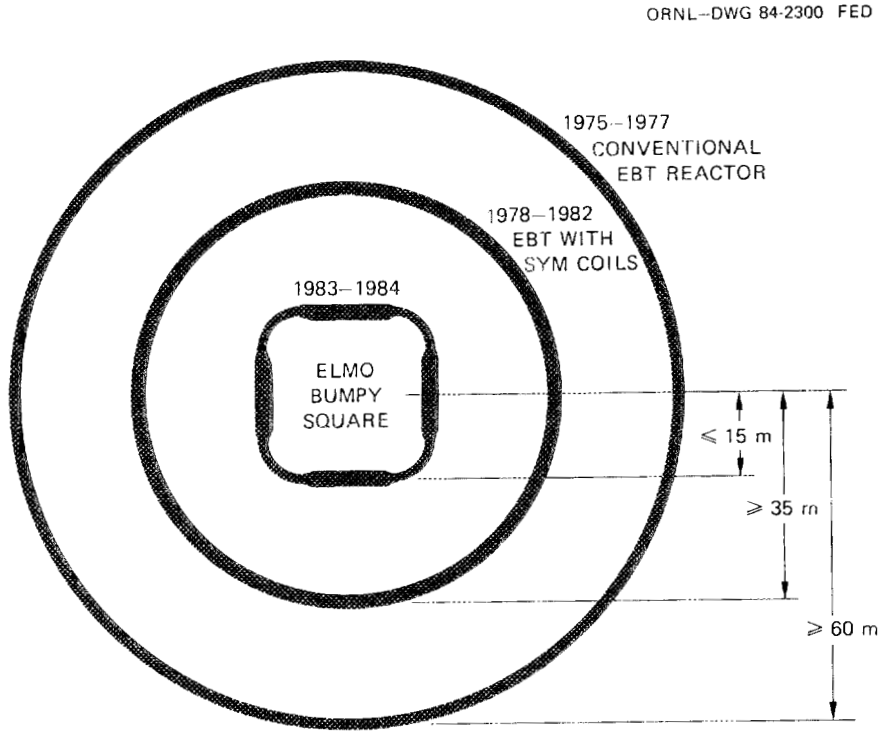

Fig. 9.16. Development of new EBT configurations continues trend to smaller EBT reactor systems.

REFERENCES

1. N. A. Uckan et al., "Reactor Assessments of Advanced Bumpy Torus Configurations," in Proceedings of the 10th Symposium on Fusion Engineering, (Philadelphia, December 5-9, 1983) IEEE No. 83CH1916-6, p. 1824.
2. N. A. Uckan et al., Reactor Assessments of Advanced Bumpy Torus Configurations, ORNL/TM-8985, Oak Ridge Natl. Lab., 1984.
3. N. A. Uckan et al., EBT Reactor Analysis, ORNL/TM-8712, Oak Ridge Natl. Lab., 1983.
4. N. A. Uckan et al., Advanced Bumpy Torus Concepts: Proceedings of the Workshop, CONF-830758, Oak Ridge Natl. Lab., 1983 (papers published therein).
5. R. L. Miller, R. A. Dandl, and G. E. Guest, "Drift Surface Studies of EBT Configurations with Noncircular Magnetic Coils," in ref. 4, p. 37.
6. L. W. Owen, D. K. Lee, and C. L. Hedrick, "ELMO Bumpy Square," in ref. 4, p. 55.
7. J. F. Pipkins, R. J. Schmitt, and W. B. Ard, "Optimized Approaches to EBTs with Simple Circular Coils," in ref. 4, p. 99.
8. A. H. Boozer, "The ELMO Snakey Torus," in ref. 4, p. 161.
9. L. W. Owen and N. A. Uckan, "EBT Reactor Magnetics and Particle Confinement," J. Fusion Energy 1, 341 (1981).
10. D. G. McAlees et al., The ELMO Bumpy Torus (EBT) Reactor Reference Design, ORNL/TM-5669, Oak Ridge Natl. Lab., 1976.
11. J. W. Van Dam et al., "Energetic Particles in Tokamaks: Stabilization of Ballooning Modes," in ref. 4, p. 167.

Appendix 10

POLOIDALLY ASYMMETRIC ELECTROSTATIC POTENTIALS IN CLOSED-LINE BUMPY TOROIDS

C. L. Hedrick and L. W. Owen

ABSTRACT

Here an analytic expression is developed for the poloidal asymmetry in the electrostatic potential observed experimentally in the T-mode of operation in the ELMO Bumpy Torus (EBT). A multiple-fluid treatment for the "cool," "warm," and "hot" electrons is used. The central idea is that the "warm" electrons dominate both the radial and poloidal structure of the electrostatic potential in the T-mode of operation.

The expression for the poloidal asymmetry in the electrostatic potential, which agrees reasonably well with experiment, is also applied to a modification of the EBT magnetic configuration. We find that a substantial reduction in the asymmetry of the electrostatic potential below that of the EBT is possible in the modification of the EBT magnetic configuration.

I. INTRODUCTION

Here we develop an analytic expression for the poloidal asymmetry in the electrostatic potential observed experimentally in the T-mode of operation in the ELMO Bumpy Torus (EBT).[1-4] We also apply this expression for the asymmetry in the potential to the ELMO Bumpy Square (EBS) magnetic configuration.[5]

We shall treat the electrons as consisting of several distinct fluids. This approach is motivated in large part by the experimental observation that the electrons in EBT consist of at least three

distinct populations.[6] The lowest energy population, which constitutes the bulk of the electrons, typically has temperatures well below the potential. This group's temperature does not correlate simply with the potential. The highest energy group, the hot electron rings, has energies well above the potential (e.g., hundreds of kilo-electron-volts versus hundreds of volts), and again the behavior of this group is not closely correlated to the potential.

An intermediate energy group, which is the focus of this paper, has a temperature, as deduced from soft X-ray measurements,[7] which is comparable to and scales with the electrostatic potential. Thus it is natural to assume that this intermediate energy population of electrons dominates the formation of the potential. The experimentally observed radial variation of the potential is relatively easy to obtain theoretically. Indeed, as we indicate by way of review in Sec. III, one can obtain the main features without specifying all of the details of the heating and loss processes.

To obtain the poloidal variation of the electrostatic potential, the main subject of this paper, we again assume that the formation is dominated by the intermediate energy electrons. The underlying idea is that the poloidal variation in the electrostatic potential is caused by the dispersion in single particle magnetic drift motion, which in turn is driven by the toroidal curvature and gradients in the magnetic field. Because of the multiple fluid treatment used here, a number of quantities which reflect *different averages of the magnetic drift* motion appear in the formalism. These quantities (denoted by U with appropriate subscripts) reduce, in the isotropic limit, to $\oint dl/B$. (The interpretive connection between single particle magnetic drift motion and the various fluid quantities is made at the end of Sec. II.)

Determining the poloidal asymmetry requires some information about the other groups of electrons and the ions. Fortunately, it is possible to make assumptions (based on limiting cases) about the other plasma constituents and thereby obtain a relatively simple expression for the asymmetry in the potential. This expression agrees relatively well with experiment.

Because the multiple fluid treatment of electrons employed here is slightly nonstandard, in Sec. II we review the kinetic equation and its first several moments for each constituent. In this same section we develop the magnetic equilibrium properties. Not surprisingly, we find that magnetic equilibria in EBT and EBS are dominated by the hot electron rings. The annihilator of equilibrium currents is also developed in Sec. II for later use in the charge conservation equation, $\nabla \cdot \underset{\sim}{j} = 0$.

In Sec. III we manipulate the density and momentum transport equations for the intermediate energy electrons to obtain a field-line-averaged density transport equation. The poloidally symmetric version of this equation is simply the one-dimensional density transport equation for the intermediate energy electrons.

In Sec. IV we discuss the main features of the poloidally symmetric solutions to the transport equations for the warm electrons. We argue that the poloidally symmetric part of the electrostatic potential is controlled (in the usual electron-cyclotron heated T-mode of operation) by the heat deposition profile through the "radial" temperature profile of the intermediate energy electrons.

In Sec. V we utilize charge neutrality and minimal assumptions about the various plasma components (based on limiting cases) to obtain

a relation between the poloidally asymmetric part of the potential and the poloidally asymmetric parts of various other macroscopic quantities.

In Sec. VI we concatenate the relations developed in the previous sections to obtain an analytic expression for the asymmetry in the potential. Using estimates of various quantities appearing in this expression, we make a comparison to the experimentally observed asymmetry of the potential in EBT. This same expression is also used to project the asymmetry in the electrostatic potential for EBS.

In Sec. VII the major points are reviewed, along with some of their implications. Some of the limitations of the present theory are discussed and suggestions for further research are made.

II. MOMENT EQUATIONS AND MAGNETIC EQUILIBRIA

The kinetic equation for species k may be written

$$\frac{\partial f_k}{\partial t} + \underset{\sim}{v} \cdot \underset{\sim}{\nabla} f_k + \frac{q_k}{m_k} (\underset{\sim}{E} + \underset{\sim}{v} \times \underset{\sim}{B}) \cdot \frac{\partial f_k}{\partial \underset{\sim}{v}} = S_k \quad , \tag{1}$$

where S_k represents the effect of scattering. We have in mind a multiple time scale analysis so that moments of S_k include sources and sinks associated with scattering by microwaves as well as by Coulomb collisions.[8] The first few moments of Eq. (1) yield the continuity, or density transport, equation for the k^{th} species,[9,10]

$$\frac{\partial n_k}{\partial t} + \underset{\sim}{\nabla} \cdot \left(n_k \underset{\sim}{V}_k \right) = \int d^3 v S_k \quad , \tag{2}$$

and the momentum transport equation for the k^{th} species,

$$n_k m_k \left(\frac{\partial \underset{\sim}{V}_k}{\partial t} + \underset{\sim}{V}_k \cdot \underset{\sim\sim}{\nabla V}_k \right) = q_k n_k \underset{\sim}{E} + q_k n_k \underset{\sim}{V}_k \times \underset{\sim}{B} - \underset{\sim}{\nabla} \cdot \underset{\approx}{P}_k + m_k \int d^3 v S_k (\underset{\sim}{v} - \underset{\sim}{V}_k) \quad . \tag{3}$$

Since charge conservation plays an important role in determining the electrostatic potential, we begin by examining the equations obtained by summing Eqs. (2) and (3) over species,

$$\frac{\partial \rho}{\partial t} + \underset{\sim}{\nabla} \cdot \underset{\sim}{j} = 0 \quad , \tag{4}$$

$$\rho_m \left(\frac{\partial \underset{\sim}{V}_c}{\partial t} + \underset{\sim}{V}_c \cdot \underset{\sim\sim}{\nabla V}_c \right) = \rho_Q \underset{\sim}{E} + \underset{\sim}{j} \times \underset{\sim}{B} - \underset{\sim}{\nabla} \cdot \underset{\approx}{P} + \sum_k \int d^3 v S_k \, m_k (\underset{\sim}{v} - \underset{\sim}{V}_c) \quad . \tag{5}$$

Here $\underset{\sim}{V}_c$ is the center of mass flow velocity, $\underset{\sim}{j}$ is the total current, and $\underset{\approx}{P}$ is the total pressure tensor in the center of mass frame:

$$\underset{\approx}{P} = \sum_k m_k \int d^3 v f_k (\underset{\sim}{v} - \underset{\sim}{V}_c)(\underset{\sim}{v} - \underset{\sim}{V}_c) \quad .$$

Since

$$\underset{\approx}{P}_k = m_k \int d^3 v \, f_k (\underset{\sim}{v} - \underset{\sim}{V}_k)(\underset{\sim}{v} - \underset{\sim}{V}_k) \quad ,$$

$$\underset{\approx}{P} = \sum_k \left(\underset{\approx}{P}_k + m_k n_k \underset{\sim}{V}_k \underset{\sim}{V}_k \right) - \rho_m \underset{\sim}{V}_c \underset{\sim}{V}_c \quad .$$

The mass and charge densities are denoted by ρ_M and ρ_Q. We note that in steady state the charge density satisfies Poisson's equation:

$$\rho_Q = \underset{\sim}{\nabla} \cdot \underset{\sim}{E} \quad . \tag{6}$$

We now estimate the relative sizes of the various terms appearing in Eq. (5). We are initially interested in the possible effects of electric fields on magnetic equilibria. Thus we estimate that $\underset{\sim}{V}_c \simeq \underset{\sim}{E} \times \underset{\sim}{B}/B^2$. Assuming that the various scale lengths for the electric field are comparable, we find, using Eq. (6), that the convective derivative term involving $\underset{\sim}{V}_c$ is larger than $\rho_Q \underset{\sim}{E} = \underset{\sim}{E}(\underset{\sim}{\nabla} \cdot \underset{\sim}{E})$ by $\omega_{pi}^2/\omega_{ci}^2$ ($\simeq$200 in EBT). Thus we will neglect $\rho_Q \underset{\sim}{E}$ in Eq. (5).

The total pressure tensor is dominated by the hot electron rings in EBT,

$$\underset{\simeq}{P} \simeq \underset{\simeq}{P}_r \quad . \tag{7}$$

Because the temperature of the hot electron ring is comparable to the rest energy of an electron, the thermal velocity of the hot electron ring is comparable to the speed of light. This is so much larger than the $\underset{\sim}{E} \times \underset{\sim}{B}$ velocity ($\lesssim 10^6$ cm/s) that even though the convective derivative term involves the ion mass and density, it is virtually impossible for this term to be comparable to $\underset{\sim}{\nabla} \cdot \underset{\simeq}{P}$. [Note that if one neglected the hot electron rings (and the warm electrons), this might not be the case.] Thus we shall neglect the convective derivative in Eq. (5).

To estimate the relative magnitude of the remaining terms in the steady-state version of Eq. (5), it is convenient to rewrite it in the form

$$\underset{\sim}{j}_{\perp} = \frac{\underset{\sim}{B} \times (\nabla \cdot \underset{\approx}{P})}{B^2} + \sum_k q_k \underset{\sim}{\Gamma}_k \quad , \tag{8}$$

where we have associated the scattering-induced particle flux, $\underset{\sim}{\Gamma}_k$, with the integral involving S_k in Eq. (5). We can estimate the magnitude of the Γ_k from the continuity equation $\Gamma_k \simeq |e| n_k L_k/\tau_k$. Because the hot electron gyroradius is relatively large [e.g., $L_r/\rho_r \lesssim O(10)$] and the electron cyclotron frequency is tens of gigahertz, one must assume lifetimes, relative densities, and/or scale lengths that are several orders of magnitude different than those estimated experimentally to make a single species' scattering-induced current comparable to the currents arising from the ring pressure tensor. Since one expects that the sum on species in Eq. (8) will provide considerable cancellation, we obtain the standard magnetic equilibrium relation

$$\underset{\sim}{j}_{\perp} \simeq \frac{\underset{\sim}{B} \times \nabla \cdot \underset{\approx}{P}}{B^2} \quad . \tag{9}$$

We will, however, retain the scattering-induced fluxes in Eq. (8) when we turn to transport.

The relative magnitudes of the scattering-induced forces and currents and those associated with the convective derivative term are somewhat more delicate matters. The convective derivative term, through its contribution to viscosity, may be important in some

high-temperature and lifetime cases by preventing certain pathological electric-field solutions. In this paper, we will not allow such pathology and will neglect the convective derivative in Eqs. (3) and (5).

Notice that in making the above estimates it was important to include the fact that the hot electrons dominate the total pressure and to use experimental estimates of scale lengths, lifetime, etc. If we had included only the coolest components of electrons and ions, we might have obtained an entirely different ordering.

Because the magnetic equilibrium currents are dominant, we can use the standard approach that allows one to decouple transport and magnetic equilibrium. In the remainder of this section, we outline the procedure necessary to determine the "pressure surfaces" for the hot electron rings. Integration over these pressure surfaces annihilates the magnetic equilibrium currents and allows one to obtain information about the "radial" component of the electron field from charge conservation ($\nabla \cdot \underset{\sim}{j} = 0$).

We may rewrite the steady-state version of Eq. (4), $\nabla \cdot \underset{\sim}{j} = 0$, in the form

$$\frac{\partial}{\partial l}\left(\frac{j_{\parallel}}{B}\right) = -\frac{1}{B}\,\nabla \cdot \underset{\sim}{j}_{\perp} = -\frac{1}{B}\,\nabla \cdot \left[\frac{\underset{\sim}{B} \times \nabla \cdot \underset{\approx}{P}}{B^2}\right] \tag{10}$$

where we have used Eq. (9). The divergence appearing on the extreme right in Eq. (10) is treated in the appendix and leads to

$$\frac{\partial}{\partial l}\left(\frac{j_{\parallel}}{B}\right) = -\frac{\partial}{\partial l}\left[(\sigma - 1)\frac{j_{\parallel}}{B}\right]$$

$$-\frac{1}{B^3}\left[\underset{\sim}{\nabla} p_{\perp} \cdot (\underset{\sim}{B} \times \underset{\sim}{\nabla} \ln B) + \hat{\underset{\sim}{\nabla}} p_{\parallel} \cdot (\underset{\sim}{B} \times \underset{\sim}{\kappa})\right] , \qquad (11)$$

where

$$\sigma \equiv 1 + \frac{p_{\perp} - p_{\parallel}}{B^2} \qquad (12)$$

and

$$\hat{\underset{\sim}{\nabla}} p_{\parallel} \equiv \underset{\sim}{\nabla} p_{\parallel} - \underset{\sim}{\nabla} B \frac{\partial p_{\parallel}}{\partial B} \quad . \qquad (13)$$

Equation (11) may be rewritten as

$$\frac{\partial}{\partial l}\left(\frac{\sigma j_{\parallel}}{B}\right) = -\frac{1}{B^3}\left[\underset{\sim}{\nabla} p_{\perp} \cdot (\underset{\sim}{B} \times \underset{\sim}{\nabla} \ln B) + \hat{\underset{\sim}{\nabla}} p_{\parallel} \cdot (\underset{\sim}{B} \times \underset{\sim}{\kappa})\right] \quad . \qquad (14)$$

This is the anisotropic or tensor pressure generalization of the more familiar scalar pressure equation for the Pfirsch-Schlüter currents. The scalar pressure limit of Eq. (14)[11,12] can appear in ways which emphasize either the curvature, $\underset{\sim}{\kappa}$, or $\underset{\sim}{\nabla}_{\perp} \ln B$, since $\underset{\sim}{\nabla} p \cdot [\underset{\sim}{B} \times (\underset{\sim}{\kappa} - \underset{\sim}{\nabla} \ln B] = 0$.[13] For tensor pressure one cannot freely interchange $\underset{\sim}{\kappa}$ and $\underset{\sim}{\nabla}_{\perp} \ln B$ except at low β [see Eq. (A.14)]. For those not wishing to follow the details in the appendix, Eq. (14) can be made partially plausible by noting that the quantities involving $\underset{\sim}{\nabla} B$ and the curvature, $\underset{\sim}{\kappa}$, are just those which arise when taking moments of the magnetic drift velocity, (i.e., $\sum q_k \int d^3v \, \underset{\sim}{v}_D \cdot \underset{\sim}{\nabla} f$). We will use this relation to single particle magnetic drift motion at the end of this

section to provide an interpretation of fluid quantities which appear in both equilibrium and transport.

Because the field lines are closed in EBT and EBS and because $j_{\|}$, B, and σ are single valued, the left side of Eq. (14) integrates to zero after one complete traversal of a field line so that

$$\oint \frac{dl}{B^3} \left[\underset{\sim}{\nabla} p_{\perp} \cdot (\underset{\sim}{B} \times \underset{\sim}{\nabla} \ln B) + \hat{\underset{\sim}{\nabla}} p_{\|} \cdot (\underset{\sim}{B} \times \underset{\sim}{\kappa}) \right] = 0 \quad . \tag{15}$$

We now assume that the ring pressure is separable and of the form

$$p_{\perp} = \hat{p}_r(\alpha,\beta) g_{\perp}(b) \quad , \quad p_{\|} = \hat{p}_r(\alpha,\beta) g_{\|}(B) \quad , \tag{16}$$

where α and β are the usual coordinates associated with the Clebsch representation of the magnetic field as introduced by Grad and Rubin:[14]

$$\underset{\sim}{B} = \underset{\sim}{\nabla}\alpha \times \underset{\sim}{\nabla}\beta \quad . \tag{17}$$

Making use of the definition of $\hat{\underset{\sim}{\nabla}} p_{\|}$, we find that

$$\hat{\underset{\sim}{\nabla}} p_{\|} = \underset{\sim}{\nabla}\alpha \frac{\partial p_{\|}}{\partial \alpha} + \underset{\sim}{\nabla}\beta \frac{\partial p_{\|}}{\partial \beta} \tag{18}$$

and that Eq. (15) takes the form

$$0 = - \frac{\partial \hat{p}_r}{\partial \alpha} \oint \frac{dl}{B} \left(g_{\perp} \frac{\partial \ln B}{\partial \beta} + g_{\|} \underset{\sim}{W}_{\beta} \cdot \underset{\sim}{\kappa} \right)$$

$$+ \frac{\partial \hat{p}_r}{\partial \beta} \oint \frac{dl}{B} \left(g_{\perp} \frac{\partial \ln B}{\partial \alpha} + g_{\|} \underset{\sim}{W}_{\alpha} \cdot \underset{\sim}{\kappa} \right) \quad , \tag{19}$$

where

$$\underset{\sim}{W}_\alpha = \underset{\sim}{\nabla}\beta \times \underset{\sim}{B}/B^2 \quad ,$$

$$\underset{\sim}{W}_\beta = -\underset{\sim}{\nabla}\alpha \times \underset{\sim}{B}/B^2 \quad . \tag{20}$$

Since

$$g_\perp = -B^2 \frac{\partial}{\partial B}\left(\frac{g_\parallel}{B}\right) \tag{21}$$

[see Eq. (A.8)], we can write Eq. (19) as

$$0 = \frac{\partial \hat{p}_r}{\partial \alpha} \oint dl \left[\underset{\sim}{\nabla}\left(\frac{g_\parallel}{B}\right) - \frac{g_\parallel}{B}\,\underset{\sim}{K}\right] \cdot \underset{\sim}{W}_\beta$$

$$- \frac{\partial \hat{p}_r}{\partial \beta} \oint dl \left[\underset{\sim}{\nabla}\left(\frac{g_\parallel}{B}\right) - \frac{g_\parallel}{B}\,\underset{\sim}{K}\right] \cdot \underset{\sim}{W}_\alpha \quad . \tag{22}$$

For an arbitrary function Q for closed field lines (or mirror geometry with Q vanishing at the end points of integration),[5]

$$\frac{\partial}{\partial \alpha} \oint dl\, Q = \oint dl \left(\underset{\sim}{\nabla} Q - Q\underset{\sim}{K}\right) \cdot \underset{\sim}{W}_\alpha \quad ,$$

$$\frac{\partial}{\partial \beta} \oint dl\, Q = \oint dl \left(\underset{\sim}{\nabla} Q - Q\underset{\sim}{K}\right) \cdot \underset{\sim}{W}_\beta \quad . \tag{23}$$

Comparing Eqs. (22) and (23), we see that

$$\frac{\partial \hat{p}_r}{\partial \alpha} \frac{\partial U_{r,\parallel}}{\partial \beta} - \frac{\partial \hat{p}_r}{\partial \beta} \frac{\partial U_{r,\parallel}}{\partial \alpha} = 0 \quad , \tag{24}$$

where

$$U_{r,\parallel} = \oint \frac{dl}{B} g_{\parallel} \quad . \tag{25}$$

Equation (24) implies that the surfaces of constant $\hat{p}_r$ are the same as the surfaces of $U_{r,\parallel}$, a result first obtained by Grad using a somewhat different procedure.[15] In the limit of isotropic ring pressure, $g_{\parallel}$ reduces to a constant (which we shall take to be 1), and we recover the familiar relation that for closed field lines the scalar pressure is a function of $\oint dl/B$. The other simple limit is for a highly anisotropic ring pressure -- more representative of EBT. In this case the surfaces of $U_{r,\parallel}$ are the same as mod-B in the midplane (for points off the midplane, one maps the mod-B contours via field lines).

Without loss of generality, we now choose the surfaces of constant α to correspond to surfaces of constant $U_{r,\parallel}$. The α-surfaces are then also surfaces of constant ring (or total) pressure. With this choice of α, the annihilator of the equilibrium currents is simply expressed as

$$\langle \ldots \rangle = \oint \frac{dl}{B} \oint d\beta (\ldots) \quad . \tag{26}$$

The constraint involving $U_{r,\parallel}$ given by Eq. (24) has a simple interpretation. We have already remarked that the quantities appearing

in Eqs. (14) and (15) arise when taking moments of the magnetic drift velocity. Equation (24), which can also be written

$$\underset{\sim}{\nabla}\hat{p}_r \cdot (-\hat{b} \times \underset{\sim}{\nabla} U_{r,\parallel}) = 0 \ ,$$

is simply a statement that the surfaces of constant $\hat{p}_r$ must be tangent to the "average magnetic drift" -- which is proportional to $\hat{b} \times \underset{\sim}{\nabla} U_{r,\parallel}$. $U_{r,\parallel}$ may then be interpreted as an "average adiabatic invariant" -- similar in spirit to the single particle longitudinal adiabatic invariant but averaged over the distribution of particles.

In the remainder of this paper, additional quantities appear, which, like $U_{r,\parallel}$, reflect averages of the magnetic drift motion. In particular, we will find that the poloidal asymmetry in the potential is driven by the average magnetic drift motion of the warm electrons, which is different than that of the ring electrons.

III. WARM ELECTRON TRANSPORT EQUATION

In this section, we combine Eqs. (2) and (3) for the intermediate energy (or warm) electrons and manipulate the resultant density transport equation into a form needed in later sections.

From Eq. (3), in steady state,

$$n_W \underset{\sim}{V}_W = n_W \frac{\underset{\sim}{E} \times \underset{\sim}{B}}{B^2} - \frac{1}{|e|} \frac{\underset{\sim}{B} \times (\underset{\sim}{\nabla} \cdot \underset{\approx}{P}_W)}{B^2} + \underset{\sim}{\Gamma}_W \ . \qquad (27)$$

Notice that in contrast to the equilibrium equation for the current, here we must retain the term involving $\underset{\sim}{E} \times \underset{\sim}{B}$ since the density, rather than the charge density, occurs. We now insert Eq. (27) into Eq. (2), and since we are only interested in field lines that do not strike material walls (coil casing or "limiter"), we perform a field line average. The resultant equation is

$$\oint \frac{dl}{B} \underset{\sim}{\nabla} \cdot \left(n_W \frac{\underset{\sim}{E} \times \underset{\sim}{B}}{B^2} \right) - \frac{1}{|e|} \oint \frac{dl}{B} \underset{\sim}{\nabla} \cdot \left[\frac{\underset{\sim}{B} \times (\underset{\sim}{\nabla} \cdot \underset{\approx}{P}_W)}{B^2} \right]$$

$$+ \oint \frac{dl}{B} \underset{\sim}{\nabla} \cdot \underset{\sim}{\Gamma}_W = \oint \frac{dl}{B} \int d^3v S_k \quad . \tag{28}$$

To evaluate the integral involving the pressure tensor, $\underset{\approx}{P}_W$, in Eq. (28), it is convenient to assume that the distribution function for the warm electrons is of the form

$$f = F(\varepsilon, \alpha, \beta) h(\varepsilon/\mu) \quad , \tag{29}$$

where ε is the kinetic energy and μ is the magnetic moment. With this assumption the density and pressure take the separable form

$$\begin{aligned} n_W &= \hat{n}_W(\alpha,\beta) G_n(B) \quad , \\ p_{W,\parallel} &= \hat{p}_W(\alpha,\beta) G_{\parallel}(B) \quad , \\ p_{W,\perp} &= \hat{p}_W(\alpha,\beta) G_{\perp}(B) \quad . \end{aligned} \tag{30}$$

The separability of the parallel and perpendicular pressures and the density for the warm electrons is similar to that assumed for the

ring electrons in the previous section. It is again convenient to introduce field line averages of the B-dependent parts of the fluid quantities:

$$U_{W,n} \equiv \oint \frac{dl}{B}\, G_n(B) \quad ,$$

$$U_{W,\parallel} \equiv \oint \frac{dl}{B}\, G_{\parallel}(B) \quad . \tag{31}$$

As discussed for the ring electrons at the end of the previous section, these quantities can also be interpreted as "average adiabatic invariants" which reflect the single particle magnetic drift motion -- in this case, of the warm electrons. Because we have several fluid quantities (e.g., pressure and density) when dealing with transport, it is necessary to have two slightly different averages or weightings of the drift motion. It is not necessary to introduce separate averages for the parallel and perpendicular pressure because, as shown in the appendix, the assumed form of the distribution function relates the parallel and perpendicular pressures [see Eq. (A.8)].

The integral involving the divergence of $\underset{\approx}{P}_W$ in Eq. (28) is similar to that encountered in Sec. II, and using the same techniques we find that

$$\oint \frac{dl}{B}\, \underset{\sim}{\nabla} \cdot \left[\frac{\underset{\sim}{B} \times (\underset{\sim}{\nabla} \cdot \underset{\approx}{P}_W)}{B^2} \right] = \frac{\partial \hat{p}_W}{\partial \alpha} \frac{\partial U_{W,\parallel}}{\partial \beta} - \frac{\partial \hat{p}_W}{\partial \beta} \frac{\partial U_{W,\parallel}}{\partial \alpha} \quad . \tag{32}$$

To evaluate the term in Eq. (28) involving $\underset{\sim}{E} \times \underset{\sim}{B}$, it is convenient to define

$$\underset{\sim}{V}_E = \underset{\sim}{E} \times \underset{\sim}{B}/B^2 \quad . \tag{33}$$

Using the vector identity for the divergence of a cross-product and the fact that in steady state $\underset{\sim}{\nabla} \times \underset{\sim}{E} = 0$, we obtain

$$\underset{\sim}{\nabla} \cdot \underset{\sim}{V}_E = -\underset{\sim}{E} \cdot \left[\underset{\sim}{\nabla} \times \left(\frac{\underset{\sim}{B}}{B^2}\right)\right] = \frac{-\underset{\sim}{E}}{B^2} \cdot \left(\underset{\sim}{\nabla} \times \underset{\sim}{B} + 2\underset{\sim}{B} \times \underset{\sim}{\nabla} \ln B\right) \quad . \tag{34}$$

Since $\underset{\sim}{E} \cdot \hat{b}$ is assumed zero, we can use [see Eq. (A.14)]

$$(\underset{\sim}{\nabla} \times \underset{\sim}{B})_\perp = \underset{\sim}{B} \times (\underset{\sim}{\kappa} - \underset{\sim}{\nabla} \ln B) \tag{35}$$

to obtain

$$\underset{\sim}{\nabla} \cdot \underset{\sim}{V}_E = -\underset{\sim}{V}_E \cdot (\underset{\sim}{\kappa} + \underset{\sim}{\nabla} \ln B) \tag{36}$$

and

$$\underset{\sim}{\nabla} \cdot (n\underset{\sim}{V}_E) = \underset{\sim}{V}_E \cdot \left[\underset{\sim}{\nabla} n_W - n_W(\underset{\sim}{\kappa} + \underset{\sim}{\nabla} \ln B)\right] \quad . \tag{37}$$

Using

$$\underset{\sim}{E} = -\underset{\sim}{\nabla}\phi \tag{38}$$

and Eq. (20), we find that

$$\underset{\sim}{V}_E = \frac{\partial \phi}{\partial \alpha} \underset{\sim}{W}_\beta - \frac{\partial \phi}{\partial \beta} \underset{\sim}{W}_\alpha \quad . \tag{39}$$

Combining Eqs. (37), (39), and (30), we obtain

$$\underset{\sim}{\nabla} \cdot (n_W \underset{\sim}{V}_E) = \frac{\partial \phi}{\partial \alpha} \left\{ \frac{\partial \hat{n}_W}{\partial \beta} G_n + \hat{n}_W \left[B \frac{\partial}{\partial \beta} \left(\frac{G_n}{B} \right) - G_n \underset{\sim}{W}_\beta \cdot \underset{\sim}{K} \right] \right\}$$

$$- \frac{\partial \phi}{\partial \beta} \left\{ \frac{\partial \hat{n}_W}{\partial \alpha} G_n + \hat{n}_W \left[B \frac{\partial}{\partial \alpha} \left(\frac{G_n}{B} \right) - G_n \underset{\sim}{W}_\alpha \cdot \underset{\sim}{K} \right] \right\} \quad . \tag{40}$$

Setting Q in Eq. (23) to G_n/B, we find that

$$\oint \frac{dl}{B} \underset{\sim}{\nabla} \cdot (n_W \underset{\sim}{V}_E) = \frac{\partial \phi}{\partial \alpha} \frac{\partial}{\partial \beta} \left(\hat{n}_W U_{W,n} \right) - \frac{\partial \phi}{\partial \beta} \frac{\partial}{\partial \alpha} \left(\hat{n}_W U_{W,n} \right) \quad . \tag{41}$$

Equations (28), (41), and (32) allow us to write the density transport equation in the form

$$\hat{S}_W = C_W \tag{42}$$

where we have collected the terms arising from scattering into $\hat{S}_W$:

$$\hat{S}_W \equiv \oint \frac{dl}{B} \left(\int d^3 v \; S_k - \underset{\sim}{\nabla} \cdot \underset{\sim}{\Gamma}_W \right) \quad . \tag{43}$$

The terms arising from "convection" of the warm electron fluid are

$$C_W = \frac{\partial \phi}{\partial \alpha} \frac{\partial}{\partial \beta} \left(\hat{n}_W U_{W,n} \right) - \frac{\partial \phi}{\partial \beta} \frac{\partial}{\partial \alpha} \left(\hat{n}_W U_{W,n} \right)$$

$$- \frac{1}{|e|} \left(\frac{\partial \hat{p}_W}{\partial \alpha} \frac{\partial U_{W,\parallel}}{\partial \beta} - \frac{\partial \hat{p}_W}{\partial \beta} \frac{\partial U_{W,\parallel}}{\partial \alpha} \right) \quad . \tag{44}$$

In the remainder of this paper we will assume that the poloidal variation in the various macroscopic quantities is small and write

$$\phi = \phi_0(\alpha) + \phi_1(\alpha,\beta) \tag{45}$$

and similarly for the other macroscopic quantities. Here it should be noted that experimental measurements indicate $|\phi_1|/|\phi_0|$ is typically less than or equal to one third. This is sufficiently large that it was not clear a priori whether this expansion would adequately describe the experimental results. The primary justification for the expansion is that it yields results for EBT which are in reasonable agreement with experiment and that it should be even better for EBS.

We note from Eq. (44) that the lowest order version of C_W is zero since none of the lowest order macroscopic quantities depend upon β. The lowest order version of Eq. (42) is then

$$\oint d\beta \oint \frac{dl}{B}\left(\int d^3v S_W - \underset{\sim}{\nabla} \cdot \underset{\sim}{\Gamma}_W\right)\Big|_0 = 0 \quad , \tag{46}$$

which is simply the one-dimensional transport equation for the warm or intermediate energy electron density in steady state.

IV. POLOIDALLY SYMMETRIC TRANSPORT SOLUTIONS

In this section, we discuss the poloidally symmetric solutions to the transport equations for the intermediate energy electrons. These equations are generally of the same form as those used in two-fluid treatments of EBT transport, for which there is a substantial body of information.[16-18]

We begin by discussing some of the general properties of $\nabla \cdot \Gamma_W$. Here we are concerned with fluxes induced by both microwave and Coulomb scattering. Fortunately, the fluxes induced by microwave scattering often have properties similar to those induced by Coulomb collisions. That is, many of the results of neoclassical transport coefficient calculations depend more upon the details of the particle drift orbits than upon the details of the scattering mechanism. Thus we limit ourselves here to the properties of neoclassical transport which carry over to the more general case which includes microwave scattering (and perhaps scattering due to other fluctuating electromagnetic fields).

It should be emphasized that we are primarily concerned in this paper with poloidal asymmetry in the electrostatic potential induced by particle motion and so, for example, we will neglect any (small) poloidal asymmetry in the microwave heat deposition. As is discussed at some length in Sec. VII, the weak focusing of the microwave energy and the small single pass absorption lead to small poloidal asymmetry in the microwave heat deposition profile.

The "radial" or α component of Γ_W typically takes the form

$$\Gamma_{W,0} = -D_W\left(\nabla\hat{n}_{W,0} - |e|\,\frac{\hat{n}_{W,0}}{T_{W,0}}\,\nabla\phi_0 + \frac{An_{W,0}}{T_{W,0}}\,\nabla T_{W,0}\right) \tag{47}$$

Because the intermediate energy electrons span the zone where $E \times B$ drifts can, to lowest order, cancel the ∇B and curvature drifts, D_W tends to be quite large (particularly at larger radii) compared to the corresponding transport coefficients for the cooler bulk electrons and ions. Typically the hot ring electrons have lifetimes which are 2 to 3 orders of magnitude larger than the bulk electrons[6,19] so their

contribution to particle fluxes is negligible. Because the more energetic of the warm electrons are lost at a higher rate than the less energetic electrons, the numerical factor A in Eq. (47) tends to be greater than unity (e.g., 2 or 3).

While there are, in general, a number of possible radial electric fields which satisfy charge conservation, the radial electric fields observed experimentally in the T-mode of operation in EBT can be obtained fairly simply. To lowest order the charge conservation condition, $\underset{\sim}{\nabla} \cdot \underset{\sim}{j} = 0$, reduces to

$$\Gamma_{i,0} = \Gamma_{W,0} + \Gamma_{c,0} + \Gamma_{r,0}$$

where $\Gamma_{i,0}$, $\Gamma_{c,0}$, and $\Gamma_{r,0}$ are the "radial" particle fluxes of the ions, the cool or bulk electrons, and the ring electrons, respectively. Because D_W is so large, this last equation is difficult to satisfy (for electric fields like those observed experimentally) unless the factor multiplying D_W in Eq. (47) is small. Thus

$$|e|\underset{\sim}{\nabla}\phi_0 \simeq A\underset{\sim}{\nabla}T_{W,0} + T_{W,0}\underset{\sim}{\nabla}\ln(n_{W,0}) \quad . \tag{48}$$

Because A is greater than unity and the logarithm is a relatively weak function, Eq. (48) has the approximate solution

$$e\phi_0 \simeq AT_{W,0} \quad . \tag{49}$$

Thus we see that the "radial" or α profile of ϕ_0 is dominated by the profile of $T_{W,0}$. Insofar as losses are concerned, the diffusive or conductive losses for $T_{W,0}$ tend to be nearly diagonal, again because

the higher energy particles are lost at a higher rate. At relatively high energy, unconfined drift orbits exist for single particles and the scattering rate is sufficiently low that, once scattered onto such an orbit, a particle drifts to the wall. This process is similar to the loss cone that occurs in a simple mirror machine except that the time scales are different (drift time scale instead of bounce time scale). These "drift losses" are relatively more important for energy transport than for particle transport because they occur at high energy. They arise formally when evaluating the integral over S_k. Here we model them by a simple loss rate, $\nu_{D,W}$.

The processes balancing the energy losses are scattering or heating due to microwaves. Formally, they arise because the part of S_k representing microwave scattering takes electrons from the cooler group and moves them into the intermediate energy population. There is, of course, also a "sink" associated with microwave heating transferring electrons from the intermediate population to the hot electron ring population.

Two types of microwave heating occur in EBT (and EBS). Fundamental electron cyclotron heating occurs at a resonant surface which crosses most of the field lines (see Fig. 1) and is relatively uniform as a function of radius or α. Second harmonic heating, on the other hand, is localized to radii in the midplane (or α) near the point where the second harmonic resonance condition is satisfied. While the relative magnitude of the two heating processes depends upon the strength of the microwave electric field at the fundamental and second harmonic resonance, it is clear that the heat deposition profile for the intermediate energy population can be peaked near the second harmonic resonance.

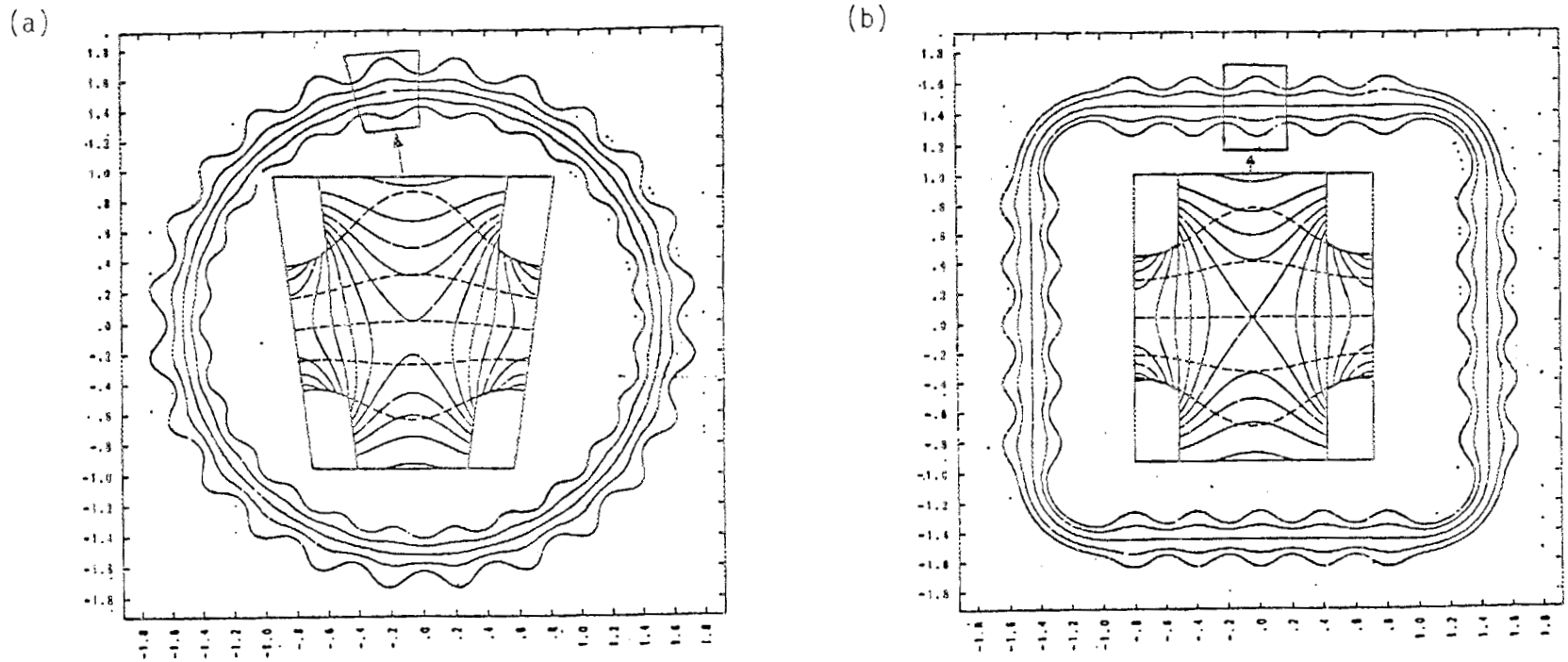

Fig. 1. Field lines in the equatorial plane for (a) EBT and (b) EBS magnetic configurations. The inset drawings show contours of mod-B for an EBT mirror cell and for a central mirror cell of the EBS magnetic configuration. Notice that the mirror cell of an EBS is very nearly axisymmetric and that all toroidal effects are concentrated in the corners.

We can now see in a qualitative way how the $T_{W,0}$ profile responds to the peaking of the heat deposition near the second harmonic resonance. If the "drift losses" are sufficiently large compared to the diffusive (or conductive) losses, then $T_{W,0}$ will peak near the second harmonic resonance. This is most easily seen if we first neglect the diffusive losses, for then $\nu_{D,W}T_{W,0}$ is simply proportional to the heat deposition profile, H, and $T_{W,0} \simeq H/\nu_{D,W}$. Because particles at larger radii or α are closer to the walls, they are more susceptible to direct loss to the walls, $\nu_{D,W}$ is larger at larger radii, and $T_{W,0}$ tends to peak slightly to the interior of the peak in the heat deposition profile. Including diffusive or conductive effects simply broadens or diffuses the profile for $T_{W,0}$.

Thus, we see that the peaking of the heat deposition profile near the second harmonic causes $T_{W,0}$ to peak near the second harmonic, which in turn causes ϕ_0 to peak near the second harmonic resonance in the midplane.

Finally, we should point out that strictly speaking, Eq. (47) applies to an isotropic distribution. For anisotropic distributions an additional term occurs which involves gradients of B. We have neglected such terms on the grounds that the gradients of B are weak compared to the gradients of the other macroscopic quantities. This is consistent with approximations we shall make for the gradients of $\oint dl/B$, $U_{W,n}$, $U_{W,\parallel}$, etc., which reflect the relatively weak gradients of B. Indeed, as we shall see in Sec. VI, neglecting such terms is what allows us to avoid using the energy transport equation when analyzing the poloidal variation of the macroscopic quantities. A consequence of

these approximations is that we will retain only the most dominant effects of magnetic drifts on the poloidal asymmetry in the electrostatic potential.

V. QUASI-NEUTRALITY

In this section we discuss approximations for the plasma constituents other than the intermediate energy electrons. We then use these approximations in the quasi-neutrality condition,

$$n_i = n_c + n_w + n_r \quad , \tag{50}$$

to obtain a relation that will be used in the next section. Here

n_i = ion density,

n_c = cool or bulk electron density,

n_r = hot electron ring density.

For both the cool or bulk electrons and the ions, we assume that their densities are functions only of ϕ. This approximation reflects the fact that for cool particles, the constancy of the total energy (kinetic plus potential) restricts the particles to follow (approximately) a potential surface. This, of course, can be deduced from the kinetic equation in the collisionless limit.

For the hot electron rings we have already assumed that the pressure tensor is separable into a function of α and a function of B. This is consistent with assuming that the hot electron ring distribution function is of the form

$$f_r = F(\varepsilon,\alpha)\ H(\varepsilon/\mu) \quad . \tag{51}$$

This in turn leads to the density for the hot electron rings being of the form

$$n_r = \hat{n}_r(\alpha)\, g_{r,n}(B) \quad . \tag{52}$$

Because $g_{r,n}(B)$ differs somewhat from $g_{r,\parallel}(B)$, the contours of constant $U_{r,\parallel} \equiv \oint \frac{dl}{B}\, g_{r,\parallel}$ differ slightly from those of $U_{r,n} \equiv \oint \frac{dl}{B}\, g_{r,n}$. While $U_{r,\parallel}$ depends solely on α (by construction), $U_{r,n}$ does have a slight β dependence. For simplicity we shall neglect this β dependence, which is equivalent to assuming that

$$\frac{\partial n_r}{\partial \beta} \simeq 0 \ . \tag{53}$$

Including the β dependence of n_r leads to terms which are small compared to similar terms involving n_W (because there are fewer ring electrons per field line than warm electrons, and because the more anisotropic rings have weaker β dependence).

We now use the above relations to eliminate $n_i - n_c$, which is potentially the difference of large numbers and, hence, is difficult to estimate accurately. To lowest order,

$$\left(\frac{dn_i}{d\phi} - \frac{dn_c}{d\phi}\right) \phi_0' = n_{W,0}' + n_r' \quad , \tag{54}$$

where prime implies differentiation with respect to α. To first order,

$$\left(\frac{dn_i}{d\phi} - \frac{dn_c}{d\phi}\right) \frac{\partial \phi_1}{\partial \beta} = \frac{\partial n_{W,1}}{\partial \beta} \quad . \tag{55}$$

Combining the previous two equations yields

$$\Phi_0' \frac{\partial n_{W,1}}{\partial \beta} = \frac{\partial \phi_1}{\partial \beta} \left(n_{W,0}' + n_r' \right) \quad . \tag{56}$$

We now integrate Eq. (56) along a field line to cast it into a form that we will need in the next section. Thus

$$\phi_0' \oint \frac{dl}{B} \frac{\partial n_{W,1}}{\partial \beta} = \frac{\partial \phi_1}{\partial \beta} \left(\hat{n}_{W,0}' U_{W,n,0} + \hat{n}_r' U_{r,n} \right) \quad , \tag{57}$$

where we have noted that ϕ is constant along field lines and have neglected integrals of the order of $U_{W,n,0}'$ and $U_{r,n}'$.

VI. POLOIDALLY ASYMMETRIC POTENTIAL

In this section, we combine the information developed in the previous sections to obtain an analytic expression for the asymmetry in the electrostatic potential in EBT and EBS. We then compare the expression with experimental observations from EBT and compare and contrast these results with those for EBS.

The first-order density transport equation [see Eq. (42)] is

$$C_{W,1} = \hat{S}_{W,1} \quad . \tag{58}$$

We will assume that $\hat{S}_{W,1}$ is small compared to $C_{W,1}$. If we approximate $\hat{S}_{W,1}$ by

$$\hat{S}_{W,1} = -\nu \left(\oint \frac{dl}{B} n_W \right)_1 \tag{59}$$

and anticipate the result that the first-order macroscopic quantities will vary as $\cos\beta$ or $\sin\beta$, we can compare the magnitude of $S_{W,1}$ with the terms occurring in Eq. (44) for C_W. Noting that in the axisymmetric limit

$$\frac{\partial\phi}{\partial\alpha} \to \phi_0' = \Omega \equiv |E/rB| \tag{60}$$

(i.e., ϕ_0' is the $\underset{\sim}{E} \times \underset{\sim}{B}$ poloidal precession frequency), we estimate that $\hat{S}_{W,1}/C_{W,1} = O(\nu/\Omega)$. Thus we anticipate that $\hat{S}_{W,1}$ being small compared to $C_{W,1}$ will be justified if the fluid loss rate induced by scattering, ν, is small compared to the $\underset{\sim}{E} \times \underset{\sim}{B}$ poloidal precession frequency.

Since the fluid loss rate vanishes as the scattering vanishes, we cannot really allow ν to vanish, since this would preclude justifying our fluid treatment. The situation here is similar to that encountered in "plateau" transport when calculating resonant neoclassical diffusion coefficients.[20,21] Indeed, the fluid equations are quite similar to (but more complex than) the first-order kinetic equation encountered in resonant neoclassical transport coefficient calculations (e.g., spatial diffusion here plays the same role as velocity space diffusion does in transport calculations), and the approximations used are similar to those often used in the plateau limit. By analogy we expect that the resultant expressions will give reasonable global results but will be poor approximations very near singularities or resonances (e.g., $\Omega \simeq 0$).

From Eq. (44) we have

$$C_{W,1} = \phi_0' \left(\frac{\partial \hat{n}_{W,1}}{\partial \beta} U_{W,n,0} + \hat{n}_{W,n,0} \frac{\partial U_{W,n,1}}{\partial \beta} \right) - \frac{\partial \phi_1}{\partial \beta} \hat{n}_{W,0}' U_{W,n,0}$$

$$- \frac{1}{|e|} \hat{p}_{W,0}' \frac{\partial U_{W,\parallel,1}}{\partial \beta} \quad , \tag{61}$$

where we have neglected the radial (or α) derivatives of $U_{W,n,0}$ and $U_{W,\parallel,0}$. By neglecting $U_{W,\parallel,0}'$ we have dropped a term proportional to $\partial \hat{p}_{W,1}/\partial \beta$. This allows us to avoid simultaneously solving the density and energy transport equations for the poloidal variation.

Using Eq. (57) we eliminate $\partial \hat{n}_{W,1}/\partial \beta$ from $C_{W,1}$:

$$C_{W,1} = \phi_0' \hat{n}_{W,0} \left(\frac{\partial U_{W,n,1}}{\partial \beta} - \oint \frac{dl}{B} \frac{\partial G_n}{\partial \beta} \right)$$

$$+ \frac{\partial \phi_1}{\partial \beta} \left(\hat{n}_r' U_{r,n} \right) - \frac{1}{|e|} \hat{p}_{W,0}' \frac{\partial U_{W,\parallel,1}}{\partial \beta} \quad . \tag{62}$$

Combining Eqs. (58), (59), and (62) we obtain

$$\frac{\partial \phi_1}{\partial \beta} + \tilde{\nu} \phi_1 = -K \phi_0 \quad , \tag{63}$$

where

$$\tilde{\nu} = \frac{\nu}{\Omega_E} \left(1 + \frac{\hat{n}_{W,0}' U_{W,n,0}}{\hat{n}_r' U_{r,n}} \right) \quad , \tag{64}$$

and

$$K = \frac{1}{U_{W,n,0}} \left(\frac{\partial U_{W,n,1}}{\partial \beta} - \oint \frac{dl}{B} \frac{\partial G_n}{\partial \beta} \right) H \quad , \tag{65}$$

$$H = \frac{\hat{n}_{W,0}}{\hat{n}'_r} \frac{U_{W,n,0}}{U_{r,n}} \frac{\phi'_0}{\phi_0} (1 - \delta) \quad , \tag{66}$$

$$\delta = \frac{1}{|e|} \frac{\hat{p}'_{W,0}}{\phi'_0 \hat{n}_{W,0}} \frac{\partial U_{W,\parallel,1}/\partial\beta}{\frac{\partial U_{W,n,1}}{\partial\beta} - \oint \frac{dl}{B} \frac{\partial G_n}{\partial\beta}} \quad . \tag{67}$$

Anticipating that $U_{W,n,1}$ and G_n are proportional to $\cos\beta$, we write

$$K \simeq K_0 \sin\beta \quad , \tag{68}$$

and Eq. (63) has solutions

$$\frac{\phi_1}{\phi_0} \simeq \frac{K_0}{1+\tilde{\nu}^2} \left(\cos\beta - \tilde{\nu} \sin\beta\right) \quad .$$

Thus the effect of small but finite $\tilde{\nu}$ is to rotate the surface of symmetry away from the equatorial plane ($\beta = 0, \pi$). In the remainder of this section, we will concentrate on estimating the magnitude and consider the limit $\tilde{\nu} = 0$.

To simplify the task of estimating the various quantities, we assume that all the radial (or α) scale lengths are comparable, so that

$$H \simeq \frac{\hat{n}_{W,0}}{\hat{n}_r} \frac{U_{W,n,0}}{U_{r,n}} (1 - \delta) \quad , \tag{69}$$

$$\delta \simeq \frac{T_{W,0}}{|e|\phi_0} \frac{\partial U_{W,\parallel,1}/\partial\beta}{\frac{\partial U_{W,n,1}}{\partial\beta} - \oint \frac{dl}{B} \frac{\partial G_n}{\partial\beta}} \quad , \tag{70}$$

or

$$\delta \simeq \frac{1}{A} \quad , \tag{71}$$

where we have used $\hat{p}_{W,0} = \hat{n}_{W,0}\, T_{W,0}$ and made use of Eq. (49). We have already noted that A tends to be large so that δ tends to be small (e.g., 1/6 to 1/2). The ratio $\hat{n}_{W,0} U_{W,n,0}/(\hat{n}_r U_{r,n})$ appearing in Eq. (69) is simply the ratio of the number of warm electrons on a field line to the number of hot electrons on the same field line. This ratio tends to be large since the warm electron density exceeds the hot electron density in the midplane of EBT and the warm electrons tend to extend farther along the field lines. To within a factor of 2, the estimate for EBT is that H is 3.[22]

For EBS we will also assume that H is approximately equal to 3. The rationale depends upon the facts that the heating geometry (on a field line) is similar for EBT and EBS and that loss processes are relatively weak in the transition region between the highly trapped ring electrons and the warm electrons. Thus the Fokker-Planck equation for the electrons takes the form $\partial/\partial \underset{\sim}{v} \cdot (\underset{\simeq}{A} \cdot \partial f/\partial \underset{\sim}{v} + \underset{\sim}{B} f) \simeq 0$ with the ratio of the elements in $\underset{\simeq}{A}$ and $\underset{\sim}{B}$ relatively constant between EBT and EBS. Since this equation is homogeneous, if f is a solution, so is any multiple of f. Thus, if the number of warm electrons per field line increases, so does the number of hot electrons, and their ratio (the dominant part of H) is unchanged.

We expect that the reduction in losses in EBS (due to better magnetics) would increase the number of both warm and ring electrons. Probably most important is a reduction of losses for the warm electrons at high values of $v_{||}/v$. Because ECH gives electrons perpendicular

energy, we expect this to be a relatively minor effect. There is, however, greater uncertainty in the value of H for EBS (e.g., an additional factor of 2).

Thus, neglecting $\tilde{\nu}$ in Eq. (63) and setting $H \simeq 3$ in Eq. (65), we obtain

$$\frac{1}{\phi_0}\frac{\partial\phi_1}{\partial\beta} \simeq -3\,\frac{1}{U_{W,n,0}}\left(\frac{\partial U_{W,n,1}}{\partial\beta} - \oint \frac{dl}{B}\frac{\partial G_n}{\partial\beta}\right), \tag{72}$$

and our remaining task is to determine the behavior of the right side of Eq. (72). We begin by noting that while the warm electrons in EBT are quite anisotropic, the right side of Eq. (72) would be simplified considerably if the warm electrons were isotropic, for in this limit

$$\frac{1}{U_{W,n,0}}\left(\frac{\partial U_{W,n,1}}{\partial\beta} - \oint \frac{dl}{B}\frac{\partial G_n}{\partial\beta}\right) \to \frac{\partial}{\partial\beta}\ln \oint \frac{dl}{B} \quad . \tag{73}$$

This suggests that we define

$$I \equiv \frac{\partial}{\partial\beta}\ln\left(\oint \frac{dl}{B}\right), \tag{74}$$

$$a \equiv \frac{1}{IU_{W,n,0}}\left(\frac{\partial U_{W,n,1}}{\partial\beta} - \oint \frac{dl}{B}\frac{\partial G_n}{\partial\beta}\right), \tag{75}$$

so that

$$\frac{1}{\phi_0}\frac{\partial\phi_1}{\partial\beta} = -3Ia \quad , \tag{76}$$

where the anisotropy function, a, is unity for an isotropic warm electron distribution.

Equation (76) shows that the drive for the poloidal asymmetry in the electrostatic potential is the poloidal asymmetry in $\oint dl/B$ or its anisotropic generalization. Recalling the interpretive remarks about $\oint dl/B$ and its anisotropic generalization at the end of Sec. II, we see that, from the microscopic point of view, it is the dispersion in the single particle magnetic drift motion which produces the asymmetry in the electrostatic potential.

Because the hot electron rings occur at relatively large radii, accurate evaluation of the factors I and a requires numerical treatment of the magnetic field. Nonetheless, considerable insight can be gained by carrying through analytic evaluation of I near the magnetic axis. Thus, prior to presenting the results of numerical computation, we give these simplified calculations.

Neglecting the bumpiness of the magnetic field, we write the magnetic field for EBT as

$$B \simeq B_0\left(\frac{R_0}{R}\right) \simeq \left(1 - \frac{r}{R_0}\cos\theta\right) B_0 \quad , \tag{77}$$

$$dl = Rd\xi = R_0\left(1 + \frac{r}{R_0}\cos\theta\right)d\xi \quad , \tag{78}$$

where R is the major radius and ξ is the toroidal angle. Then

$$\frac{dl}{B} \simeq \frac{R_0}{B_0}\left(1 + 2\frac{r}{R_0}\cos\theta\right) \quad . \tag{79}$$

Here θ is the poloidal angle referenced to the minor axis. Neglecting the fact that θ and β are measured about different axes, we see that

$$U \equiv \oint \frac{dl}{B} \approx \frac{2\pi R_0}{B_0} \left(1 + 2\frac{r}{R_0} \cos\beta\right) \quad . \tag{80}$$

This particular formula is in reasonable agreement with the numerical calculation of U at the ring position in EBT:

$$\frac{U_1}{U_0} \approx \frac{1}{10} \cos\beta \quad . \tag{81}$$

Thus for EBT

$$I \approx \frac{1}{10} \frac{\partial}{\partial\beta} (\cos\beta) \quad . \tag{82}$$

Because all toroidal effects in EBS are concentrated in the corners (see Fig. 1), the situation is somewhat different in EBS. In the sides, we again neglect the bumpiness so that the contribution from the sides is simply

$$U_{side} = 4L/B_s \quad ,$$

where L is the length of a single side and B_s is a "mean" value of B in the side. In the corners, where the field is essentially that of a toroidal solenoid,

$$dl \approx R_c\left(1 + \frac{r_c}{R_c} \cos\theta\right) \quad , \tag{83}$$

$$B \simeq B_c\left(1 - \frac{r_c}{R_c}\cos\theta\right) \quad , \tag{84}$$

where R_c is the radius of the magnetic axis in the corner, and B_c, r_c, and θ are the magnetic field on axis, minor radius, and poloidal angle, respectively, in the corner. Thus in the corners

$$\frac{dl}{B} \simeq \frac{R_c}{B_c}\left(1 + 2\,\frac{r_c}{R_c}\cos\theta\right) \quad , \tag{85}$$

and the contribution of all four corners to $\oint dl/B$ is

$$U_{corner} = \frac{2\pi R_c}{B_c}\left(1 + 2\,\frac{r_c}{R_c}\cos\theta\right) \quad . \tag{86}$$

Thus for EBS

$$U \simeq \frac{4L}{B_s} + \frac{2\pi R_c}{B_c}\left(1 + 2\,\frac{r_c}{R_c}\cos\theta\right) \quad . \tag{87}$$

To minimize the toroidal effects (the $2r_c/B_c \cos\theta$ term in the present instance), the ratio of the length of the sides to the length of the corners is kept as large as practical:

$$\frac{4L}{2\pi R_c} >> 1 \quad . \tag{88}$$

The global mirror ratio

$$M_G = B_c/B_s$$

is also made as large as practical. (Because we have neglected the bumpiness of the sides, this definition of global mirror ratio is slightly different from the standard one.) Thus in EBS

$$U \simeq \frac{4L}{B_s}\left[1 + \left(\frac{2\pi R_c}{4L}\right)\frac{1}{M_G} \cdot 2\frac{r_c}{R_c}\cos\theta\right] \quad . \tag{89}$$

Because the global mirror ratio is large (e.g., 3 to 10) the radius of a field line in the corner is less than the minor radius in the midplane, r_s, of a side by approximately $M_G^{1/2}$. Thus

$$U \simeq \frac{4L}{B_s}\left[1 + \left(\frac{2\pi R_c}{4L}\right)\left(\frac{1}{M_G^{3/2}}\right)\frac{2r_s}{R_c}\cos\theta\right] \quad , \tag{90}$$

and

$$\frac{U_1}{U_0} \simeq \left(\frac{2\pi R_c}{4L}\right)\frac{1}{M_G^{3/2}} \cdot \frac{2r_s}{R_c}\cos\theta \quad . \tag{91}$$

The above formula reveals the strong dependence of the asymmetry of $\oint dl/B$ in EBS on the global mirror ratio (a readily controlled parameter). It also shows that the asymmetry in $\oint dl/B$ is relatively insensitive to the corner radius, R_c. The reduction caused by adding more mirror cells to the sides is contained in the dependence on L. Because of the approximations made, it does not show the effect of

local mirror ratio (bumpiness of the sides) or the importance of carefully tailoring the transition between the sides and corners.

Numerical calculations show that U_1/U_0 in EBS can be reduced by as much as an order of magnitude from that of EBT. Thus

$$I_{EBS} \lesssim \frac{1}{10} I_{EBT} \quad . \tag{92}$$

Of course, by decreasing the global mirror ratio (e.g., decreasing B_c) I_{EBS} can be increased considerably.

In EBT, soft X-ray measurements[6] in the midplane and coil plane indicate that less than 10% of the intermediate energy or warm electron population is passing or transitional. That is, more than 90% of the warm electron population is trapped, and only the remaining 10% is isotropic. Thus it is important to study the effect of anisotropy.

In both EBT and EBS, the anisotropy factor, a, must approach zero as the anisotropy of the warm electrons approaches that of the highly anisotropic hot electron rings. This follows from the fact that in this case $U_{W,n}$ would approach $U_{r,\parallel}$, which by definition is only a function of α. On the other hand, for purely isotropic distribution, a is unity by construction. Because the toroidal effects are more or less uniformly distributed in EBT, we would expect that the rise to the isotropic limit would occur even when the distribution consisted of only trapped particles. For EBS, however, the magnetic field in the sides is axisymmetric to a high level of accuracy so that we would expect this same trapped particle distribution to yield zero asymmetry in EBS.

Since a wide variety of distributions is possible, we first examine G_n of the form

$$\hat{G}_n = \begin{cases} 1 & ; \quad B < B_c \\ 0 & ; \quad B > B_c \end{cases} . \tag{93}$$

We can then decompose more realistic distribution functions in terms of these functions and deduce those corresponding to the more realistic G_n. Thus, for example, if we approximate the distribution for EBT so that

$$G_n = f_1 \hat{G}_n(B_{c1}) + f_2 \hat{G}_n(B_{c2}) \tag{94}$$

with $f_1 \approx 90\%$ and $f_2 \approx 10\%$, then for this distribution

$$a = f_1 \hat{a}(B_{c1}) + f_2 \hat{a}(B_{c2}) \quad , \tag{95}$$

where $\hat{a}(B_c)$ is obtained by inserting $\hat{G}_n$ in Eq. (75).

Figure 2 shows the result of numerically calculating $\hat{a}$ for both EBT and EBS. The features described earlier are apparent from these graphs. The only new feature is the relative maxima in $\hat{a}$ which occur near the transition between trapped and passing (or isotropic) for both EBT and EBS. While somewhat exaggerated by our choice of $\hat{G}_n$, these maxima reflect the fact that transitional particle magnetic drift orbits are the most asymmetric.

It will be noticed from Fig. 2 that for purely trapped particle distributions in EBT, $\hat{a}$ is nearly the same as for the isotropic case.

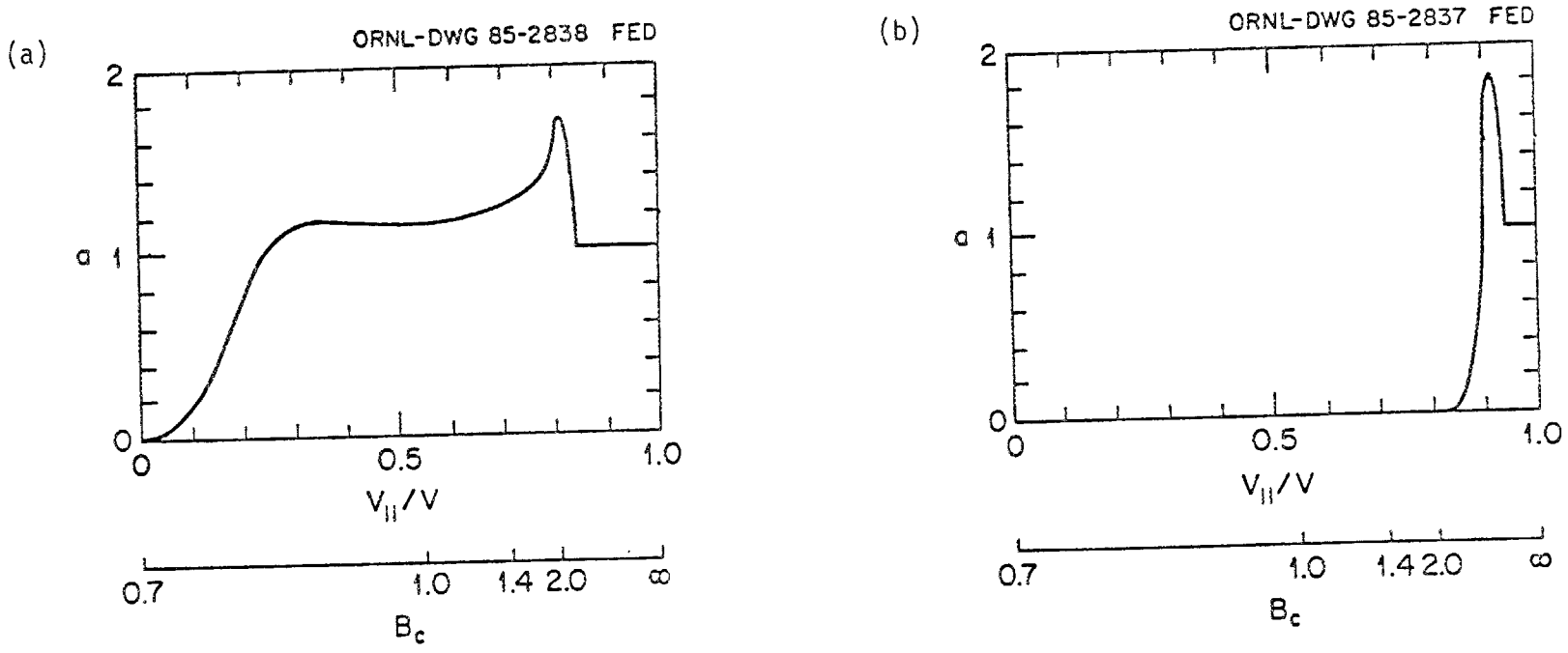

Fig. 2. Anisotropy factor, a, for (a) EBT and (b) EBS. Two scales are used: B_c (normalized to the value of B in the midplane on the magnetic axis) and $v_{||}/v = (1 - B_2/B_c)^{1/2}$, where B_2 (here equal to 0.7) is the value of B at the second harmonic electron cyclotron resonance. The fundamental resonance of the electron cyclotron resonance occurs at $B_c = 1.4$. For EBT the boundary between trapped and passing occurs near $B_c = 2$, while for EBS it occurs near $B_c = 5$.

Thus for EBT the effect of anisotropy is relatively small (e.g., 30%). Since this effect is small compared to the factor of 2 uncertainty in H, we set a = 1 for EBT, so that using Eqs. (76) and (82) we obtain

$$\frac{\phi_1}{\phi_0} \simeq -\frac{1}{3}\cos\beta \quad . \tag{96}$$

Thus at $\beta = 0$, $\phi \simeq 2/3\phi_0$ while at $\beta = \pi$, $\phi \simeq 4/3\phi_0$, so

$$\frac{\phi(\beta = 0)}{\phi(\beta = \pi)} \simeq \frac{1}{2} \quad , \tag{97}$$

which is typical of EBT experimental data (to within the aforementioned factor of 2) in the T-mode.[1-4]

For EBS, we see that the effect of anisotropy is very important since $\hat{a}$ for the trapped portion is zero. Using Eq. (95), we see that for $f_2 \simeq 10\%$

$$a \simeq \frac{1}{10} \quad .$$

Because ECH gives electrons perpendicular energy we do not expect the fraction of passing (or isotropic) warm electrons in EBS to be substantially larger than in EBT -- even though these less well trapped particles would be better confined in EBS than in EBT.

Thus the asymmetry in ϕ for EBS is reduced below that of EBT by two factors. The first factor comes from the improvement in global confinement properties as indicated by the reduced asymmetry in $\oint dl/B$. The second factor arises from the anisotropic character of the warm

electrons and the near-perfect axisymmetry of the magnetic field in the sides. Each of these factors, if one uses EBT parameters, yields an order of magnitude reduction in the poloidal asymmetry in ϕ. Because of the greater uncertainty in H and f_2 for EBS, we estimate that the overall decrease in the poloidal asymmetry in ϕ is reduced by one to two orders of magnitude.

VII. SUMMARY

In this paper we have obtained an analytic expression for the poloidal asymmetry in the electrostatic potential which is in reasonable agreement with experimental observation. Applying this expression to the EBS configuration reveals that the asymmetry in the potential is reduced due to two factors. One factor is the overall improvement in magnetic confinement of single particles as manifested through the reduced asymmetry in $\oint dl/B$. The second factor arises because the intermediate energy population of electrons consists primarily of trapped particles that are confined to the very nearly axisymmetric mirror cells in the sides of an EBS.

One reason that this reduction in the poloidal asymmetry in the potential for EBS is important is that it greatly reduces the loss of cooler electrons and ions that constitute the bulk of the plasma.[23] The Monte Carlo calculations carried out in Ref. 23 indicate that strong poloidal asymmetry in the potential (as in EBT) leads to "convective" losses that are about an order of magnitude larger than the purely diffusive losses usually assumed. For the greatly reduced poloidal asymmetry in the potential predicted for EBS, these "convective" losses

become negligible compared to diffusive losses, and the overall lifetimes of EBS are increased by one to two orders of magnitude above those of EBT. The calculations of Ref. 23 (see particularly Fig. 10) indicate that once the poloidal asymmetry in the potential is sufficiently small (i.e., in the range predicted here), the lifetime in EBS depends far more on the global mirror ratio than on the poloidal asymmetry in the electrostatic potential.

To obtain the expression for the asymmetry in the potential, it has been necessary to make a number of approximations. In particular, the problem was greatly simplified by neglecting radial (or α) derivatives of $\oint dl/B$ (and similar anisotropic generalizations of $\oint dl/B$) compared to the radial derivatives of other macroscopic quantities. While justifiable for the global information developed here, this approximation cannot be justified very near the x-point in the potential. Thus, to obtain more fine-grained information about the potential (especially for lower scattering rates relative to the $\underset{\sim}{E} \times \underset{\sim}{B}$ precession), it appears necessary to simultaneously solve the first-order density and energy transport equations for the warm electrons including the differential character of (diffusive) scattering effects. However, the problem is further complicated by the breakdown of the assumptions made here for the cooler electrons and ions near the x-point in ϕ.

The Monte Carlo calculations of Ref. 23 suggest that at least for the cooler electrons and ions, both radial and poloidal diffusion are important near the x-point in ϕ. This suggests that all six transport equations (density and energy transport equations for warm electrons, cool electrons, and ions) should include both radial and poloidal diffusion. Leaving aside the question of how one determines the

various transport coefficients, six coupled second-order partial differential equations in two dimensions is clearly a complicated system to solve.

In the absence of two-dimensional diffusion, each of these transport equations is of the type considered when calculating resonant neoclassical transport coefficients [see particularly Eq. (1) of Ref. 20]. Thus it seems that a logical next step would be to examine the behavior of a single differential equation of this type which included scattering in two dimensions rather than one. Comparison with Monte Carlo results could further illuminate the "fluid" behavior near the x-point in the potential.

Finally, we note that we have neglected poloidal asymmetry in the microwave heat deposition. Our initial motivation for this was the fact that no strong correlation was observed experimentally between the poloidal asymmetry in the microwave launching structure and the poloidal asymmetry in the electrostatic potential.[24] Note that experiments were conducted with microwave launch structures at poloidal angles which differed by 135^{o}, so that if a strong correlation existed it would have been observed. This is not to say that no poloidal asymmetry in the microwave heat deposition occurred -- it simply did not appear to be a strong effect.

There are, however, theoretical reasons to believe that the poloidal asymmetry in the microwave heat deposition is small. In contrast to Tandem Mirror experiments,[25] the microwave antenna patterns in EBT are not strongly focused and the microwave single pass absorption is small.[26] A consequence of this is that microwave energy is reflected from walls many times before it is absorbed. These wall reflections tend to randomize the initial poloidal asymmetry.

While a definitive calculation of the poloidal asymmetry in the microwave heat deposition is clearly beyond the scope of this paper, it is possible to make estimates of the order of magnitude of the asymmetry. We estimate that in EBT the poloidal asymmetry in the microwave heat deposition is of the order of a percent or less. Including this asymmetry in $\hat{S}_{W,1}$ and using the techniques and approximations of Sec. VI, we estimate that the effect of poloidal asymmetry in the microwave heat deposition on the poloidal asymmetry in the electrostatic potential is at least an order of magnitude less than that produced by magnetic drift motion -- the subject of this paper.

Using this same estimate of the poloidal asymmetry in the microwave heat deposition for EBS leads to a poloidal asymmetry in the electrostatic potential which falls in the range produced by magnetic drift motion. As we have already mentioned, within this range of electrostatic potential asymmetry the bulk lifetimes do not differ appreciably.[23]

Of course, it might be possible that the EBS configuration would achieve such large densities and temperatures that the microwave single pass absorption would be significantly increased. In this case, it would probably be necessary to utilize a more symmetric launch structure to symmetrize the microwave heat deposition -- much as was conceived for Tandem Mirror applications.[25]

This research was sponsored by the Office of Fusion Energy, U.S. Department of Energy, under contract DE-AC05-840R21400 with Martin Marietta Energy Systems, Inc.

APPENDIX

A Useful Tensor Pressure Relation

In both magnetic equilibrium [see Eq. (10)] and transport [see Eq. (28)] calculations one encounters a quantity of the form

$$Q \equiv \underset{\sim}{\nabla} \cdot \left[\frac{\underset{\sim}{B} \times (\underset{\sim}{\nabla} \cdot \underset{\approx}{P}_k)}{B^2} \right] . \tag{A.1}$$

Here we express Q in a form which facilitates analysis and allows interpretation of fluid quantities in terms of single particle drift motion. It is assumed that the pressure tensor has the standard form:

$$\underset{\approx}{P}_k = p_\perp (\underset{\approx}{1} - \hat{b}\hat{b}) + p_\parallel \hat{b}\hat{b} \tag{A.2}$$

Our first task is to develop a relation between $p_\perp$ and $p_\parallel$ for the case when $\underset{\approx}{P}_k$ represents the pressure tensor of a single species and hence does not necessarily obey the magnetic equilibrium relation $\underset{\sim}{j} \times \underset{\sim}{B} = \underset{\sim}{\nabla} \cdot \underset{\approx}{P}$. (When $\underset{\approx}{P}_k$ refers to the total pressure, then one can obtain the relation between $p_\perp$ and $p_\parallel$ from the equilibrium relation.) Thus for the moment we assume that $p_\perp$ and $p_\parallel$ arise from a single species and that

$$p_\parallel = m \int d^3 v f v_\parallel^2 \quad , \tag{A.3}$$

$$p_\perp = \frac{m}{2} \int d^3 v f v_\perp^2 \quad , \tag{A.4}$$

where f is a function of ε, μ, α, and β so that

$$p_{\parallel} = 2\left(\frac{4\pi}{2^{1/2}m^{3/2}}\right) \int d\varepsilon d\mu B(\varepsilon - \mu B)^{1/2} \, f \quad , \tag{A.5}$$

$$p_{\perp} = \left(\frac{4\pi}{2^{1/2}m^{3/2}}\right) \int d\varepsilon\phi\mu \, \frac{B^2 \mu f}{(\varepsilon - \mu B)^{1/2}} \quad . \tag{A.6}$$

We notice that it is natural to write $p_{\perp}$ and $p_{\parallel}$ as functions of α, β, and B. If we form

$$B\frac{\partial p_{\parallel}}{\partial B} - p_{\parallel} = -\left(\frac{4\pi}{2^{1/2}m^{3/2}}\right) \int \frac{d\varepsilon d\mu B^2 \mu f}{(\varepsilon - \mu B)^{1/2}} \quad , \tag{A.7}$$

we see that

$$B\frac{\partial p_{\parallel}}{\partial B} = p_{\parallel} - p_{\perp} \quad . \tag{A.8}$$

Equation (A.8) can also be derived from the parallel component of $\underset{\sim}{j} \times \underset{\sim}{B} = \underset{\sim}{\nabla} \cdot \underset{\approx}{P}$. We emphasize that this equilibrium relation need not, however, be invoked.

From Eqs. (A.2) and (A.8), we find that

$$\underset{\sim}{\nabla} \cdot \underset{\approx}{P}_k = \underset{\sim}{\nabla}_{\perp} p_{\perp} + (p_{\parallel} - p_{\perp})\underset{\sim}{\kappa} \tag{A.9}$$

so that

$$Q = \frac{1}{B^2}\left(D_1 + D_2 - D_3\right) \quad , \tag{A.10}$$

where

$$D_1 = \nabla \cdot (\underset{\sim}{B} \times \nabla p_\perp) \quad ,$$

$$D_2 = 2\nabla p_\perp \cdot (\underset{\sim}{B} \times \nabla \ln B) + 2(p_\perp - p_\parallel)\nabla \ln B \cdot (\underset{\sim}{B} \times \underset{\sim}{\kappa}) \quad , \tag{A.11}$$

$$D_3 = \nabla \cdot \left[(p_\perp - p_\parallel)(\underset{\sim}{B} \times \underset{\sim}{\kappa})\right] \quad .$$

Using the vector identity for the divergence of a cross-product and the fact that the curl of a gradient is zero, we find that

$$D_1 = \nabla p_\perp \cdot (\nabla \times \underset{\sim}{B}) \quad . \tag{A.12}$$

Since

$$\nabla \times \underset{\sim}{B} = \underset{\sim}{j} = \underset{\sim}{j}_\perp + j_\parallel \hat{b} \tag{A.13}$$

and

$$\underset{\sim}{j}_\perp = \underset{\sim}{B} \times (\underset{\sim}{\kappa} - \nabla \ln B) \tag{A.14}$$

[which follows from the vector identity for the gradient of the inner product of $\underset{\sim}{B}$ with itself and Eq. (A.13)], we find that

$$D_1 = j_\parallel \frac{\partial p_\perp}{\partial l} + \nabla p_\perp \cdot \left(\underset{\sim}{B} \times \underset{\sim}{\kappa} - \underset{\sim}{B} \times \nabla \ln B\right) \tag{A.15}$$

so that

$$D_1 + D_2 = j_\parallel \frac{\partial p_\perp}{\partial l} + \nabla p_\perp \cdot \left(\underset{\sim}{B} \times \underset{\sim}{\kappa} + \underset{\sim}{B} \times \nabla \ln B\right)$$

$$+ 2(p_\perp - p_\parallel)\, \nabla \ln B \cdot (\underset{\sim}{B} \times \underset{\sim}{\kappa}) \quad . \tag{A.16}$$

To evaluate D_3, we use Eq. (A.14) to obtain

$$\nabla \cdot (\underset{\sim}{B} \times \underset{\sim}{\kappa}) = \nabla \cdot \left(\underset{\sim}{j} - j_\parallel \hat{b} + \underset{\sim}{B} \times \nabla \ln B\right) \quad . \tag{A.17}$$

From $\underset{\sim}{\nabla} \cdot \underset{\sim}{j} = 0$, we obtain

$$\underset{\sim}{\nabla} \cdot (\underset{\sim}{B} \times \underset{\sim}{K}) = \frac{-\partial j_{\parallel}}{\partial l} + j_{\parallel} \frac{\partial \ln B}{\partial l} + \underset{\sim}{\nabla} \cdot (\underset{\sim}{B} \times \underset{\sim}{\nabla} \ln B) \quad . \tag{A.18}$$

Using the vector identity for the divergence of a cross-product and the facts that the curl of a gradient is zero and $\underset{\sim}{j} = \underset{\sim}{\nabla} \times \underset{\sim}{B}$, we write

$$\begin{aligned} \underset{\sim}{\nabla} \cdot (\underset{\sim}{B} \times \underset{\sim}{\nabla} \ln B) &= \underset{\sim}{j} \cdot \underset{\sim}{\nabla} \ln B \\ &= j_{\parallel} \frac{\partial \ln B}{\partial l} + \underset{\sim}{j}_{\perp} \cdot \underset{\sim}{\nabla} \ln B \\ &= j_{\parallel} \frac{\partial \ln B}{\partial l} + \underset{\sim}{\nabla} \ln B \cdot (\underset{\sim}{B} \times \underset{\sim}{K}) \quad , \end{aligned} \tag{A.19}$$

where we have used Eq. (A.14) to perform the last step. Combining Eqs. (A.18) and (A.19), we obtain

$$\underset{\sim}{\nabla} \cdot (B \times \underset{\sim}{K}) = - \frac{\partial j_{\parallel}}{\partial l} + 2 j_{\parallel} \frac{\partial \ln B}{\partial l} + \underset{\sim}{\nabla} \ln B \cdot (\underset{\sim}{B} \times \underset{\sim}{K}) \quad . \tag{A.20}$$

Thus Eqs. (A.11) and (A.20) yield

$$\begin{aligned} D_3 = (p_{\parallel} - p_{\perp}) &\left(\frac{\partial j_{\parallel}}{\partial l} - 2 j_{\parallel} \frac{\partial \ln B}{\partial l} \right) \\ &+ (\underset{\sim}{B} \times \underset{\sim}{K}) \cdot \left[\underset{\sim}{\nabla} p_{\perp} - \underset{\sim}{\nabla} p_{\parallel} + (p_{\perp} - p_{\parallel}) \underset{\sim}{\nabla} \ln B \right] \quad . \end{aligned} \tag{A.21}$$

We next define

$$\hat{\underset{\sim}{\nabla}} p_{\parallel} = \underset{\sim}{\nabla} \alpha \frac{\partial p_{\parallel}}{\partial \alpha} + \underset{\sim}{\nabla} \beta \frac{\partial p_{\parallel}}{\partial \beta} = \underset{\sim}{\nabla} p_{\parallel} - \frac{\partial p_{\parallel}}{\partial B} \underset{\sim}{\nabla} B \quad . \tag{A.22}$$

Combining Eq. (A.22) with Eq. (A.8), we find that

$$\underset{\sim}{\nabla} p_{\parallel} = \hat{\underset{\sim}{\nabla}} p_{\parallel} - (p_{\perp} - p_{\parallel}) \underset{\sim}{\nabla} \ln B \quad , \tag{A.23}$$

and Eq. (A.21) becomes

$$\begin{aligned} D_3 = {} & (p_{\parallel} - p_{\perp}) \left(\frac{\partial j_{\parallel}}{\partial l} - 2 j_{\parallel} \frac{\partial \ln B}{\partial l} \right) \\ & + (\underset{\sim}{\nabla} p_{\perp} - \hat{\underset{\sim}{\nabla}} p_{\parallel}) \cdot (\underset{\sim}{B} \times \underset{\sim}{\kappa}) \\ & + 2(p_{\perp} - p_{\parallel}) \underset{\sim}{\nabla} \ln B \cdot (\underset{\sim}{B} \times \underset{\sim}{\kappa}) \quad , \end{aligned} \tag{A.24}$$

where we have used Eq. (A.8).

Combining Eqs. (A.16) and (A.24) yields

$$\begin{aligned} D_1 + D_2 - D_3 = {} & \underset{\sim}{\nabla} p_{\perp} \cdot (\underset{\sim}{B} \times \underset{\sim}{\nabla} \ln B) + \hat{\underset{\sim}{\nabla}} p_{\parallel} \cdot (\underset{\sim}{B} \times \underset{\sim}{\kappa}) \\ & + (p_{\perp} - p_{\parallel}) \frac{\partial j_{\parallel}}{\partial l} + j_{\parallel} \left[-2(p_{\perp} - p_{\parallel}) \frac{\partial \ln B}{\partial l} + \frac{\partial p_{\perp}}{\partial l} \right] \quad . \end{aligned} \tag{A.25}$$

Since

$$\begin{aligned} B^3 \frac{\partial}{\partial l} \left[\left(\frac{p_{\perp} - p_{\parallel}}{B^3} \right) j_{\parallel} \right] &= (p_{\perp} - p_{\parallel}) \left(\frac{\partial j_{\parallel}}{\partial l} - \frac{3 j_{\parallel}}{B} \frac{\partial B}{\partial l} \right) + j_{\parallel} \left(\frac{\partial p_{\perp}}{\partial l} - \frac{\partial p_{\parallel}}{\partial l} \right) \\ &= (p_{\perp} - p_{\parallel}) \frac{\partial j_{\parallel}}{\partial l} + j_{\parallel} \left[-2(p_{\perp} - p_{\parallel}) \frac{\partial \ln B}{\partial l} + \frac{\partial p_{\perp}}{\partial l} \right] \end{aligned} \tag{A.26}$$

[where we have used Eq. (A.8) to eliminate $\partial p_{\parallel}/\partial l$], we find that

$$D_1 + D_2 - D_3 = \underset{\sim}{\nabla} p_{\perp} \cdot (\underset{\sim}{B} \times \underset{\sim}{\nabla} \ln B) + \hat{\underset{\sim}{\nabla}} p_{\parallel} \cdot (\underset{\sim}{B} \times \underset{\sim}{\kappa}) + B^3 \frac{\partial}{\partial l}\left[\left(\frac{p_{\perp} - p_{\parallel}}{B^2}\right)\frac{j_{\parallel}}{B}\right] . \tag{A.27}$$

Combining Eqs. (A.1), (A.10), and (A.27), we obtain

$$\underset{\sim}{\nabla} \cdot \left[\frac{\underset{\sim}{B} \times (\underset{\sim}{\nabla} \cdot \underset{\approx}{P}_k)}{B^2}\right] = \frac{1}{B^2}\left[\underset{\sim}{\nabla} p_{\perp} \cdot (\underset{\sim}{B} \times \underset{\sim}{\nabla} \ln B) + \hat{\underset{\sim}{\nabla}} p_{\parallel} \cdot (\underset{\sim}{B} \times \underset{\sim}{\kappa})\right] + B \frac{\partial}{\partial l}\left[\left(\frac{p_{\perp} - p_{\parallel}}{B^2}\right)\frac{j_{\parallel}}{B}\right] . \tag{A.28}$$

REFERENCES

[1] L. Solensten, J. R. Goyer, K. A. Connor, and R. L. Hickok, Bull. Am. Phys. Soc. 29, 1418 (1984).

[2] D. L. Hillis, J. B. Wilgen, J. A. Cobble, W. A. Davis, S. Hiroe, D. A. Rasmussen, R. K. Richards, T. Uckan, E. F. Jaeger, O. E. Hankins, J. R. Goyer, and L. Solensten, Phys. Fluids 28, 2848 (1985). (See particularly Figs. 12a and 13a).

[3] J. R. Goyer, Ph.D. dissertation, Rensselaer Polytechnic Institute, Troy, New York, 1984. See particularly Fig. 2-8.

[4] K. A. Connor, L. Solensten, J. R. Goyer, and R. L. Hickok, in Proceedings of the 1984 International Conference on Plasma Physics, edited by M. Q. Tran and R. J. Verbeck (Centre de Recherches en

Physique des Plasmas, Ecole Polytechnique, Federale de Lausanne, 1984), p. 318.

[5]N. A. Uckan, C. L. Hedrick, D. A. Spong, T. Uckan, L. A. Berry, L. W. Owen, D. K. Lee, W. E. Bryan, T. J. McManamy, P. B. Thompson, W. L. Wright, R. L. Miller, W. B. Ard, J. F. Pipkins, and R. J. Schmidt. See National Technical Information Service Document No. DE85000664 (Oak Ridge National Laboratory Report ORNL/TM-9110). Copies may be ordered from the National Technical Information Service, Springfield, Virginia 22161. The price is $22.00 plus a $3.00 handling fee. All orders must be prepaid.

[6]D. W. Swain, J. A. Cobble, D. L. Hillis, R. K. Richards, and T. Uckan, Phys. Fluids 28, 1922 (1985).

[7]R. J. Colchin, T. Uckan, F. W. Baity, L. A. Berry, F. M. Bieniosek, L. Bighel, W. A. Davis, E. Dullni, H. O. Eason, J. C. Glowienka, G. A. Hallock, G. R. Haste, D. L. Hillis, A. Komori, T. L. Owens, R. K. Richards, L. Solensten, T. L. White, and J. B. Wilgen, Plasma Phys. 25, 597 (1983). (See particularly Fig. 8.)

[8]I. B. Bernstein and D. C. Baxter, Phys. Fluids 24, 108 (1981).

[9]D. C. Mongomery and D. A. Tidman, Plasma Kinetic Theory (McGraw-Hill, New York, 1964), pp. 196-199.

[10]N. A. Krall and A. W. Trivelpiece, Principles of Plasma Physics (McGraw-Hill, New York, 1973), pp. 88-92.

[11]J. M. Greene and J. L. Johnson, Phys. Fluids 4, 875 (1961).

[12]J. B. Taylor, Phys. Fluids 6, 1529 (1963).

[13]J. L. Johnson (private communication).

[14]H. Grad and H. Rubin, in Proceedings of the Second United Nations International Conference on the Peaceful Uses of Atomic Energy (The United Nations, Geneva, 1958), Vol. 31, p. 190.

[15]H. Grad, in Plasma Physics and Controlled Nuclear Fusion, 1971 (International Atomic Energy Agency, Vienna, 1971), Vol. 3, p. 229.

[16]E. F. Jaeger, C. L. Hedrick, and D. A. Spong, Nucl. Fusion 19, 1627 (1979).

[17]E. F. Jaeger, C. L. Hedrick, and W. B. Ard, Phys. Rev. Lett. 43, 855 (1979).

[18]E. F. Jaeger, D. A. Spong, and C. L. Hedrick, Phys. Rev. Lett. 40, 866 (1978).

[19]N. A. Uckan and EBT Group, Plasma Phys. 25, 129 (1983).

[20]D. A. Spong and C. L. Hedrick, Phys. Fluids 23, 1903 (1980).

[21]D. E. Hastings, E. F. Jaeger, C. L. Hedrick, and J. S. Tolliver, Phys. Fluids 26, 1516 (1983).

[22]D. L. Hillis (private communication).

[23]J. S. Tolliver and C. L. Hedrick, submitted to Phys. Fluids.

[24]J. C. Glowienka, D. L. Hillis, and G. R. Haste (private communication).

[25]B. W. Stallard, W. F. Cummins, A. W. Molvik, P. Poulsen, and T. C. Simonen, in Proceedings of the Fourth International Symposium on Heating in Toroidal Plasmas (International School of Plasma Physics, Varenna, 1984), Vol. II, p. 931.

[26]D. B. Batchelor, R. C. Goldfinger, and D. A. Rasmussen, Phys. Fluids 27, 948 (1984).

Appendix 11

COMPARISON OF ELECTRON CYCLOTRON HEATING THEORY AND EXPERIMENT IN EBT

D. B. Batchelor

INTRODUCTION

The ELMO Bumpy Torus (EBT) device consists of 24 simple mirrors joined end-to-end so as to form a closed field line torus. The mirror ratio in each simple mirror sector is 1.9:1. The device is heated by fundamental and second harmonic electron cyclotron resonance interaction. When operated at a central midplane magnetic field of 5 kG and microwave power up to 60 kW at 18 GHz, the device is called EBT-I. When operated at a central midplane magnetic field of 7.2 kG with microwave power up to 200 kW at 28 GHz, the device is referred to as EBT-S.

For most of the time that EBT has been in operation the experimental emphasis has been on confinement experiments and stability studies. Although electron cyclotron heating (ECH) is fundamental to EBT operation, it is difficult to measure wave fields in the plasma, heating rates, or other phenomena that give information directly about the wave physics. Hence, the study of ECH on EBT began as a theoretical program whose first objective was to understand the gross features of microwave power flow and power deposition in each of the plasma components. This was accomplished by using ray tracing /1,2/ techniques and by developing a zero-dimensional (0-D) wave energy balance model that takes into account the many passes through the plasma and essentially random reflections which a typical ray makes before being absorbed /3/. Over the last several years experiments have been performed with simple microwave calorimeters that are in good agreement with the power flow calculations for a wide variety of operating conditions /2/. Now we report experimental results that directly test and calibrate some of the assumptions of the power flow and absorption modeling. That is, the single-pass wave power absorption by the hot electron rings has been measured, the microwave losses to the EBT cavity walls have been measured, and the essentially complete opacity of the fundamental resonance to extraordinary

mode waves propagating from the high-field side has been verified. In section 1 of this paper we outline the general features of microwave propagation and absorption in EBT and describe the most recent experiments.

Recent experiments and theoretical results indicate that confinement physics and heating physics in EBT devices are inextricably coupled. The picture that had previously emerged can be summarized as follows. An annular plasma of relativistic electrons ($T_A \sim 500$ keV) forms in a region near where the mod B contour for second harmonic resonance is tangent to a magnetic field line (Fig. 1). This relativistic electron component is diagnosed by hard X-ray detectors, synchrotron radiation, and diamagnetic loops. When the stored energy in the annuli becomes sufficiently large, flute instabilities associated with bad mirror curvature and plasma pressure are stabilized. It has conventionally been assumed that the stabilization mechanism is the formation of a radial magnetic well due to hot electron beta although other processes have recently been proposed /4/. The plasma radially outside the

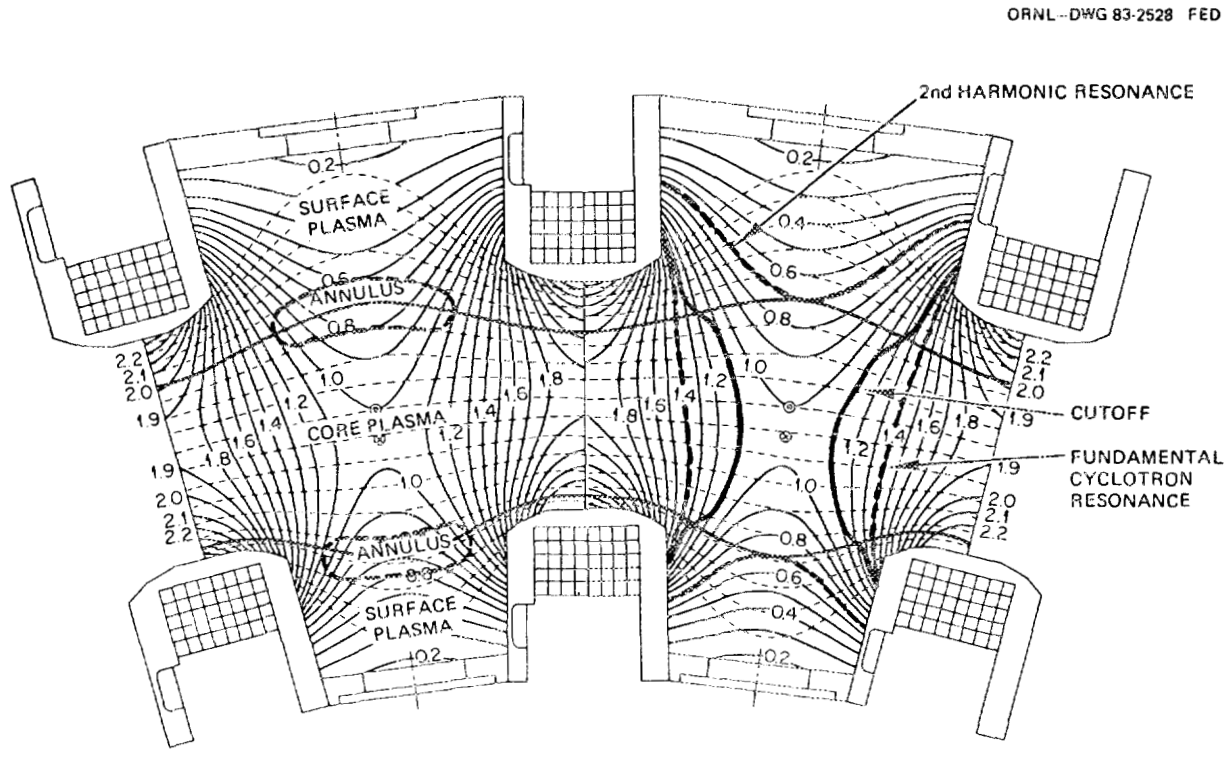

Fig. 1. Equatorial cross section of two EBT-S cavities.

annuli, referred to as the surface plasma, is unstable and very poorly confined. The plasma radially inside the annuli is called the core plasma and is believed to be stable in the usual machine operating mode, the T-mode. For a discussion of EBT operating modes see Ref. /5/. Measurements of core plasma density using microwave interferometry and of core density and temperature using soft X-ray techniques at the mirror midplane indicated core densities somewhat less than $10^{12}/cm^3$ and temperatures in the range 200 to 1200 eV in EBT-S, depending on microwave power and gas feed rate.

The temperature of the "core" component was observed to scale with decreasing collisionality in a way which strongly suggested classical or neoclassical confinement. In particular, for collisionless electrons the simplist neoclassical theory of Kovrizhnykh /6/ for bumpy tori that predicts an energy confinement time τ_E that scales as $\tau_E \propto T_e^{3/2}/n_e F(R_T, R_B, R_E, \ell)$, where F is a function of R_T = toroidal major radius, R_B = magnetic field ∇B scale length, R_E = ambipolar electric field scale length, and ℓ = plasma radius. Assuming that a constant fraction f of the input microwave power P_μ is absorbed by the core plasma, the power balance can be expressed as

$$P_\mu = \frac{n_e T_e}{\tau_E f} \propto \frac{n_e^2}{T_e^{1/2}} \frac{F(R_T, R_B, R_E, \ell)}{f} .$$

In experiments for which the neutral gas flow was adjusted so as to maintain constant plasma scale lengths, the quantity $n^2/T_e^{1/2}$ was indeed found to scale linearly with P_μ over a considerable range (Fig. 2). Also, the experimental densities and electron temperatures were consistent with 1-D transport modeling using more realistic transport coefficients and experimentally observed ambipolar potentials /7/.

Recent experiments however have shown that the core plasma confinement is considerably more complicated than is indicated by the midplane soft X-ray measurements. Thomson scattering measurements indicate that the bulk of the core density (50% to 90%) is composed of a collisional isotropic core component with T_e = 70–120 eV. Also, other recent experiments (mirror throat soft X-ray, throat-launched microwave power, and power feed turnoff experiments) demonstrate that the T_e = 200–1200 eV component seen by the midplane

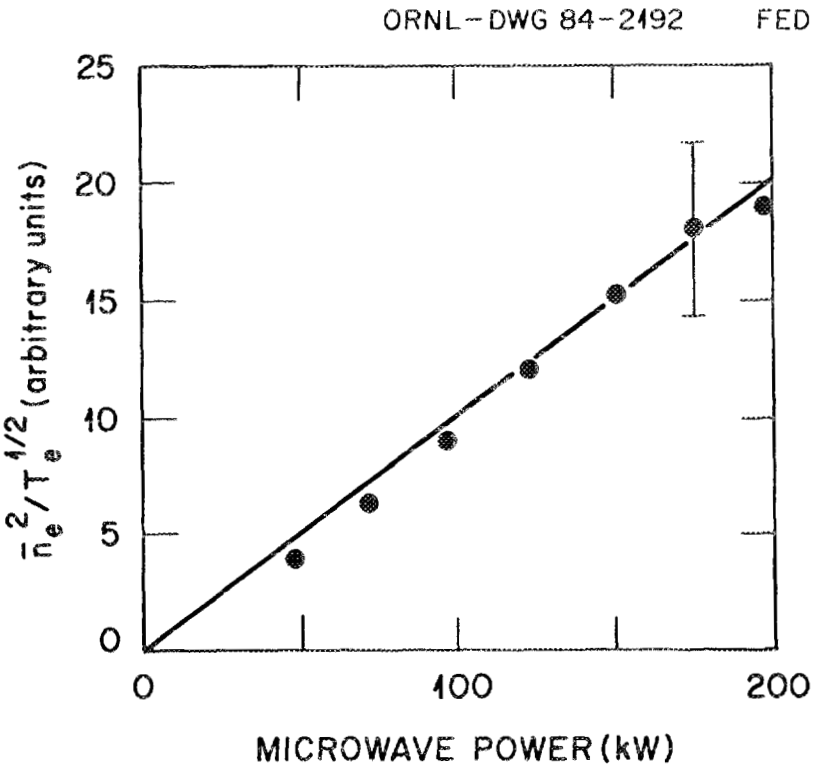

Fig. 2. $\bar{n}_e^2/T_e^{1/2}$ as determined from midplane soft X-ray vs microwave power.

soft X-ray diagnostic is in fact a collisionless anisotropic hot tail. In section 2 we describe some of these experiments and give a theoretical interpretation of that data.

1. MICROWAVE POWER FLOW AND WAVE ABSORPTION

The microwaves in EBT-I (18 GHz) are injected from waveguides located at the midplane of each mirror sector. The 28-GHz power for EBT-S operation is distributed to each sector through a toroidal manifold which is fed by the gyrotron and serves simultaneously as an overmoded waveguide distribution system and a vacuum pumping manifold. In neither case is any directive or polarizing antenna structure present.

Numerous theoretical studies undertaken to elucidate the role of propagation and absorption processes in EBT have led to a qualitative understanding of ECH in EBT-I/S:

(1) Because of strong gradients in B along field lines, any extraordinary mode energy propagating from the high-field side of the fundamental resonance is totally absorbed. This is true even for the low density surface plasma.

(2) However, the extraordinary mode right-hand cutoff prevents extraordinary mode energy launched near the mirror midplane from propagating directly to the fundamental cyclotron resonance.

(3) The ordinary mode can propagate throughout the plasma, including the high-field region.

(4) A rapid equilibration between ordinary and extraordinary modes occurs due to mode conversion at wall reflection.

(5) The density and temperature of the core and surface plasmas in EBT-I/S are sufficiently small that absorption of the ordinary mode is quite small at both fundamental and second harmonic resonances.

(6) The extraordinary mode is moderately absorbed and the ordinary mode is weakly absorbed by the hot electron annuli.

The picture that emerges is one of weakly damped rays making many transits across the device, with wall reflections and repeated ordinary-extraordinary mode conversions playing an important role in the ultimate energy deposition. In order to deal with the complicated, essentially random nature of the wave propagation after a few wall reflections, a simple 0-D power balance model was developed that treated the sources, sinks, and conversion properties in a globally averaged way. The plasma is divided into regions bounded by cavity walls, resonant surfaces, or the right-hand cutoff surface. It is assumed that each mode propagates freely inside each region. At a wall boundary surface the waves are totally reflected and partially converted to the other mode. At a boundary surface in the plasma, waves can be reflected, partially absorbed, and partially transmitted to the adjacent plasma region. The power flux for each mode in each region is assumed to be isotropic in angle and uniform in space. Details of the 0-D model are given in Refs. /2,3/. Using this model we are able to estimate the wave energy density in each mode and the fraction of the total input power P_μ which is absorbed by each

component. Using a combination of ray tracing calculations and the 0-D model we estimate that of the total power launched into the device during T-mode operation in EBT-S about 40% is deposited in the lossy surface plasma. This is because the surface plasma covers more than half of the fundamental resonance surface, and extraordinary mode energy is strongly absorbed there even for comparatively small plasma density and temperature. Approximately 33% of P_μ is deposited directly in the core plasma and about 28% goes to the hot electron annuli.

The calculations of absorption by the annulus are carried out using a relativistic form of Poynting's theorem /2,8/:

$$\frac{d}{ds}\,|\underset{\sim}{S}| = \frac{4\pi}{c}\,\underset{\sim}{E}^{*} \cdot \underset{\approx}{\sigma}^{H} \cdot \underset{\sim}{E} \,.$$

Here, s is the arc length along a ray, $\underset{\sim}{S} = \mathrm{Re}[\underset{\sim}{E}^{*} \times (\underset{\sim}{n} \times \underset{\sim}{E})]$ = Poynting's vector, $\underset{\sim}{n} = c\underset{\sim}{k}/\omega$ = real refractive index, and $\underset{\approx}{\sigma}^{H}$ = Hermitian part of the relativistic conductivity tensor. The real refractive index and the electric field polarization eigenvectors are determined from the ray tracing code, which uses the cold plasma dispersion relation. In calculating $\underset{\approx}{\sigma}^{H}$ an isotropic relativistic Maxwellian distribution function is assumed:

$$F(\underset{\sim}{p}) = \frac{1}{m^3c^3}\,\frac{\rho n_A}{4\pi K_2(\rho)}\,\exp\left[-\rho\left(1 + \frac{p_\parallel^2 + p_\perp^2}{m^2c^2}\right)^{1/2}\right],$$

where $\rho = m_e c^2/T_A$ and $K_2(\rho)$ is the modified Bessel function. An arbitrary number of cyclotron harmonics can be retained and all Bessel functions containing finite Larmor radius effects are included without expansion. Now measurements have been made of the single-pass microwave transmission through the hot electron annuli.

The experiment involves transmitting a swept frequency (18- to 26-GHz) wave through the hot electron ring, across the EBT midplane, using a pair of highly directive horns. Measurement of the difference in transmission amplitude with and without the presence of a hot electron population allows a determination of the ring absorption. The 18-GHz (EBT-I) system was used for plasma heating because it allows the flexibility to turn a cavity feed off,

thereby reducing the ring density. Simultaneous hard X-ray and perpendicular stored energy measurements were made of the rings to determine the ring density and temperature for fed and unfed cavities.

Single-pass ring absorption was measured with the polarization of the microwaves perpendicular and parallel to the magnetic field corresponding to the extraordinary and ordinary modes of propagation. The measurements were made at a pressure just above the T-M transition where the rings have a large stored energy but remain stable. The ring temperature and density were also measured with the hard X-ray diagnostic. Figure 3 shows the measured transmission as a function of frequency with and without a ring present. Note the lower level of transmission with a ring present, indicating absorption. The detailed structure apparent in the transmission signals is primarily due to reflections, of the cavity walls, of the horn radiation that is not coupled in a single pass.

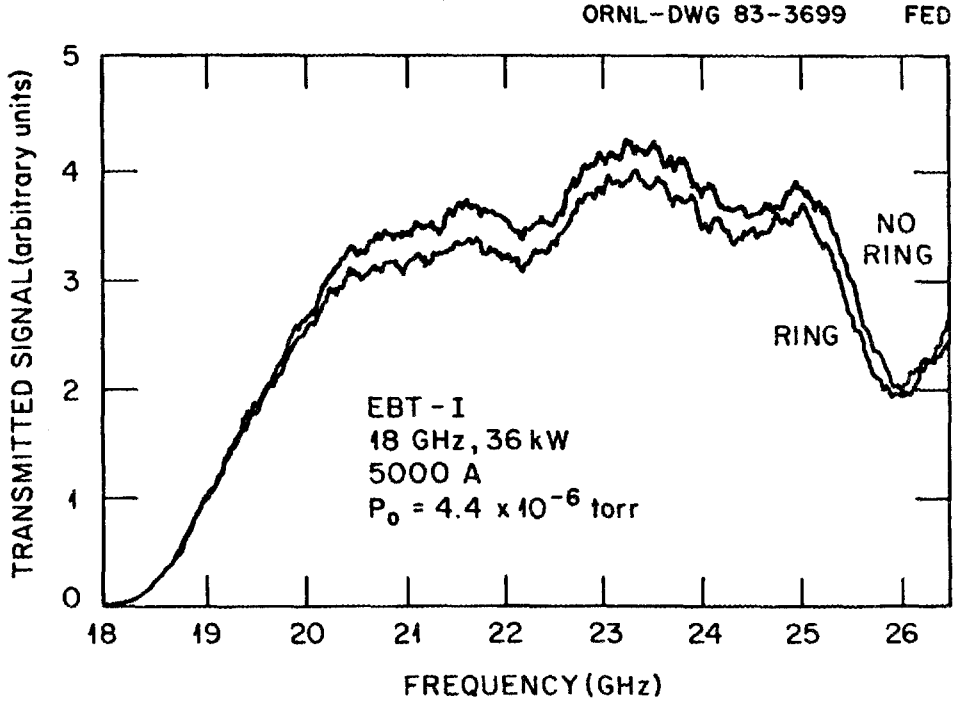

Fig. 3. Microwave transmission through a cavity midplane with and without a ring present.

To calculate the fractional power absorption the two signals were digitally subtracted and divided by the signal present without a ring. This fraction decreases with frequency from about 12% at 18 GHz to about 5% at 26 GHz. The ray tracing calculations follow this downward trend but tend to give somewhat higher absorption. The agreement is relatively good if one takes the ring parameters to be $n_A = 1.2 \times 10^{11}/cm^3$, $T_A = 200$ keV, but the theoretical result is about a factor of 2 higher than the experiment if one takes $n_A = 1.7 \times 10^{11}/cm^3$, $T_A = 120$ keV.

For the O-mode, no significant change in transmission was observed with and without a ring present. The ray tracing code predicts a ring absorption less than 1% for the O-mode consistent with the measurement. In addition, the single-pass absorption was measured above the T-C transition pressure with and without a heating microwave feed for both the O- and X-modes. For both modes no change in transmission was observed, indicating that changes in the core or surface plasma caused by the lack of a microwave feed were not responsible for the change in transmission observed at lower pressure. We feel therefore that the agreement between the measured absorption and the ray tracing calculations is quite good and that the ring power deposition predicted by the power balance model should be accurate to within a factor of 2.

Single-pass microwave absorption by the plasma in EBT is sufficiently weak that the microwaves undergo multiple reflections from the cavity walls before being absorbed. With each reflection some of the microwave energy is dissipated in the aluminum cavity walls. A set of measurements was made to determine this loss by measuring the power coupled out of a 3-in. port in one of the cavities into a waterload microwave calorimeter. An intercavity transport code was used to predict the power coupled to the calorimeter for various cavity microwave feed configurations and losses due to microwave absorbing diagnostic portholes as a function of the single bounce wall loss coefficient.

The data were obtained with the torus filled with nitrogen to atmospheric pressure. The total microwave power fed to the torus was held to $\sim$400 W. The input microwave frequency was swept $\pm$25 MHz about the central 18-GHz frequency in order to scramble standing wave modes, thereby spatially averaging the power received by the calorimeter.

Various power feed and porthole loss configurations were used during the measurement. Power was fed to the torus at different cavities or sets of cavities to study the transport to the cavity with the calorimeter. A second set of measurements was made after nine 4-in.-diam port covers were removed to artifically increase the microwave losses. The transport code was used to model the experimental results. It was found that a wall loss coefficient of 0.7% per wall bounce matched the data quite well.

To determine the power lost to the wall in the presence of a plasma the 0-D microwave power balance model was modified to include a wall loss coefficient. For a wall loss coefficient of 0.7% the power balance model predicts a total (multibounce) wall loss of ∿5% the input microwave power. Thus, the wall losses can be considered an almost negligible microwave loss.

In order to improve the efficiency of core plasma heating, a program was initiated to launch extraordinary mode power directly from the high magnetic field side of the fundamental resonance. Calculations using the 0-D power balance model predicted that improvement would be marginal unless two constraints were satisfied: (1) that the power be beamed toward the plasma center and (2) that the microwaves be highly polarized in the extraordinary mode. To meet these requirements a high-power, linearly polarized, directive launcher was developed /9/. The extraordinary mode is elliptically polarized when propagating at an oblique angle to the magnetic field. In order to launch the waves perpendicular to B such that the extraordinary mode is linearly polarized, it was necessary to "snake" the launcher through the fundamental resonance zone and launch back toward the resonant layer (Fig. 4). In initial experiments, up to 24-kW net power from the high-field launcher was delivered to the plasma. Preliminary experiments with a microwave calorimeter located on the low-field side of the cavity into which the power was directed indicate that virtually none of the throat-launched power penetrates to the low magnetic field side when the launcher is indeed on the high-field side of the resonance. However, if the field strength is lowered such that the resonance moves to a higher field than the launcher, very high power levels are received by the calorimeter. We believe this indicates that the throat launcher does indeed excite predominantly extraordinary mode and that the extraordinary mode power is absorbed in a single pass through resonance.

ORNL-DWG 83-2446A FED

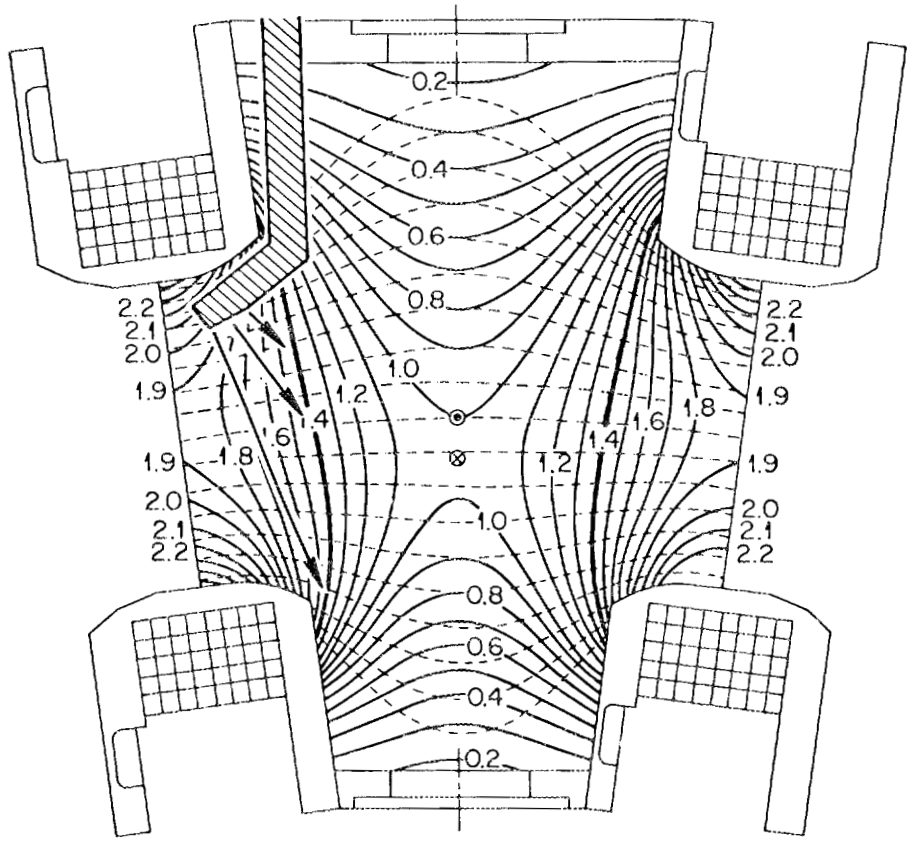

Fig. 4. High-field, polarized extraordinary mode launcher "snaked" through the fundamental resonance.

2. RECENT RESULTS IN CORE HEATING AND CONFINEMENT

There have been a number of improvements in the Thomson scattering diagnostic, resulting in an improved signal-to-noise ratio, a vastly increased data base with computer acquisition, and radial scanning capability. The experiments establish the existence of a cold electron component with temperature about one-third that given by soft X-ray measurements. Figure 5 shows T_e as determined by both soft X ray and laser as a function of gas pressure. The laser is sensitive to electrons primarily with energy below about 200 eV, whereas the soft X ray is most sensitive to electrons in the range 500 eV to 2 keV. Therefore, both diagnostics are compatible with the concept of a two-temperature distribution. In fact, data in the higher

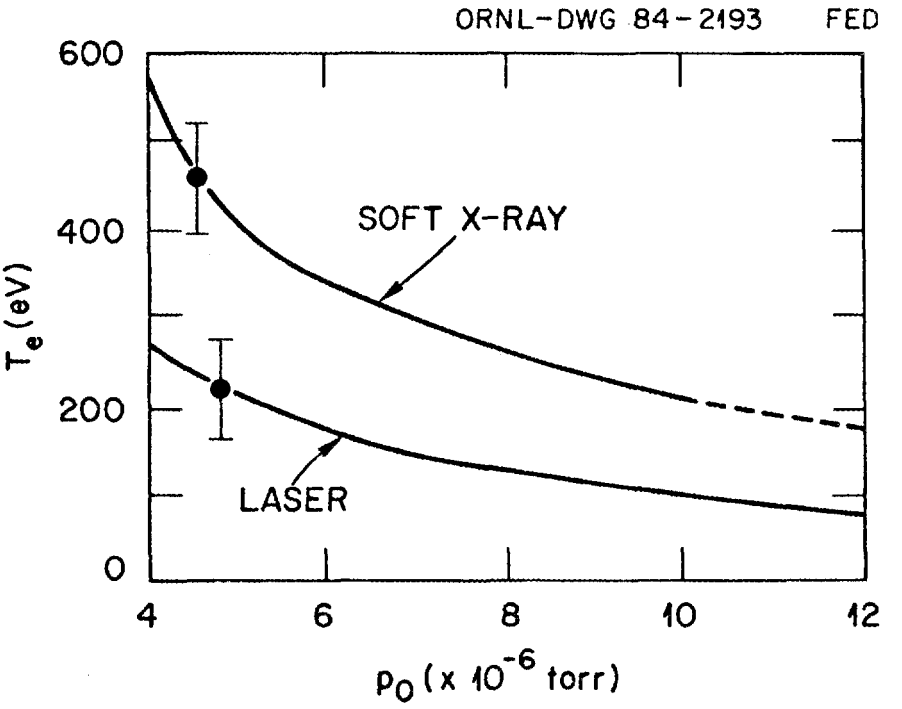

Fig. 5. Core electron temperature as determined by midplane soft X-ray and laser Thomson scattering vs torus field pressure.

energy laser channels are consistent with the presence of an energetic tail although it is difficult to establish the density and temperature of such a tail component.

Another recent enhancement is the installation of split coils in some of the mirrors, which allows diagnostic access to the plasma in the mirror throats. Interferometer measurements at the throat indicate the plasma density to be nearly equal to that at the midplane throughout the T-mode of operation. However, $(n_e)_{throat}/(n_e)_{mid}$ drops as the T-M transition is approached. Measurements with a soft X-ray detector located at the throat show that an energetic component is indeed present with $(T_h)_{throat} \cong (T_h)_{mid}$ but with much smaller density $(n_h)_{throat} \lesssim 0.1(n_h)_{mid}$. We regard this as strong evidence that the low temperature bulk component is isotropic whereas the energetic tail is highly anisotropic. In addition, one can infer that the electric field along $\underset{\sim}{B}$ is small.

There is also clear evidence that the tail component is locally produced at the fundamental cyclotron resonance. The cavity containing the midplane soft X-ray detector is not fed with microwave power since bremstrahlung associated with the hot electron ring would mask the soft X-ray emission from the ∿600-eV component. However, there is a flux of extraordinary mode power on the fundamental resonance surfaces in this cavity from adjacent cavities that are powered. Now, if the microwave power is removed from these adjacent cavities, the extraordinary mode power flux on the fundamental resonances of the soft X-ray cavity drops essentially to zero according to the power balance model described in the last section. Indeed, it is observed that the soft X-ray signal drops effectively to zero under these conditions.

This behavior can be understood theoretically if one carefully takes into account the correlation between the spatial structure of the microwave electric field $\underset{\sim}{E}_\mu(\underset{\sim}{x})$ and the velocity space structure of the plasma distribution function $f(\varepsilon,\mu)$, where $\varepsilon = mv^2/2$ = particle energy and $\mu = mv_\perp^2/2B$ = particle magnetic moment. For fixed position along a magnetic field line s, the condition for fundamental cyclotron resonance including the Doppler effect is

$$v_\parallel^{res}(s) = \frac{\omega - \Omega_e(s)}{k_\parallel(s)} \quad ,$$

where $v_\parallel^{res}(s)$ is the parallel velocity necessary for resonance at location s and $k_\parallel(s)$ is the real part of the parallel wave number at s. As an extraordinary mode wave approaches the fundamental resonance from the high magnetic field side, absorption begins and wave power starts to decrease where the velocity for Doppler-shifted resonance is a few times the thermal speed, $v_\parallel^{res}(s) = O(v_e)$ with $v_e = (2T_e/m_e)^{1/2}$.

For a Maxwellian plasma the profile of wave power $P_\mu(s)$ can be obtained by solving the dispersion relation. For $k_\perp = 0$ this dispersion relation takes the simple form

$$n_\parallel^2 = 1 - \frac{\omega_{pe}^2}{\omega^2}\frac{1}{n_\parallel}\frac{c}{v_e} Z\left(\frac{\omega - \Omega_e}{k_\parallel v_e}\right) ,$$

where $n_{\|} = ck_{\|}/\omega$ is the refractive index and $Z(\xi)$ is the plasma dispersion function. Figure 6(a) shows profiles of $k_r(\Omega_e/\omega)$ and $k_i(\Omega_e/\omega)$ for extraordinary waves propagating parallel to the field in a Maxwellian plasma or density $n_e = 10^{12}/cm^3$ and temperature $T_e = 300$ eV. Shown in Fig. 6(b) is the wave power profile $P_\mu(\Omega_e/\omega)$ for various temperatures determined from

$$P_\mu\left(\frac{\Omega_e}{\omega}\right) = P_\infty \exp\left\{-\int_{s(\Omega_e/\omega)}^{\infty} ds'\, 2k_i\left[\frac{\Omega_e}{\omega}(s')\right]\right\},$$

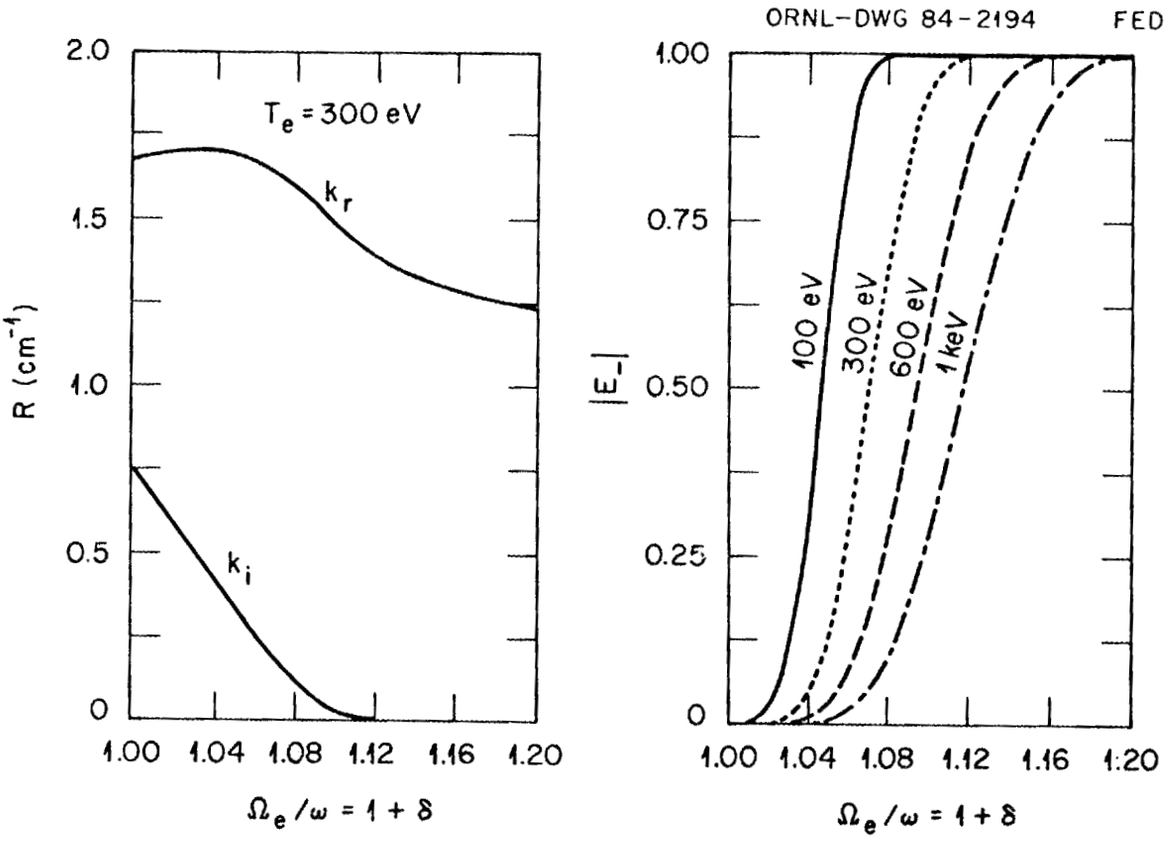

Fig. 6. (a) k-real and k-imaginary vs Ω_e/ω for parallel propagating extraordinary mode waves in a 300-eV Maxwellian plasma. (b) Wave power density profiles $\alpha|E_-|^2$ for various plasma temperatures.

Where we have approximated the magnetic field profile near resonance as $\Omega_e(s)/\omega = 1 + s/L$ ($L = 20$ cm for application to the central region of EBT-I/S). Defining $\delta(s) \equiv \Omega_e(s)/\omega - 1$, we see for example in the $T_e = 300$-eV case that 50% of the power is absorbed by $\delta = 0.07$ ($s = 1.4$ cm) and that 90% of the power is absorbed by $\delta = 0.04$ ($s = 0.8$ cm). The importance of this observation is that only particles with comparatively large $v_\parallel$ are heated, i.e., those with $\delta^{res} \gtrsim 0.04$, where $P_\mu(s)$ is large.

The condition for resonance at a given location s or fractional shift δ away from the non-Doppler-shifted resonance, $v_\parallel^{res}(\delta) = -c\delta/n_\parallel(\delta)$, can be related to the energy and pitch angle at the mirror midplane. Invoking μ conservation gives

$$v_\parallel^{res}(\delta) = \pm\sqrt{\frac{\varepsilon}{2m}}\left(1 - \frac{v_{\perp 0}^2}{v^2}\frac{B^{res}}{B_0}\right)^{1/2} = \pm\sqrt{\frac{\varepsilon}{2m}}\,[1 - (1 - \zeta^2)r(1 + \delta)]^{1/2} ,$$

where B_0 = is the field strength at the midplane, $\zeta^2 = v_{\parallel 0}^2/v^2$, $v_{\parallel 0} = v_\parallel$ at the midplane, and $r = \omega/\Omega_{e0}$. Equating the two expressions for $v_\parallel^{res}$ and solving for the resonant energy we obtain

$$\varepsilon^{res}(\delta) = \frac{mc^2}{2}\,\frac{\delta^2/n_\parallel^2(\delta)}{1 - r(1 + \delta)(1 - \zeta^2)} .$$

It is important to note that to be resonant at a given δ there is a minimum required energy $\varepsilon_{min}^{res}(\delta) = 256\ \text{keV} \times \delta^2/n_\parallel^2(\delta)$ and that the minimum energy is obtained for purely passing particles, $\zeta = v_{\parallel 0}/v = 1$. The resonant energy increases with increasing μ, becoming infinite for particles turning just at the point δ. This somewhat counterintuitive result simply indicates that it is not sufficient to reach the magnetic field δ for an electron to be heated there; rather, it must also have $v_\parallel(\delta) = v_\parallel^{res}(\delta)$. For example, assuming $n_\parallel = 1.7$ and $r = 1.4$, which would be appropriate for a 2:1 mirror ratio as in EBT-S, for passing particles $\zeta = 1$ at $\delta = 0.07$ [the location at which half the power has been absorbed in the $T_e = 300$-eV case in Fig. 6(b)], one obtains $\varepsilon_{min}^{res} = 430$ eV. Also, for a trapped particle $\zeta \leq 0.707$ to be resonant at this location, it must have energy $\varepsilon^{res} = 1.7$ keV. We can conclude that

if the bulk electron distribution in EBT were a Maxwellian at 300 eV most of the power would be absorbed by passing particles with energy above about $1.5T_e$ and by trapped particles with energy above about $6T_e$.

We see that there is considerable velocity space structure in the microwave heating operator. This comes about not only through the explicit velocity dependence but also because of the velocity dependence of the spatial location of the Doppler-shifted resonance and the strong spatial variation in wave power density due to heavy damping. Of course particles with $\zeta < (1 - 1/r)^{1/2}$ (i.e., particles which turn before reaching resonance) are not heated at all.

The primary effect of fundamental extraordinary mode heating is to increase the electron's perpendicular energy at the resonance location. Parallel heating comes about only through μ conservation as the particle moves to lower magnetic field. Therefore, ζ tends to decrease as the heating progresses, passing particles become trapped, and trapped particles turn ever closer to the midplane, until electric field profile effects effectively shut off the heating. For the particles that are resonant at large values of δ, where the wave electric field is large, the heating is quite rapid. We can estimate the average heating rate as

$$\frac{\Delta\varepsilon_\perp}{\Delta t} = \frac{1}{\tau}\,\frac{\pi e^2 E_-^2}{2m\Omega_e}\,\frac{L}{v_\parallel}\Bigg|_{s^{res}},$$

where $\varepsilon_\perp$ is the perpendicular electron energy, E_- is the amplitude of the right circular component of the field, L is the magnetic field scale, τ is the transit time between successive passes through resonance, and s^{res} is the location of the Doppler-shifted resonance. Using parameters appropriate for EBT-S with 100 kW of ECH power (giving the asymptotic value for $E_- \cong 20$ V/cm), one obtains $\Delta\varepsilon_\perp/\Delta t \cong 3 \times 10^7$ eV/s. On the other hand, particles in the bulk of the distribution, $\varepsilon \lesssim T_e$, can only be heated by collisions with those energetic particles that are directly heated by the microwaves.

It is clear that the heating process has the potential for forming a cold, isotropic collisional bulk as well as an anisotropic, energetic tail in consonance with the experimental observations. Whether a significant tail

actually forms depends upon how well the directly heated population is confined and how tightly the directly heated particles are collisionally coupled to the bulk. Now the confinement of energetic particles in EBT (i.e., particles with $\varepsilon > e\phi/a$, where E_0 is the ambipolar potential $\sim$100 to 400 V and a is the plasma minor radius) is very pitch-angle dependent. Since EBT relies on poloidal particle drifts Ω_D to cancel the vertical drift v_y due to toroidicity, those particles with small values of Ω_D have large neoclassical step sizes and large shifts inward in major radius, which can result in direct (i.e., nondiffusive) particle and energy loss. In particular, those particles that are transitional between trapped and passing tend to be very lossy. This situation is illustrated in Fig. 7. The effect of the rf is to push passing or energetic trapped particles into the lossy region of velocity space.

Quantitative evaluation of these processes requires detailed modeling of the spatial dependence of the microwave field profiles and the velocity space dependence of power absorption by particles, collisional relaxation, radial diffusion of heat and particles, direct loss of heat and particles on open drift surfaces, and particle sources. Although this is an inherently 4-D problem, involving radial and poloidal variations as well as velocity space variations, we have initiated a program of Fokker-Planck modeling based on the 2-D finite-element code of Matsuda. The direct losses are being modeled as velocity-dependent particle sinks, and we hope to be able to model neoclassical radial diffusion in a similar manner. The preliminary results of this code indeed show the formation of an anisotropic tail and a cold collisional bulk component. In addition, the direct particle losses result in significant energy losses and reduction in bulk heating efficiency.

In summary we can see that the microwave power P_μ effectively vanishes near $\Omega_e(s) \cong \omega$. The implication of this is that for fixed ε passing particles are preferentially heated and for fixed pitch angle high energy particles are preferentially heated. The effect of the heating is to increase $v_\parallel$, pushing passing particles toward the trapped-passing boundary where confinement is poor.

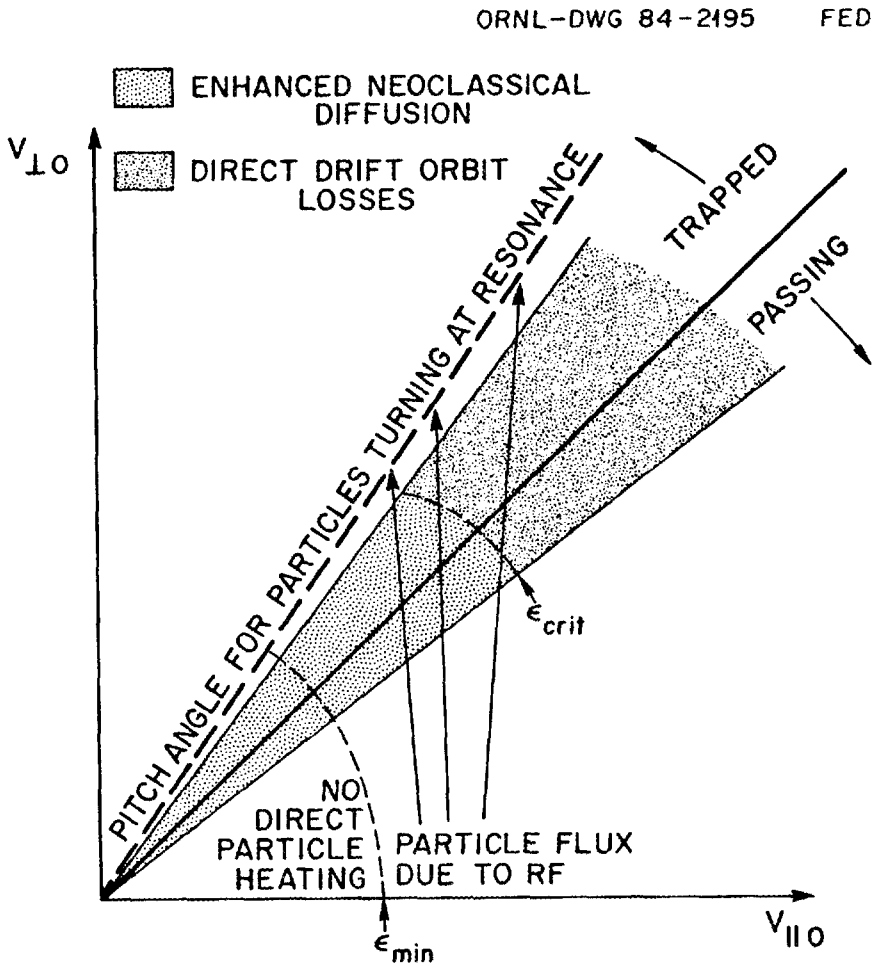

Fig. 7. Velocity space geometry for ECH-enhanced neoclassical transport and direct particle loss in EBT.

REFERENCES

/1/ BATCHELOR, D. B., and GOLDFINGER, R. C., Nucl. Fusion, 20 (1980) 403.

/2/ BATCHELOR, D. B., GOLDFINGER, R. C., and RASMUSSEN, D. A., Oak Ridge National Laboratory Report ORNL/TM-8770 (1983).

/3/ BATCHELOR, D. B., Nucl. Fusion, 21 (1981) 1615.

/4/ SPONG, D. A., Bull. Am. Phys. Soc., 28 (1983) 1228.

/5/ COLCHIN, R. J., et al., Plasma Phys., 25 (1983) 597.

/6/ KOVRIZHNYKH, L. M., Zh. Eksp. Teor. Fiz. (Sov. Phys. JETP), 29 (1969) 475.

/7/ HASTINGS, D. E., and KAMIMURA, T., accepted by Nucl. Fusion.

/8/ BATCHELOR, D. B., GOLDFINGER, R. C., and WEITZNER, H., Oak Ridge National Laboratory Report ORNL/TM-9075 (1984).

/9/ WHITE, T. L., invited paper this symposium.

Appendix 12

MONTE CARLO ESTIMATES OF PARTICLE AND ENERGY CONFINEMENT TIMES IN A BUMPY TORUS AND A BUMPY SQUARE WITH POLOIDAL ELECTRIC FIELDS

J. S. Tolliver and C. L. Hedrick

Since significant poloidal structure in the electrostatic potential in Elmo Bumpy Torus (EBT) has been observed experimentally and predicted theoretically, a Monte Carlo calculation has been used to make estimates of the particle and energy confinement times in EBT with varying degrees of asymmetry in the electric field. The code is applicable to the bulk ion population and the "cool" electron population in EBT but not to the intermediate-energy electrons believed to be responsible for the formation of the potential. A similar calculation is possible for the proposed Elmo Bumpy Square (EBS) device, which is expected to have much more symmetric potential profiles because of much better centering of the particle orbits. The calculations indicate that the confinement time in EBS will be two to three orders of magnitude better than in EBT.

I. INTRODUCTION

Transport theories for most magnetic plasma confinement devices have traditionally assumed that the electrostatic potential does not vary poloidally. Only recently has serious consideration been given to poloidal electric fields.[1,4-7] In EBT, experimental evidence suggests that, under certain operating conditions, the potential does have a significant poloidal structure.[2,3] This asymmetry can be understood theorectically[1] by assuming that the formation of the potential is dominated by the "warm" or intermediate-energy electrons[8]—in keeping with the experimental observation that the magnitude of the potential scales with the "temperature" of the warm electrons.[9] By using limiting-case descriptions of the lowest order behavior of the ions and the "cool" and "hot" electron populations, a fluid treatment of the warm electrons leads to an expression for the poloidal asymmetry in the potential which is in reasonable agreement with experiment. This expression shows that the poloidal asymmetry in the potential is driven by asymmetry in the magnetic field which, in an isotropic warm electron distribution, manifests itself through poloidal asymmetry in $\oint dl/B$. More generally, the asymmetries in the gradient-B and curvature drifts manifest themselves in a slightly more complicated expression which reflects the density and pressure weighting along field lines of anisotropic distributions.

In answer to the question of how do the bulk ions and the "cool" electrons respond to this asymmetric potential, we have utilized a bounce-averaged Monte Carlo code[10] to calculate the particle and energy lifetimes of these particles by simulating their orbits and collisions in the EBT-I/S device with varying

degrees of potential asymmetry. The lifetimes are estimated by keeping proper statistics on the rate at which particles leave the plasma through the last closed flux surface in the device. Because these cool particles are not expected to participate significantly in the formation of the potential, they can be expected to have loss rates incapable of producing the assumed electric field. To the extent that the cool and warm populations are decoupled, no inconsistency exists. In reality, of course, there is always some coupling between the different populations, and the losses of the cool particles would be expected to modify the warm population and the self-consistent potential somewhat. However, by the computational nature of the Monte Carlo technique, it is impractical, if not impossible, to calculate a completely self-consistent electric field within the limit of finite computer resources. A complete description would require inclusion of the microwave heating physics, the relativistic electron rings, coupling among these "hot" ring particles and the warm and the cool populations, and coupling among the various ion and electron populations. In order to have statistically meaningful reults, it would be necessary to have enough Monte Carlo test particles to represent adequately the ring electrons in the sparsely populated high-energy electron tail. Orders of magnitude more particles than practical would be required. Furthermore, the significant advantages of bounce-averaging would have to be discarded for the high-energy ring particles, costing another 2–3 orders of magnitude in computer time. It is clear that a complete description is far beyond present day computational resources. Despite the shortcomings of the Monte Carlo method, it has the advantage of offering increased realism in the treatment of geometry effects in a finite aspect ratio device—realism that is impossible in analytic calculations. It is just these geometry effects (for example, inverse aspect ratio expansion parameters of order 1/3, large orbit deviations from flux surfaces, nonlocal diffusion, and direct losses) that are important in understanding the behavior of plasmas in finite-sized devices. By understanding the response of the bulk ions and electrons to asymmetric potential profiles similar to that seen experimentally, we are able to make one step toward a more complete understanding of the poloidal potential structure and its effect on plasma confinement in magnetic confinement devices.

In the proposed EBS experiment,[11] with a much more nearly axisymmetric magnetic field structure, the poloidal asymmetries in the potential are expected to be much smaller than in EBT. To quantify the associated improvement in confinement times, we have calculated lifetime estimates for EBS that show an increase of two to three orders of magnitude over EBT lifetimes.

Section II describes the bounce-averaged Monte Carlo code as it is applied to a device the size of the EBT-I/S or EBS experiment. Section III demonstrates the beneficial effect of a radial electric field on confinement, and Sec. IV presents the Monte Carlo lifetime estimates for EBT and EBS. In Sec. V we draw conclusions and speculate on the implications of the present results to other devices.

II. THE BOUNCE-AVERAGED MONTE CARLO CODE AND ITS APPLICATION TO A FINITE ASPECT RATIO DEVICE

The ORNL bounce-averaged EBT Monte Carlo transport code[10] uses the bounce-averaged Monte Carlo differential Coulomb collision operator previously derived by Tolliver[10,12] and follows particles using the Northrop and Teller[13] equations:

$$\langle\dot{\alpha}\rangle = \frac{1}{Ze\tau}\left(\frac{\partial J}{\partial \beta}\right)_{\alpha,\epsilon,\mu} \tag{1a}$$

$$\langle\dot{\beta}\rangle = -\frac{1}{Ze\tau}\left(\frac{\partial J}{\partial \alpha}\right)_{\beta,\epsilon,\mu} \tag{1b}$$

$$\tau = \left(\frac{\partial J}{\partial \epsilon}\right)_{\alpha,\beta,\mu} \tag{1c}$$

where $J = \oint m\,dl\,v_{\|}$ is the second adiabatic invariant; ϵ and μ are the total energy and magnetic moment, respectively; Ze is the charge state (e = absolute value of the electron charge); α and β are Clebsch coordinates[14] with $\nabla\alpha \times \nabla\beta = \mathbf{B}$; the angle brackets mean "bounce-averaged"; and τ is the bounce time. In a bumpy torus or bumpy square it is convenient to choose $2\pi\alpha$ as the flux through an $\oint dl/B$ pressure surface; then β is a generalized poloidal angle with period 2π. A pressure surface contour and its relation to the vacuum vessel and the geometric center of the magnetic field coils is shown schematically in Fig. 1(a). Actual numerically computed α and β lines for a realistically sized bumpy torus—the EBT-I/S experiment at ORNL—are shown in Fig. 1(b). It should be noted that the pressure surfaces are not mere shifted circles but are vertically elongated with nonconcentric centers such that the radial distance from $\alpha = 0$ to the outermost flux surface is much greater along the $\beta = 0$ line than along the $\beta = \pi$ line. Recent analytic theories[4,5] that attempt to include the pressure surface geometry are restricted to the much simpler shifted circle approximation. As a result of the assumption of circular pressure contours, the analytic treatments require that the poloidal angle β be equivalent to a true polar angle θ centered at $\alpha = 0$; then the β = constant lines are straight radial rays. For a very large aspect ratio, the actual β lines are indeed nearly straight rays, but for the realistic case shown in Fig. 1(b), the lines of β = constant are obviously not radial. Analytic treatments also assume that the shift Δ of the pressure surfaces from the geometric center is ordered small in the inverse aspect ratio expansion—that is, that $\Delta/r \sim O(a/R_t)$, where r is the radius to some point in the plasma, R_t is the major radius of the torus, and a is the plasma radius. While Δ/r can be genuinely small for most radii in a very large aspect ratio device, it is evident from Fig. 1(b) that Δ is of the same order as the plasma size for a realistic device. We know of no analytic calculations that remain valid for such a large value of Δ. Only a numerical calculation can adequately include the pressure surface geometry of a realistically sized experimental device.

For a hypothetical bumpy torus with a very large aspect ratio, the analytic assumptions of small Δ and approximately circular pressure contours are valid. In addition, the average orbit displacement from the flux surfaces is small, making the transport local and diffusive. In such a limiting case, the diffusion coefficients have been calculated analytically.[5] Our Monte Carlo code has been successfully benchmarked[10,12] against

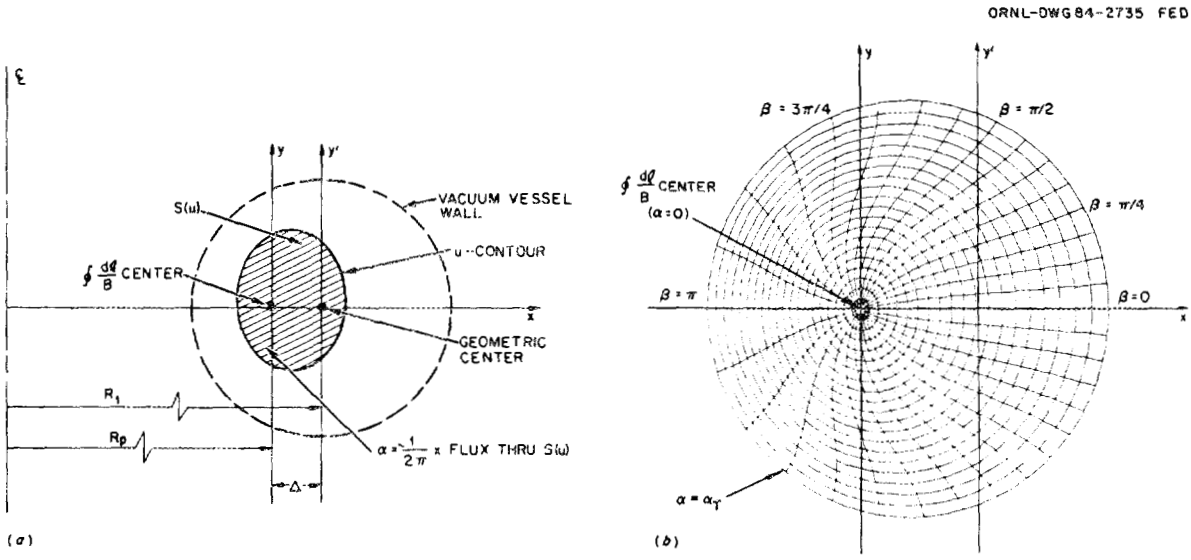

FIG. 1. (a) Schematic geometry of a $u = \oint dl/B$ pressure surface in an EBT midplane and its relation to the geometric center of the magnetic field coils. The major radius of the torus, R_t, measures the distance from the torus centerline to the geometric center, and R_p is the distance from the centerline to the $\oint dl/B$ center. $S(u)$ is the surface enclosed by the u = constant contour, and $2\pi\alpha$ is the magnetic flux through $S(u)$. (b) Contours of constant α and β for EBT-I/S. In both (a) and (b), the cartesian (x, y) axes have their origin at the $\oint dl/B$ center, and the y'-axis passes through the geometric center.

the theory in the special case of low collision frequency and small radius—a regime where the theory remains valid. When the aspect ratio is not large (such as in EBT-I/S or any realistically sized device), the finite shift Δ and the noncircularity of the pressure surfaces become relevant. More important, however, the transport can be nonlocal and nondiffusive. In such a case, the concept of a local diffusion coefficient loses meaning as convection and mass flow become the dominant transport processes. We show that the presence of a poloidal electric field can transform the plasma transport from a diffusive to a convective behavior. No analytic calculations have been made that treat such convective behavior in a bumpy torus.

Although analytic treatment of finite-sized devices and nonlocal, nondiffusive transport is difficult, the Monte Carlo remains valid and can be easily generalized to treat such cases. Instead of a diffusion coefficient, we calculate a particle confinement time τ_p by running the Monte Carlo simulation until each of a large initial number of particles is lost by striking the wall. For the purposes of this calculation, the "wall" is defined as some closed α = constant flux surface that is near the vacuum vessel wall but completely contained within the device. The particles are initially given a Maxwellian distribution in energy and pitch angle and a uniform distribution in β. Conceptually, as each particle is lost, its lifetime t_i and energy E_i upon crossing the wall are recorded, and it is then dropped from the simulation. Obviously, some particles will live much

longer than others, but it is those that are rapidly lost that contribute most to the confinement time. After each of the original N particles has been lost, we calculate the particle confinement time τ_p as

$$\frac{1}{\tau_p} = \frac{1}{N} \sum \frac{1}{t_i} . \tag{2a}$$

Similarly, the energy confinement time τ_E can be calculated as

$$\frac{1}{\tau_E} = \frac{1}{N} \frac{2}{3T} \sum \frac{E_i}{t_i} , \tag{2b}$$

where T is the temperature of the initial Maxwellian (both T and E measured in eV). In practice, for best use of cpu time and memory, the code is vectorized to treat 64 independent particles simultaneously. After each particle is lost, its statistics are recorded, and a new particle is started with random initial conditions. Thus, there are always 64 particles in the simulation. This scheme makes effective use of computer memory and also allows vectorization for speed. The simulation should be continued until each particle has been lost and replaced at least once, preferably several times for good statistics. Then, N in Eqs. (2) is the total number of wall collisions that have occurred. In practice, the simulation must be run for 10–100 times the eventual confinement time. It should be clear that configurations with excellent confinement properties are very expensive to simulate.

To examine the sensitivity of our results to the choice of the initial radial, or α, distribution, we have tested various options and settled on an initial delta-function distribution at $r \approx a/2$ as the most representative and convenient choice. When a poloidal electric field is present, crescent-shaped potential islands exist with an "x-point" somewhere inside the plasma radius a. If the delta function is placed beyond this x-point, the particles will be rapidly lost. This behavior is somewhat analogous to the cold and lossy edge plasma beyond the hot electron rings in EBT and certainly does not represent the behavior of the bulk plasma, with which we are concerned here, in the center of the device. We have also tested a number of approximately parabolic initial radial distributions. If the parabola extends much past the x-point, those particles that are initially near the center will be well-confined, while those beyond the x-point will be rapidly lost. However, if the parabola is entirely contained within the x-point, analogous to considering a parabolic bulk plasma distribution while ignoring the edge, comparatively good confinement will be seen. Our numerical results show that an initial delta function at $r \approx a/2$ produces confinement times comparable to those obtained with such an initial parabolic distribution, and also in rough agreement with experimental results.

A useful diagnostic tool to demonstrate graphically the motion of the particles is a multiple exposure graph of the (α, β) coordinates of each of the 64 particles in the simulation. This multiple exposure plot is similar to a puncture plot that shows a particle's position each time it crosses some reference plane. In a bounce-averaged description, however, all information about a particle's position along a field line is lost. So instead of a puncture plot, we show a particle's actual (α, β) coordinates which are independent

of position along the field line, at equal time intervals. Since α and β uniquely define a field line, we can project any (α, β) coordinate along that field line to any reference plane to obtain the physical coordinates at the reference plane. We use the EBT (or EBS) midplane as the reference plane in all plots shown in this paper and transform from the nonorthogonal (α, β) coordinates to real cartesian space. Thus, each point in the multiple exposure plots represents not where a particle crosses the midplane, but the physical position where the field line specified by a particle's instantaneous (α, β) coordinates crosses the midplane.

III. THE EFFECT OF A RADIAL ELECTRIC FIELD AND COULOMB COLLISIONS

The existence of a purely radial electric field is understandably beneficial to confinement. By "purely radial," we mean an electrostatic potential Φ that is a function of α (the "radial" variable) but has no β dependence. In EBT and EBS, the poloidal precession necessary to cancel the toroidally induced vertical drift comes from gradient-B and curvature drifts and the $\mathbf{E} \times \mathbf{B}$ drift. Particles in an EBT that are toroidally passing or transitional (i.e., near the trapped-passing boundary in phase space) have very small gradient-B and curvature poloidal precession frequencies and thus are poorly confined if no electric field exists. But if a radial electric field is present, the $\mathbf{E} \times \mathbf{B}$ drift can provide significant poloidal precession, thus providing good confinement. (Actually, the loss region is not totally removed, just moved to much higher energies, where only a few particles exist.) This effect holds for both ions and electrons since both species feel the $\mathbf{E} \times \mathbf{B}$ drift. Also, there is little difference if the field is inward-pointing or outward-pointing.

To demonstrate graphically the beneficial effects of an electric field, Figs. 2(a) and 2(b) show multiple exposure plots of the collisionless orbits of 64 electrons in EBT with no electric field and with a purely radial electric field that is inward-pointing at small radii and outward-pointing at large radii. All 64 particles were started on the birth surface $\alpha/\alpha_T = 1/4$, where α_T is the outermost flux surface shown in Fig. 1(b), and with random β's uniformly distributed on the range $(0, 2\pi)$. This birth surface corresponds to a radius $r \approx a/2$, where the plasma center ($r = 0$) is assumed to be at the minimum of $\oint dl/B$. The kinetic energies and pitch angles of the 64 particles were chosen randomly from a 100-eV Maxwellian distribution. The electrostatic potential used in Fig. 2(b) has the form $\Phi = 400(\alpha_n - \alpha_n^2)$ volts where $\alpha_n = \alpha/\alpha_T$ is a normalized flux variable. Thus, Φ rises to a maximum of 100 V at $\alpha_n = 1/2$ and falls back to zero at $\alpha_n = 1$. The poor confinement properties when no electric field is present are obvious from the many particles in Fig. 2(a) whose orbits carry them far from the birth surface with some orbits that intersect the wall. In 1 ms of simulation time nearly the entire cross-section has been filled from an initial distribution of 64 particles at $r \approx a/2$. In contrast, when the purely radial electric field is included, the confinement improves dramatically, as shown in Fig. 2(b). The initial positions, energies, and pitch angles are identical to those shown in Fig. 2(a), but most of the 64 particles remain close to the birth surface, and there are no direct losses. The EBT and EBS concepts are based partly on the existence of radial electric fields to improve particle confinement. In like manner, modern-day stellarator designs depend on strong radial electric fields for good confinement.[15]

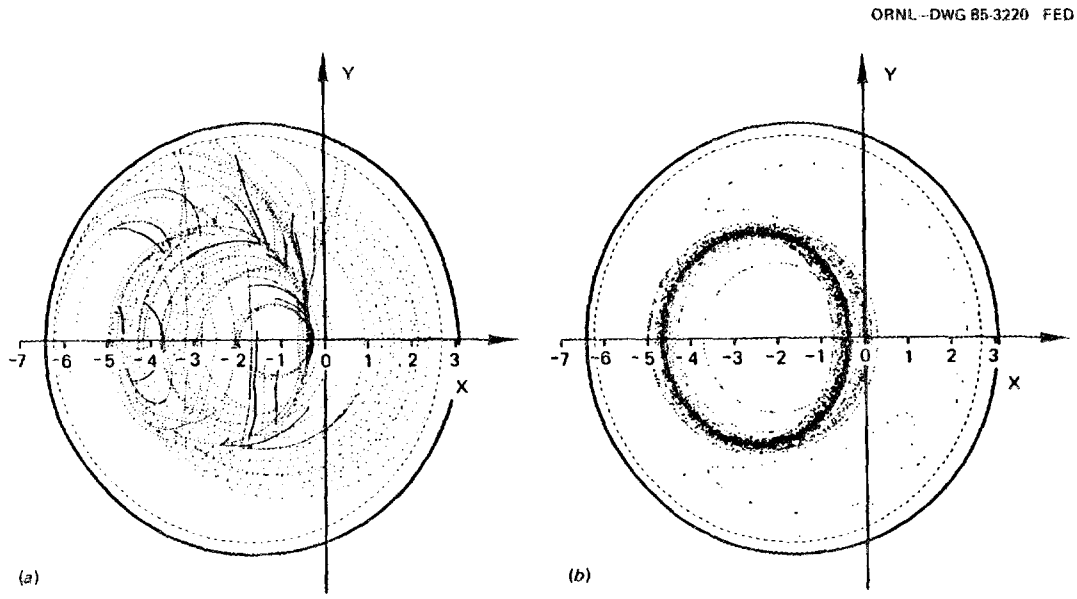

FIG. 2. Multiple exposure (α, β) coordinates (projected to the midplane and transformed to real cartesian space) depicting the orbits of 64 Monte Carlo test electrons without collisions in EBT-I/S (a) with no electric field and (b) with a purely radial radial electric field (with $\Delta\Phi = T_e$).

Although the collisionless confinement is poor when no electric field is present, the presence of Coulomb collisions can limit the detrimental effect of direct losses because collisional particles are unable to complete orbits that intersect the wall. When e-e and e-i Coulomb collisions appropriate to a background density of about $9 \times 10^{11}\,\mathrm{cm}^{-3}$ are included in the simulation, the transport becomes more diffusive in nature, as evidenced in Figs. 3(a) and 3(b). Of course, in the low collisionality reactor regime, the direct losses remain troublesome when no field is present.

It should be pointed out here that the magnetic confinement properties of EBS are much better than EBT because of much better centering of the collisionless orbits. Figure 4(a) shows contours of constant α and β for a "minimal" EBS design with 4 coils per side and a global mirror ratio of about 3.7. Since the "average" particle motion is on a flux surface, it is clear from the figure that the average particle orbits are much better centered than in EBT [cf. Fig. 1(b)]. With 6 coils per side and a global mirror ratio of about 6.4, an EBS becomes even more axisymmetric as evidenced in Fig. 4(b). Multiple exposure (collisionless) particle motion plots for the EBS coordinate system of Fig. 4(b) are shown in Figs. 5(a) and 5(b), respectively. All initial conditions and the functional form of Φ are identical to those used in Figs. 2. Obviously, with or without an electric field, the particles remain much closer to the birth surface, and there are far fewer "bad" orbits than in EBT.

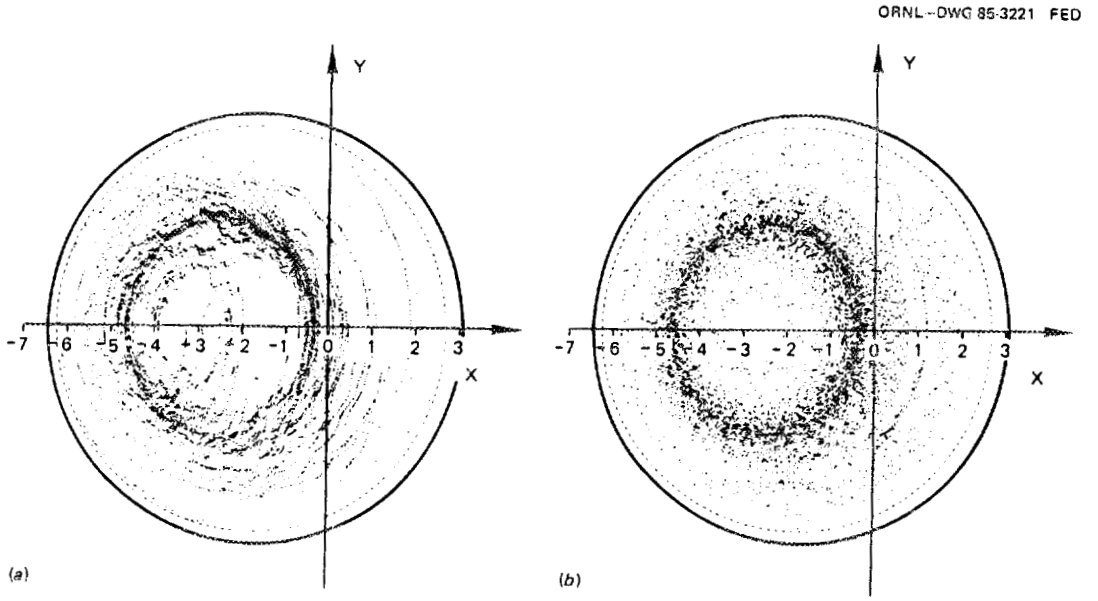

FIG. 3. Multiple exposure positions of 64 test electrons in EBT undergoing e-e and e-i collisions appropriate to about $9 \times 10^{11}\,\mathrm{cm}^{-3}$ background plasma density (a) with no electric field and (b) with a radial electric field.

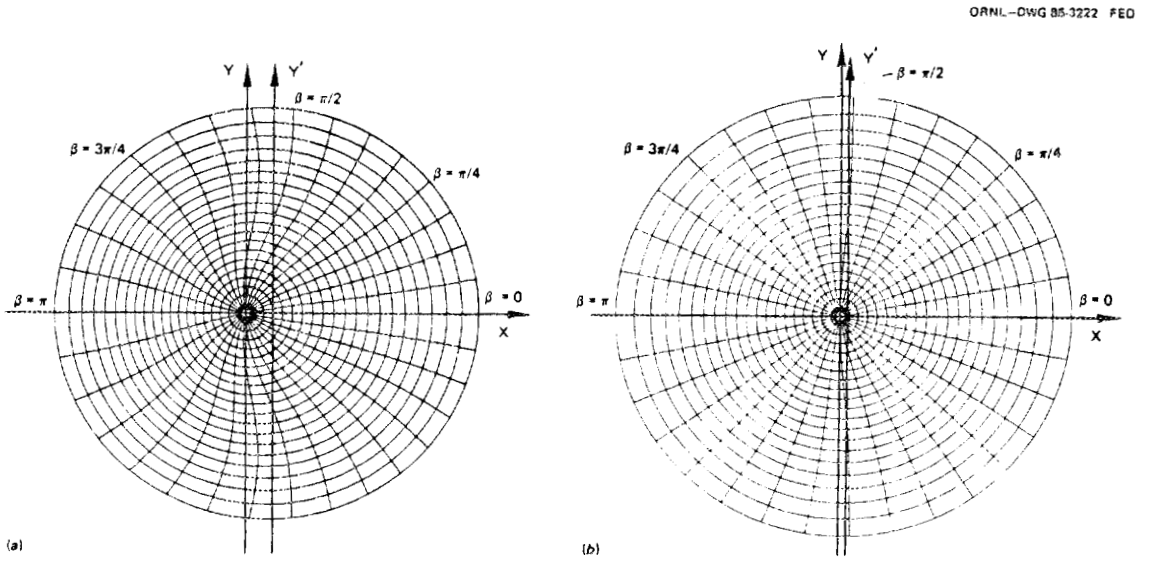

FIG. 4. Contours of constant α and β for (a) a "minimal" EBS design with 4 coils per side and a global mirror ratio of 3.7 and (b) an improved EBS with 6 coils per side and a global mirror ratio of 6.4.

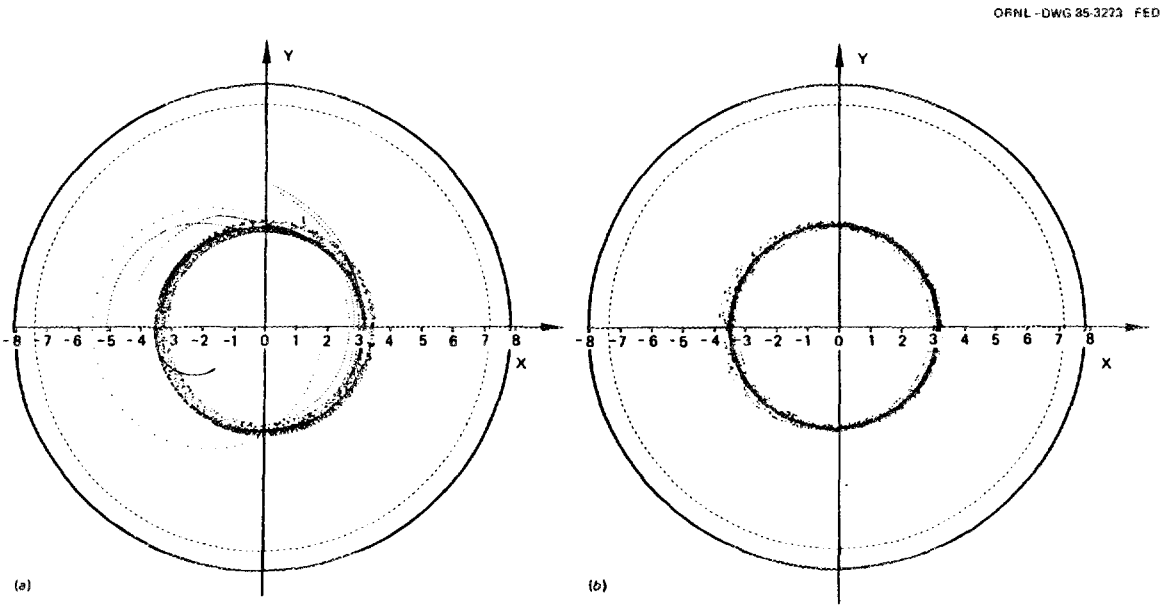

FIG. 5. Multiple exposure positions of 64 collisionless electrons in an EBS (a) with no electric field and (b) with a radial electric field.

IV. THE EFFECT OF POLOIDAL ASYMMETRY IN THE ELECTROSTATIC POTENTIAL

It is evident that a radial electric field is very valuable for charged particle confinement. However, if Φ has some poloidal dependence, potential islands exist that can have an extremely detrimental effect on transport rates. Low-energy particles will approximately follow the potential contours because they are strongly affected by the $\mathbf{E} \times \mathbf{B}$ drift and only weakly affected by the energy-dependent gradient-B and curvature drifts. Because of the potential island structure, such particles can take large neoclassical stepsizes, leading to large diffusive loss rates. More seriously, if the potential contours intersect the wall, particles can experience electrostatic direct losses. These direct losses and large orbits are much more troublesome than the magnetic direct losses and wide orbit dispersion in Fig. 2(a) because particles of all pitch angles are affected, not just the passing and transitional particles. Therefore, pitch angle collisions cannot improve the situation. Only energy-scattering collisions up to energies several times the potential well depth (so that the gradient-B and curvature drifts are large compared to the $\mathbf{E} \times \mathbf{B}$ drift) can produce particles with orbits that do not approximately follow the potential contours. If, as observed experimentally in EBT, the potential is of the same order as or greater than the (cool population) electron temperature, only very few particles will be scattered to such high energies. As a result, most particles will be strongly affected by the potential island structure.

To quantify these effects, we have made Monte Carlo calculations for EBT and EBS with a range of poloidal asymmetries in the potential. We have chosen an *ad hoc* potential of the form

$$\Phi(\alpha_n, \beta) = \Phi_0(\alpha_n - \alpha_n^2 - \eta\,\alpha_n \cos\beta)\ , \tag{3}$$

where the asymmetry parameter η determines the magnitude of the poloidal asymmetry. When $\eta = 0$, the potential depends on α_n only, and since α_n is approximately proportional to $(r/a)^2$, is nearly parabolic near the center, rising to a peak of $\Phi_0/4$ at $\alpha_n = 1/2$ and falling back to zero at $\alpha_n = 1$. Figures 2, 3, and 5 were made with $\eta = 0$ and $\Phi_0 = 400\,\mathrm{V}$. The actual potential in EBT-S is not sufficiently well known to be representable in a simple analytic form, but theoretical calculations[1] predict an asymmetry of about 15-20%, and η of order 15-20% in Eq. (3) leads to potential contours with large potential islands not unlike the potential profiles sometimes seen in EBT.[2,3]

As a benchmark case, we first show EBT-S results for $\eta = 0$. Thus, the potential contours coincide with the α contours, and there is no island structure. We use a 100-eV Maxwellian distribution of electrons and $\Phi_0 = 400\,\mathrm{V}$ so that the maximum potential well depth is $\Delta\Phi = T_e$. Particles are launched at $\alpha_n = 1/4$ with a uniform random distribution in β and pitch angle. The particles experience e-e and e-i collisions appropriate to a background density of about $9 \times 10^{11}\,\mathrm{cm}^{-3}$. Figure 6 shows the potential contours and the multiple-exposure (α, β) coordinates (projected to the midplane and transformed to real space) depicting the essentially diffusive nature of the particle motion. Using Eqs. (2) the particle confinement time may be

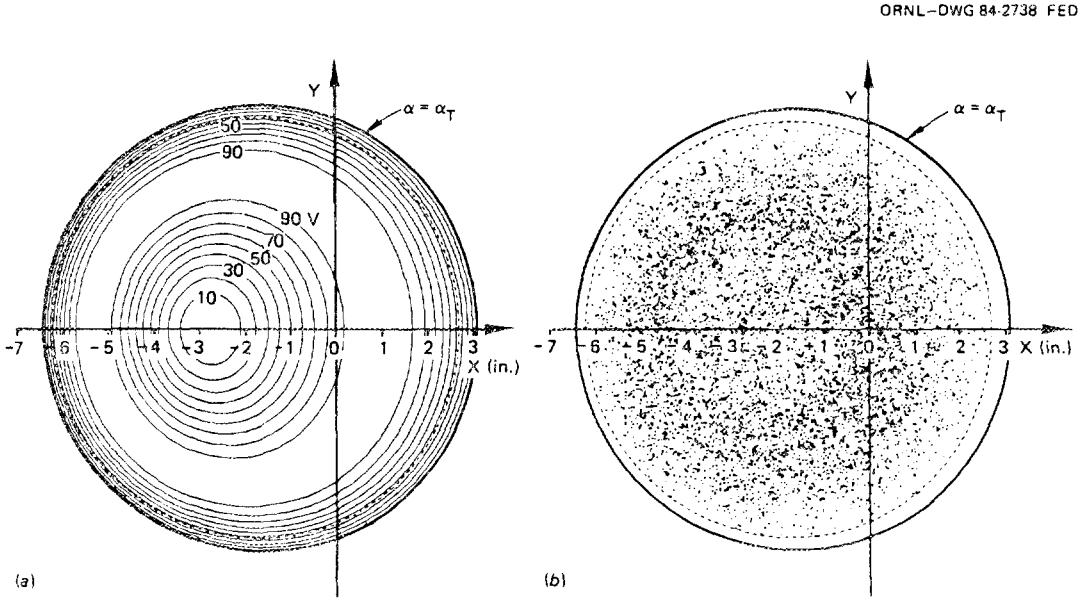

FIG. 6. Potential contours (with contour values shown in volts) and the associated long-time particle motion in EBT for the case of closed symmetric potential contours having no island structure.

calculated to be $\tau_p \approx 4\,\text{ms}$, and the energy confinement time $\tau_E \approx 2\,\text{ms}$. These results can be regarded as the "neoclassical" confinement times, the bases with which to compare all other confinement times when a poloidal electric field is present. Although no analytic theory exists that is valid for this realistic geometry $[\Delta/r \sim \mathcal{O}(1)]$, we rely on the fact that our Monte Carlo code has been benchmarked against the theory for large aspect ratio to justify the claim that $\tau_p = 4\,\text{ms}$ is the "neoclassical" result.

As an example of the plasma behavior when a substantial poloidal electric field exists, we show results in Fig. 7 for $\eta = 16\%$. This choice produces closed, nearly circular potential contours in the center surrounded

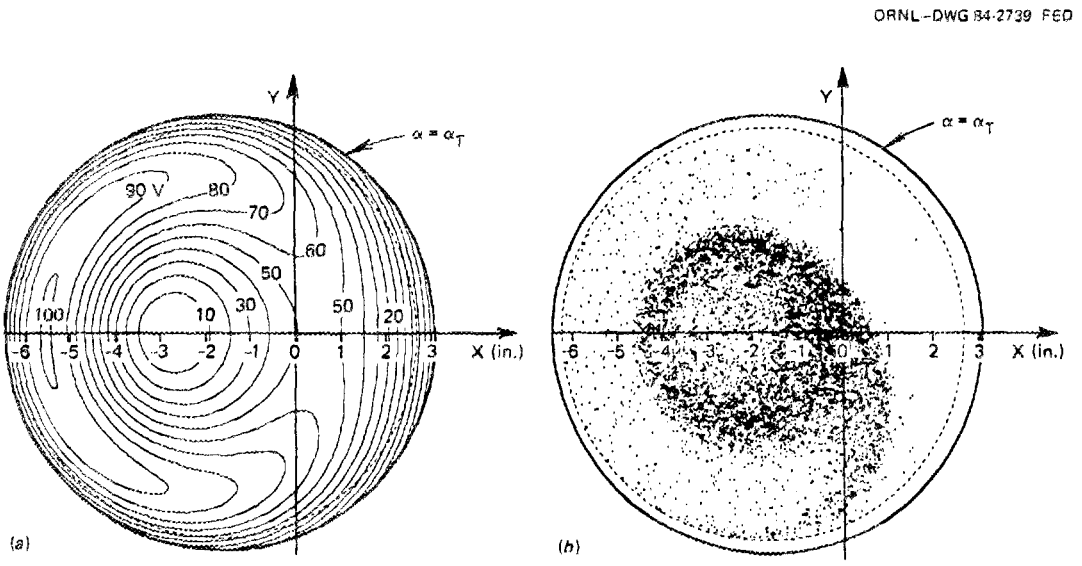

FIG. 7. Asymmetric potential contours in EBT with asymmetry parameter $\eta = 16\%$ producing crescent-shaped potential islands and the associated particle motion.

by concentric crescent-shaped potential islands with the outermost crescents barely intersecting the wall. All other parameters (i.e., Φ_0 and all initial conditions) are identical to those used in the previous case. From the multiple-exposure plot in Fig. 7, it is obvious that the transport is strongly convective in nature, with most particles following the potential contours once they get outside the central region where the poloidal asymmetry is small. Of course, a relatively small diffusive motion is superimposed onto the convective orbits because of collisional effects. The particle and energy confinement times for this case are $\tau_p \approx \tau_E \approx 0.2\,\text{ms}$.

We have systematically varied the poloidal asymmetry over a range of $\eta = 1\%$ to $\eta = 16\%$ and calculated the particle and energy confinement times for both EBT and a simple EBS design. These results are shown in Fig. 8. In order to make a lower limit estimate of the confinement time possible in EBS, we have chosen the "minimal" EBS design with $\alpha\beta$-coordinate system shown in Fig. 4(a). Based on the theoretical results

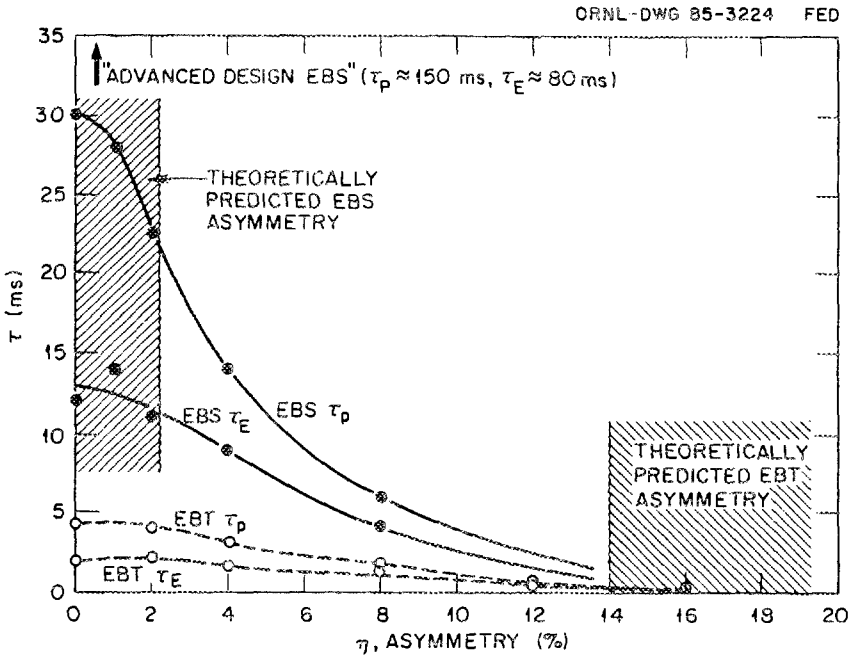

FIG. 8. Particle and energy confinement times for electrons in EBT and a minimal EBS design as functions of the asymmetry parameter η. The confinement times for an "advanced design EBS" are off the scale of this plot.

in Ref. 3, the expected asymmetry in such a design is about 1 or 2 percent. An advanced EBS design with a global mirror ratio of about 6 might have only 0.5% or less asymmetry. Not surprisingly, the confinement time improves dramatically as the asymmetry decreases, and EBS has substantially better confinement than EBT. But the important conclusion to be drawn is the gain to be expected in going from EBT with $\eta \gtrsim 15\%$ to EBS with $\eta \lesssim 2\%$—easily two orders of magnitude improvement in confinement time. The particle confinement time for an improved EBS design with nearly zero asymmetry is about 150 ms, compared with 20–30 ms for the minimal EBS. Thus, an overall improvement of two to three orders of magnitude over EBT is possible.

V. CONCLUSION

It is evident (and not surprising) that an electrostatic potential with only radial dependence is good for confinement. However, a "bad" potential, with strong poloidal dependence, can destroy neoclassical confinement, producing confinement times one to two orders of magnitude smaller than the "good" potential case. Because of poloidal asymmetries in the magnetic field, the electrostatic potential in EBT can have relatively large asymmetries, leading to very poor confinement. In EBS, however, the potential asymmetry should be much smaller, leading to dramatic improvements of two to three orders of magnitude in the particle and energy confinement times.

Although these results were calculated for a EBT and EBS, qualitatively similar behavior should be expected for other devices if a poloidal electric field exists. Tokamaks and stellarators would be expected to have only small poloidal electric fields because of the presence of rotational transform, which allows poloidally varying potentials to be easily short-circuited. Conversely, tandem mirrors, which—like bumpy tori—do not have closed flux surfaces, might have significant poloidal electric fields. Indeed, other authors[6] have shown that the presence of poloidal variations in the potential in a tandem mirror contribute significantly to the radial particle flux. However, Ref. 6 remains a diffusive calculation and makes no attempt to treat the convective behavior seen in Fig. 6. We speculate that, for sufficiently large poloidal electric fields, tandem mirrors might experience radial particle losses qualitatively similar to those shown here.

ACKNOWLEDGMENT

This research was sponsored by the Office of Fusion Energy, U.S. Department of Energy, under Contract No. DE-AC05-84OR21400 with Martin Marietta Energy Systems, Inc.

REFERENCES

[1] C. L. Hedrick, submitted to Phys. Fluids, 1985.

[2] D. L. Hillis, J. B. Wilgen, J. A. Cobble, W. A. Davis, S. Hiroe, et al., submitted to Phys. Fluids (1985). See particularly Fig. 13a.

[3] L. Solensten, J. R. Goyer, K. A. Conner, and R. L. Hickock, Bull. Am. Phys. Soc. **29**, 1418 (1984).

[4] D. E. Hastings, Phys. Fluids **27**, 2272 (1984).

[5] L. M. Kovrizhnykh, Nucl. Fusion **24**, 851 (1984).

[6] X. S. Lee, J. R. Myra, and P. J. Catto, Phys. Fluids **27**, 2248 (1984).

[7] D. E. Hastings and J. S. Tolliver, submitted to Phys. Fluids, 1985.

[8] D. W. Swain, J. A. Cobble, D. L. Hillis, R. K. Richards, and T. Uckan, Phys. Fluids **28**, 1922 (1985).

[9] R. J. Colchin, T. Uckan, F. W. Baity, L. A. Berry, F. M. Bieniosek, et al., Plasma Physics **25**, 597 (1983). See particularly Fig. 8.

[10] J. S. Tolliver, "A Bounce-Averaged Monte Carlo Transport Code for Elmo Bumpy Torus," Ph.D. dissertation, The University of Tennessee, Knoxville, 1984.

[11] N. A. Uckàn, C. L. Hedrick, D. A. Spong, T. Uckan, L. A. Berry, et al., "Elmo Bumpy Square," Oak Ridge National Laboratory Report ORNL/TM-9110, 1984.

[12] J. S. Tolliver, Phys. Fluids **28**, 1083 (1984).

[13] T. G. Northrop and E. Teller, Phys. Rev. **117**, 215 (1960).

[14] H. Grad and H. Rubin, in *Proceedings of the Second United Nations International Conference on the Peaceful Uses of Atomic Energy*, (The United Nations, Geneva, 1958), Vol. 31, p. 190.

[15] R. H. Fowler, J. A. Rome, and J. F. Lyon, Phys. Fluids **28**, 338 (1985).

Appendix 13

ALTERNATIVE CORNER COILS

Introduction

The method for making the corner coil sections as contained in the main body of this proposal has a number of attractive features:

1) There is high confidence in the design and fabrication of these coils. The conductor (rectangular copper with a circular hole for water cooling) has been used before, and the techniques for winding it into coils have been demonstrated in the existing EBT coils. The performance and reliability have been established through extensive use.

2) Diagnostic access to the plasma is possible using ports between these coils. Since there is a great deal of interest in the physics of the corner region, this access is quite important.

On the other hand, the use of these coils raises some concerns, principally because of the high power requirements for operation. The high field in the corner will require about 12 MW. That much power would be a major expense in operating the facility. In addition, the reliability of the power source (MG sets) is a concern for experimental availability, and the maintenance of the power source would also increase the operating costs.

These concerns have prompted an investigation of two options for the corners, one a novel copper coil configuration, the other a superconducting coil assembly. Each of these options offers a significant reduction in power consumption for maintaining the corner magnetic field. These two options are described below. The advantages of each are given, as well as some of the operational and developmental concerns.

Parameters of the coils for the Corner Section

The magnetic field required in the corner region is determined by the global mirror ratio. As demonstrated in Chapter 1, plasma confinement in EBS depends sensitively on this quantity. To investigate this dependence, global mirror ratio values of up to 6 should be available. A resonant field (at 28 GHz) of 1T results in a field of 0.5T at the ring location. A global mirror ratio of 6 leads to a field requirement of 3T in the corner; a desire for some flexibility in locating the ring raises this to 3.5T.

The current required to generate that field is roughly $1.5 - 2 \times 10^6$ A-t per corner. The current distribution differs in the various options, and is given below.

Copper Option

The resistive losses in the corner regions can be decreased by increasing the amount of copper available to carry the current required to produce the magnetic field. An obvious way to accomplish this is to use wedge-shaped coils which nose together tightly on the inside radius of the coil array and which completely fill the outer radius regions. Another method is to extend the conductor radially to the top, bottom, and outside. In this case the coil bore would no longer be in the center of the coil. Such a coil could be built using wedge-shaped rectangular plate with a spiral cut to produce the turns. A cooling channel using imbedded copper tubing would be used to remove the heat generated in the coils. These concepts, together with the baseline design, are shown in Fig. 13.1.

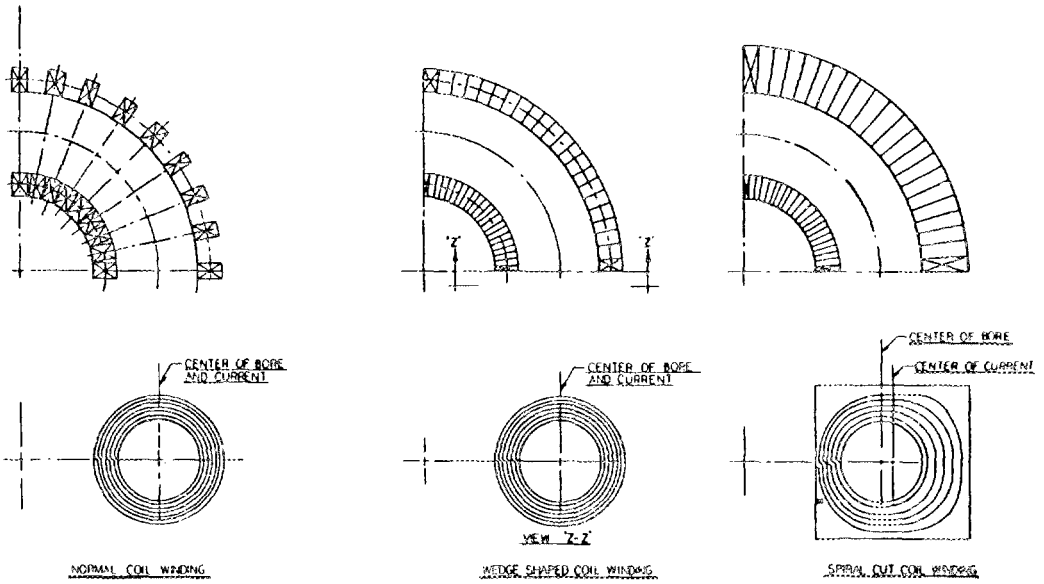

Fig. 13.1

This coil concept has been termed the spiral cut plate concept and has been studied for feasibility, cost, and schedule. In order to match the current/voltage characteristics of the existing MG power supplies, a configuration consisting of 22 coils of 8 turns each has been considered. A more detailed plan view of this concept is given in Fig. 13-2, and the side view is shown in Fig. 13.3. To optimize this concept (minimize the resistance) the locations of the spiral cuts have been chosen so that the resistance of each turn is nominally equal.

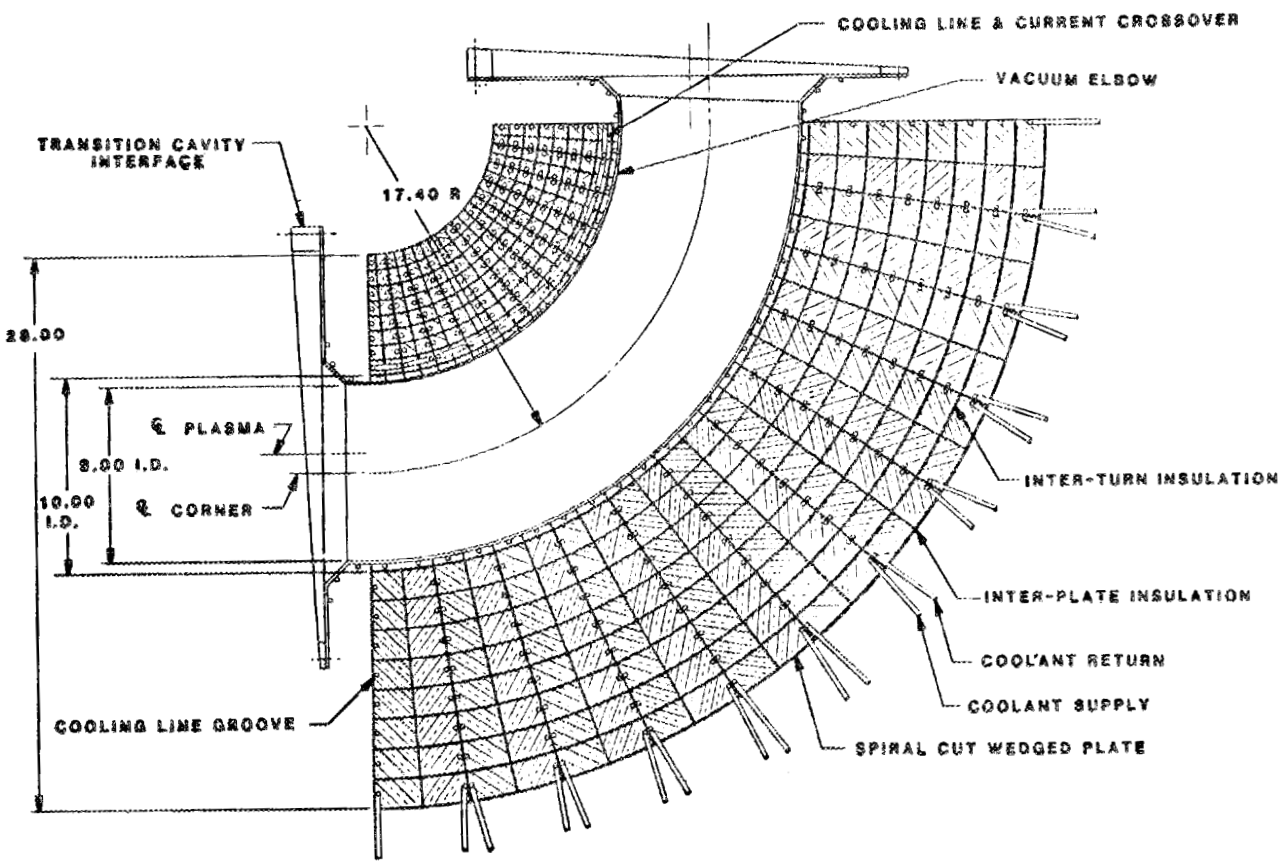

Fig. 13.2

The coil insulation would consist of sheet insulation inserted between turns and sheet insulation between the plates. The plates would be connected electrically in series using cross-overs to connect adjacent plates. A cooling circuit would consist of two plates, with the water spiralling in on one plate, then out on the adjacent plate. That two-plate combination would be potted using glass filled epoxy to maintain structural integrity and to carry the turn-to-turn loads. Special purpose potting molds have been considered in the estimate.

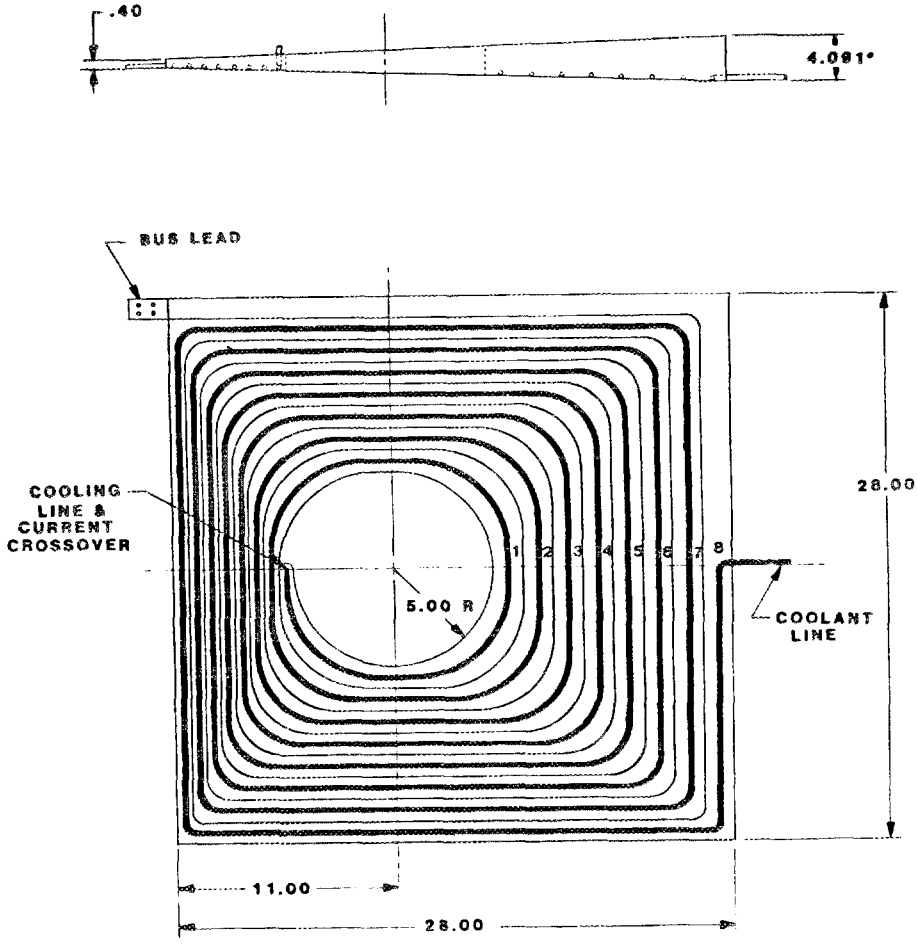

SPIRAL CUT PLATE

Fig. 13.3

These coils could be supported, and the utilities provided, in a manner very similar to that in the baseline approach. Development issues are:

(a) Wedge-shaped copper plate has not been produced. Although a manufacturer has expressed interest in rolling such plates, the availability has not been demonstrated. If flat plates were to be necessary, then the costs to machine it into a wedge shape would be about $50K.

(b) Diagnostic access in the corner region is eliminated, thereby precluding measurements of the corner plasma properties.

Superconducting Option

In this option the magnetic field in the corner would be produced by eight superconducting winding bundles in each corner. Each bundle consists of 112 turns, which results in 896 turns per corner. The coil current of 2.3 kA would be provided by a new, low voltage power supply. Coil operation at such low currents would give excellent stability. The arrangement of the corner coil array and its dewar are shown in Fig. 13-4.

The coils would be wound using surplus EBT-P superconductor, so there would be no procurement cost for the wire. Similarly, no procurement cost would be expected for the helium refrigerator, since there would be cryogenic equipment available from the Large Coil Program, which would be terminated by the time EBS would be operational. In the summary of the costs for the various options, the costs for the refrigerator and conductor are shown in parentheses, to indicate the increment which would be necessary, were these resources not available.

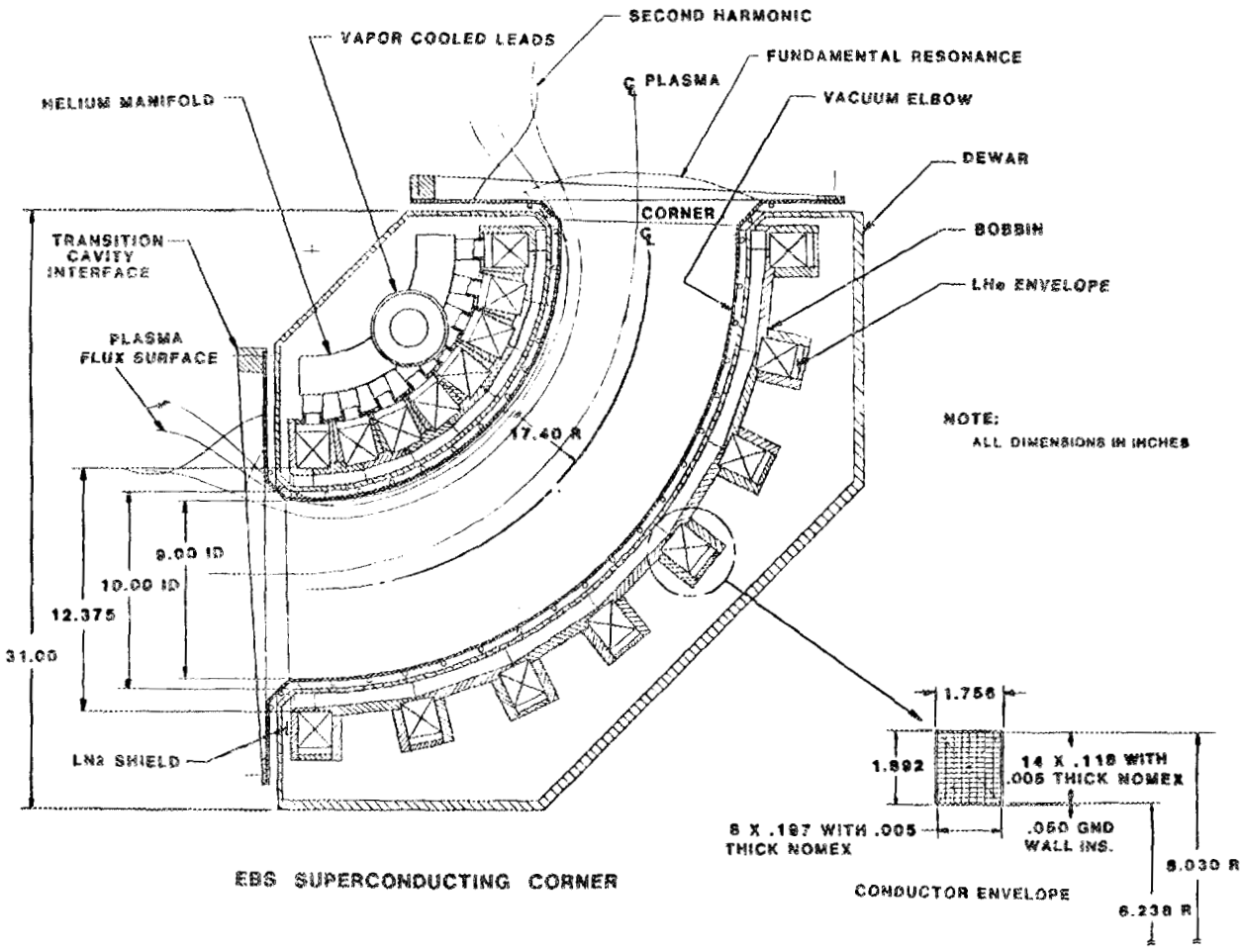

Fig. 13.4

The initial study of the concept has assumed that there would be one pair of vapor cooled leads per corner assembly. The operating costs could be further reduced by using a superconducting bus to connect the corners, thereby minimizing the heat load for the refrigerator. The heat load due to X-ray heating has been evaluated, and would be less than 1/2 W per corner.

Developmental issues are:

(a) The complex shape of the dewar within the limited space of the corner causes it to be a major influence in the overall cost.

(b) Installation of the liquid nitrogen shield and insulation will be a critical point due to minimal space between the cold mass and the dewar wall. However, it is felt that a viable design is possible within the space available.

(c) Fabrication of the bobbin as a monolithic unit will be of the same order of difficulty as the baseline corner concept, and does not require any development activities.

(d) A winding technique must be developed which minimizes the number of joints in the superconducting windings.

(e) Adequate space exists for the design of a realizable cold mass support scheme.

(f) The added space requirement of the dewar complicates the interface between the vacuum elbow (passing through the dewar) and the adjacent transition cavities. It may become necessary to modify the transition cavity design.

(g) Diagnostic access in the corner region is eliminated, thereby precluding measurements of the corner plasma properties.

(h) An adequate protection system for the coils would have to be designed and implemented.

Cost Comparison of the Various Options

The costs for individual elements for the various coil options are summarized below, in table 13-1.

As shown in this table, the capital costs for the two alternate options are, respectively, 50% and 100% greater than for the baseline design. However, the large reduction in power costs would offset the higher capital costs within a period of 1 to 2 years.

These estimates have been based on a variety of sources, including EBT-P magnet development, RFTF cryogenic installation, shop estimators, and vendors.

TABLE I

ELMO BUMPY SQUARE CORNER MAGNET STUDY

CONCEPT COSTS
($ IN THOUSANDS)

	WATER COOLED		SUPERCONDUCTING
	BASELINE DESIGN	SPIRAL CUT PLATE	
FACILITY COST			
FABRICATION	876	1,220	1,340
OTHER			
ELECTRICAL & CRYOGENICS	-	-	360
COIL MATERIAL	(50)*	90	(100)*
REFRIGERATION SYSTEM	-	-	(250)*
ENGINEERING	140	200	260
SUBTOTAL	1,016	1,510	1,960
OPERATING COST - (44 TEST WEEKS, 2.25 DAYS/WEEK, 8 HOURS/DAY: 800 HOURS)			
POWER ($41.5/MW HR)	400	60	35
SUBTOTAL	400	56	35

*COST OF REFRIGERATION SYSTEM AND COIL MATERIAL IF PURCHASED

Discussion

Both of these options meet the objectives of greatly reducing the operating costs due to power charges, and both suffer the disadvantage of eliminating diagnostic access in the corner region.

Each concept has some historical basis for confidence in producing the coils. Numerous superconducting coils have been built, with higher fields and more complex shapes (e.g. Baseball, Ying-Yang, etc.). A spiral cut plate coil, with flat plate, was built as a prototype for the ORMAK toroidal field coil.

The superconducting option would require the purchase of a new power supply. This would slightly increase the capital cost, but would result in a more reliable supply, and in decreased maintenance costs.

ORNL/TM-9994
Dist. Category UC-20f,g

INTERNAL DISTRIBUTION

1. F. W. Baity
2. D. B. Batchelor
3. L. A. Berry
4. W. E. Bryan
5. M. D. Carter
6. R. J. Colchin
7–16. R. A. Dory
17. G. R. Haste
18. C. L. Hedrick
19. D. L. Hillis
20. S. Hiroe
21. E. F. Jaeger
22. H. D. Kimrey
23. D. K. Lee
24. T. J. McManamy
25. L. W. Owen
26. D. A. Rasmussen
27. R. K. Richards
28. J. Sheffield
29. D. A. Spong
30. D. W. Swain
31. P. B. Thompson
32. J. S. Tolliver
33–42. N. A. Uckan
43. T. Uckan
44. T. L. White
45. J. B. Wilgen
46. W. L. Wright
47–48. Laboratory Records Department
49. Laboratory Records, ORNL-RC
50. Document Reference Section
51. Central Research Library
52. Fusion Energy Division Library
53. Fusion Energy Division Publications Office
54. ORNL Patent Office

EXTERNAL DISTRIBUTION

55. W. B. Ard, McDonnell Douglas Astronautics Co., P.O. Box 516, St. Louis, MO 63166
56. H. L. Berk, Institute for Fusion Studies, University of Texas, Austin, TX 78712
57. R. A. Dandl, Applied Microwave Plasma Concepts, Inc., 2210 Encinitas Boulevard, Encinitas, CA 92024
58. H. Grad, Courant Institute for Mathematical Sciences, New York University, 251 Mercer Street, New York, NY 10012
59. G. E. Guest, GA Technologies, Inc., P.O. Box 81608, San Diego, CA 92138
60. D. E. Hastings, Massachusetts Institute of Technology, 77 Massachusetts Avenue, Cambridge, MA 02139
61. H. Ikegami, Institute of Plasma Physics, Nagoya University, Nagoya 464, Japan
62. N. A. Krall, JAYCOR, P.O. Box 85154, San Diego, CA 92138

63. N. H. Lazar, TRW Defense and Space Systems, 1 Space Park, Redondo Beach, CA 92078
64. J. B. McBride, Science Applications International Corporation, P.O. Box 2351, La Jolla, CA 92037
65. R. L. Miller, Applied Microwave Plasma Concepts, Inc., 2210 Encinitas Boulevard, Encinitas, CA 92024
66. K. Moses, JAYCOR, 2811 Wilshire Boulevard, Suite 690, Santa Monica, CA 90403
67. J. F. Pipkins, McDonnell Douglas Astronautics Co., P.O. Box 516, St. Louis, MO 63166
68. M. N. Rosenbluth, RLM 11.218, Institute for Fusion Studies, University of Texas, Austin, TX 78712
69. R. J. Schmidt, McDonnell Douglas Astronautics Co., P.O. Box 516, St. Louis, MO 63166
70. J. W. Van Dam, Institute for Fusion Studies, University of Texas, Austin, TX 78712
71. H. Weitzner, Courant Institute for Mathematical Sciences, New York University, 251 Mercer Street, New York, NY 10012
72. Office of the Assistant Manager for Energy Research and Development, U.S. Department of Energy, Oak Ridge Operations Office, P. O. Box E, Oak Ridge, TN 37831
73. J. D. Callen, Department of Nuclear Engineering, University of Wisconsin, Madison, WI 53706-1687
74. J. F. Clarke, Director, Office of Fusion Energy, Office of Energy Research, ER-50 Germantown, U.S. Department of Energy, Washington, DC 20545
75. R. W. Conn, Department of Chemical, Nuclear, and Thermal Engineering, University of California, Los Angeles, CA 90024
76. S. O. Dean, Fusion Power Associates, 2 Professional Drive, Suite 248, Gaithersburg, MD 20879
77. H. K. Forsen, Bechtel Group, Inc., Research Engineering, P. O. Box 3965, San Francisco, CA 94105
78. J. R. Gilleland, GA Technologies, Inc., Fusion and Advanced Technology, P.O. Box 81608, San Diego, CA 92138
79. R. W. Gould, Department of Applied Physics, California Institute of Technology, Pasadena, CA 91125
80. R. A. Gross, Plasma Research Laboratory, Columbia University, New York, NY 10027
81. D. M. Meade, Princeton Plasma Physics Laboratory, P.O. Box 451, Princeton, NJ 08544
82. M. Roberts, International Programs, Office of Fusion Energy, Office of Energy Research, ER-52 Germantown, U.S. Department of Energy, Washington, DC 20545

83. W. M. Stacey, School of Nuclear Engineering and Health Physics, Georgia Institute of Technology, Atlanta, GA 30332
84. D. Steiner, Nuclear Engineering Department, NES Building, Tibbetts Avenue, Rensselaer Polytechnic Institute, Troy, NY 12181
85. R. Varma, Physical Research Laboratory, Navrangpura, Ahmedabad 380009, India
86. Bibliothek, Max-Planck Institut fur Plasmaphysik, D-8046 Garching, Federal Republic of Germany
87. Bibliothek, Institut fur Plasmaphysik, KFA, Postfach 1913, D-5170 Julich, Federal Republic of Germany
88. Bibliotheque, Centre des Recherches en Physique des Plasmas, 21 Avenue des Bains, 1007 Lausanne, Switzerland
89. F. Prevot, CEN/Cadarache, Departement de Recherches sur la Fusion Controlee, 13108 Saint-Paul-lez-Durance Cedex, France
90. Documentation S.I.G.N., Departement de la Physique du Plasma et de la Fusion Controlee, Centre d'Etudes Nucleaires, B.P. 85, Centre du Tri, 38041 Grenoble Cedex, France
91. Library, Culham Laboratory, UKAEA, Abingdon, Oxfordshire, OX14 3DB, England
92. Library, FOM-Instituut voor Plasma-Fysica, Rijnhuizen, Edisonbaan 14, 3439 MN Nieuwegein, The Netherlands
93. Library, Institute of Plasma Physics, Nagoya University, Nagoya 464, Japan
94. Library, International Centre for Theoretical Physics, Trieste, Italy
95. Library, Laboratorio Gas Ionizatti, CP 56, I-00044 Frascati, Rome, Italy
96. Library, Plasma Physics Laboratory, Kyoto University, Gokasho, Uji, Kyoto, Japan
97. Plasma Research Laboratory, Australian National University, P.O. Box 4, Canberra, A.C.T. 2000, Australia
98. Thermonuclear Library, Japan Atomic Energy Research Institute, Tokai Establishment, Tokai-mura, Naka-gun, Ibaraki-ken, Japan
99. G. A. Eliseev, I. V. Kurchatov Institute of Atomic Energy, P. O. Box 3402, 123182 Moscow, U.S.S.R.
100. V. A. Glukhikh, Scientific-Research Institute of Electro-Physical Apparatus, 188631 Leningrad, U.S.S.R.
101. I. Shpigel, Institute of General Physics, U.S.S.R. Academy of Sciences, Ulitsa Vavilova 38, Moscow, U.S.S.R.
102. D. D. Ryutov, Institute of Nuclear Physics, Siberian Branch of the Academy of Sciences of the U.S.S.R., Sovetskaya St. 5, 630090 Novosibirsk, U.S.S.R.
103. V. T. Tolok, Kharkov Physical-Technical Institute, Academical St. 1, 310108 Kharkov, U.S.S.R.
104. Library, Academia Sinica, P.O. Box 3908, Beijing, China (PRC)

105. D. Crandall, Experimental Plasma Research Branch, Division of Applied Plasma Physics, Office of Fusion Energy, Office of Energy Research, ER-542 Germantown, U.S. Department of Energy, Washington, DC 20545
106. N. A. Davies, Office of the Associate Director, Office of Fusion Energy, Office of Energy Research, ER-51 Germantown, U.S. Department of Energy, Washington, DC 20545
107. D. B. Nelson, Director, Division of Applied Plasma Physics, Office of Fusion Energy, Office of Energy Research, ER-54 Germantown, U.S. Department of Energy, Washington, DC 20545
108. E. Oktay, Division of Confinement Systems, Office of Fusion Energy, Office of Energy Research, ER-55 Germantown, U.S. Department of Energy, Washington, DC 20545 Washington, DC 20545
109. W. Sadowski, Fusion Theory and Computer Services Branch, Division of Applied Plasma Physics, Office of Fusion Energy, Office of Energy Research, ER-541 Germantown, U.S. Department of Energy, Washington, DC 20545
110. P. M. Stone, Fusion Systems Design Branch, Division of Development and Technology, Office of Fusion Energy, Office of Energy Research, ER-532 Germantown, U.S. Department of Energy, Washington, DC 20545
111. J. M. Turner, International Programs, Office of Fusion Energy, Office of Energy Research, ER-52 Germantown, U.S. Department of Energy, Washington, DC 20545
112. R. E. Mickens, Atlanta University, Department of Physics, Atlanta, GA 30314
113. Theory Department Read File, c/o D. W. Ross, Institute for Fusion Studies, University of Texas, Austin, TX 78712
114. Theory Department Read File, c/o R. C. Davidson, Director, Plasma Fusion Center, NW 16-202, Massachusetts Institute of Technology, Cambridge, MA 02139
115. Theory Department Read File, c/o R. White, Princeton Plasma Physics Laboratory, P.O. Box 451, Princeton, NJ 08544
116. Theory Department Read File, c/o L. Kovrizhnykh, Lebedev Institute of Physics, Academy of Sciences, 53 Leninsky Prospect, 117924 Moscow, U.S.S.R.
117. Theory Department Read File, c/o B. B. Kadomtsev, I. V. Kurchatov Institute of Atomic Energy, P.O. Box 3402, 123182 Moscow, U.S.S.R.
118. Theory Department Read File, c/o T. Kamimura, Institute of Plasma Physics, Nagoya University, Nagoya 464, Japan
119. Theory Department Read File, c/o C. Mercier, Departemente de Recherches sur la Fusion Controlee, B.P. No. 6, F-92260 Fontenay-aux-Roses (Seine), France
120. Theory Department Read File, c/o T. E. Stringer, JET Joint Undertaking, Culham Laboratory, Abingdon, Oxfordshire OX14 3DB, England

121. Theory Department Read File, c/o F. Briscoe, Culham Laboratory, Abingdon, Oxfordshire OX14 3DB. England
122. Theory Department Read File, c/o D. Biskamp, Max-Planck-Institut fur Plasmaphysik, D-8046 Garching, Federal Republic of Germany
123. Theory Department Read File, c/o T. Takeda, Japan Atomic Energy Research Institute, Tokai Establishment, Tokai-mura, Naka-gun, Ibaraki-ken, Japan
124. Theory Department Read File, c/o J. Greene, GA Technologies, Inc., P.O. Box 81608, San Diego, CA 92138
125. Theory Department Read File, c/o L. D. Pearlstein, L-630, Lawrence Livermore National Laboratory, P.O. Box 5511, Livermore, CA 94550
126. Theory Department Read File, c/o R. Gerwin, CTR Division, Los Alamos National Laboratory, P.O. Box 1663, Los Alamos, NM 87545
127. Duk-In Choi, Department of Physics, Korea Advanced Institute of Science and Technology, P.O. Box 150, Chong Ryang-Ri, Seoul, Korea

128–318. Given distribution according to TIC-4500, Magnetic Fusion Energy (Distribution Categories UC-20 f,g: Experimental Plasma Physics and Theoretical Plasma Physics)